

Sheffield Hallam University

Lattice modelling of liquid crystal mixtures

YARMOLENKO, Viktor

Available from the Sheffield Hallam University Research Archive (SHURA) at:

<http://shura.shu.ac.uk/9771/>

A Sheffield Hallam University thesis

This thesis is protected by copyright which belongs to the author.

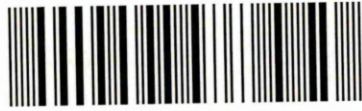
The content must not be changed in any way or sold commercially in any format or medium without the formal permission of the author.

When referring to this work, full bibliographic details including the author, title, awarding institution and date of the thesis must be given.

Please visit <http://shura.shu.ac.uk/9771/> and <http://shura.shu.ac.uk/information.html> for further details about copyright and re-use permissions.

SHEPHERD ST. 193

101 746 229 1



REFERENCE

ProQuest Number: 10701232

All rights reserved

INFORMATION TO ALL USERS

The quality of this reproduction is dependent upon the quality of the copy submitted.

In the unlikely event that the author did not send a complete manuscript and there are missing pages, these will be noted. Also, if material had to be removed, a note will indicate the deletion.



ProQuest 10701232

Published by ProQuest LLC (2017). Copyright of the Dissertation is held by the Author.

All rights reserved.

This work is protected against unauthorized copying under Title 17, United States Code
Microform Edition © ProQuest LLC.

ProQuest LLC.
789 East Eisenhower Parkway
P.O. Box 1346
Ann Arbor, MI 48106 – 1346

LATTICE MODELLING OF LIQUID CRYSTAL MIXTURES

VIKTOR YARMOLENKO, BSc MSc

A thesis submitted in partial fulfilment of the requirements

of Sheffield Hallam University for the degree of

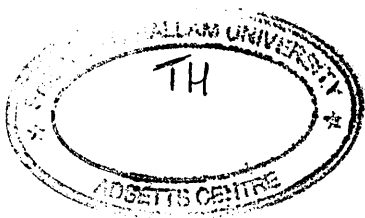
Doctor of Philosophy

20 November, 2003

Materials Research Institute, Sheffield Hallam University.

in collaboration with QinetiQ (Malvern).





I thought to myself, "Look, I have grown and increased in wisdom more than anyone who has ruled over Jerusalem before me; I have experienced much of wisdom and knowledge." Then I applied myself to the understanding of wisdom, and also of madness and folly, but I learned that this, too, is a chasing after the wind. For with much wisdom comes much sorrow; the more knowledge, the more grief.

King Solomon, Book of Ecclesiastes 1:16-18, The Bible

Man's greatest asset is the unsettled mind.

Isaac Asimov

Abstract

This Thesis is dedicated to computer simulation investigations of the phase behaviour of binary and ternary liquid crystals mixtures represented using the Lebwohl-Lasher lattice model. The binary mixture is studied in the Canonical and Semi Grand Canonical Ensembles over a comprehensive set of temperatures, concentrations and the relative coupling constants. The ternary mixture is studied in the Canonical Ensemble only, over a comprehensive set of temperatures and concentrations and single set of coupling constants.

In order to determine the boundaries between different phase regions in the Canonical Ensemble, the thermal and concentration dependencies of three different observables are used. The first observable is the potential energy of the system, the second is the second rank orientational order parameter and the third is the short-range radial distribution function. The long-range radial distribution function and the system snapshots are used as auxiliary observables.

In order to determine the phase boundaries in the Semi Grand Canonical Ensemble, the concentration dependence of the chemical potential is used. The order parameter is also used as an auxiliary observable in order to establish the symmetries of the phases on each side of the various coexistence regions encountered.

Some features of the phase diagram (e.g. phase re-entrance) are shown to be difficult to determine in the Canonical Ensemble, whereas other features (e.g. the boundary between two phase coexistence regions) are difficult to determine in the Semi Grand Canonical Ensemble. The remaining data from both ensembles are found to be in good agreement.

As well as homogeneous nematic (N) and isotropic (I) phases, regions of N+I and N+N phase coexistence are identified. For mixtures of similar particle types, two distinct coexistence regions are found, but as the particle types are made increasingly dissimilar, these two regions are found to coalesce. This leads to a distortion of the I-N transition temperature curve away from the behaviour predicted by classical ideal mixing rules.

The ternary mixture results show further departures from ideal mixing behaviour, while maintaining consistency with the data obtained from the equivalent binary systems. Also, unexpectedly, the cooperative ordering and phase separating of the intermediate particle type takes place at the same temperature for all concentrations considered. Overall, the results from ternary mixtures provide a focus for future work into the phase behaviour of multi-component and poly-disperse mesogenic systems.

Acknowledgements

In this thesis I have used the term "we" rather than "I". It could not be otherwise, after the help and support I have received from a number of people and bodies, whom I mention below.

First of all, I would like to thank my supervisors Dr Doug Cleaver and Prof Chris Care for their professionalism, continuing support, discussions and patience during this research project. They had a great deal of responsibilities to the University, the sponsors of the project, and me. I believe that they have done their jobs exceedingly well.

Secondly, I would like to acknowledge QinetiQ (Malvern) and the Materials Research Institute of Sheffield Hallam University who sponsored this PhD. Thank you to these bodies for their financial support.

Also, I would like to thank colleagues from the Modelling Group for their discussions, in particular Dr. Ian Halliday and Dr. Dmytro Antypov as well as computer support staff, in particular Mr. Kevin Blake.

I would like to acknowledge Ms Vivien Culver, whose English editorial skills helped me to transform a chunk of information into a written document that is fit for its purpose.

Finally, I am very grateful to my wife Iryna, who supported me morally and financially and helped me not to lose focus and motivation in turbulent times. I love you.

Advanced Studies

The following is a selection of related work undertaken and meetings attended during the course of study:

- British Liquid Crystal Society (BLCS) Winter Workshop, University of Hull, 20-22 December 1998
- Materials Research Institute Open Day, Sheffield Hallam Univeristy, 25 May 1999
- Level 3 Research Methods unit, SET Graduate School, Sheffield Hallam Univeristy, 1999-2000
- Level 3 Research Studies unit, SET Graduate School, Sheffield Hallam Univeristy, 1999-2000
- Collaborative Computational Project 5 (CCP5) Methods in Molecular Simulation Summer School, UMIST, 21-29 June 1999
- Presentation: Computer Modelling of Liquid Crystals, Materials Research Institute, Sheffield Hallam Univeristy, 2000
- Poster presentation: Mesoscopic Modelling of Liquid Crystal Coexistence, International Conference On Complex Fluids, Sheffield Hallam Univeristy, 11-13 September
- Poster presentation: Lattice Modelling Of Liquid Crystal Mixtures, European Liquid Crystals Conference, Halle, Germany, March 2001
- Poster presentation: Effect Of Binary Mixtures On Isotropic-Nematic Transition - A Lattice Model Study, European Conference on Computational Physics, Aachen, Germany, September 2001

Contents

1	Introduction	1
1.1	Liquid Crystals	2
1.1.1	Nematic Liquid Crystals	3
1.1.2	Ordering In LC	6
1.1.3	The Nematic Order Parameter	7
1.1.4	Radial Distribution Function	8
1.1.5	Second-Rank Orientational Correlation Function	9
1.2	LC Mixtures	10
2	Experimental Approaches And Theory	13
2.1	Order Parameters	14
2.2	Phase Transition	17
2.3	Theoretical Background	21
3	Simulation Approach	23
3.1	Monte Carlo Technique	26
3.2	The Lebwohl-Lasher Lattice Model	29
4	Model Basis And Details	35
4.1	General Details - $NcVT$, $N\Delta\mu VT$ Ensembles	36
4.1.1	Canonical Ensemble	37

4.1.2	Semi-Grand Canonical Ensemble	38
4.2	Interaction Potentials	39
4.3	Moves	41
4.4	Calculation of Microscopic Parameters	46
4.4.1	The Director And The Orientational Order Parameter	46
4.4.2	Radial Distribution Function Calculations	47
4.4.3	Orientational Correlation Function Calculations	49
4.4.4	Histogram Re-weighting Technique	51
4.4.5	Estimating Errors	52
5	Results And Discussion. Bi-Dispersed System. NcVT	55
5.1	Results for systems with varying ε	57
5.1.1	System with $\varepsilon = 0.9$	57
5.1.2	System with $\varepsilon = 0.6$	69
5.1.3	System with $\varepsilon = 0.45$	78
5.1.4	System with $\varepsilon = 0.3$	94
5.1.5	System with $\varepsilon = 0.1$	103
5.1.6	System with $\varepsilon = 0.0$	112
5.2	Phase Diagram Visualizer	118
5.3	Results for systems with varying c	119
5.3.1	System with $c = 0.7$	119
5.3.2	System with $c = 0.5$	120
5.3.3	System with $c = 0.2$	121
5.4	Interpretation and Discussion	123
5.4.1	The isotropic-nematic transition of the homogeneous system at $T_{tr}(c)$	128
5.4.2	Two component demixing at $T_d(c)$	132

5.4.3	Cooperative ordering and demixing.	133
5.4.4	Entering N+N coexistence at $T'_{tr}(c)$	134
5.4.5	Summary, phase diagrams, expectations, hypothesis	137
6	Results And Discussion. Bi-Dispersed System. $N\Delta\mu VT$.	150
6.1	System Evaluation And Introduction To The Results	152
6.2	Systems with $\varepsilon = 0.90, \varepsilon = 0.60, \varepsilon = 0.55$	157
6.3	System with $\varepsilon = 0.53, \varepsilon = 0.52, \varepsilon = 0.50$	173
6.4	System with $\varepsilon = 0.45, \varepsilon = 0.00$	190
6.5	Discussion Of $N\Delta\mu VT$ Results.	197
6.5.1	$T_{IN}(c_1, c_2)$ coexistence region	202
6.5.2	Nematic-nematic coexistence region	204
6.5.3	Coupled single coexistence region	205
6.5.4	Alternative Interpretation. Generalizing.	207
6.5.5	Conclusions Based on the NcVT, $N\Delta\mu VT$ Discussions	215
7	Results And Discussion. Ternary System. NcVT	217
7.1	Geometry Of The Phase Diagram For The Ternary Mixture	218
7.2	What We Know From Binary Systems	222
7.3	Results From Ternary Systems	223
7.3.1	Phase Behaviour in the A-Plane.	224
7.3.2	Phase Behaviour in B-bisector Plane.	235
7.3.3	Phase Behaviour in C-bisector Plane.	245
7.4	Discussion	253
7.4.1	Interesting Observations	259
8	Conclusions And Future Work	262

Chapter 1

Introduction

In this chapter, we give a brief outline of this thesis. The work described in this thesis relates to computer simulations performed with the aim of promoting greater understanding of the mechanisms responsible for ordering and phase separation in liquid crystal (LC) mixtures, since no single theoretical model has completely described these processes satisfactorily. Specifically, attention has been focussed on the phase behaviour of the Lebwohl-Lasher [1] lattice model, which has been modified to simulate binary and ternary mixtures.

Aside from this introduction, this thesis is organised as follows. A brief introduction to LCs and a description of the main types of LC and their properties follows in Section 1.1. In Chapter 2, a background to theoretical and experimental approaches is given, including various methods of measuring the order parameter and structural behaviour of LC systems. Next, in Chapter 3 we give a background to the simulation development. Here, Monte Carlo techniques and the Lebwohl-Lasher lattice model are introduced. This is followed in Chapter 4, by a detailed description of the model used to generate the results presented in this Thesis. Here, the implementation of Canonical and Semi-Grand Canonical Ensemble simulation are discussed, along with other simulation details, such as the calculation of relevant observables. In Chapter 5 we present the results from the first systems of interest. These are binary mixtures of mesogenic particles studied in the Canonical Ensemble. We present data from these simulations, and use the same to construct phase diagrams, before discussing the results. In Chapter 6 we present simulation results from the same set of binary mixtures of mesogenic particles, but this time studied in the Semi-Grand Canonical

Ensemble. In Chapter 7 we present the last systems of interest - ternary mixtures of mesogenic particles. In Chapters 5-7 we adopt the following structure when presenting the results. The original data are presented first, followed by a discussion of the presented results. The discussion for each chapter builds on those of the previous chapters. In Chapter 8 we summarize, briefly, all of the results presented and discussed in previous chapters and suggest possible future developments and research. Two appendices and a bibliography are also included.

1.1 Liquid Crystals

LCs are organic materials which exhibit an intermediate phase (a mesophase) between the isotropic liquid and crystalline solid states. Most of the mechanical properties exhibited by LCs are found in other liquids, the difference being that the properties of LCs are anisotropic, that is, they vary according to the direction in which they are measured. In addition, in ordered fluid phases, LCs exhibit long range orientational order. Long range translational order may also be present, in LCs, but they do not exhibit the full three-dimensional order of ordinary solid crystals. Owing

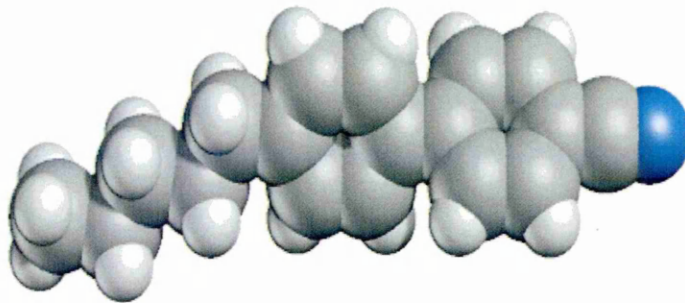


Figure 1.1: Structure of 5CB, a typical mesogen.

to their ability to form mesophases, LCs are often called mesogens. Mesogens are classified into two distinct categories: thermotropic and lyotropic. Thermotropic LCs form different mesophases due to changes of temperature, whereas lyotropic LCs do so with a change in concentration. Thermotropic mesogens are called enantiotropic if the process of moving from one mesophase to another is reversible; where the reverse process does not return the material into its original mesophase, they

are known as monotropic. Thermotropic mesophases have been found to be produced by two distinct types of molecular shape. The first of these is rod-like; LCs of this type are called calamatic ($\kappa\alpha\lambda\alpha\mu\omicron\varsigma$ - ‘reed’ or ‘straw’ in Greek) [2], and were discovered by Vorländer [3] at the beginning of the twentieth century. The second type, which are disk-like, are called discotic LCs ($\delta\iota\sigma\kappa\omicron\varsigma$ - ‘disk’ or ‘plate’ in Greek) and were discovered only relatively recently [4]. The molecular structure of 5CB, a typical calamatic, is presented in (Figure 1.1).

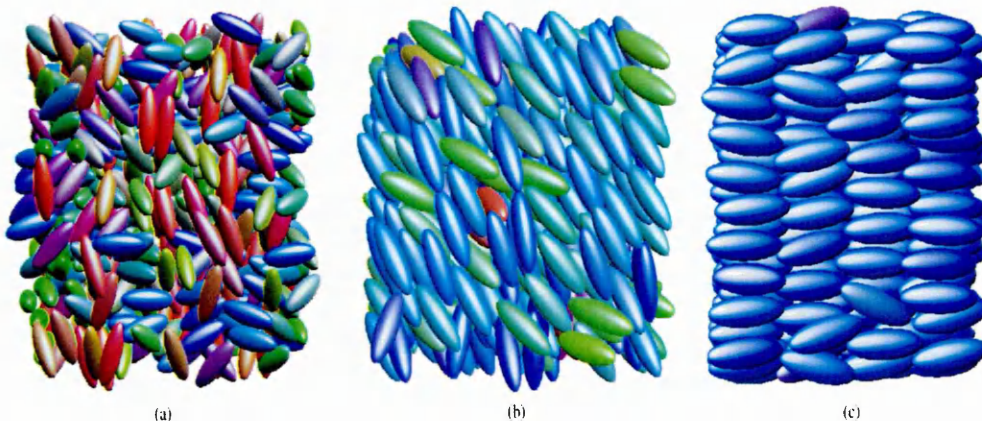


Figure 1.2: Isotropic (a), nematic (b) and smectic (c) phases of LC [5]

There are two main types of LC phase (Fig.1.2): nematic ($\nu\epsilon\mu\alpha\tau\omicron\varsigma$ - ‘thread’, ‘web’) and smectic ($\sigma\mu\eta\gamma\gamma\mu\alpha$ - ‘soap’, and $\sigma\mu\eta\kappa\tau\iota\kappa\omicron\varsigma$ - ‘that which is used for cleaning’). In the nematic phase there is orientational order, such that the long axes of the molecules are aligned in a preferential direction, but there is no translational order. In the smectic phases, the molecules are arranged in regularly spaced layers, such that there is a density wave running through the material, but the molecules have only short range positional order within these layers. Other phases formed are simply derivatives of these two main phases with additional properties - for example: cholesterics, chiral nematics, ferroelectric LCs, epitropic LCs [6] and so on.

1.1.1 Nematic Liquid Crystals

Of all LC phases, the nematic has the highest symmetry [7,8]. As was mentioned earlier, a nematic LC has long range orientational order, but no long range translational order. Thus it differs from the isotropic liquid (Fig.1.2) in that its molecules

are spontaneously oriented with their long axes approximately parallel to the director. The director is the preferred orientation of the molecules. The director usually varies from point to point in the medium, but a uniformly aligned specimen is optically uniaxial, positive and strongly birefringent. The mesophase owes its fluidity to the ease with which the molecules slide along one another while still retaining their mutual alignment.

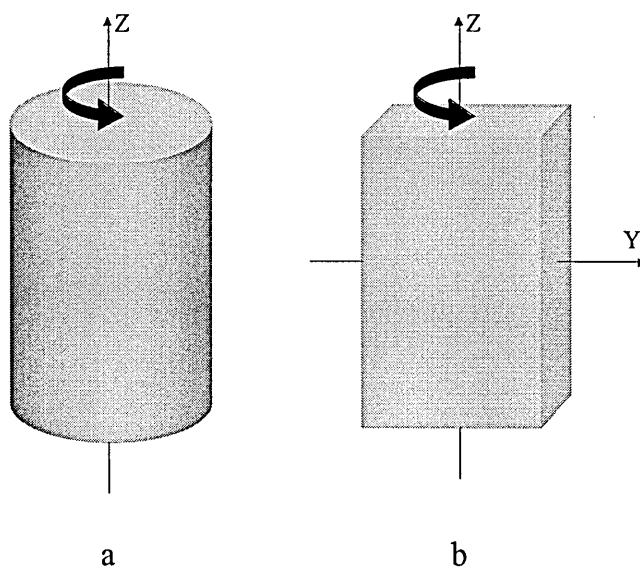


Figure 1.3: Uniaxial (a) and biaxial (b) symmetries

In order to avoid confusion concerning the terminology used to describe nematic mesophases, let us begin by clarifying the definitions of the various types of symmetry. We call an object uniaxial if it possesses cylindrical symmetry. Thus rotation about the Z axis by any angle translates the object into itself and its orientation is explicitly defined by only one axis Z (Figure 1.3(a)). Biaxial objects, on the other hand, are affected by rotation around the Z axis and their orientation requires two axes, Z and Y , to be defined (Figure 1.3(b)).

Another difference in symmetry relates to polarity. If an object is indifferent to the inversion through a point (or mirror reflection in the plane perpendicular to the Z axis), so that ‘head’ and ‘tail’ prove to be interchangeable, then such an object is called apolar (Fig.1.4(a)). If however, such an inversion (reflection) does not translate an object into itself then the object is polar (Fig.1.4(b)).

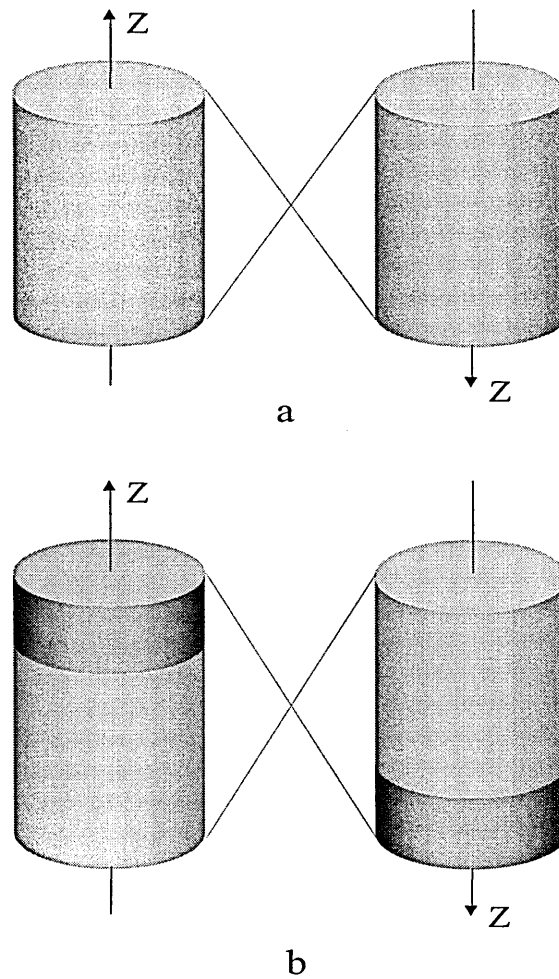


Figure 1.4: apolar (a) and polar (b) symmetries

Another consideration is the distinction between two types of symmetry: that of the mesogen and that of the mesophase. Biaxial mesogens may form a uniaxial mesophase, and polar mesogens may give an apolar mesophase, but uniaxial particles very rarely form biaxial phases and apolar mesogens do not form polar phases. One of the usual cases is that of a rod-like LC with longitudinal quadrupoles, which can yield chiral phases. In practice, however, the symmetry of the mesophase is almost always the same as or higher than that of the mesogens which form it, unless an external force (field, pressure, confinement) is applied to lower the symmetry of the mesophase.

1.1.2 Ordering In LC

Most phases differ with respect to their symmetry; they may be, for example, isotropic (spherical) or nematic (cylindrical). The transition between different phases usually corresponds to the breaking of a particular symmetry and can be described in terms of an order parameter Q . In general, the order parameter characterising the transition between the isotropic and nematic phases must satisfy the following requirements:

- $Q = 0$ in the less ordered, isotropic phase (higher symmetry), and
- $Q \neq 0$ in the more ordered, nematic phase (lower symmetry).

There are two approaches to measuring or defining the order parameter in LC: microscopic (mainly theoretical) and macroscopic (mainly experimental).

Microscopic order parameters are functions that give a description of the system on the intermolecular scale. They are constructed in relation to a specific molecular model and, by definition, may contain information above that which relates to the symmetry of the phase. It is convenient to present the microscopic order parameters of various LC mesophases as expansion coefficients of the singlet distribution function ρ , which depends on orientational (Ω) and positional (\hat{r}) coordinates [9–11]:

$$\rho(\hat{r}, \Omega) = \rho_0 \sum_{\hat{G}} \sum_{l,m,n} (2l+1) e^{-i[\hat{G}\cdot\hat{r}]} D_{m,n}^l(\Omega) \langle e^{-i[\hat{G}\cdot\hat{r}']} D_{m,n}^{l*}(\Omega') \rangle \quad (1.1)$$

The functions $D_{m,n}^l(\Omega)$ are the Wigner rotation matrices, the angular brackets represent an ensemble average and \hat{G} is the set of reciprocal lattice vectors of the crystalline phase [12]. Equation (1.1) can be rewritten as

$$\rho(\hat{r}, \Omega) = \rho_0 \sum_{\hat{G}} \sum_{l,m,n} Q_{lmn}(\hat{G}) e^{-i[\hat{G}\cdot\hat{r}]} D_{m,n}^l(\Omega) \quad (1.2)$$

where $Q_{lmn}(\hat{G})$ is a set of order parameters. These are logically divided into three sub-categories:

- $Q_{000}(\hat{G})$ are positional order parameters for a monoatomic lattice,
- $Q_{lmn}(0)$ (or $\bar{D}_{m,n}^{l*}$) are the orientational order parameters and
- $Q_{l00}(\hat{G})$ are the mixed (orientational-positional) order parameters.

1.1.3 The Nematic Order Parameter

The most fundamental characteristic of LCs is their property of long range orientational order. From Equation(1.2), all orientational order parameters read:

$$Q_{lmn}(0) \equiv (2l + 1)\langle D_{m,n}^{l*} \rangle = \left(\frac{2l + 1}{N} \right) \int d\hat{r} d\Omega \rho(\hat{r}, \Omega) D_{m,n}^{l*}(\Omega) \quad (1.3)$$

The orientation of a molecule can be described by the Euler angles (θ, γ, ψ) . In the apolar nematic mesophase, only terms with even l can contribute to Equation (1.3). In addition, if one assumes that the mesogenic molecules possess cylindrical symmetry then n must be equal to zero. Finally, if the coordinate system is chosen such that the director coincides with the Z axis, then m must also equal zero. Thus, the orientational order parameter $Q_{l00}(0)$ depends on only one of the Euler angles (θ) - the angle between the long axis of each molecule and the director:

$$Q_{l00}(0) = \langle P_l(\cos \theta) \rangle \quad (1.4)$$

where $\langle P_l(\cos \theta) \rangle$ is an ensemble average of an even Legendre polynomial, and the angular brackets denote an average over all molecules in the system. Legendre polynomials are a convenient tool for use in this situation, since they were designed to deal with problems of broken spherical symmetry.

Higher rank Legendre polynomials ($l = 4, 6, 8, \dots$) are seldom used, owing to their relatively insignificant contribution to ρ in Equation (1.2). Only after the 1970s did the measuring of P_4 become possible experimentally [13]. Ranks six and higher are still hard to obtain experimentally [14] owing to the fluctuations in the systems. Usually, only the second rank Legendre polynomial P_2 is used to define uniaxial nematic order parameter S , as was first proposed by Tsvetkov in 1942 [15]:

$$S = \langle P_2(\cos \theta) \rangle = \frac{1}{2} \langle (3 \cos^2 \theta - 1) \rangle \quad (1.5)$$

In most cases, the microscopic order parameters, as described above, provide an adequate description of real mesogenic systems. However, in some experimental situations, this is not readily accessible and some other means must be found to specify the order parameter. A significant difference between the isotropic and liquid crystalline phases is observed in the measurements of all macroscopic tensor properties (diamagnetic susceptibility, refractive index, etc); these properties can, therefore, be

used to identify the macroscopic order parameter. One of the macroscopic properties of an LC which has been measured experimentally [8] is the diamagnetic susceptibility $\hat{\chi}$. The relationship between $\hat{\chi}$ and molecular properties is relatively well understood when compared with other macroscopic properties. The relationship between the value of an applied field \hat{H} and the magnetic moment \hat{M} reads as:

$$M_i = \chi_{ij} H_j \quad (1.6)$$

where i, j are the x, y, z indices of $\hat{\chi}$. The tensor $\hat{\chi}$ is symmetric in the case of static \hat{H} , and its diagonal elements in the case of the isotropic (I) and uniaxial nematic (UN) phases read as:

$$\chi_{\hat{I}} = \begin{pmatrix} \chi & 0 & 0 \\ 0 & \chi & 0 \\ 0 & 0 & \chi \end{pmatrix} \quad \chi_{\hat{UN}} = \begin{pmatrix} \chi_{\perp} & 0 & 0 \\ 0 & \chi_{\perp} & 0 \\ 0 & 0 & \chi_{\parallel} \end{pmatrix} \quad (1.7)$$

where χ_{\parallel} and χ_{\perp} are the susceptibility components, respectively, parallel and perpendicular to the Z axis. To determine \hat{Q} from the diamagnetic susceptibility, the requirement

$$Q_{ij} = \frac{\Delta\chi_{ij}}{\Delta\chi_{max}}, \text{ or } \hat{Q} = \frac{1}{\Delta\chi_{max}} \begin{pmatrix} -\frac{1}{3}(\chi_{\parallel} - \chi_{\perp}) & 0 & 0 \\ 0 & -\frac{1}{3}(\chi_{\parallel} - \chi_{\perp}) & 0 \\ 0 & 0 & -\frac{2}{3}(\chi_{\perp} - \chi_{\parallel}) \end{pmatrix} \quad (1.8)$$

is imposed where $\Delta\chi_{max}$ is the maximum anisotropy which would be observed for a perfectly ordered mesophase, chosen as normalization.

1.1.4 Radial Distribution Function

From Equation.(1.2), all positional order parameters $Q_{000}(\hat{G})$ read:

$$Q_{000}(\hat{G}) = \frac{1}{N} \int d\hat{r} d\Omega \rho(\hat{r}, \Omega) e^{-i[\hat{G} \cdot \hat{r}]} \quad (1.9)$$

Positional order parameters for a monoatomic lattice are characterized by the set of reciprocal lattice vectors \hat{G} . Therefore this function does not contain information about molecular orientations. Often, the radial distribution function is denoted

$g(r)$. $g(r)$ provides structural information about the system. It is defined as the probability of finding a pair of molecules separated by distance r , relative to the probability expected for a completely random distribution at the same density.

A further extension of the radial distribution function is its use in defining the degree of positional order in mixtures. In this case Equation (1.9) is rewritten to calculate the probability of finding a pair of like ($g_{AA}(r)$, $g_{BB}(r)$) or unlike ($g_{AB}(r)$) molecules at distance r . In our simulations, the distribution function $g_{AB}(r)$ is used to measure the positional correlations of unlike spins on the lattice employed. The like distribution functions, $g_{AA}(r)$ and $g_{BB}(r)$ are found to adopt very similar shapes, the only difference being their amplitudes which depend on the concentration ratio of the compounds. It is also the case that $g_{AB}(r) \equiv g_{BA}(r)$. However, this identity does not hold for real systems, where these functions can be used to characterise transitions between liquid and solid crystal phases as well as different mesophases (nematic, smectic, etc).

1.1.5 Second-Rank Orientational Correlation Function

Using Equation (1.2), orientational-positional order parameters are given by:

$$Q_{l00}(\hat{G}) = \left(\frac{2l+1}{N} \right) \int d\hat{r} d\Omega \rho(\hat{r}, \Omega) e^{-i[\hat{G} \cdot \hat{r}]} P_l(\cos \theta) \quad (1.10)$$

In the present work only the second-rank ($l = 2$) orientational correlation function is used, this being denoted $g_2(r)$. This correlation function can be looked on as being the orientational order parameter for molecules separated by distance r and allows for independent evaluation of short range and long range orientational order correlations.

The value of $g_2(r)$ levels off at large separations r and can be related to the usual nematic order parameter via:

$$S = \sqrt{g_2(r \gg 1)} \quad (1.11)$$

In small systems, such as those investigated in this thesis, short range orienta-

tional correlations become significant when calculating the average order parameter $\langle P_2(\cos \theta) \rangle$. Also, the value of $\langle P_2(\cos \theta) \rangle$ fluctuates considerably in the vicinity of the isotropic-nematic transition, which makes it difficult to detect the exact temperature of the transition. Because of this, both $g_2(r)$ and $\langle P_2(\cos \theta) \rangle$ were used to calculate the orientational order parameter of the system. The method used to obtain the $g_2(r)$ function is described in Section 4.4.3.

1.2 LC Mixtures

The use of LC mixtures is now widespread, each application having its own set of requirements. These requirements can be met by using specially designed mixtures of various compounds. LC mixtures can be divided into two main categories:

- Mesogen-mesogen [16]. These are either mixtures that include LCs which are of the same type, but have different properties (elastic constants, I-N transition point, etc), such as, a nematic-nematic mixture; or mixtures that include LCs of different types, for example, smectic-nematic, discotic-calamatic, etc.
- Mesogen-non-mesogen [17]. These are mixtures that include isotropic materials, polymers and other non-mesogens, for example, LC-isotropic mixture, LC and chiral dopant, LC and dye molecules, PDLC, PNLC, etc.

In addition, mixtures can be either bi-dispersed (binary) or poly-dispersed (ternary, quaternary, etc). Most theoretical and simulation studies have been devoted to the former. However, real LC mixtures are almost always poly-dispersed, owing to the technological difficulty of obtaining 100% pure material. Binary LC systems have been widely exploited in contemporary technology because of the facility with which they change their physical parameters in response to changes in composition [18,19]. For example, mixing LCs that have different phase transition temperatures T_{tr} usually results in a lower transition temperature for the mixture (Figure 1.5) than that of the pure component with the higher T_{tr} [20], while the Fréedericksz transition point for the critical field may either remain at the level of one of the components or change in either direction [21–24].

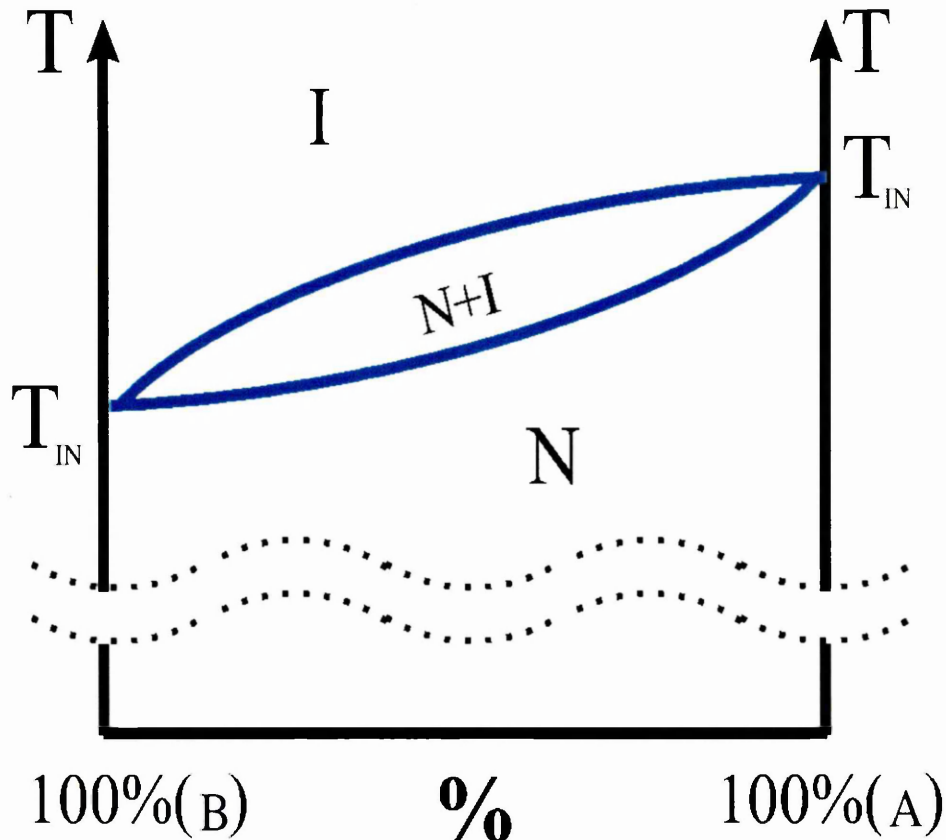


Figure 1.5: Isotropic-nematic transition temperature of a generic binary mixture [7, 8].

Theoretical studies of binary mixtures predict rather more complicated phase behaviour than that presented in Figure 1.5. In such studies, the coexistence region in the vicinity of the isotropic-nematic phase transition not only becomes narrower near to the region of high concentration, but also deviates from having approximately linear dependence on the concentration; this was predicted by Maier-Saupe theory, which was later extended by Humphries *et al* [25]. Subsequently, Palffy-Muhoray *et al* [26] developed another theory designed to investigate the properties of binary mixtures. These investigations have led to the following conclusions:

- For certain values of the parameters, it is possible to have a nematic-nematic coexistence region. Coexisting nematic phases have been observed in mixtures of LC polymers [27], other low molecular mass LCs [28], and in mixtures of rod-shaped and disc-shaped nematogens [29].

- The order parameter of the mixture and its variation with temperature agree with the Maier-Saupe universal curve. However, the order parameter of the individual components of the mixture may differ from each other significantly [30].

In theory, it is possible to obtain a mixture with virtually any combination of required characteristics. In practice, however, certain difficulties can arise, such as phase separation between the various components under certain conditions. Therefore the investigation of mixtures, and particularly of their phase behaviour and their dependence on the parameters of each LC involved (weight percentage, coupling constants, elastic constants, etc.), has attracted major interest. Further progress in the study of LC mixtures depends on better understanding of the processes and theoretical background, since the physical properties of LCs change non-trivially when other compounds are added.

Chapter 2

Experimental Approaches And Theory

For a considerable period after their discovery in the late nineteenth century by the Austrian botanist Reinitzer [31], LCs were the subject of very few studies [32–36]. The earliest of these involved, essentially, optical observation through a polarizing microscope [32]. Some attempts were made to synthesize mesogens [3, 37–39] and to understand the structure of their phases [35, 36]. In the early twentieth century, nematic, cholesteric and smectic A mesophases were observed and their structures clarified by Friedel [32]. Thereafter, interest in mesogenic materials seemed to diminish; there were a few publications in the 1930s [40–42] on the discovery of the electro-optical effect in LC [40], in the 1940s [15, 43, 44] on the high magnetic birefringence of LCs, and in the 1960s on the Kerr effect in LCs [45], along with studies of LC mixtures [22, 46]. Only in the 1970s was the importance of potential applications to thermography and electro-optic devices realized, and this gave a new impetus to the investigation of the properties of LCs, employing such experimental techniques as switching measurements [47–49], dielectric spectroscopy [50–53], electro-optic spectroscopy [54, 55] and pyroelectric measurements [56]. Recent developments in experimental techniques such as scanning probe microscopy have been developed mainly in relation to the behaviour of LCs near the surface.

2.1 Order Parameters

Let us consider the properties of mesogenic materials in the isotropic and nematic phases. One of the signs of an I-N phase transition is a change in the order parameter S . Experimental observations using various techniques show that the order parameter decreases monotonically as the temperature is raised in the mesophase range, and drops suddenly to zero at the transition temperature $T/T_{tr} = 1$ (Figure 2.1). The fact that the I-N transition is first order leads to large pretransitional changes in other thermodynamic properties (which can be measured experimentally), such as the specific heat. However, the I-N transition is a weak first-order transition. The changes in entropy and volume associated with this transition are typically only a few percent of the corresponding values for the solid-nematic transition. For example, the energetic barrier between the equilibrium states of the isotropic and nematic phases at the transition temperature T_{tr} is only of the order 1kJ/mol.

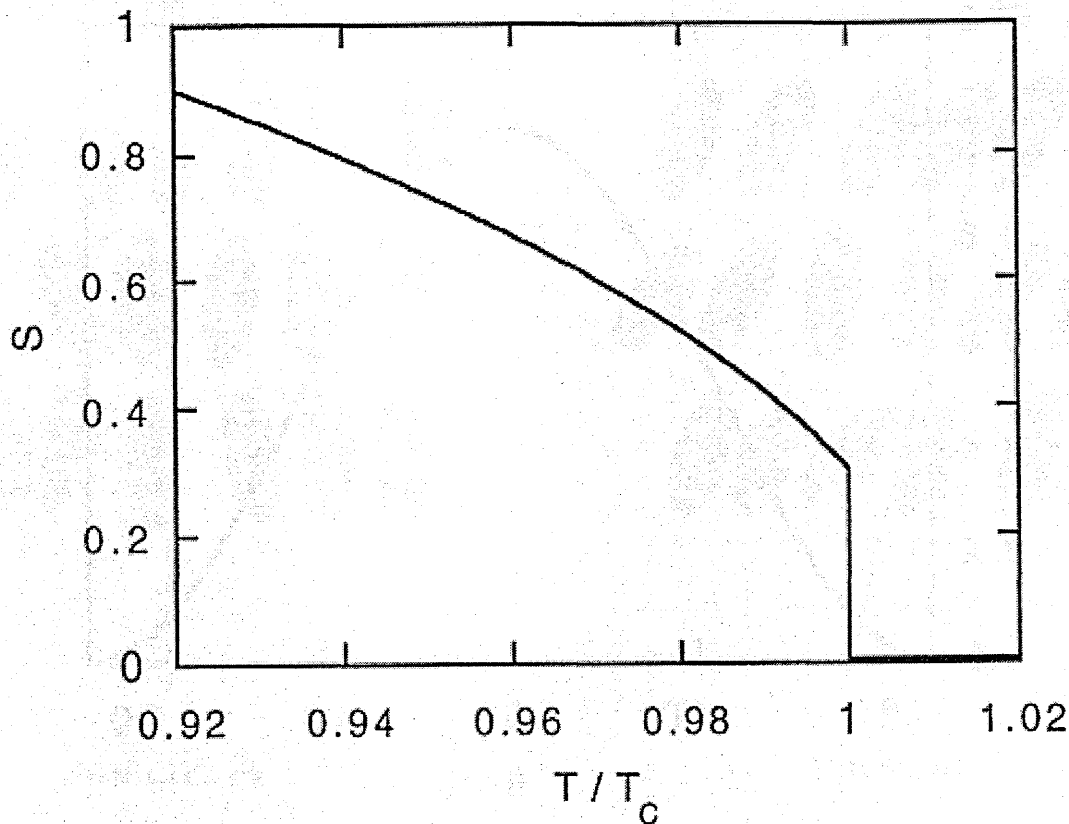


Figure 2.1: Orientational nematic order parameter [57]. Notation T_c used in [57] is equivalent to T_{tr} .

A number of different techniques have been employed to determine the second-rank orientational order parameter: optical birefringence experiments [31, 38] and magnetic susceptibility measurements [8] as well as the conventional X-ray diffraction [58–61] technique (which found its application in the shear flow studies of LC [59, 62–64]), etc. However, the usefulness of these techniques is limited because microscopic order parameters calculated from measured macroscopic properties are based on assumptions about molecular properties such as, for these examples, the magnetic polarizability and the optical polarizability.

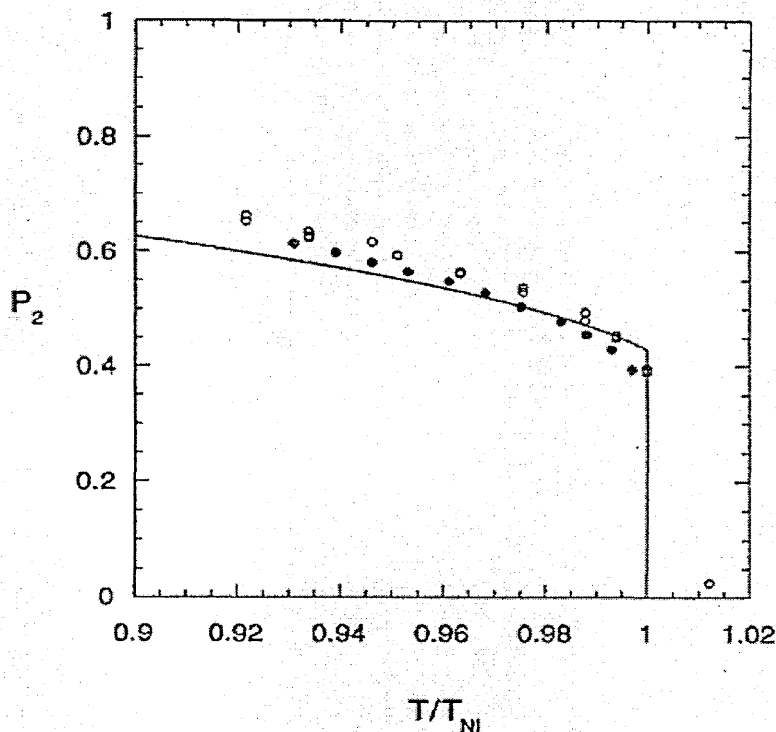


Figure 2.2: Second Rank Orientational Order Parameters: obtained from SANS (open circles) and NMR (filled circles) experiments. The solid line shows the prediction of the Maier-Saupe theory. [14]

Other methods which study the molecular orientational ordering in the nematic phase, and which have been widely used recently, are the various spectroscopic techniques such as nuclear magnetic resonance (NMR) [65–77], electron spin resonance (ESR) [78–80], fluorescence depolarization [81] and polarized Raman spectroscopy [82–84], etc. Most of these techniques can provide results for order parameters up to rank four.

Spectroscopic techniques have also been used in measurements of LC mixtures. Bunnell *et al* [76] investigated the temperature dependence of the NMR spectra of the

solutes. Measured order parameters were related to the intermolecular forces of mean field theory. In [66] the anisotropic intermolecular forces that are responsible for the orientational ordering in LC were studied by comparing computer simulations of hard ellipsoids with experimental NMR results for solutes in a nematic LC. All long range interactions were ‘minimized’ with a special LC mixture. The short range interactions calculated from the NMR experimental solute order parameters were in good agreement with the simulation results. In [70] NMR was used to determine the degree of order of the solute and solvent molecules of a nematic LC in a zero gradient electric field. The comparison indicated that for a variety of molecules differing in size, shape and flexibility, the degree of order could be described by a single orientation mechanism. This mechanism was found to be adequately modelled by a simple phenomenological mean field model based on the size and shape anisotropy of the dissolved species. The use of zero field gradient in mixtures, in combination with this mean field model, allowed the prediction of solute order parameters to an accuracy of approximately 10%.

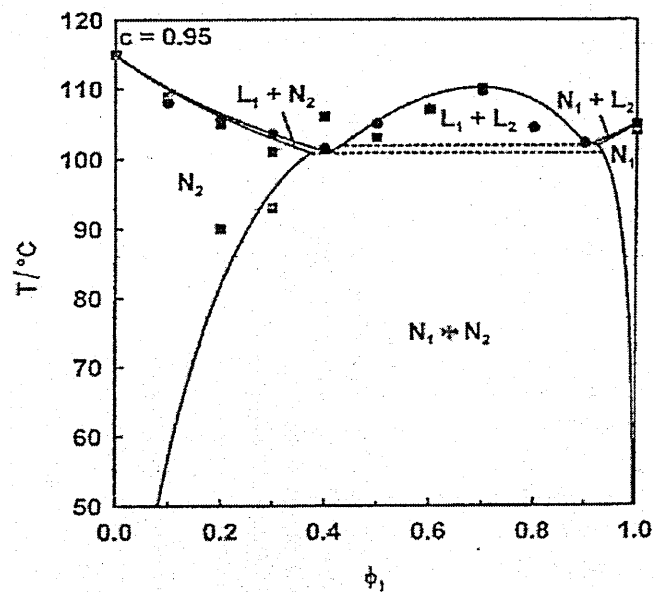
In the 1990s, small angle neutron scattering (SANS) was employed to study the long range orientational order in LCs [14]. The advantage of this method is that the diffraction does not depend on the properties of a certain rank and, according to [85], can be used to obtain a virtually complete set of orientational order parameters. In [14], however, it was found that in practice a significant statistical contribution could be made only to the second- and fourth-rank terms in the expansion of the single molecule scattering, which means that only the second- and fourth-rank order parameters could be obtained. These order parameters were obtained from the anisotropic single molecule scattering, isolated at small scattering angles. The results for the orientational order parameters were compared with those obtained by NMR, and with those predicted by the Maier-Saupe theory. For the studied nematogen, the Maier-Saupe theory was found to underestimate the second-rank order parameter and its dependence on the reduced temperature T/T_{NI} . However, the measured values of the fourth-rank order parameter were in very good agreement with the theory. For the same materials, order parameters obtained by NMR were found to be slightly lower than those determined by the SANS experiment (Fig.2.2).

A number of approaches such as Raman spectroscopy [84], neutron scattering experiments [86] and others [87] have been adopted in the study of orientational order and radial distribution functions, using the so-called Guest-Host technique. In [86],

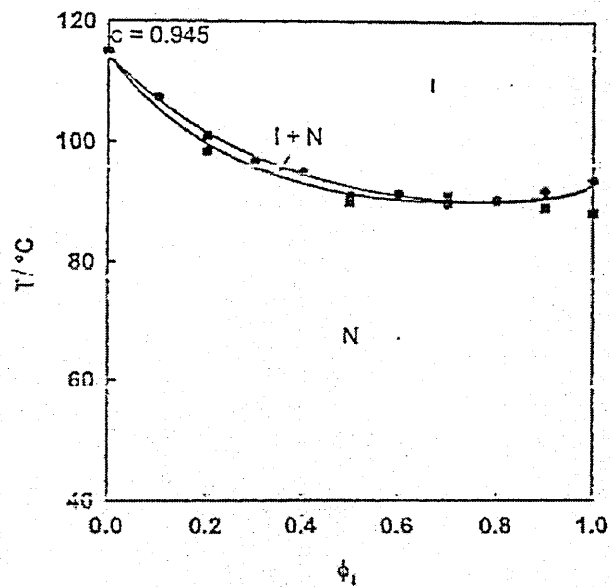
the orientational distribution function in an LC was studied. Isotropically labelled guest molecules were inserted into a host-LC environment and studied by means of the neutron scattering technique. A very similar approach was used in both infrared linear dichroism experiments on nematic solutions [87], designed to investigate the orientation of guest molecules in nematic hosts, and in FT-Raman polarization spectroscopy of non-mesogenic guest molecules oriented in nematic LC solvents [84]. Attempts were made to obtain an orientational distribution function from the inversion of the wide angle scattering data [88].

2.2 Phase Transition

The early experimental determination of the critical-like behaviour of the I-N phase transition employed a light scattering technique [89–91]. Later, the Kerr effect [92], the Cotton-Mouton effect [93–96] and the non-linear dielectric effect [97–101] were used. Differential scanning calorimetry (DSC) [102–104] was also used in locating phase transitions. All of these studies showed a pretransitional anomaly in the isotropic phase of nematogens. Nematic LCs have long range correlations even well away from critical points or hydrodynamic instabilities [105]. The results of early investigations [106–108] of the heat capacity anomaly near the I-N transition were so contradictory that at times they did not allow even a qualitative interpretation. Anisimov *et al* [109] measured the temperature dependence of the specific heat for MBBA near the I-N transition, and analysis of this dependence showed that fluctuations of the order parameter were not inconsiderable at the phase transition point. Recently, Rzoska *et al* [98,99] discussed the critical behaviour of the dielectric permittivity in the isotropic phase of nematogens, and showed that near the I-N transition the dielectric permittivity follows the same pattern found in binary solutions at critical points. Subsequently, high-pressure studies [100] were made of the pretransitional effects of the I-N transition of MBBA, and of the low-frequency non-linear dielectric effect in the isotropic phase of the mesogen. This investigation also showed the close relationship between the pretransitional behaviour in the isotropic phase of nematogens and that in the homogeneous phase of solutions at critical temperatures. All of these studies of fluctuation phenomena near to weakly first-order phase transitions contributed to an understanding of the physical reasons for their ‘closeness’ to the second order.



(a)



(b)

Figure 2.3: Phase diagrams (filled symbols) of mixtures (a) s-SCLCP and E_{44} , (b) s-SCLCP and E_{48} [20]. Solid lines represent theoretical prediction based on FH-MS theory with relative strength of the cross-nematic interaction to that of the pure mesogens taken to be (a) $c=0.95$. (b) $c=0.945$.

Mixed liquid crystal formation has been extensively studied by Dave and Vasanth [46], Yu and Labes [110], and Gupta and Vora [16], and their work has provided a foundation for studies of systems consisting of both mesogens and non-mesogens. Binary [111], ternary [112] and quaternary [113] mixtures of both enantiotropic and monotropic LC were studied by Naoum *et al* [114]. Unfortunately, the materials they used exhibited not a nematic, but a smectic, phase. However, the behaviour of the isotropic - liquid crystalline curve on the phase diagrams from [111] may have some relevance to our simulation results for the I-N curve for binary mixtures.

Also, nematic mixtures (mainly binary) which contain polymers have been extensively studied experimentally with a view to informing the design of novel devices (PDLC [115], PNLC [116], etc. [117]). In such mixtures of LCs and polymers (isotropic or mesogenic), miscibility and phase separation boundaries are of great importance in photopolymerization [118] and other processes [119]. Recently, many experimental studies have been devoted to this problem [20, 120–122]. As will be shown shortly, there are two main mechanisms whereby phase separation may occur in the mixture: immiscibility driven separation (leading to liquid-liquid phase coexistence) and nematic order driven separation (leading to nematic-nematic phase coexistence). With regard to the former, it was found that the most significant characteristic of LC-polymer mixtures was the molecular mass of the compound containing a polymer; whereas the latter was largely controlled by the difference in I-N transition temperatures for the pure compounds.

Experimental investigation of such mixtures was conducted and reported in 1998 [20]. Using the methods of light scattering and optical microscopy, two different systems were studied. For both systems, the mixtures used contained both LC polymer (*s*-SCLCP [20]) and another compound, this being a low molecular mass mesogen which was different for each system (E_{44} and E_{48} [20]). The main difference between the two systems was the I-N transition temperature of the two types of LC component. Photo pictures of both samples at various temperatures, which explicitly showed droplet formations and phase separation, were used to construct phase diagrams of the experimental mixtures (Figure 2.3(a),(b)). The results were compared in the context of a combination of the Flory-Huggins theory for isotropic mixing and the Maier-Saupe theory of nematic ordering [123]. These phase diagrams revealed the existence of liquid-liquid as well as $N_1 - N_2$ coexistence phases in one of the mixtures (Fig. 2.3(b)), while in another, the system formed a single

nematic phase instead of $N_1 - N_2$, which is indicative of miscibility (Fig. 2.3(a)). A similar phase diagram was reported in 1982 by Finkelmann and co-workers [120] for a different LC-polymer mixture.

In another study, an LC - isotropic polymer mixture was studied using light scattering, optical microscopy and DSC techniques [121]. The resultant phase behaviour was found to be influenced by the molecular mass of the polymer. In such mixtures, liquid-liquid coexistence was present when there was a high molecular mass isotropic polymer. As the molecular mass of the polymer was decreased, however, the liquid-liquid coexistence region disappeared. The results were compared with other studies of such mixtures [122], with the Flory-Huggins theory for isotropic mixing and with the Maier-Saupe theory of nematic ordering.

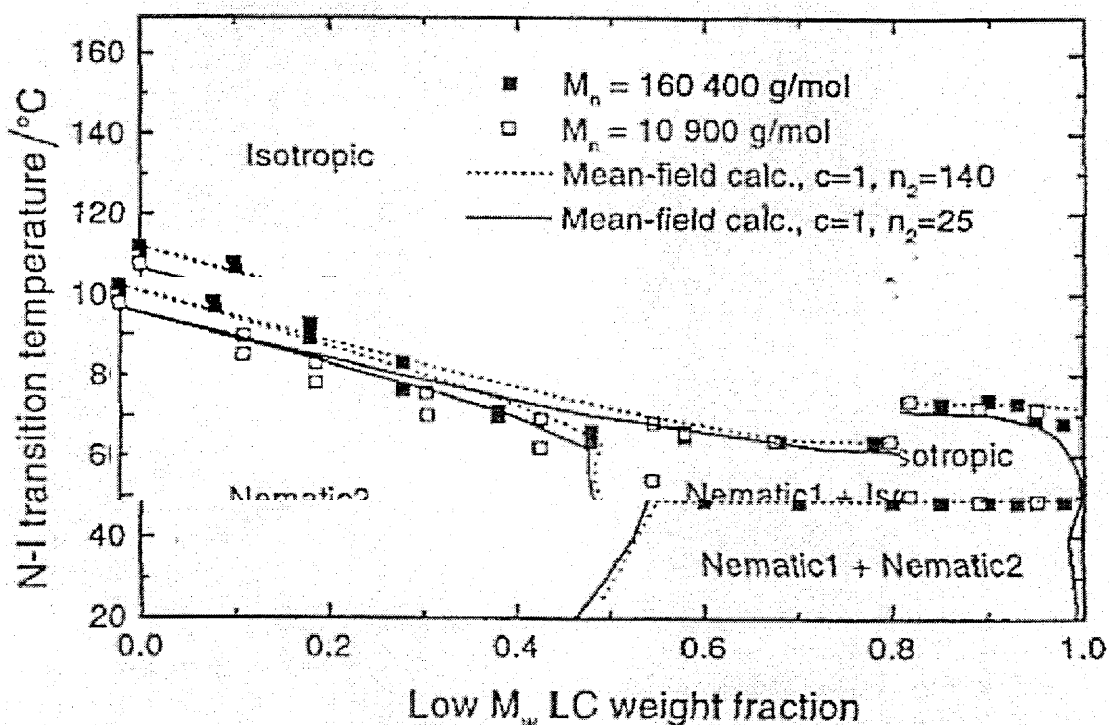


Figure 2.4: Phase diagram of LC and PLC with larger (filled square) and smaller (open square) chain size [104] obtained from the experiment. Dashed and solid lines respectively represent theoretical calculations for different lengths of the polymer chain.

However, the molecular mass of the polymer compound of the mixture is not always the main factor in the phase behaviour of the system. Experimental data from [104] show only a slight dependence of the I-N transition curve and miscibility regions on the molecular mass of the polymer chain in the solution. Such a mixture of

two mesogens (LC and polymer LC each having low molecular mass molecules) was investigated by Benmouda *et al* using DSC and optical microscopy [104]. The experimental technique they used allowed them to obtain thermograms with errors in the range of less than 1°C . Studies were concentrated on the phase separation and miscibility of the solution. A phase diagram (Fig.2.4) obtained from the experimental data was compared with the Maier-Saupe and Flory-Huggins theories.

According to the rule of Arnold and Sackman [124], a mixture consisting of types of mesogens with the same mesomorphic structure should be miscible over a wider range of concentrations than was found to be the case in this experiment (Figure 2.4). The miscibility region starts at a very low concentration of the polymer compound and continues up to a concentration of 50%. In spite of the lack of data at concentrations lower than 10%, there is strong evidence from other experimental data [20], that one might expect no changes in that region. In the area of higher polymer concentrations, the binodal is virtually a horizontal line coinciding with the nematic-isotropic transition of the monomer rich phase. The demixing is induced by the nematic order. While the polymer and the monomer are miscible in the isotropic state, they demix as soon as the nematic order appears. The authors of [104] concluded that the mixture of the polymer LC and its low molecular mass equivalent exhibit an extended miscibility gap and an increase in the I-N transition temperature, which were due to the influence of the polymer backbone.

2.3 Theoretical Background

Theoretical understanding of the nematic phase both at and in the vicinity of its phase transitions has been developed in several directions. A density-functional theory by Onsager [125] minimizes the grand potential $\Omega = F - \mu N$ with respect to variations of the single-particle density; this theory is based on the fact that the isotropic-nematic transition occurs at low density for highly elongated molecules. Another approach uses the theory of Landau and de Gennes [126, 127], in which the Helmholtz free energy is expressed in powers of the order parameter and its gradients. Yet another approach, developed by Faber [128], treats the nematic phase as a continuum, in which a set of modes involving periodic distortion of an initially uniform director field is thermally excited. All orientational order is assumed to

be due to mode excitation. Unfortunately, this theory works well only near the solid-nematic transition and fails close to the isotropic-nematic transition. Maier-Saupe theory [129] attributes the formation of the ordered phase to the anisotropic attractive interactions only. This theory describes nematic ordering, while Flory-Huggins theory for example, describes isotropic mixing and ignores orientational properties of the particles. In many theories of the van der Waals type [130–132], both anisotropic repulsions and attractions are included. These latter types of theory are physically more precise than of Maier and Saupe; however, the main difficulty attending them is that they require precise knowledge of intermolecular interactions.

Different approximations are used for describing different phenomena and different properties of the system. As described in Section 1.1.2, long range order vanishes abruptly at T_{IN} . However, certain anomalous effects in the isotropic phase reveal that a significant degree of quasi-nematic short range order persists above the transition point. The most direct evidence of this is the very high value of the magnetic birefringence, which in the neighbourhood of T_{IN} may be of the order of 10^2 as compared with an ordinary organic liquid [42, 43]. Similar anomalies are seen in the flow birefringence [44], the Kerr effect [45] and the nuclear spin lattice relaxation [133], and this confirms the existence of strong orientational correlations between the molecules. Foex observed in 1933 that the magnetic birefringence exhibits behaviour similar to that of a ferromagnet above the Curie temperature [41]. More recently, de Gennes proposed a phenomenological description of these pretransitional effects - the Landau-de Gennes (LDG) theory [126, 134]. The LDG theory is based on Landau's general description of phase transitions [127] which was further developed by de Gennes [126]. The strengths of the LDG theory are its simplicity and its ability to encapsulate the most important elements of the phase transition. Landau's original theory was restricted to second-order phase transitions. The reason for this limitation lies in the continuity of the change of state in a second order phase transition, as a result of which the order parameters show continuous values near the transition point. Mathematically it is simpler than the mean field theory. The inclusion of the spatial variation of the order parameters gives it an additional dimension not found in mean field theory. More detailed analysis can be found in [126, 127].

Chapter 3

Simulation Approach

It is well known that theory is often a crude projection of the true processes that operate in the real world. Nevertheless, theoretical approximations and models have served well in furthering an understanding of nature and in applying, in numerous ways, the knowledge thus gathered. Only relatively recently, through advances in the mathematical apparatus of statistical mechanics, has it become possible, for example, to solve analytically the two-dimensional Ising model. A number of problems in many-body models are, however, insoluble.

On the other hand, experimental measurements are the only way in which science can make contact with nature; and here too there are many problems. A large number of these flow from our inability to create ideal conditions for experiments: inability to switch off heat transfer in the isothermal bath, for example, or to avoid mechanical vibration in obtaining an interference picture. In other cases, the impossibility of studying the system directly is due to the fact that the very process of trying to measure it changes its state. The list of problems, including financial ones, could be extended indefinitely.

A middle way or a bridge between theory and experiment may, perhaps, be found in simulation. Simulation plays an important role in providing essentially exact results for problems in statistical mechanics without too frequent a use of approximation. Simulation experiments (as they are sometimes called) allow one to verify theories in an accurate way without producing undesirable effects. Simulation as a recognised science started in the twentieth century. Morrell and Hildebrand [135] represented molecules as large gelatinous balls, packed in a three-dimensional volume. The BZ

Reaction, discovered in 1951 [136] by Belousov and later studied by Zhabotinskiy in 1958 [137], was analogous to many systems occurring in nature, such as the growth pattern of fungi, the fibrillation of heart tissue and circadian rhythms [138]. Biochemists, biophysicists and mathematicians therefore used the BZ reaction as a model for their studies. Mathematicians also saw the oscillatory nature of the BZ reaction as arising from problems of differential equations yet to be explored, while biologists found that the chemical model furthered their understanding of the reason behind malfunctioning heart tissue.

Along with physical and chemical models, a number of mathematical or computer models were also being developed. However, owing to the limited processing power (or complete absence) of computers, mathematical or computer simulations started to develop only in the late twentieth century. The problems involved in physical simulations (the influence of gravity on a model consisting of metal balls, for example), as well as the increasing power of computers, made it logical to move towards to mathematical, rather than physical, models.

It is now almost half a century since the first computer simulation of liquids was performed, on the most powerful computer of that time, by Metropolis *et al* [139]. Computer simulation is both a test of the underlying model being used, and an aid to interpretation of new experimental results. Computer simulations are also often designed to check the accuracy of a particular approximation employed in the analytical treatment of a model. Opinions vary concerning the role of simulation relative to other methods. Allen and Tildesley, in their book on computer simulation, give one view when they assert the dual role of simulation, as a bridge between models and theoretical predictions on the one hand, and between models and experimental results on the other [140]. Computer simulation is a direct link between the microscopic scale of the system and the macroscopic details of the experiment.

The simulation technique used to obtain the dynamic properties of many-particle systems is called Molecular Dynamics (MD). It is based on the solving the classical equations of motion for a set of molecules. This was first accomplished, for a system of hard spheres, by Alder and Wainwright [141, 142], but it was several years before a successful attempt was made to solve the equation of motion for a set of Lennard-Jones particles [143]. Unlike those performed using MD, a simulation which employs the Monte Carlo (MC) method does not operate with true dynamics, but rather uses

an abstract mathematical-statistical approach which achieves averaged results in agreement with the correct statistical mechanics ensemble. The MC method can be used in various guises and can even be used in combination with MD. In other words, the MC method can be defined in general as the branch of experimental mathematics which is concerned with experiments which employ random numbers [144].

In liquid physics, the term MC is now universally reserved for the technique devised by Metropolis *et al* [145] to evaluate statistical averages. If we consider a system with known potential energy U , then in the Canonical Ensemble (constant N, V, T) any time-independent configurational property of interest can be written as the average weighted with the Boltzmann factor $e^{-\beta U}$, where $\beta = \frac{1}{k_B T}$. The system evolves through a series of trial moves generated using random numbers. If a subsequently generated random number (usually this number is distributed uniformly between 0 and 1) is less than a certain value, the move is accepted and the system changes its configuration; otherwise, the move is rejected and the system remains in its original configuration. This value is given by $e^{-\beta(U_o - U_n)}$ where U_o and U_n are the total energies of the system before and after the trial move, respectively. The procedure is then repeated hundreds or thousands of times. It should be noted that the processes involved in proceeding along the MC trajectory have no relationship with real time. A crucial difference between the MC and MD techniques is, therefore, that in MD the true dynamics are followed whereas in MC all that can be said is that the process leads eventually to equilibrium, in the sense that configurations will occur with a frequency proportional to their Boltzmann factors.

As mentioned earlier in this section, it is possible to use not only different techniques (MC or MD), but also different models to describe a given system of interest. Various different potentials between particles can be used: the Lennard-Jones potential, the Gay-Berne potential, the hard particle potential, the Maier-Saupe potential etc. In our work we have used the Lebwohl-Lasher lattice model, based on the simple Maier-Saupe pair potential [129, 146, 147]. We have used the MC technique to perform the simulations. This technique and model are described further in the following sections.

3.1 Monte Carlo Technique

If a system is ergodic, then an observable can be calculated either as an average measured during a time interval $t \rightarrow \infty$, or as an ensemble average of n trials where $n \rightarrow \infty$. In a MD simulation, the total energy E and the total linear momentum P are constants of motion. Motion involves time in the calculations. Therefore, MD must measure time averages in an ensemble for which the thermodynamic constants are N , V , E , and the momentum P . MC simulations often operate in the Canonical Ensemble, where the number of particles N , the system volume V , and the temperature T are constants. Depending on the model used and the observables measured, however, alternative ensembles can be used. For MC, the range of ensembles is very wide: the isobaric-isothermal (N, P, T) [148], the constant-stress-isothermal [149], the grand-canonical (μ, V, T) [150], the microcanonical (N, V, E) [151], and the so-called Gibbs-ensemble [152, 153] have all been successfully implemented. In the present work, MC simulations have been conducted using the Canonical and the Semi Grand-Canonical Ensembles. The Canonical Ensemble is the most appropriate ensemble to work with, taking into account the Lebowitz-Lasher model and the observables to be measured, there being no pressure or momentum involved. The weakness of this ensemble, when applied to a lattice model of a binary mixture, is that phase coexistence can be found at some state points. For this reason, the Semi Grand-Canonical Ensemble was also used so as to clarify various phase boundaries.

Let us consider first a system where the number of particles, the temperature and the volume are constant. The partition function for the Canonical Ensemble is:

$$Q(N, V, T) \equiv \frac{1}{h^{3N} N!} \int d\mathbf{r}^N d\mathbf{p}^N \exp[-\beta\mathcal{H}(\mathbf{r}^N, \mathbf{p}^N)] \quad (3.1)$$

The kinetic (momentum dependent) part of the integral (3.1), called the partition function for an ideal gas $Q(N, V, T)^{id}$, can be solved analytically, leaving only the potential part of \mathcal{H} under the integral:

$$\begin{aligned} Q(N, V, T) &\equiv \frac{1}{\Lambda^{3N} N!} \int d\mathbf{r}^N \exp[-\beta\mathcal{U}(\mathbf{r}^N)] = \frac{V^N V^{-N}}{\Lambda^{3N} N!} \int d\mathbf{r}^N \exp[-\beta\mathcal{U}(\mathbf{r}^N)] = \\ &= Q(N, V, T)^{id} V^{-N} \int d\mathbf{r}^N \exp[-\beta\mathcal{U}(\mathbf{r}^N)] = Q(N, V, T)^{id} Q(N, V, T)^{ex} \end{aligned} \quad (3.2)$$

where $\Lambda = \sqrt{h^2/(2\pi m k_B T)}$ is the thermal de Broglie wavelength. The use of the V^N factor is essential in making $Q(N, V, T)^{ex}$ dimensionless, and so the thermodynamic

function of the Canonical Ensemble (the Helmholtz free energy) can be written as:

$$\mathcal{A} = -\frac{\ln Q^{ex}(N, V, T)}{\beta} \quad (3.3)$$

From this point onward, only the excess part of the partition function will be considered. Moreover, in numerical calculations, the V^N factor can be set to unity, since it is constant throughout the simulation. This is a common device - the use of the configurational integral $Z(N, V, T)$ instead of $Q(N, V, T)^{ex}$ (Equation 3.4):

$$Z(N, V, T) = \int d\mathbf{r}^N \exp[-\beta U(\mathbf{r}^N)] \quad (3.4)$$

The partition function provides information about probability distribution - that is, about the probability of finding any configuration of the system at a given energy. If all momenta and all coordinates (locations and orientations) of the system are written as components of a generalised ‘hyper-vector’ Γ , then any of the set of states can be represented by a point in ‘hyper-space’. The probability of finding a configuration can then be represented as a density distribution within this ‘hyper-space’ :

$$\mathcal{N}(\Gamma) \propto \exp[-\beta \mathcal{H}(\Gamma)] \quad (3.5)$$

On the lattice, Γ has potentially only $6N$ dimensions, since there are no momenta involved (N being the total number of particles). For the systems considered in this thesis, another N dimensions disappear owing to the cylindrical symmetry of the particles, leaving only $5N$ dimensions for Γ . Thus, the average value of the order parameter $\langle S \rangle$, described in Section 1.1.2, can be written as an integral over all states Γ , normalised with the configurational integral $Z(N, V, T)$ (3.1):

$$\langle S \rangle = \frac{1}{Z(N, V, T)} \int d\Gamma \exp[-\beta U(\Gamma)] S(\Gamma) \quad (3.6)$$

The application of MC in equilibrium statistical mechanics consists in approximating equation (3.6) initially by replacing integrals with sums over all possible states $\Gamma\{\Gamma_1, \Gamma_2, \dots\}$. Equation 3.4 can be rewritten as :

$$Z(N, V, T) = \sum_{\Gamma} \exp[-\beta U(\Gamma)] \quad (3.7)$$

Let us consider the average value of an observable A . The average A is:

$$\langle A(\Gamma) \rangle = \frac{1}{Z(N, V, T)} \sum_{\Gamma} \exp[-\beta U(\Gamma)] A(\Gamma) \quad (3.8)$$

However, to make calculations covering all possible states of the system would be immensely time-consuming; but by employing the Monte Carlo method, an acceptable calculation of this sum is achieved through the use of random numbers. Instead of calculating the contribution from all possible states Γ , effort is concentrated on those states with greatest significance. The sum over these states must then be normalised, yielding a result with an accuracy proportional to the number of random trials. Simple random sampling is not efficient in practice because random states (points on a surface) are not chosen according to their importance. In fact, nothing is gained by visiting states that make a zero contribution to the average, and the exclusion of these requires the use of importance sampling.

In the simple sampling, each successive state Γ_i does not depend on its predecessor - each is chosen independently of what went before it. In 1953, Metropolis *et al* [139] introduced the Markov process into the sampling procedure, such that each state Γ_{i+1} is derived from the previous state Γ_i via a suitable transition probability. Therefore each step in the Markov chain depended solely on the preceding state of the system but remained independent of all previous states. In an ergodic system, two more conditions must be satisfied. The first is that it must eventually be possible for all states to be accessible as the system moves along the chain. The second is that in transition probabilities from state Γ_n to state Γ_m a detailed balance must be satisfied (Equation (3.9)).

$$\rho(\Gamma_n)\pi_{nm} = \rho(\Gamma_m)\pi_{mn} \quad (3.9)$$

Here, the matrix $\hat{\pi}$ contains information about the probabilities of transition from state to state and $\rho(\Gamma_m)$ is the probability of the state Γ_m (Equation (3.10)):

$$\rho(\Gamma_m) = Q(N, V, T)^{-1} \exp[-\beta\mathcal{H}(\Gamma_m)] \quad (3.10)$$

Under the Metropolis scheme, an element π_{nm} of the transition matrix $\hat{\pi}$ is given by:

$$\pi_{nm} = \begin{cases} \alpha_{nm} & \rho(\Gamma_m) \geq \rho(\Gamma_n) \quad n \neq m \\ \hat{\alpha}_{nm} \frac{\rho(\Gamma_m)}{\rho(\Gamma_n)} & \rho(\Gamma_m) < \rho(\Gamma_n) \quad n \neq m \\ 1 - \sum_{n \neq m}^{\Gamma} \pi_{nm} & n = m \end{cases} \quad (3.11)$$

where $\hat{\alpha}$ is a symmetrical stochastic matrix, often called the underlying matrix of the Markov chain ($\alpha_{nm} = \alpha_{mn}$).

In a biased MC simulation, $\hat{\alpha}$ can be made non-symmetrical. In the present work, symmetrical $\hat{\alpha}$ are used and in the calculation of Equation (3.11) all of its elements

are set to 1. The sum of probabilities for transitions from state Γ_n to all states of Γ must necessarily return 1:

$$\sum_i^{\Gamma} \pi_{ni} = 1 \quad (3.12)$$

In the Canonical Ensemble we wish to sample the distribution (3.5). This can be done using the following scheme:

1. Select a particle (either at random or according to a predetermined pattern) and calculate the potential energy of the current configuration of the system U_{curr} . In this work, a chess board pattern was used to select particles for trial moves. This technique is described in Section 4.3.
2. Give the chosen particle a random deviation. The energy for the next configuration is denoted as U_{next} .
3. Depending on energy difference $\Delta U = U_{next} - U_{curr}$ and a randomly generated number, decide whether to accept the move. A key role in making this decision is played by ρ_{curr} and ρ_{next} , probabilities respectively of the current (Γ_{curr}) and the next (Γ_{next}) states or configurations of the system. Therefore the probability of the transition from Γ_{curr} to Γ_{next} is given by

$$\frac{\rho_{next}}{\rho_{curr}} = \frac{Q(N, V, T)^{-1} \exp[-\beta U_{next}]}{Q(N, V, T)^{-1} \exp[-\beta U_{curr}]} = \exp[-\beta \Delta U] \quad (3.13)$$

In accepting a move with a probability of $\exp[-\beta \Delta U]$, a random number χ is generated uniformly on the interval (0,1). If this random number is less than the calculated Boltzmann factor, then the move is accepted:

$$\chi < \exp[-\beta \Delta U] \quad (3.14)$$

3.2 The Lebwohl-Lasher Lattice Model

The history of the development of computer simulation techniques began about fifty years ago, when the first computer simulation of a liquid was carried out. This very earliest work [139] laid the foundations of modern MC methods. The original models were highly idealized representations of molecules, such as hard spheres, but

within a few years MC simulations were carried out using the Lennard-Jones [154] interaction potential [155]. Such potentials were used in early chemical models of mesogens, where the individual molecule was approximated to a set of soft Lennard-Jones particles representing atoms [156]. The concept of the soft potential with both attractive and repulsive parts was also exploited by Berne and coworkers [157], who devised a series of anisotropic single site potentials.

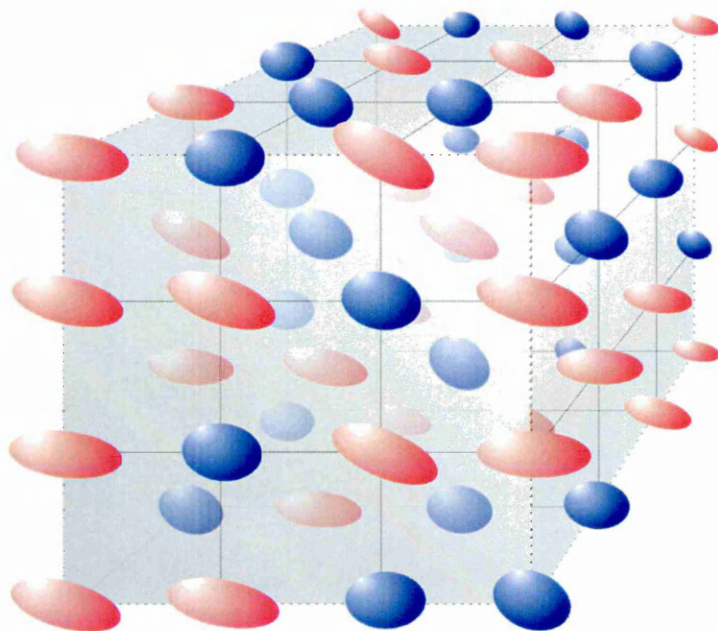


Figure 3.1: Schematic view of the Lebwohl-Lasher lattice model for a two component mixture.

In a crystal, molecular translation is restricted, while rotational motion may still occur (plastic crystal). A simplified model of this situation may be devised, in which the molecular centres of mass are fixed at their equilibrium crystal lattice sites, and the potential energy is written as a function of molecular orientations. The model may be further simplified in that interactions may be restricted to nearest neighbours only. This is exactly what Lebwohl and Lasher proposed in 1972. Their model for a liquid crystal consisted of particles with cylindrical symmetry located on the sites of a simple cubic lattice (Figure 3.1). The interactions are restricted to nearest neighbours and for these the intermolecular potential takes a purely anisotropic form [1]. Basically, the Lebwohl-Lasher model is the lattice version of the Maier-Saupe model [129] of an anisotropic liquid. Thus, the system energy is defined by the sum of interaction potentials, full details of which are given in Section 4.2.

The Lebwohl-Lasher model neglects the coupling between translational variables and orientational variables which is present in a real nematogen. It is, therefore, an approximate model for orientational ordering in a solid, which neglects several important properties of liquid crystals. Nevertheless, it is believed that this model is capable of revealing some of the essential properties of a LC near the nematic-isotropic phase transition.

It may be deemed unwise to use a model of a LC in which the molecules are constrained on lattice sites, since one of the characteristics of a nematic LC is that orientational order coexists with translational freedom. However, this objection may be countered by pointing out that in choosing a lattice model the aim is not to seek to reproduce the properties of a real LC; such an aim would be somewhat over-ambitious. Rather, the main reason for studying a lattice model lies in its simplicity, which makes it capable of being studied to greater precision or for a larger number of particles than would otherwise be possible.

In the Lebwohl and Lasher model [1] particles are allowed to rotate on their sites around their centres of mass, interacting via a simple pair potential. In other words, molecules are represented by centres of interaction located at the sites of a simple cubic lattice and interacting with an anisotropic pair potential:

$$U_{ij} = -\varepsilon_{ij}P_2(\cos \phi_{ij}) \quad (3.15)$$

where ε_{ij} is a positive coupling constant for neighbouring sites i and j . ϕ_{ij} is the relative orientation of particles i and j and $P_2(x)$ is the second Legendre polynomial.

The model works remarkably well even for a relatively small number of particles, compared to real life LC. In fact, experimental measurements of the order parameter dependence on temperature on cyanobiphenyl nematics [158, 159] were consistent with the simulation studies of the model by Pasini *et al* [160]. A particle in the Lebwohl-Lasher model is usually thought to represent a closely packed group of molecules. This domain of mesogens maintains its local structure at various temperatures across the nematic-isotropic phase transition [161]. According to Zannoni *et al* [162], these domains seem to include a few tens of particles.

To investigate LC behaviour near its orientational phase transition, Fabbri and Zannoni in 1986 performed an extensive study of the Lebwohl-Lasher model. Their

system consisted of a cubic lattice of size $30 \times 30 \times 30$ [163], to which they applied periodic boundary conditions. This was continuation of the work published in [11], where the phase transition of the model was located by monitoring, as a function of temperature, the constant volume specific heat. In [163], the authors also increased significantly the number of runs near the transition to allow a more precise determination of the orientational transition temperature. The transition temperature was found to be $k_B T / \varepsilon_{ij} = 1.1232 \pm 0.0006$, refining previous estimates. Orientational order parameters $\langle P_2 \rangle$, $\langle P_4 \rangle$ were also calculated and a new algorithm was proposed for the computation of $\langle P_4 \rangle$. Particular attention was devoted to pre-transitional properties. Pair correlation functions $g_2(r)$ and $g_4(r)$, as well as the second-rank g_2 -factor were reported. g_2 was found to diverge at a temperature $k_B T / \varepsilon_{ij} = 1.1201 \pm 0.0006$ and to fit the Landau-de Gennes behaviour except in the proximity of the transition. These results indicated that the Lebwohl-Lasher model can show the small difference between the nematic-isotropic transition temperature and the isotropic phase limiting instability temperature without the introduction of additional terms in the potential. Later, Pasini *et al* [164] determined transition by solving an integral equation, since the smoothing required at times by the numerical differentiation, made the transition impossible to identify. Apart from investigating the heat capacity [11, 163, 164] and orientational order parameters [160, 165], these and other authors also investigated the orientational correlation functions [166, 167] as well as working on generalisations of the model [160, 165, 168, 169] and its further development [170–172] to investigate other aspects of LC, not covered in this thesis.

The studies of Zhang *et al* in 1992 revealed more detail concerning the nature of the orientational phase transition. Using the three-dimensional Lebwohl-Lasher model, along with reweighting techniques and finite-size scaling analysis, they calculated the ordering susceptibility and energy distribution function. From this, they found the transition temperature to be $k_B T / \varepsilon_{ij} = 1.1232 \pm 0.0001$ [173]

In 1997 Gonin and Windle described structural aspects of the nematic-isotropic transition in a LC [174]. Using the Lebwohl-Lasher model, they calculated an order parameter, which supplied information about the average director structure. They also calculated the angular pair correlation function $g_2(r)$, so as to form a picture of orientational order as a function of distance between the sites. The $g_2(r)$ results were limited by the size of the lattice. Preliminary studies of the model were made below the transition temperature in order to investigate the influence of boundary

conditions. A structural description of the transition was used, based on molecular director maps and the identification of more ordered and less ordered regions. This was achieved by dividing the distribution of local energies into two sub-distributions with widths in accord with the mean values of their energies. The existence of such a double-well structure of the free energy had already been found by Zhang and Zuckermann in 1993 [175]. As the transition was approached from above, the isotropic melt structure was seen to contain nematic nuclei which increased in volume fraction as the temperature was decreased. It was shown that, at the transition, these nuclei appeared to join in the network to produce a percolating phase having a single orientation across the whole system. As the temperature was decreased within the nematic region, isolated regions of disorder were continuously reduced, with a corresponding increase in the overall order parameter.

The situation becomes even more complicated with simulations of mixtures. The first testing of the validity of the molecular field approximation in the Humphries-James-Luckhurst theory of liquid crystalline mixtures was performed by Hashim *et al* in 1985 [176]. They used the standard cubic lattice model described previously, but with the extension to three pair potentials, each with a particular interaction parameter ε_{aa} , ε_{bb} and ε_{ab} . They further assumed that ε_{bb} could be ignored, owing to the low concentration of the more anisotropic particles *b* which they used. Because the concentration of particles *b* was very small, these were referred to as a solute, while particles *a* were referred to as a solvent. It is important to note that the solute was placed at random on the lattice sites (with the additional constraint that no two *b*-particles were allowed to be nearest neighbours) and that this random distribution remained unchanged during the simulation so that phase separation could not occur. Hashim *et al* showed that the results did not depend on the particular random distribution used. They obtained results for the heat capacity and ascertained the transition temperature for the mixture. The results for the second-rank order parameter for both the solvent and the solute yielded the expected behaviour; the order parameter for the solute was considerably larger than that for the solvent.

In 1990 same authors improved their model, making it capable of phase separation. They now used a mixture of which one component was a nematic LC, the other consisting of isotropic particles. The model chosen for the nematogenic solvent was, once again, that proposed by Lebwohl and Lasher. This choice enabled them, as

they point out in their paper [177], to construct a phase diagram for the mixture of cylindrical and spherical particles predicted by the Humphries-Luckhurst molecular field theory, and also to devise a test of that theory for spherical solutes. It should be noted that the isotropic particles were represented as vacancies on the simple cubic lattice and the cylindrical particles were allowed to move onto vacant sites. The simulation results which were obtained confirmed the existence of the biphasic regions predicted by molecular field theory for such mixtures.

In 1997 Polson and Burnell, in an investigation into the phase behaviour of a Lebwohl-Lasher binary LC mixture, calculated the nematic-isotropic phase coexistence region and the orientational order parameters for the two mesogens along the phase boundaries. For a system with equal concentrations of the two types of mesogen, they found that the free-energy barrier between the two minima at the I-N transition increased monotonically with lattice size, and, since it varied with the square of the lattice size, they were able to deduce the first-order nature of the phase transition. They also found deviations from the results predicted by mean field theory. In particular, they found that an increase in the difference between the isotropic components of the pair potential of the two species comprising the mixture resulted in a broadening of the coexistence region [178].

When this section was written, Bates published a simulation study on a LC-isotropic fluid mixture performed using a Lebwohl-Lasher type model [179]. In this he used a modified interaction potential in the Semi-Grand Canonical Ensemble. He extended the model by adding an isotropic term to the interaction potential, achieving the isotropic-isotropic coexistence (termed isotropic-vapor in [179]). He found that depending on the strength of the isotropic term, the model exhibits either a diagram containing isotropic fluid and nematic phases or distinct isotropic-isotropic coexistence in addition to the orientationally ordered nematic. More on this will be discussed in Chapter 6 where our own Semi-Grand Canonical Ensemble results are presented for binary LC mixtures.

Chapter 4

Model Basis And Details

As was mentioned earlier, it is possible to use not only different simulation approaches (MC or MD), but also different models to study a system of interest. In the present work the Lebwohl-Lasher model is used to study ordering and phase behaviour in a liquid crystalline system, particularly in the region of the I-N transition. The model is based on a cubic lattice, each site of which contains a vector representing the net orientation of a liquid crystalline domain (henceforward called a particle). No empty sites are present in the model and the ‘density’ distribution of the particles on the lattice is uniform in all directions irrespective of the director. The energy of each particle is determined by the relative orientations of its six nearest neighbours, and the probability of a vector being rotated to another, randomly chosen, orientation depends on the Boltzmann factor of the difference between the current and new energies (Equation (4.2)). All simulations were performed using an importance MC technique similar to that described in [177] (Section 4.3). To simulate the bulk properties of the system Periodic Boundary Conditions (PBC) were applied [180]. Polydispersity (i.e. binary and ternary systems) in the system was simulated by introducing the notion of an ‘identity’ for each particle. The interaction potential between two neighbouring sites were then made to depend on the ‘identities’ of the sites (Section 4.2). In the simulation, a number of global observables were obtained, such as the order parameter, heat capacity, radial distribution function, etc.

4.1 General Details - $NcVT$, $N\Delta\mu VT$ Ensembles

In the simulation, the bulk properties of the model are of great interest. Unfortunately, the power of the computer does not allow operations with $N = 10^{23}$ particles. Usually, computer simulations are performed on a relatively small number of particles $N \lesssim 10^4$. The size of the system is limited mainly by the speed and the memory capacity of the computer. It will be shown later in this chapter that many of the calculations performed in a simulation are proportional to N^2 . Therefore, it is necessary to keep the number of particles in the system relatively low. On the other hand, in a cubic lattice model with a size of, say $N = 16 \times 16 \times 16 = 4096$, the number of particles which appear on the surface is 1536. This means that 37.5% of the particles experience forces very different from those that obtain in the bulk. In such system, the contribution of the particles on and near the surface is immense. Thus, for bulk property studies one must employ approximations which reduce this surface effect; here it was effectively avoided by implementation of PBC [181]. As an aid to picturing PBC in 3D space, let us first consider a simpler example - a 2D lattice whose opposite edges are connected to each other (Figure 4.1), so that the 2D lattice forms a toroidal topology in 3D space. As is shown in Figure 4.1, a site $s_{n+1,m+1}$ next to the site on the edge $s_{n,m}$ is an ‘imaginary’ site which, in fact, corresponds to $s_{1,1}$ owing to the way in which the edges are connected to each other. In such a system there are no particles at the surface, because there is no surface as such, even though the system is finite.

Owing to the finite size of the system, there remain, in spite of the approximation of PBC, some limitations. One is that for such parameters as radial distribution functions it is possible to calculate correct data only for distances $r < r_{cutoff}$, where r_{cutoff} relates to the system size as:

$$r_{cutoff} \leq \frac{\mathcal{L}}{2} \quad (4.1)$$

Here \mathcal{L} is the size of the smallest side of the simulation box (if the sizes of the sides differ). In this way, the minimum image convention can be satisfied. This means that in PBC only the closest distance between particles is considered and particles cannot be counted twice. Another effect of the system size is the long range orientational correlation it imposes between the mesogenic particles, which increase the transition temperatures of the system; finite size scaling can be applied

in order to correct for this effect. The running of large-scale MC simulations requires the generation of a uniform distribution of non-correlated random variables. *RAN2* is a random generator based on [182], the repeat period of which is virtually infinite. It provides random numbers χ between 0 and 1 with precision of seven digits after the floating point for use in the definition of new rotation angles (4.15) and for acceptance (4.2), etc.

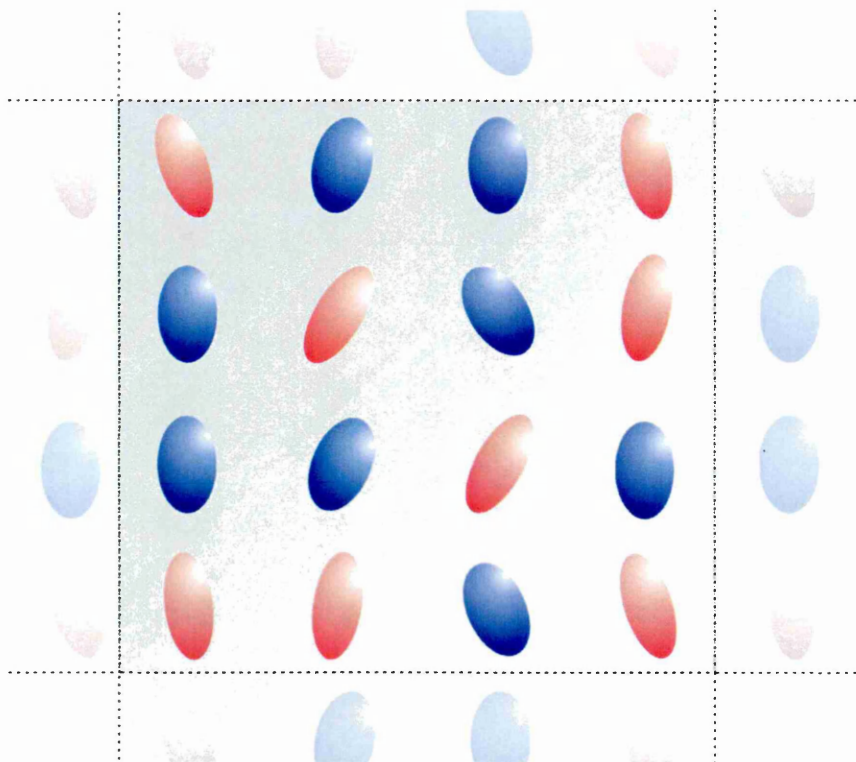


Figure 4.1: The Periodic Boundary Conditions in 2D lattice.

4.1.1 Canonical Ensemble

In MC simulation, the decision regarding acceptance and rejection of a move is based on the calculation of the energy of the system (Equation (4.2)). To be more precise, it is based on the energy difference ΔE between the present state of the system and the state to which it is attempting to transform (see Section 3.1). So the general acceptance/rejection condition (3.14) reads as:

$$\text{accept if } \chi < \exp(-\beta\Delta E) \quad (4.2)$$

where χ is a random number between 0 and 1 and $\beta = 1/k_B T$. In Section 3.1 the partition function for the Canonical Ensemble was introduced and the distribution sampling scheme of relation (3.5) was explained. The probability of a transition from any state Γ_{curr} to a new configuration Γ_{next} was presented in Equation (3.13). The general acceptance condition (3.14) is then applied to the system. In the lattice model used here only one site was changed at a time, so that it was not necessary to calculate the energy difference of the entire system. Rather ΔE in this model was given by the local energy change ($E_{loc}^{curr} - E_{loc}^{next}$) between the current and the next local configuration respectively.

$$E_{loc}^{curr} = \sum_{j=1}^6 U_{ij}^{curr} \quad E_{loc}^{next} = \sum_{j=1}^6 U_{ij}^{next} \quad (4.3)$$

The local energies E_{loc}^{curr} and E_{loc}^{next} in Equation 4.3 are the sums over the six interaction potentials U_{ij} between particle i (in the current (*curr*) and prospective (*next*) orientations) and its six neighbouring particles j (which remain unchanged in both the *curr* and *next* local configurations). The analytical view of interaction potentials will be given in Section 4.2.

4.1.2 Semi-Grand Canonical Ensemble

At the end of Chapter 5 and the beginning of Chapter 6, it will be suggested that it is much more convenient to carry out simulations in a Grand Canonical Ensemble when dealing with sharp thermal dependencies of the phase boundaries. Owing to the ‘incompressibility’ of the lattice model used in our simulations it was appropriate to use a Semi-Grand Canonical Ensemble ($N\Delta\mu VT$) in which the total number of particles ($N = N_A + N_B$) and the difference in chemical potential $\Delta\mu$ are constant, while the concentration c ($N_A : N_B$ ratio) is subject to variation. The partition function for this ensemble is:

$$Q_{SG} = \sum_{\Gamma} \exp(\beta(\Delta E + \Delta\mu\Delta N)) \quad (4.4)$$

where $\Delta N = N_A - N_B$ and can be $\Delta N = -N \dots 0 \dots + N$. $\Delta\mu$ is the chemical potential difference between the two species and ΔE is the difference between the

total energy of the system before and after the move. As in the Canonical Ensemble simulations, ΔE was calculated as the difference in local energies (see Equation 4.3), since attempts to exchange particles with those of an unlike type were performed singly, and involved only one particle at a time ($\Delta N = \pm 2$). The acceptance rule for such a move is then easily formulated by modifying that of the Canonical Ensemble to incorporate an additional term into the Boltzmann factor:

$$P_{acc} = \min \left(1, \exp \left[-\frac{\Delta E \pm \frac{1}{2}\Delta\mu\Delta N}{kT} \right] \right) \quad (4.5)$$

The sign before the $\Delta\mu\Delta N$ term depends on whether a particle of type A is being exchanged with one of type B or vice versa; and a $\frac{1}{2}$ is introduced for convenience.

4.2 Interaction Potentials

The energy difference ΔE , used in formulating acceptance rules for both ensembles used is calculated from the interaction potential between neighbouring particles (Equation 4.3). The interaction potential describes how particles interact in the system. The interaction potential used in the simulation is presented in Equation 4.6 and is that proposed by Lebwohl and Lasher [1]. The anisotropic interaction potential between two particles, then, is given as:

$$U_{ij} = -\varepsilon_{ij}P_2(\cos \phi_{ij}) \quad (4.6)$$

where ε_{ij} is a positive coupling constant for neighbouring sites i and j . The relative orientation of two particles is denoted by the angle ϕ_{ij} . In the model, only the interactions between nearest neighbours are taken into account, which means that the local energy minimum of each particle is defined by its six neighbouring particles only. This allows a relatively rapid simulation timescale. In the case of a single component system, $\varepsilon_{ij} \equiv \varepsilon$ is a positive scalar value which is normally set to 1. However, for binary and ternary mixtures the coupling constant in the interaction potential (Equation 4.6) needs to be modified. For the sake of clarity, the value of ε_{ij} is selected from a $n \times n$ symmetric matrix of positive scalar values (Definition 4.7). Here, n is the number of components in the mixture and c_1, c_2, \dots, c_n are values used in determining the coupling ($C_{\alpha,\beta}$). c_i value selects the ‘identity’ of the particle from the various types present in the mixture.

$$\hat{C} \equiv \begin{array}{cccc}
 c_\alpha^{c_\beta} & c_1 & c_2 & \cdot & c_n \\
 c_1 & C_{11} & C_{12} & \cdot & C_{1n} \\
 c_2 & C_{21} & C_{22} & \cdot & C_{2n} \\
 \cdot & \cdot & \cdot & \cdot & \cdot \\
 c_n & C_{n1} & C_{n2} & \cdot & C_{nn}
 \end{array} \quad (4.7)$$

Each individual element $C_{\alpha,\beta}$ of the matrix \hat{C} denotes the coupling between two different types of particle, where $\alpha, \beta = 1 \dots n$. If particles i and j have identities c_1 and c_n respectively, then $\varepsilon_{ij} = C_{1n}$. The identities $c_{(1 \dots n)}$, in fact, represent the magnitude of anisotropy for the particles and range between 0 and 1, so that the two extremes (0 and 1) represent a sphere-like and a strongly rod-like particle respectively. The presentation of ε_{ij} as an array of elements is convenient when further modifications to the interaction potential are needed. For example, in our simulations we used a simple relation between the identity of the particles and the coupling constant:

$$\varepsilon_{ij} = C_{\alpha,\beta} = c_\alpha \cdot c_\beta \quad (4.8)$$

and this relation can be changed to satisfy more sophisticated relations between particles, such as, for example, the addition of a further interaction coefficient for interactions of like particles:

$$\varepsilon_{ij} = C_{\alpha,\beta} = \frac{c_\alpha \cdot c_\beta \pm \delta_{\alpha\beta}}{2} \quad (4.9)$$

Thus, following from Equation (4.8), in the case of the binary system the difference in coupling between particles is expressed as a product of identities, $c_1=1$ (for type 1, henceforward referred to as type A) and $c_2=0.5$ (for type 2, also referred to as type B). ε_{ij} for the binary system with the parameters described above reads:

$$\begin{array}{lll}
 \varepsilon_{ij} = 1 & \text{A - A interaction} & \begin{array}{ccc} c_\alpha^{c_\beta} & c_1 & c_2 \\ \leftarrow & 1.00 & 0.50 \end{array} \\
 \varepsilon_{ij} = 0.5 & \text{A - B interaction} & \\
 \varepsilon_{ij} = 0.25 & \text{B - B interaction} & \begin{array}{ccc} c_2 & 0.50 & 0.25 \end{array}
 \end{array} \quad (4.10)$$

For the sake of convenience, the identity (or magnitude of anisotropy) of type A particles is always set to 1, so the coupling between particles can be defined by only one value of $\varepsilon = c_2$. Thus, depending on the types of both particles involved, Equation (4.6) appears as:

$$U_{ij} = -P_2(\cos \phi_{ij}) \quad \text{A - A interaction} \quad (4.11)$$

$$U_{ij} = -\varepsilon P_2(\cos \phi_{ij}) \quad \text{A - B interaction} \quad (4.12)$$

$$U_{ij} = -\varepsilon^2 P_2(\cos \phi_{ij}) \quad \text{B - B interaction} \quad (4.13)$$

Therefore, the interaction potentials (Equations (4.11), (4.12), (4.13)) depend on the identities of both interacting particles. Similarly, as a third type of particle (C) is introduced, more values of ε_{ij} are calculated, based on Equation (4.8).

4.3 Moves

There are three types of move in the simulation: rotation of a particle; exchange of location of two neighbouring unlike particles (swap); and change of particle type or identity (N $\Delta\mu$ VT Ensemble only). Each of the moves requires the generation of random numbers. Two numbers were needed for obtaining random angles for the rotation move; four numbers for the swap move (random location of the site (x, y, z) and random choice of one of the six neighbours with which the original site is exchanged); and three numbers for the change of particle type. In addition, further random numbers were needed to assess the relevant acceptance criteria. There now follows a detailed description of the algorithms involved in making each of these moves.

The rotation move involves a random deviation from the original orientation of the particle. On the one hand, the trial rotation move will frequently be rejected if the maximum deviation angle θ_{max} is set too high. On the other hand, when the maximum deviation angle θ_{max} is very small, the move will virtually always be accepted but phase-space exploration will be limited. In both cases, the system is likely to reach equilibrium after a very large number of simulation steps. In order to set θ_{max} to the optimal value, a number of equilibration runs can be performed at the beginning of the simulation, until the percentage of attempted moves being accepted falls in the interval of 40%-60%. No calculation of observables is attempted at the time of the equilibration runs. After this procedure, θ_{max} needs to be held constant during the entire simulation run. The procedure is repeated for every simulation in which any of the parameters change, such as temperature, chemical potential difference, etc. The trial rotation moves, limited by θ_{max} , must always satisfy the following conditions:

- Two angles, θ and φ , which fully determine the orientational deviation of the uniaxial particle from its current position \hat{u}_{curr} , must be selected randomly.
- The set of randomly chosen orientations of the particles must form the uniform distribution of the points made on the surface ξ of the imaginary partial sphere that is embraced by θ_{max} .

Equation 4.14 ensures the uniform distribution of points on the surface ξ . All values from f_d are generated by random number χ and are homogeneously distributed on surface ξ , which is limited by the angle θ_{max} . χ ranges uniformly in the interval $[0...1]$. In this way the local density of points does not depend on θ and is constant across surface ξ .

$$f_d = \chi(1 - \cos \theta_{max}) \quad (4.14)$$

Using distribution f_d for $\cos \theta$ and uniform distribution for φ , random values of $\cos \theta$, $\sin \theta$ and $\cos \varphi$, $\sin \varphi$ can be derived (Equation (4.15)).

$$\begin{aligned} \cos \theta &= 1 - f_d \\ \sin \theta &= \sqrt{1 - \cos^2 \theta} \\ \cos \varphi &= \cos(\chi 2\pi) \\ \sin \varphi &= \sin(\chi 2\pi) \end{aligned} \quad (4.15)$$

Equation 4.15 ensures angle ranges $0 < \varphi < 2\pi$ and $0 < \theta < \pi/2$. These values form the transponent rotation matrix \hat{R}^T (Equation (4.16)).

$$\hat{R}^T(\chi) = \begin{bmatrix} \cos \theta \cos \varphi & \cos \theta \sin \varphi & -\sin \theta \\ -\sin \varphi & \cos \varphi & 0 \\ \sin \theta \cos \varphi & \sin \theta \sin \varphi & \cos \theta \end{bmatrix} \quad (4.16)$$

\hat{R}^T denotes the random deviation of the particle from its current orientation \hat{u}_{curr} . The relationship between \hat{u}_{curr} and a new \hat{u}_{next} orientation is given by Equation (4.17). These two vectors are then used in Equations (4.3) and (4.6) and in condition (4.2), which determines the acceptability of the trial move. In the case of a successful move, \hat{u}_{curr} is set to \hat{u}_{next} whereas when the move is rejected, the present orientation of the particle \hat{u}_{curr} is preserved. In successive runs this operation is repeated for every particle in the system.

$$\hat{u}_{next} = \hat{R}^T(\chi) \times \hat{u}_{curr}^T \quad (4.17)$$

For the rotation move, each successive site must be chosen in a way that it is uncorrelated with the location of the site visited previously. This is due to possible commensurabilities, which might interfere with the equilibration process in the system. One way of solving this problem is to pick sites randomly. We, however, have chosen a different route, which is a chess-board order. The locations in the 3D lattice were designated as notional ‘black’ and ‘white’ sites, as on a chess board. Next, for each particle on a ‘white’ site the rotation move is attempted according to step 2 as set out in Section 3.1. The acceptance decision was made according to Equation (3.13), given in step 3, and the operation repeated for all particles on ‘white’ sites one by one in any order. After this, the particles on ‘black’ sites were treated in exactly the same manner. It is important to note, however, that when the periodic boundary conditions are applied, the size of the lattice must always be of even number, so that the chess-board pattern is continuously propagated throughout the periodic boundaries without neighbouring sites being marked in the same colour. It should be noted, however, that for the swapping move the chess-board pattern was not used; instead, each particle was chosen randomly. After rotation trials had been performed on all particles, 20% of them were chosen randomly and an attempt made to swap their identities with those of neighbouring particles.

For calculation of the order parameter and the correlation function, the angular coordinates of the particles must be noted in the global system of coordinates. However, the rotation move of the particle vector involves random angles used with respect to the orientation of a particle within its local system of coordinates. Therefore, the standard geometrical formula of a rotational matrix was applied so as to transform the coordinates of the particles from their local to the global system of coordinates and vice versa. Since the number of rotation moves made during the simulation run exceeded the number of calculations that used global coordinates, only the rotational matrixes of the particles were stored.

The next step is to allow particles to move within the simulation box (swap). This adds an extra degree of freedom (translational) and allows new phenomena to emerge. The swapping of particles was kept as simple as possible, the main points being as follows:

- Since there were no empty sites in the lattice, the move was implemented by attempting to swap neighbouring sites that had different identities. It should

be noted that only particles of different types were considered. For example if, of a site's six neighbours only m were different from it in type, then the probabilities of a successful move were $\frac{1}{m}$ for each of the m unlike particles and 0 for the other (like), particles. It worth noting, however, that in some circumstances, such a method does not satisfy the accepted rule of microscopic reversibility [140, 144, 180]. Justification for this approach follows in Section 6.5.5.

- Moving the entire particle (both its identity and orientation) is a disruptive procedure, as most moves are likely to be rejected. Thus, the orientations of the particles were kept unchanged and only the identities were exchanged. This is based on the assumption that the local energy associated with the orientation is already minimized.
- The local current E_{loc}^{curr} and prospective E_{loc}^{next} energies of the two particles considered have to be calculated in a different way from that used in the case of the rotation trial move (Equation (4.3)), since this kind of move involves a configurational change in not one, but two sites. Therefore, in the calculation of local energies, integration with the nearest neighbours of both particles must be taken into account.

In order for the notation for local energies to be consistent with that used in Equation (4.3), let us then write local energies $(E_{loc}^{curr})'$ and $(E_{loc}^{next})'$ for the two particles which are to be swapped. These will contribute to the local energies (E_{loc}^{curr}) and (E_{loc}^{next}) from Equation (4.3). Current and prospective local energies for particle A, whose identity is changed, are denoted as:

$$({}^A E_{loc}^{curr})' = \sum_{j=1}^6 U_{ij}^{curr} = \sum_{j=1}^6 -\varepsilon_{ij} P_2(\cos \phi_{ij}) \quad (4.18)$$

$$({}^A E_{loc}^{next})' = \sum_{j=1}^6 U_{ij}^{next} = \sum_{j=1}^6 -\varepsilon'_{ij} P_2(\cos \phi_{ij}) \quad (4.19)$$

And for particle B, current and prospective energies are denoted as:

$$({}^B E_{loc}^{curr})' = \sum_{l=1}^6 U_{kl}^{curr} = \sum_{l=1}^6 -\varepsilon_{kl} P_2(\cos \phi_{kl}) \quad (4.20)$$

$$({}^B E_{loc}^{next})' = \sum_{l=1}^6 U_{kl}^{next} = \sum_{l=1}^6 -\varepsilon'_{kl} P_2(\cos \phi_{kl}) \quad (4.21)$$

Here ε_{ij} and ε'_{ij} are the coupling constants chosen from matrix \hat{C} , but each corresponds to a different element of the matrix, since the identity of particle A in the *curr* and *next* configurations is different. The same situation applies to particle B and the coupling constants ε_{kl} and ε'_{kl} . i is the index of the particle (particle A), the identity of which is to be exchanged with one of its neighbouring particles of a different type (particle B), the indexing of which is denoted by k in Equations (4.20,4.21). j and l are indices for particles that neighbour the particle of type A and type B respectively.

Therefore, the local energy (E_{loc}^{curr}) (Equation (4.22)) used in the definition of ΔE comprises the sum of (E_{loc}^{curr})' of both particles, A and B .

$$E_{loc}^{curr} = ({}^A E_{loc}^{curr})' + ({}^B E_{loc}^{curr})' = \sum_{j=1}^6 -\varepsilon_{ij} P_2(\cos \phi_{ij}) + \sum_{l=1}^6 -\varepsilon_{kl} P_2(\cos \phi_{kl}) \quad (4.22)$$

Following an analogous procedure, the local energy (E_{loc}^{next}) (Equation (4.23)) comprises the sum of (E_{loc}^{next})' of particles A and B .

$$E_{loc}^{next} = ({}^A E_{loc}^{next})' + ({}^B E_{loc}^{next})' = \sum_{j=1}^6 -\varepsilon'_{ij} P_2(\cos \phi_{ij}) + \sum_{l=1}^6 -\varepsilon'_{kl} P_2(\cos \phi_{kl}) \quad (4.23)$$

So the full equation for the energy change reads:

$$\begin{aligned} \Delta E &= \sum_{j=1}^6 -\varepsilon'_{ij} P_2(\cos \phi_{ij}) + \sum_{l=1}^6 -\varepsilon'_{kl} P_2(\cos \phi_{kl}) \\ &\quad - \sum_{j=1}^6 -\varepsilon_{ij} P_2(\cos \phi_{ij}) - \sum_{l=1}^6 -\varepsilon_{kl} P_2(\cos \phi_{kl}) \end{aligned} \quad (4.24)$$

The value of the coupling constant for the interaction between particles A and B is the same before and after the move, $\varepsilon_{ij} = \varepsilon_{kl} = \varepsilon'_{ij} = \varepsilon'_{kl}$, as is the relative orientation between particles. Thus, this part of the sum does not contribute to the local energy difference. In addition, owing to the fact that the coupling constant is constructed via the simple product of two numbers (identities), there is no need to recalculate the potentials in the sum fully, since all the neighbouring particles (j and l) remain unchanged. Therefore, in the case of the binary mixture being modelled, where ε_{ij} is denoted only as a product of the identities of two interacting particles, further simplification of Equation (4.24) is possible. Let us therefore, rewrite the coupling constants for this specific case as a product of the two constants, which

make up each element in matrix \hat{C} :

$$\begin{aligned}
 \varepsilon_{ij} &= c_\alpha c_\beta & \text{where } \alpha &\equiv \alpha(A), \text{ and } \beta \equiv \beta(j) \\
 \varepsilon'_{ij} &= c_\alpha c_\beta & \text{where } \alpha &\equiv \alpha(B), \text{ and } \beta \equiv \beta(j) \\
 \varepsilon_{kl} &= c_\alpha c_\gamma & \text{where } \alpha &\equiv \alpha(B), \text{ and } \gamma \equiv \gamma(l) \\
 \varepsilon'_{kl} &= c_\alpha c_\gamma & \text{where } \alpha &\equiv \alpha(A), \text{ and } \gamma \equiv \gamma(l)
 \end{aligned} \tag{4.25}$$

Here, α is the index corresponding to the identity of particle A or B, depending on whether the system is in its current or prospective configuration. β is the index corresponding to the identities of all the neighbouring particles. c_α can possess only two values c_A and c_B , which are the identities of particles A and B respectively. Equation (4.24) for this case is rewritten in the following way:

$$\begin{aligned}
 \Delta E &= \sum_{j=1, j \neq k}^6 -(c_B c_\beta) P_2(\cos \phi_{ij}) + \sum_{l=1, l \neq i}^6 -(c_A c_\gamma) P_2(\cos \phi_{kl}) - \\
 &- \sum_{j=1, j \neq k}^6 -(c_A c_\beta) P_2(\cos \phi_{ij}) - \sum_{l=1, l \neq i}^6 -(c_B c_\gamma) P_2(\cos \phi_{kl}) = \\
 &= -c_B \left(- \sum_{l=1, l \neq i}^6 c_\gamma P_2(\cos \phi_{kl}) + \sum_{j=1, j \neq k}^6 c_\beta P_2(\cos \phi_{ij}) \right) - \\
 &- c_A \left(\sum_{l=1, l \neq i}^6 c_\gamma P_2(\cos \phi_{kl}) - \sum_{j=1, j \neq k}^6 c_\beta P_2(\cos \phi_{ij}) \right) = \\
 &= (c_B - c_A) \left(\sum_{l=1, l \neq i}^6 c_\gamma P_2(\cos \phi_{kl}) - \sum_{j=1, j \neq k}^6 c_\beta P_2(\cos \phi_{ij}) \right)
 \end{aligned} \tag{4.26}$$

Mathematically this may seem an insignificant simplification, but in a system with over 4,000 particles, 20% of which are processed at each of the 20,000 to 100,000 sweeps comprising a typical simulation, it is a useful improvement.

4.4 Calculation of Microscopic Parameters

4.4.1 The Director And The Orientational Order Parameter

The orientation of the uniaxial particle i is defined by unit vector \vec{e}_i , which in turn is defined by the three components in the cubic system of coordinates. We rewrite Equation 1.5 for the nematic order parameter in terms of the 'direct vector product'

\hat{E}_i , where the x -, y - and z - components of \vec{e}_i in the global coordinate system are used instead of angles:

$$\hat{Q} \equiv Q_{\alpha\beta} = \frac{1}{N} \sum_{i=1}^N \left(\frac{3}{2} [\hat{E}_i]_{\alpha\beta} - \frac{1}{2} \delta_{\alpha\beta} \right) \quad (4.27)$$

Here \hat{E}_i is obtained according to Equation (4.28), α and β are the coordinates of \hat{E}_i and N is the number of unit vectors (particles) in the system.

$$\hat{E}_i = \begin{pmatrix} \alpha & \beta & 1 & 2 & 3 \\ 1 & x \cdot x & x \cdot y & x \cdot z \\ 2 & y \cdot x & y \cdot y & y \cdot z \\ 3 & z \cdot x & z \cdot y & z \cdot z \end{pmatrix} \quad (4.28)$$

The \hat{Q} tensor has three eigenvectors n_1 , n_2 and n_3 . The next step is to determine which of these represents the director of the system n . For this purpose, the \hat{Q} tensor is diagonalised using the Jacobian Transformation [182]. The trace of \hat{Q} is equal to 0. The highest eigenvalue of the diagonalised matrix Q_{ii} ($i = 1, 2, 3$), relates to the second-rank order parameter of the apolar uniaxial mesophase as:

$$S \equiv \langle P_2 \rangle = Q_{ii} \quad (4.29)$$

The eigenvector corresponding to this highest value of Q_{ii} is, in fact, the director of the mesophase of the system \vec{n} . It should be noted that this eigenvector denotes the true director of the apolar uniaxial mesophase, since the signs of \vec{e}_i have disappeared in $\langle \hat{E} \rangle$.

4.4.2 Radial Distribution Function Calculations

In a lattice model where all the sites are occupied, the $g(r)$ function is fixed and does not yield useful information. However, in a system of two or more components, which can move within the simulation box, the distribution functions of the like (e.g. $g_{AA}(r)$) and unlike (e.g. $g_{AB}(r)$) particles can yield information on the phase behaviour and micro-structure of the system. As was explained in Section 1.1.4,

the generic function $g(r)$ can be described as the average probability of finding a particle at distance r from another particle, the result being normalized by the random uniform distribution. However, owing to the discretisation of a lattice model, the distribution of the particles is normalized not by the probability expected for a completely random distribution at the same density, but by the ‘density’ expected for a 100% distribution in that lattice at a given radius r . This normalization function, $\eta(r)$, is constant and determined by the nature of the (cubic) lattice used in the model. In the simulation of the binary system, the calculation of the distribution functions of the like and unlike particles was performed according to the following steps:

1. Select a particle i . Calculate $g_i^{AA}(r)$, which is the distribution of all particles having the same identity as the selected particle i , normalized by $\eta(r)$. $\eta(r)$ represents the total number of particles at a radius $r = 1, \sqrt{2}, 2, \sqrt{5} \dots r_{cutoff}$.

$$g_i^{AA}(r) = \frac{1}{\eta(r)} \sum_{j=1}^{\eta(r)} \delta(c_i, c_j) \quad (4.30)$$

Here, $\delta(c_i, c_j)$ is the Kroneker symbol, which equals one if the identities of particles i and j are the same, and is zero otherwise. The information carried by $g_i^{AA}(r)$ about the distribution of like particles at various distances r relates to particle i only.

2. In a manner similar to Step 1, calculate the distribution of unlike particles ($g_i^{AB}(r)$ for the binary and $g_i^{AC}(r)$, $g_i^{BC}(r)$ for the ternary mixture). The analytical view of unlike distribution functions for particle i is similar to that shown in Equation (4.30), except that the term under the sum returns one if the identities of particles i and j are different, and zero otherwise.
3. Visit all particles in the system one by one repeating steps 1 and 2, calculating like and unlike distributions.
4. Calculate the averages of all N single-particle radial distribution functions $g_i(r)$ (like and unlike), following the general rule in Equation (4.31) (suffices are omitted for simplicity):

$$g(r) = \frac{1}{N} \sum_i^N g_i(r) \quad (4.31)$$

5. Repeat steps 1-4 with appropriate frequency during the simulation run, to ensure that the resulting average functions have acceptable accuracy (a satisfactory number of repetitions for the system of size $N = 16 \times 16 \times 16$ was found to be $\mathcal{R} = 10,000$). The distribution functions are then given by the following general equation, angular brackets denoting an ensemble average (NcVT or $N\Delta\mu$ VT):

$$g(r) \equiv \langle g(r) \rangle = \frac{1}{\mathcal{R}} \sum^{\mathcal{R}} g(r) \quad (4.32)$$

For the system size mentioned above, the calculation of distribution functions in step 3 would require N^2 *if*-statements. The final result, obtained from step 5 requires $\mathcal{R}N^2$ *if*-statements, which is equal to $1.67721 \cdot 10^{11}$.

4.4.3 Orientational Correlation Function Calculations

As was shown in Section 1.1.5, $g_2(r)$ in general describes a second-rank order parameter of the particles separated by distance r . Like the radial distribution function, the orientational correlation function $g_2(r)$ is subject to normalization by the total number of sites present at each discrete radius r , i.e. the normalization factor $\eta(r)$. Thus, for the calculation of $g_2(r)$, we further develop the algorithm of the calculation of $g(r)$. Briefly, the total $g_2(r)$ function was normalized by the same $\eta(r)$ factor as was used for $g(r)$, but the $g_2(r)$ function when calculated separately for each individual type of particle, was normalized by the number of particles of the same type present at each radius r , this being the distribution function of like particles, $g_i^{c_\alpha}(r)$ ($g_i^{c_\alpha}(r) = \{g_i^{AA}(r), g_i^{BB}(r), g_i^{CC}(r)\}$). Thus, in the general case of the n -dispersed system (binary, ternary, etc), the calculation of the orientational correlation functions of the total ($g_2(r)$) and subsystems $g_2^{c_\alpha}(r)$ where the identities $c = \{c_1, c_2, \dots, c_n\}$ was performed according to the following steps:

1. Select a particle i and note its identity c_α ($\alpha = 1, 2, \dots, n$). Calculate $g_i^{c_\alpha}(r)$ for particle i (using the procedure Step 1 in Section 4.4.2). Using the method described in Section 4.4.1, calculate the sum of the second Legendre polynomials $P_{2(ij)}^{c_\alpha}(r)$ for particle i and all like particles j (i.e. those of identity c_α) at radius r . Finally normalize the result with $g_i^{c_\alpha}(r)$:

$$g_{2(i)}^{c_\alpha}(r) = \frac{1}{g_i^{c_\alpha}(r)} \sum_{j=1}^{g_i^{c_\alpha}(r)} P_{2(ij)}^{c_\alpha}(r) \quad (4.33)$$

2. Repeat Step 1 for all N particles in the system. This results in N functions, the analytical view of which is $g_{2(i)}^{c_\alpha}(r)$.
3. Average all $g_{2(i)}^{c_\alpha}(r)$ functions with the same c_α . It should be noted that although the sum in Equation (4.34) is over all N functions, only the functions which correspond to particles of the same identity actually contribute.

$$g_2^{c_\alpha}(r) = \frac{1}{x_\alpha \cdot N} \sum_i^N g_{2(i)}^{c_\alpha}(r) \quad (4.34)$$

Here, the normalization is equal to the number of particles which have appropriate identity, hence $(x_\alpha \cdot N)$, where x_α is the concentration of particles in the system with identity c_α . The result is n functions, $g_2^{c_\alpha}(r)$, each of which represents the orientational correlation between particles of like type (identity c_α). For binary and ternary mixtures $n = 2$ and $n = 3$, respectively.

4. Average the $g_{2(i)}^{c_\alpha}(r)$ functions over all N particles, irrespective of their identities c_α , to obtain the total orientational correlation function of the system.

$$g_2(r) = \frac{1}{N} \sum_{i=1}^N \sum_{\alpha=1}^n g_{2(i)}^{c_\alpha}(r) \quad (4.35)$$

This yields a function that ignores particle identity, i.e. the total second-rank orientational correlation function $g_2(r)$. Note that the orientational correlation function is already normalized here (see Equation (4.33)).

5. Perform Steps 1 and 4 with satisfactory periodicity throughout the simulation to gain the necessary accuracy (a satisfactory number of repetitions for a system of size $N = 16 \times 16 \times 16$ was found to be $\mathcal{R} = 10,000$). Thus the correlation functions $g_2(r)$ and $g_2^{c_\alpha}(r)$ ($c = \{c_1, c_2, \dots, c_n\}$) are given by the following equations:

$$g_2^{c_\alpha}(r) \equiv \langle g_2^{c_\alpha}(r) \rangle = \frac{1}{\mathcal{R}} \sum^{\mathcal{R}} g_2^{c_\alpha}(r) \quad (4.36)$$

$$g_2(r) \equiv \langle g_2(r) \rangle = \frac{1}{\mathcal{R}} \sum^{\mathcal{R}} g_2(r) \quad (4.37)$$

As was mentioned earlier, for N particles in the system the calculation of the $g(r)$ function is a process of N^2 steps. In the calculation of $g_2(r)$, however, this scaling increases to at least N^4 , since the calculation of the order parameter itself is a process

of N^2 . For this reason, the Fast Fourier Transform (FFT) procedure was used [182] instead for the majority of the $g_2(r)$ calculations. FFT reduces the scaling of the calculation time to N^2 . Both direct and FFT techniques were compared and found to yield the same results.

4.4.4 Histogram Re-weighting Technique

The histogram re-weighting technique was introduced in 1988 [183], and then modernised 1993 [175]. It allows data obtained from a single simulation to be used to generate ‘continuous’ thermodynamic functions across a chosen region of parameter space. The technique has been found to be useful when the behaviour of the system displays sharp peaks, as for example near phase transitions, and it has proven to be a useful tool for determining the nature of various transitions.

The histogram re-weighting technique allows one to reproduce an energy histogram for a new set of input parameters using an existing one, obtained with a relatively close set of input parameters. This means, for example, that it becomes possible to determine the many histograms that represent the state of the system at different temperatures, using data from a single long simulation run performed at one fixed temperature. The concept behind this technique is fairly simple. Histograms are obtained from equilibrium statistical mechanics calculations. The form of the partition function is:

$$Z = \sum_{\Gamma} e^{-\frac{\mathcal{H}}{k_B T}} \quad (4.38)$$

By calculating a distribution at a particular temperature, pressure, density, etc. that part of the partition function which is significant for those constant parameters is sampled. Let us consider an example of two histograms (\mathcal{P}_β and $\mathcal{P}_{\beta'}$) obtained at a slightly different values of the input parameter $\beta = 1/k_B T$.

$$\mathcal{P}_\beta(\sigma_i) = \frac{\exp(-\sigma_i \beta)}{Z} \quad (4.39)$$

$$\mathcal{P}_{\beta'}(\sigma_i) = \frac{\exp(-\sigma_i \beta')}{Z} \quad (4.40)$$

The partition function Z is unchanged in both cases, since it is a sum over all states. More accurately, only the sum over limited range of $-\sigma_i$ is used, which is sufficient

for Equations 4.39 and 4.40, providing that β and β' are close. Thus

$$\frac{\mathcal{P}_\beta(\sigma_i)}{\exp(-\sigma_i\beta)} = \frac{\mathcal{P}_{\beta'}(\sigma_i)}{\exp(-\sigma_i\beta')} \quad (4.41)$$

Thus, if the difference in value between β and β' is sufficiently small, the region of Z sampled in the calculations at β can also be used to calculate a new histogram at β' . Following this notion through more formally, it can be shown that [175]

$$\mathcal{P}_{\beta'}(\sigma_i) = \mathcal{P}_\beta(\sigma_i) \frac{\exp(-\sigma_i(\beta - \beta'))}{\langle \exp(-\sigma_i(\beta - \beta')) \rangle_\beta} \quad (4.42)$$

In theory, this method could be used to cover a large parameter space. In practice, however, the original histogram is sampled with finite statistics; energy values σ_i are approximated by discrete bins and the distribution function itself, $\mathcal{P}(\sigma_i)$, is not continuous and, as a result, is truncated at both sides of σ_i axis. For this reason, care has to be taken when extrapolating too far from the original simulation point.

4.4.5 Estimating Errors

As with real life experiments, computer simulations are subject to systematic and statistical errors. Sources of systematic error include size-dependence, the possible effects of poor random number generators, non-equilibration, etc. Another significant cause of statistical error in the calculated mean values is the finite length of a simulation run. The general approach to estimating statistical error is based on finding the mean $\langle \mathcal{A} \rangle_\tau$ and the variance $\sigma^2(\langle \mathcal{A} \rangle_\tau)$ of the measured values \mathcal{A}_i , where τ is the length of the simulation run. In simulation, τ is a discrete value and usually represents the number of measurements taken.

$$\langle \mathcal{A} \rangle_\tau = \frac{1}{\tau} \sum_{i=1}^{\tau} \mathcal{A}_i \quad (4.43)$$

$$\sigma^2(\langle \mathcal{A} \rangle_\tau) = \frac{\langle \delta \mathcal{A}^2 \rangle_\tau}{\tau}, \quad \text{where} \quad \langle \delta \mathcal{A}^2 \rangle_\tau = \frac{1}{\tau} \sum_{i=1}^{\tau} (\mathcal{A}_i - \langle \mathcal{A} \rangle_\tau)^2 \quad (4.44)$$

We assume that \mathcal{A} is a Gaussian process, such that $\langle \delta \mathcal{A}^2 \rangle_\tau$ is essentially given by the sum of a large number of ‘random’ quantities. Eventually, when $\tau \rightarrow \infty$, $\langle \mathcal{A} \rangle_\tau$ gives a true value of \mathcal{A} . However, for finite τ , $\langle \mathcal{A} \rangle_\tau$ almost always differs from \mathcal{A} . In addition, the data points from which $\langle \mathcal{A} \rangle_\tau$ is calculated may not be truly independent; they may have been stored sufficiently frequently that they are highly correlated with one another. Therefore the τ measurements that were taken during simulation cannot necessarily be treated as being the ‘true’ simulation length in Equation 4.44. The correct number of measurements is actually the number that were taken from configurations of the system that were totally independent of each other. In this case the error of evaluation of $\langle \mathcal{A} \rangle_\tau$ can be estimated as:

$$\sigma(\langle \mathcal{A} \rangle_\tau) = \sqrt{\frac{\xi}{\tau} \langle \delta \mathcal{A}^2 \rangle_\tau} \quad (4.45)$$

Here the correlation length ξ , due to Friedberg and Cameron [184], is defined as being the limiting ratio of the observed variance of an average to the limit expected on the assumption of uncorrelated Gaussian statistics (Eq.4.46).

$$\xi = \lim_{\tau_b \rightarrow \infty} \frac{\tau_b \sigma^2(\langle \mathcal{A} \rangle_\tau)}{\sigma^2(\mathcal{A})} \quad (4.46)$$

This ratio can be determined on the computer as follows. Take a data set of length τ and divide it into blocks each of length τ_b , to give $n_b = \frac{\tau}{\tau_b}$ blocks. Calculate the mean value of \mathcal{A} for each block, following Equation 4.43. This gives n_b mean values $\langle \mathcal{A} \rangle_b$, one for each block b . These values for all the blocks can be further used to estimate the variance

$$\sigma^2(\langle \mathcal{A} \rangle_{\tau_b}) = \frac{1}{n_b} \sum_{b=1}^{n_b} (\langle \mathcal{A} \rangle_b - \langle \mathcal{A} \rangle_{\tau_b})^2 \quad (4.47)$$

Then change the length of the block and recalculate the variance. The dependence of this variance on the reciprocal length (or number) of data blocks can then be plotted and ξ obtained by extrapolating to the limit in 4.46. ξ also can be used as an indicator of inefficiency in the simulation. More accurate data are obtained when ξ is small, so various algorithms can be tested objectively by finding which has most efficient value for ξ .

Having said this, for most of our simulations we used a run length τ of only 20,000 steps per particle plus 5,000 steps for equilibration, whilst for our system the cor-

relation length ξ calculated from total energy data was found to be between 1,500 and 5,000 steps depending on the temperature. Thus, in the worst case scenario, effectively we obtained and used only 4 independent values to estimate the mean energy value for each point on the phase diagram. Below follows a justification for such a choice.

The data for the P_2 values presented in the next chapter were calculated using run lengths of at least 200,000 steps per particle plus 15,000 steps for equilibration. Here, each successive simulation run was performed with a different value of T , starting from the previous configuration, with $\Delta T = 0.1$. It was later discovered that by decreasing ΔT to 0.005, we could significantly reduce τ , yet obtain similar results. The values of P_2 calculated using long runs and the large temperature step matched those calculated using short runs and tiny temperature step. In both methods the previous configuration was used to start the next simulation. In addition, a number of long run simulations were performed at different temperatures, each starting from the same, random or isotropic configuration. The results obtained from this were also consistent with those obtained from the other two methods. Also, the consistency of the mean values for P_2 and U at neighbouring temperatures indicates small error bars. Finally, the same observable dependencies on T , obtained using both decreasing and increasing temperature cycles did not yield a hysteresis loop. The calculations of the energy histograms at 3,000,000 steps per particle in the area of phase transition were also consistent with the values obtained from short simulation runs. In conclusion to all this, we would like to point to the work of Cleaver and Allen [185], published on the single component Lebwohl-Lasher model, which used the simulation lengths of a similar magnitude, 50,000 steps. Values for τ of a similar magnitude were also used for simulations of binary mixtures using the Lebwohl-Lasher model in the works of Bates [179] and Luckhurst [177]. The long correlation length in our simulations, could be explained by the fact that we used the total energy to estimate ξ , while in [185] the primary observables, the elastic constants, were used. Also, the introduction of binary mixture might have increased the value of ξ in our simulations.

Thus, for calculations of U and $g(r)$ we used $\Delta T = 0.005$ and $\tau = 20,000$. The reason for using such a small ΔT value was the desire to identify, to high resolution, the location of any phase transition exhibited by the simulated system.

Chapter 5

Results And Discussion.

Bi-Dispersed System. NcVT

In this chapter we present and discuss the results for the phase behaviour of binary system, based on the Lebwohl-Lasher lattice model. The results were obtained by performing Monte Carlo simulations in the Canonical Ensemble (NcVT). The model basis was described in Chapter 4. For most calculations we used a system in which the cubic simulation box consisted of sixteen sites on each side of the box (i.e. a system size of 16x16x16 particles). All results presented in this chapter were obtained using this unless otherwise stated. The correlation length of runs for the given system was estimated around 5,000 run steps. Therefore, for such observables as average energy function $\langle E(T) \rangle_{NcVT}$, and the average radial distribution function $\langle g^{AB}(r = 1, T) \rangle$ runs with 20,000 steps per point were performed, with an additional 5,000 steps included for equilibration. At low temperatures these run-lengths were doubled. For the calculation of the energy histograms number of steps per point was increased to 3,000,000. For the calculation of the second rank order parameter $\langle P_2(T) \rangle_{NcVT}$ we used from 50,000 to 200,000 steps per point. The temperature step for all $\langle E(T) \rangle_{NcVT}$ and $\langle g^{AB}(r = 1, T) \rangle$ data was $\Delta T = 0.005$. The largest temperature step used for calculation of $\langle P_2(T) \rangle_{NcVT}$ was $\Delta T = 0.1$. The energy histograms were only calculated for a few specific temperatures, normally in the vicinity of the transition.

In Section 5.1 we present a set of results for six binary systems with coupling constants $\varepsilon = 0.9, 0.6, 0.45, 0.3, 0.1, 0.0$. The lower the coupling constant ε , the less

anisotropic is one of the components of the binary mixture in the system. The set of results for each system is divided into four main parts. In the first part, we present calculations of the average internal energy of the system $\langle E \rangle_{NCVT}$ and its dependence on temperature T and concentration c , $\langle E(T, c) \rangle_{NCVT}$. The energy of the system was calculated using the Hamiltonian of the system described in Section 4.2 of Chapter 4. In the second part we present results of the second rank orientational order parameter $\langle P_2 \rangle_{NCVT}$ and its dependence on temperature T and concentration c , $\langle P_2(T, c) \rangle_{NCVT}$. We used the second rank correlation function $g_2(r)$ to calculate the value of $\langle P_2 \rangle_{NCVT}$. More on $g_2(r)$ is covered in Section 4.4.1 of Chapter 4. The second rank orientational order parameter indicates the level of orientational order in the system of anisotropic particles, hence the symmetry of the system or phase. When $\langle P_2 \rangle = 0$ - or, in the case of the finite system we investigated, when $\langle P_2 \rangle \approx 0$ - then the system exhibits an isotropic phase. When $\langle P_2 \rangle \neq 0$ (or $\langle P_2 \rangle > 0$ in case of the investigated system) then the system exhibits an anisotropic phase. In addition we present the results of the second rank orientational order parameter calculated for each component of the binary system separately. In the third part, we present the results of the radial distribution function of unlike particles $g^{AB}(r)$. Owing to the specifics of the model, the all-particle radial distribution function has static periodicity and hence gives no information. However, the properties of the model considered here allow us to calculate the radial distribution functions of the like and unlike particles. The method of calculation of $g^{AB}(r)$ in the binary lattice system was described in Section 4.4.2 of Chapter 4. The results in this part are organised into two categories - results for the short range and the long range radial distribution function. These functions show how well the system was mixed and indicate any structural changes. In the fourth and last part of each set of results we present a phase diagram based on the results presented previously.

In Section 5.3 of this chapter we present an alternative view of these phase diagrams by considering three slices with fixed concentrations $c = 0.2, 0.5, 0.7$. The difference between phase diagrams presented in this section and those presented in Section 5.1 is that the former show the phase behaviour of the system in a phase space plane perpendicular to that considered in the latter - coupling constant versus temperature.

In Section 5.4 of this chapter we discuss the results presented in Sections 5.1-5.3 and present additional results to clarify some particular characteristics of the behaviour of the system. The discussion in Section 5.4 proceeds in the following order. Firstly,

we examine the results of the energy dependencies and discuss energy histograms. Then we consider the dependencies of the order parameter, the radial distribution function and their correlation with the results of the internal energy and with each other. After that, we move on to explain phase diagrams and compare with our predictions and expectations. This is followed by an explanation of certain anomalous phase behaviour in the light of further results and the existing literature.

Since all observables presented in this chapter were obtained at constant $NcVT$, we omit the index ($NcVT$) in our notation. In this chapter, the more anisotropic particles are indexed as particles A and the less anisotropic particles, as particles B. In all the systems covered in this chapter, only ε , the anisotropy of particles B, is subject to change.

5.1 Results for systems with varying ε

5.1.1 System with $\varepsilon = 0.9$

The first system investigated is the binary system with coupling constant $\varepsilon = 0.9$. Of all the systems presented here, this system has the smallest difference between the anisotropies of its two components. Thus this system is the closest to its single component counterpart. The first observable of the system that we present is the average internal energy of the system $\langle E \rangle$. Figure 5.1 shows the dependencies of the energy $\langle E(T) \rangle$ on temperature for various concentrations c . For all concentrations the energy decreases with decreasing temperature. Apart from this anticipated behaviour, we observe a deviation from the characteristic curve at temperatures $T_{tr}(c)$ on the $\langle E(T) \rangle$ curves for the entire concentration range. Numerical differential of $\langle E(T) \rangle$ (heat capacity) reveals peak at $T_{tr}(c)$. Thus we consider this temperature as a point of discontinuity of $\langle E(T) \rangle$ and, thus, a transition of the system. At first, the energy $\langle E \rangle$ has a low negative value at high temperatures. Then it decreases slowly with the lowering of temperature until at $T \approx T_{tr}(c)$ it decreases quite rapidly. The internal energy $\langle E(T) \rangle$ then decreases continuously, but with a changed slope, until it reaches temperature $T = 0$. The temperature of the maximum gradient $T_{tr}(c)$ is unique for each concentration in the given system with $\varepsilon = 0.9$. The values of such temperatures $T_{tr}(c)$ are presented in Table 5.1. From the Table it is clear that $T_{tr}(c)$ increases monotonically with increase in concentration c . The tendency

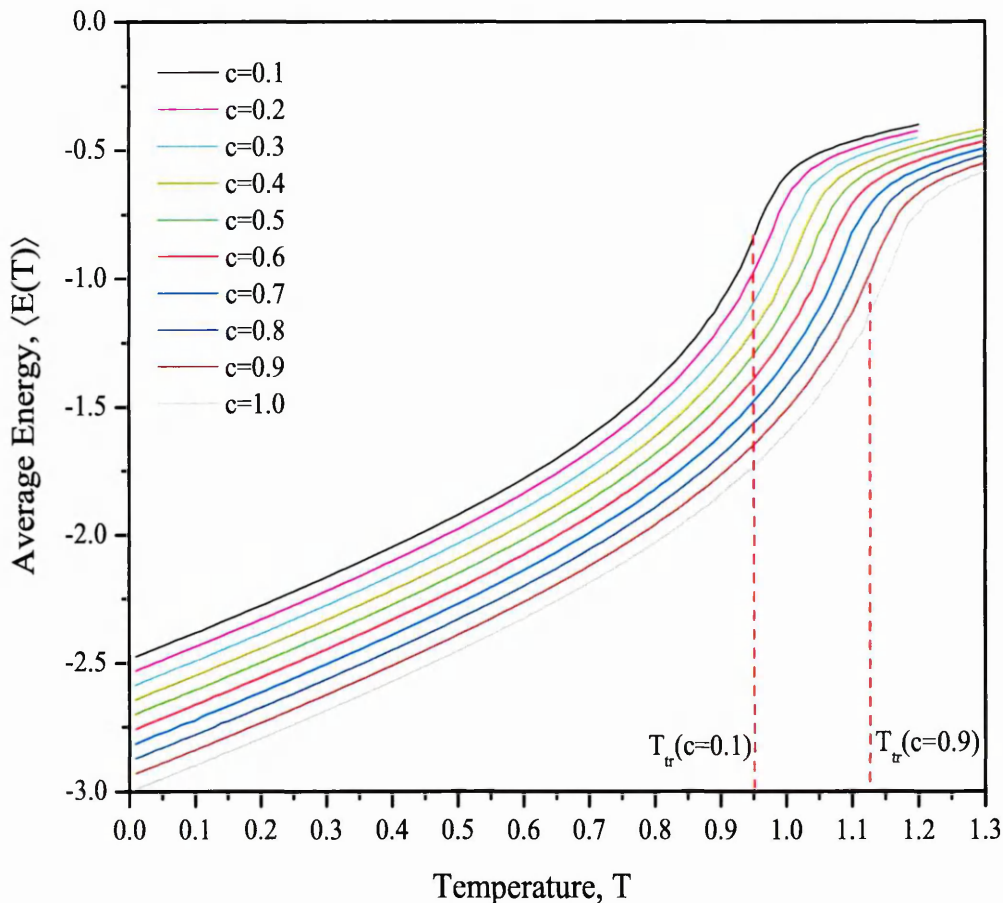


Figure 5.1: Dependence of the average internal energy on the temperature, $\langle E(T) \rangle$. Each curve represents $\langle E(T) \rangle$ dependence for the unique concentration c .

for all $\langle E(T) \rangle$ curves is that the entire curve displaces down in energy with a decrease in the concentration c of the more anisotropic particles (A). All $\langle E(T) \rangle$ curves seem to be ‘parallel’ to each other for the region of the temperatures below $T_{tr}(c)$. At temperatures above $T_{tr}(c)$, they approach a common point ($E, T \rightarrow \infty$). Equal steps of concentration change shift the $\langle E(T) \rangle$ curve in equal steps of energy value throughout the entire concentration range.

The next observable we present for the system with $\varepsilon = 0.9$ is the second rank orientational order parameter ($S = \langle P_2 \rangle$). Both in experiment and theory, there are a number of approaches to calculating $\langle P_2 \rangle$. We obtain results for the order parameter from the pair correlation function $g_2(r)$ (Sec. 4.4.1, 4.4.3). $g_2(r)$ shows how well the orientation of the anisotropic particles is correlated throughout the bulk. In Fig.5.2

concentration c	Temperature $T_{tr}(c)$
0.0	0.93 ± 0.01
0.1	0.95 ± 0.01
0.2	0.98 ± 0.01
0.3	1.00 ± 0.01
0.4	1.02 ± 0.01
0.5	1.04 ± 0.01
0.6	1.06 ± 0.01
0.7	1.08 ± 0.01
0.8	1.11 ± 0.01
0.9	1.13 ± 0.01
1.0	1.15 ± 0.01

Table 5.1: Table of Temperatures $T_{tr}(c)$ obtained from $\langle E(T) \rangle$ data. $T_{tr}(c)$ were derived as a point where the tangent of $\langle E(T) \rangle$ is the steepest. System with $\varepsilon = 0.9$.

we present the dependence of the orientational correlation on distance $g_2(r)$ for the system with $\varepsilon = 0.9$ and concentration $c = 0.5$. Each $g_2(r)$ curve represents the pair correlation function taken at a different temperature. From Fig.5.2 it is clear that at short range ($r \lesssim 3$) there is a higher orientational correlation between particles than at the long range ($r \gg 3$) at most temperatures. At high temperature, $g_2(r \lesssim 3)$ grows with the reduction of T , while the long range correlation function $g_2(r \gg 3)$ remains unchanged and is equal to ≈ 0 . Then, as temperature decreases further, at $T_{tr}(c)$ the long range correlation function starts to increase rapidly, catching up with the value of the correlation function at the short range. As the temperature decreases, the difference between the short range and long range correlations becomes smaller. Eventually, it becomes the same for all values of r as $T \rightarrow 0$. Figure 5.3 shows how the value of the pair correlation function at long range $g_2(r \gg 3)$ changes with temperature T in the system with $\varepsilon = 0.9$. The value on the vertical axis, $\langle P_2(T) \rangle$, relates to the $g_2(r \gg 3)$ as a square root of the latter (Eq.1.11). Let us study the graphs in Fig. 5.3, starting from the highest concentration and moving down.

With the concentration of more anisotropic particles $c = 1.0$ the system is pure or single-component ($\varepsilon = 1.0$). For such a system, the order parameter exhibits a transition from the isotropic to nematic phase at the temperature $T_{IN} \approx 1.18$ (See Table 5.2). When the concentration c is reduced to $c = 0.9$ (Fig.5.3) the

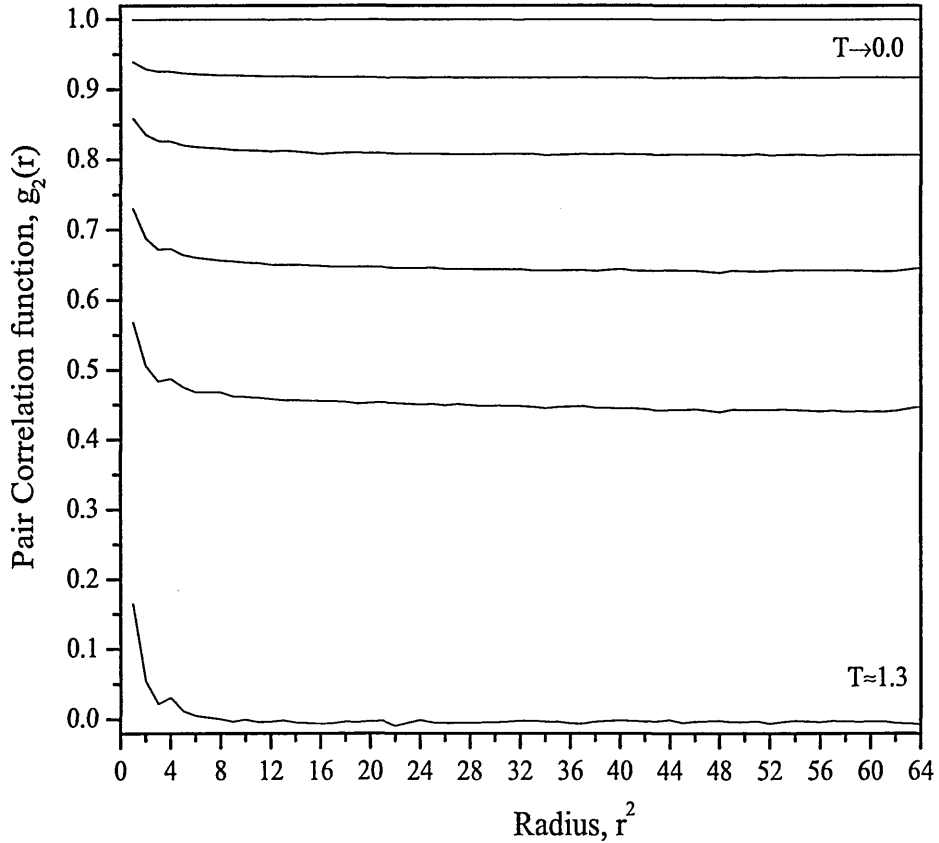


Figure 5.2: The pair correlation function, $g_2(r)$ for the system with $\varepsilon = 0.9$, $c = 0.5$. Dependence on r^2 . Different curves represent the function taken at different temperatures.

system undergoes isotropic-nematic (I-N) transition at a lower temperature. Moving down the concentration we find the system exhibiting similar behaviour. Let us consider the system with $c = 0.5$ in Fig. 5.3 and refer to Fig.5.2. Starting from $T = 1.2 \gg T_{tr}(c = 0.5)$, the value of $\langle P_2 \rangle$ remains unchanged and equal to ≈ 0 , which corresponds to the value of $g_2(r \gg 3)$ in Figure 5.2. Then, at $T_{tr}(c) \approx 1.08$, $\langle P_2 \rangle$ starts to increase rapidly with increasing temperature and levels off to the value of $\langle P_2 \rangle \rightarrow 1.0$ at $T \rightarrow 0$. As the concentration of the mixture decreases, the transition temperature reduces, until $c \rightarrow 0.0$. As $c \rightarrow 0.0$ the transition temperature of the mixture approaches the transition temperature of the pure system $T_{tr}(c = 0.0) = 0.96$ with all the particles of type B (See Table 5.2 and discussion in Section 5.4).

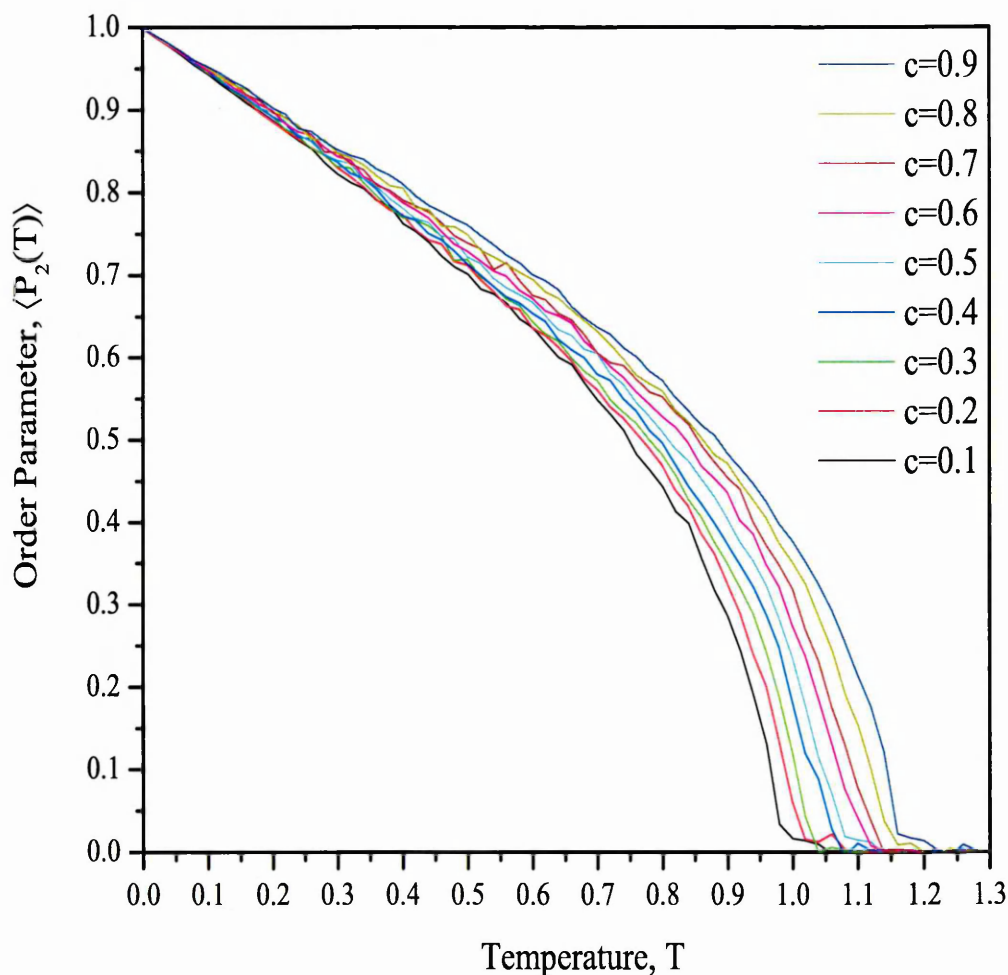


Figure 5.3: Dependence of the second rank orientational order parameter on temperature, $\langle P_2(T) \rangle$. Different curves represent different concentrations c in the binary mixture with $\varepsilon = 0.90$.

Table 5.2 shows the values of $T_{tr}(c)$ for the full set of concentrations. From the Table we see that the I-N transition temperature $T_{tr}(c)$ decreases with reduction of concentration c . These values of $T_{tr}(c)$ are found to be in good agreement with the values of $T_{tr}(c)$ obtained from the energy calculations, presented earlier (Table 5.1). Note, $T_{tr}(c)$ in Table 5.2 was determined as point of inflection of the $\langle P_2(T) \rangle$ curve projected on T axis. This is different from the usually used notion of $T_{tr}(c)$ being at the point of $\langle P_2(T) \rangle \approx 0.3$, which partially explains higher values of $T_{tr}(c)$ compared to the energy data.

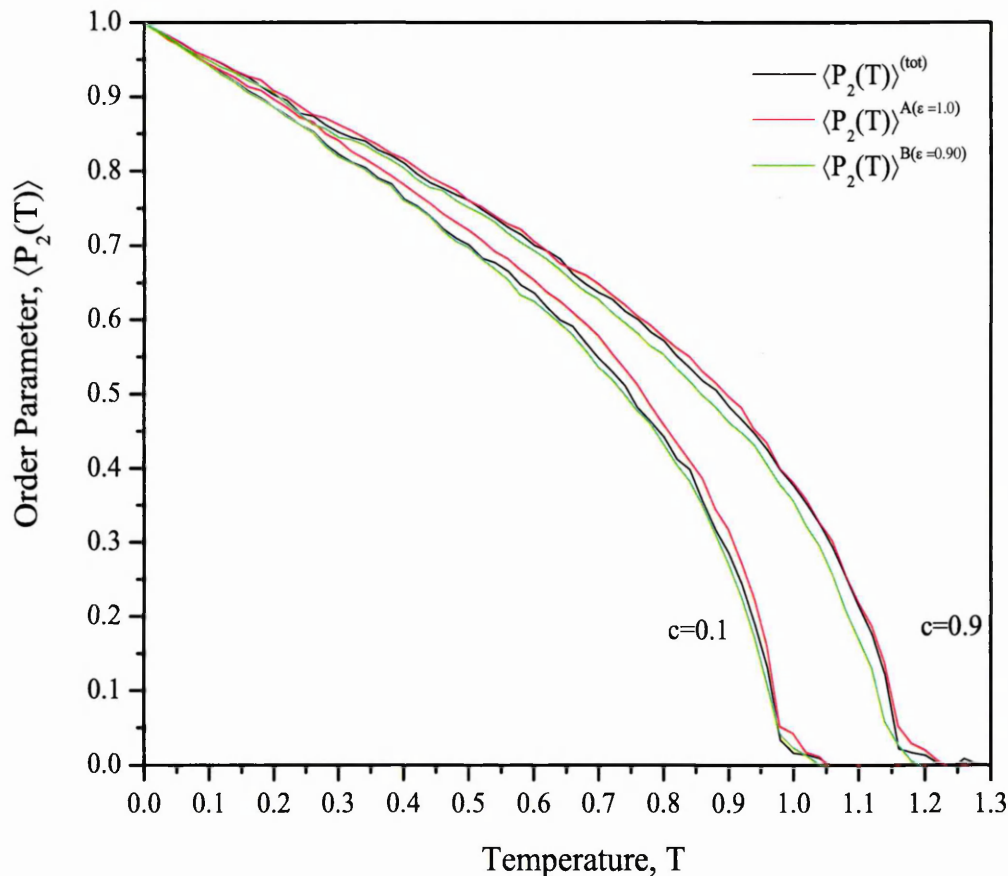


Figure 5.4: Dependence of the second rank orientational order parameter on temperature, $\langle P_2(T) \rangle$, individually for particles A and B.

For the $\epsilon = 0.9$ system, the shape of the $\langle P_2 \rangle$ curve does not seem to change significantly with concentration. In general, here, the $\langle P_2(T) \rangle$ curves are simply superpositions of the order parameter curves of each individual component. Therefore, separate consideration of the results of $\langle P_2(T) \rangle$ curves for the more anisotropic (A) and for less anisotropic (B) components might give us more insight into the nature of phase transition. One of the advantages of simulation is that in the binary mixture it is straightforward to calculate such observables separately for each component. In Figure 5.4 we present separately the results of the order parameter for the more $\langle P_2^A(T) \rangle$ and less $\langle P_2^B(T) \rangle$ anisotropic particles. From this Figure we see that though the transition occurs at the same temperature for both types of particle, the shapes of the order parameter functions for the two species vary slightly. B particles tend to align in a less orderly manner than A particles. However, the values of $\langle P_2(T) \rangle$ for both particles approach the same value at $T \rightarrow 0$.

concentration c	Temperature $T_{tr}(c)$
0.0	0.96 ± 0.05
0.1	0.98 ± 0.05
0.2	1.00 ± 0.05
0.3	1.02 ± 0.05
0.4	1.06 ± 0.05
0.5	1.08 ± 0.05
0.6	1.10 ± 0.05
0.7	1.12 ± 0.05
0.8	1.14 ± 0.05
0.9	1.16 ± 0.05
1.0	1.18 ± 0.05

Table 5.2: Table of Temperatures $T_{tr}(c)$ obtained from $\langle P_2(T) \rangle$ data. $T_{tr}(c)$ were derived as a point where the tangent of $\langle P_2(T) \rangle$ is the steepest.

The next observable we present is the radial distribution function of the unlike particles ($g^{AB}(r)$). In Figure 5.5 we present typical radial distribution functions ($g^{AB}(r)$) for the unlike particles of the binary mixture for the system with $\varepsilon = 0.90$ and $c = 0.5$. The curves represent $g^{AB}(r)$ taken at different temperatures. As is the case for the results for the correlation function, the value of $g^{AB}(r)$ varies with distance r . At the highest temperature starting from the maximum radius the distribution of the unlike particles roughly equals 0.5. Please note that the maximum radius available to the system is $r = 8$, owing to the size of the system investigated (16^3). The value of the distribution function $g^{AB}(r)$ remains virtually unchanged as the distance r decreases, until at a very short range of $r \lesssim 3$ it goes down slightly. With decrease in temperature, the value of the distribution function at short range $g^{AB}(r \lesssim 3)$ starts to decrease further, while its value at the long range $g^{AB}(r \gg 3)$ remains virtually unchanged. In Section 5.1.3 we will show that although, for systems with smaller ε changes at long range of $g^{AB}(r)$ are more significant, the short-range behaviour of $g^{AB}(r)$ still reflects all the changes that happen at long range. For the rest of this chapter (except Section 5.1.3), therefore, we will present results only from the short range part of the function and omit graphs similar to that shown in Figure 5.5.

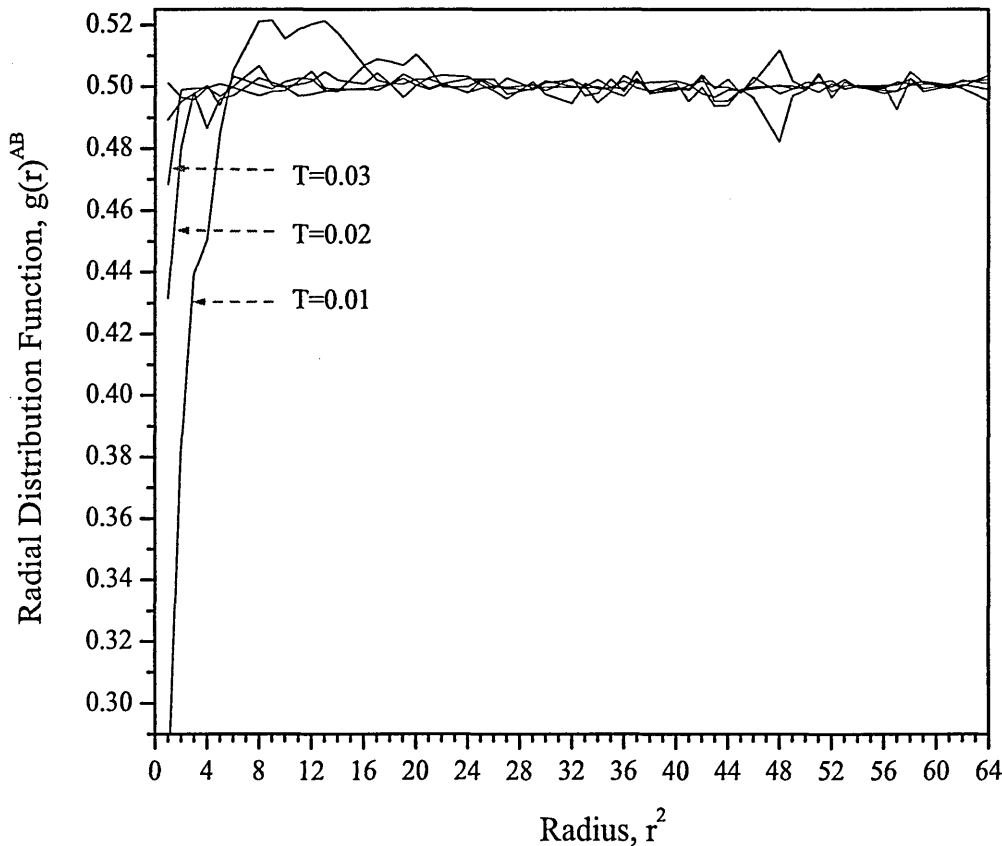


Figure 5.5: Radial Distribution Function $g^{AB}(r)$ for $\varepsilon = 0.90$ and $c = 0.5$. Different curves represent $g^{AB}(r)$ taken at different temperatures.

The thermal dependence of the radial distribution function at short range $g^{AB}(r = 1, T)$ should be able to indicate both slight changes in the structure of the mixture as well as the more significant changes which result from demixing. In Figure 5.6 we present $g^{AB}(r = 1, T)$ for the set of concentrations c .

From this Figure the following features can be seen. Firstly, for all concentrations, we see no significant changes happening with the reduction of temperature, except for a slight decline (Figure 5.7(a)), until a low temperature of the order $T_d(c) \sim 0.05$ is reached, at which the value of $g^{AB}(r = 1, T)$ decreases markedly (Fig. 5.7(a)). The temperature $T_d(c)$, at which the large discontinuity in $g^{AB}(r = 1, T)$ occurs, varies only slightly with concentration c . Table 5.3 presents values of $T_d(c)$ for each concentration. This temperature of discontinuity is highest at a concentration of approximately 0.5 and equals ≈ 0.04 (Table 5.3). The criterion used to set $T_d(c)$ was taken to be a 10% decrease of the $g^{AB}(r = 1, T)$ value.

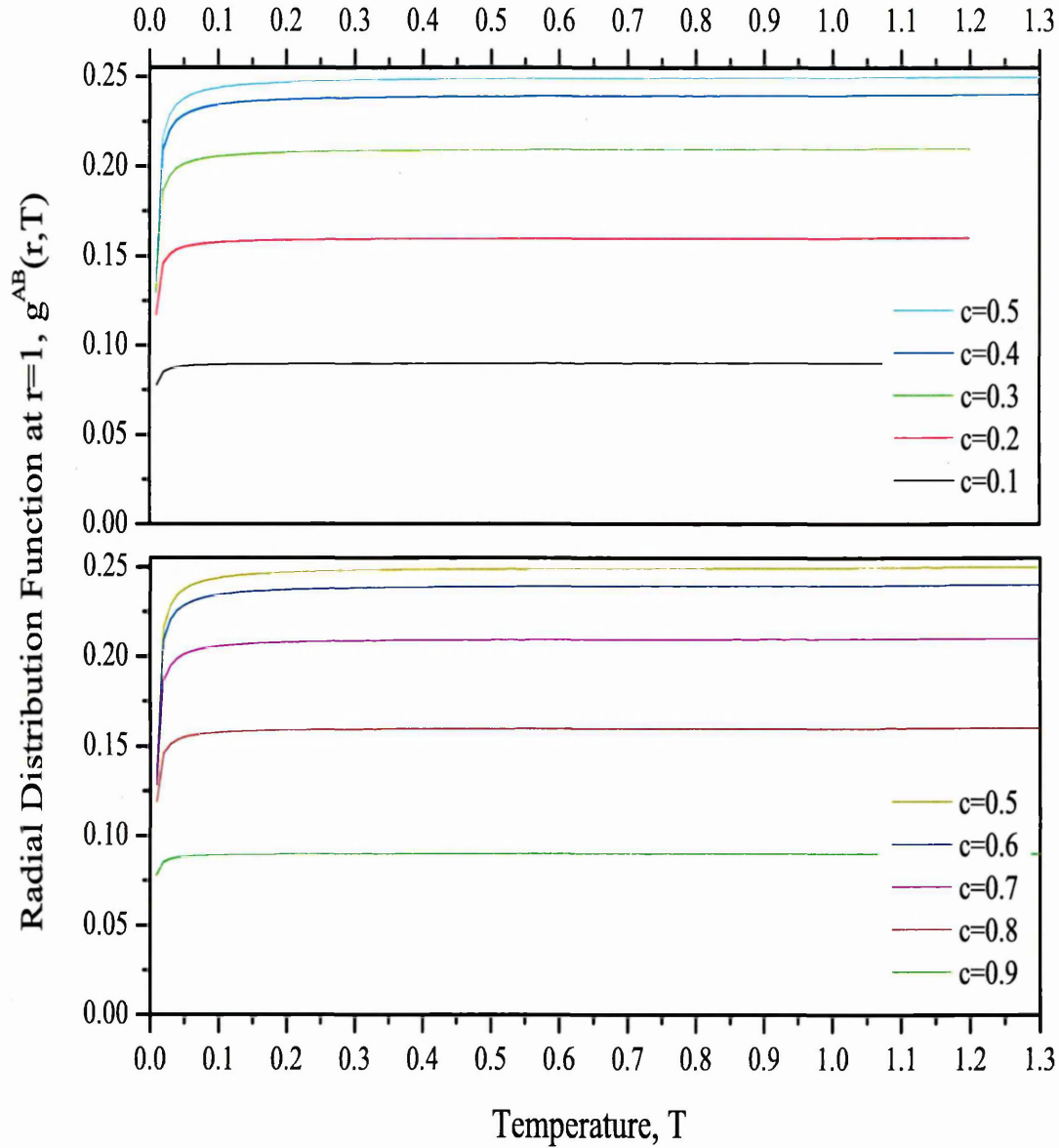


Figure 5.6: Dependence of the radial distribution function $g^{AB}(r = 1)$ on temperature, T . Different curves represent different concentration c . System with $\varepsilon = 0.90$.

Figure 5.7(b) illustrates graphs of $g^{AB}(r = 1, T)$ from Figure 5.6 for concentrations $c = 0.4, 0.6$ in high temperature region, but at a greater resolution. The value of $g^{AB}(r = 1, T)$ drops sharply, but by a relatively small value at $T_{tr}(c)$. Then it continues to fall slowly until the marked fall described earlier. The temperature of the discontinuity $T_{tr}(c)$ decreases slightly as the concentration in the system decreases. In Table 5.3 the values of $T_{tr}(c)$ are presented for the entire set of concentrations.

Criterion for $T_{tr}(c)$ was also taken to be a 10% decrease in the value of $g^{AB}(r = 1, T)$. The results are consistent with the data obtained from energy (Table 5.1) and order parameter (Table 5.2) calculations, though these values are overestimated.

The last feature of the $g^{AB}(r = 1, T)$ graphs is the ratio of the decreases in $g^{AB}(r = 1, T)$ that happen at temperatures $T_{tr}(c)$ and $T_d(c)$. This ratio is roughly the same for the entire set of concentrations studied with $\varepsilon = 0.9$ and approximately equals 0.01.

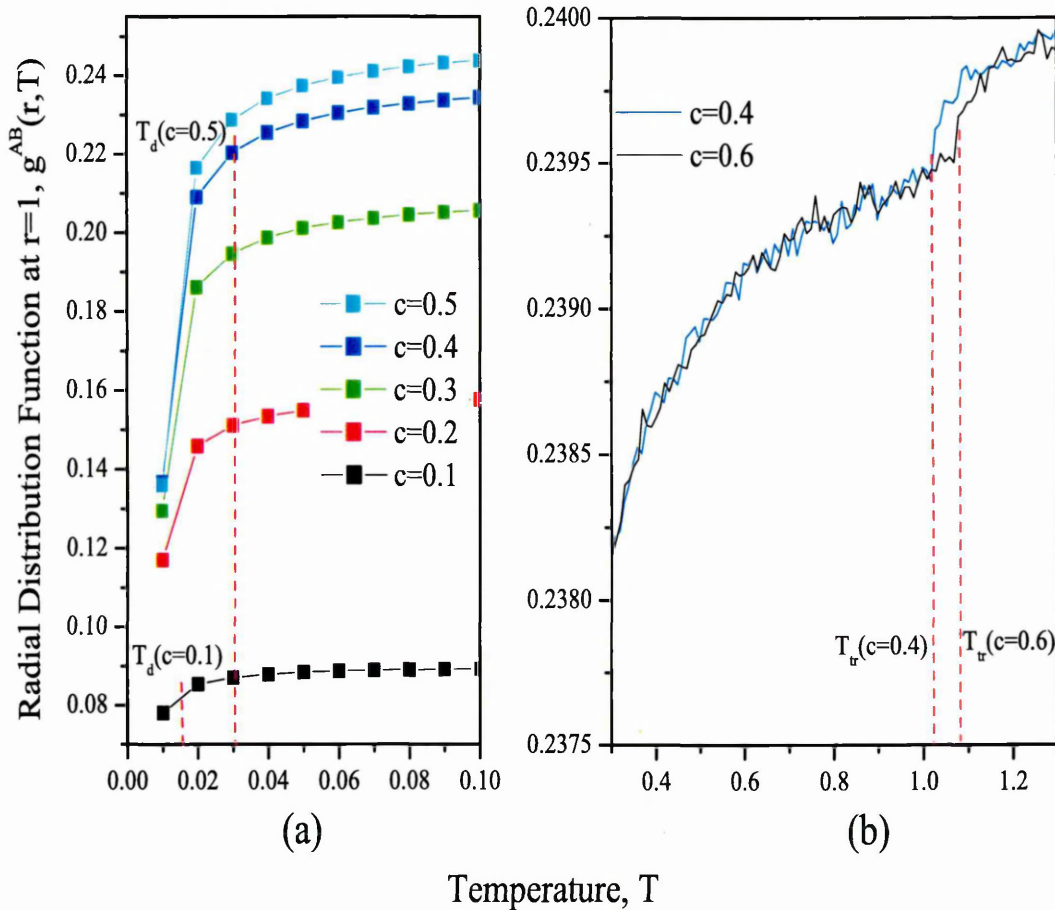


Figure 5.7: Magnified graph of the radial distribution function $g^{AB}(r = 1)$ presented in Fig. 5.6. Different curves represent different concentrations c .

Having presented results for various observables calculated for the system with coupling constant $\varepsilon = 0.9$ and the set of concentrations c , we are now going to use them to produce a phase diagram. In Figure 5.8 we show an example of the contribution of various observables, presented above, to the phase diagram. The graphs in the Figure were juxtaposed and Temperature-Energy, Temperature- $\langle P_2(T) \rangle$, and Temperature-

concentration c	Temperature $T_{tr}(c)$	Temperature $T_d(c)$
0.0	N/A	N/A
0.1	0.95 ± 0.02	0.01 ± 0.02
0.2	0.98 ± 0.02	0.02 ± 0.02
0.3	1.00 ± 0.02	0.02 ± 0.02
0.4	1.03 ± 0.02	0.04 ± 0.02
0.5	1.06 ± 0.02	0.04 ± 0.02
0.6	1.08 ± 0.02	0.03 ± 0.02
0.7	1.10 ± 0.02	0.02 ± 0.02
0.8	1.13 ± 0.02	0.02 ± 0.02
0.9	1.16 ± 0.02	0.01 ± 0.02
1.0	N/A	N/A

Table 5.3: Table of Temperatures based on results obtained from $g^{AB}(r = 1, T)$ data.

$g(r)$ ordinates-abscissae were transposed for the sake of clarity. As shown in Figure 5.8 the temperatures of discontinuity in the gradient of the energy value on graph (a) and $\langle P_2(T) \rangle$ on graph (c) were used to estimate isotropic-nematic boundaries on the phase diagram in the middle graph (b). The short range $g^{AB}(r = 1)$ function (d) was mainly used to determine the boundaries of the demixing region, shown in blue on the diagram in the middle graph (b). As we see in Figure 5.9, this allowed us to produce a phase diagram. Owing to the finite resolution on the concentration scale, the finite temperature step and the difficulties mentioned in Section 4.4.5 of Chapter 4, the phase diagram in Figure 5.9 is presented as a set of finite points in temperature-concentration space.

Each point on the phase diagram is displayed in a particular colour which relates to the corresponding phase and structure of the system with $\varepsilon = 0.9$. Thus, black points represent the isotropic phase; red points, the nematic phase; blue points, the nematic-nematic phase coexistence. For some sets of input parameters we were unable to determine unambiguously the phase of the system or resolve the values of the observables measured. These are represented as green points on the diagram.

Let us comment on the isotropic-nematic boundary first ($T_{IN}(c)$ curve). At both ends of the concentration axis ($c = 0.0$ and $c = 1.0$), the system exhibits an I-N transition at the temperatures of its pure components $T_{IN}(c = 0.0) = 0.93$ and $T_{IN}(c = 1.0) = 1.15$ respectively. At concentrations between $c = 0.0$ and $c = 1.0$, the $T_{IN}(c)$ curve follows a simple linear dependence. The system undergoes an I-N

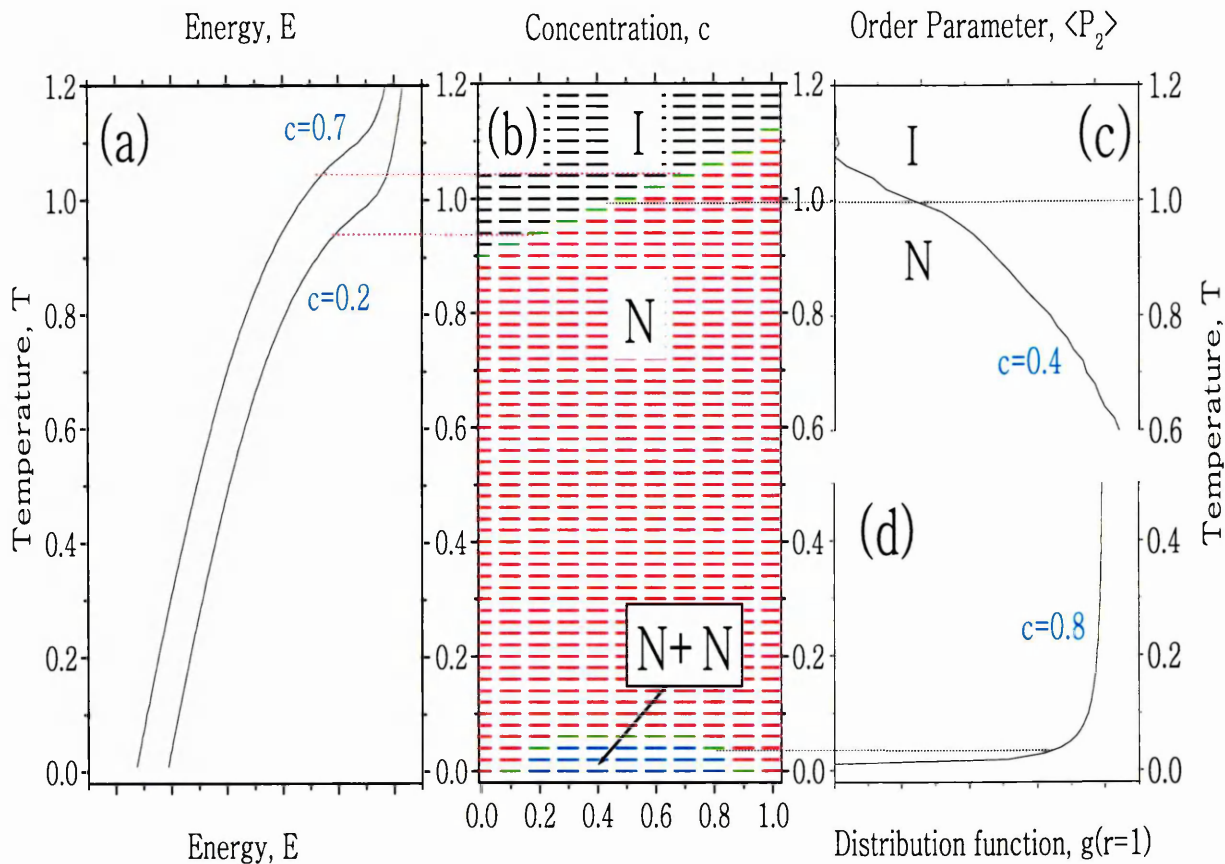


Figure 5.8: Constructing of the phase diagram from $\langle E(T) \rangle$, $\langle P_2(T) \rangle$ and $g^{AB}(r=1)$ data for the system with $\varepsilon = 0.9$.

transition at all concentrations. The radial distribution functions indicate the system to be homogeneous at temperatures above and below the transition throughout the entire concentration range. In other words, different particles of the system are well mixed in both phases the isotropic (black area) and the nematic (red area) (Fig. 5.9). However, at considerably lower temperatures we observe another phase envelope, coloured blue on the diagram. This corresponds to the demixed system in which two nematic phases, each rich in one of the two components of the mixture, coexist. This area of the phase diagram occupies a very small part of it in the region of $T \lesssim 0.1$.

The nematic mixed phase occupies most of the phase space considered. Note that, owing to the specifics of the model, the isotropic phase extends to infinity on the

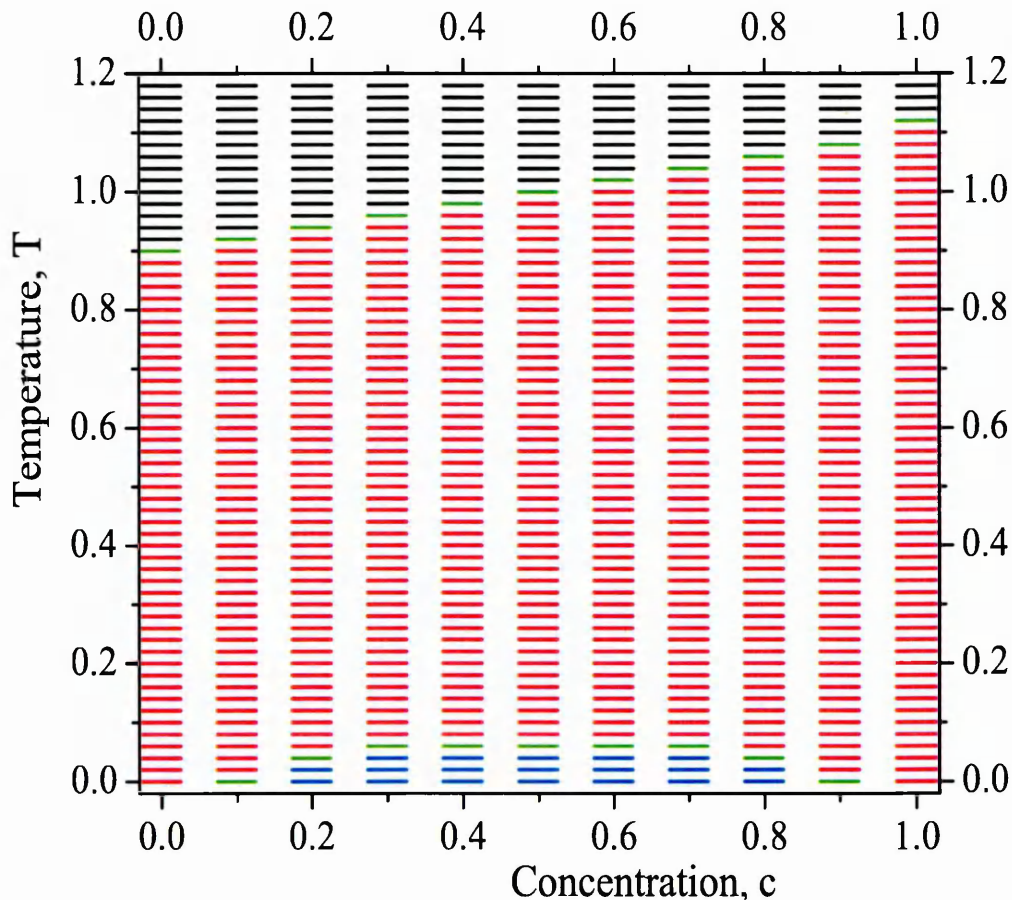


Figure 5.9: Phase diagram for the system with $\varepsilon = 0.9$.

temperature scale rather than going into a gas phase, etc. However, we restricted the upper limit in the diagram to $T = 1.2$ in the interests of convenience in presenting and discussing the results. Further discussion of the results presented so far follows in Section 5.4.

5.1.2 System with $\varepsilon = 0.6$

The next system to be presented is the mixture with $\varepsilon = 0.6$. This system differs from the former only by virtue of the coupling constant ε , which indicates that particles of type B are less anisotropic than their equivalents in the system with $\varepsilon = 0.9$.

Following the same procedure as that adopted in the previous section, we consider first the average energy of the system $\langle E \rangle$. In Figure 5.10 we present the dependence of the energy $\langle E \rangle$ on temperature for various concentrations c . The $\langle E(T) \rangle$ curves for the system do not differ significantly from those observed in the system with $\varepsilon = 0.9$ apart from one feature that was not previously seen.

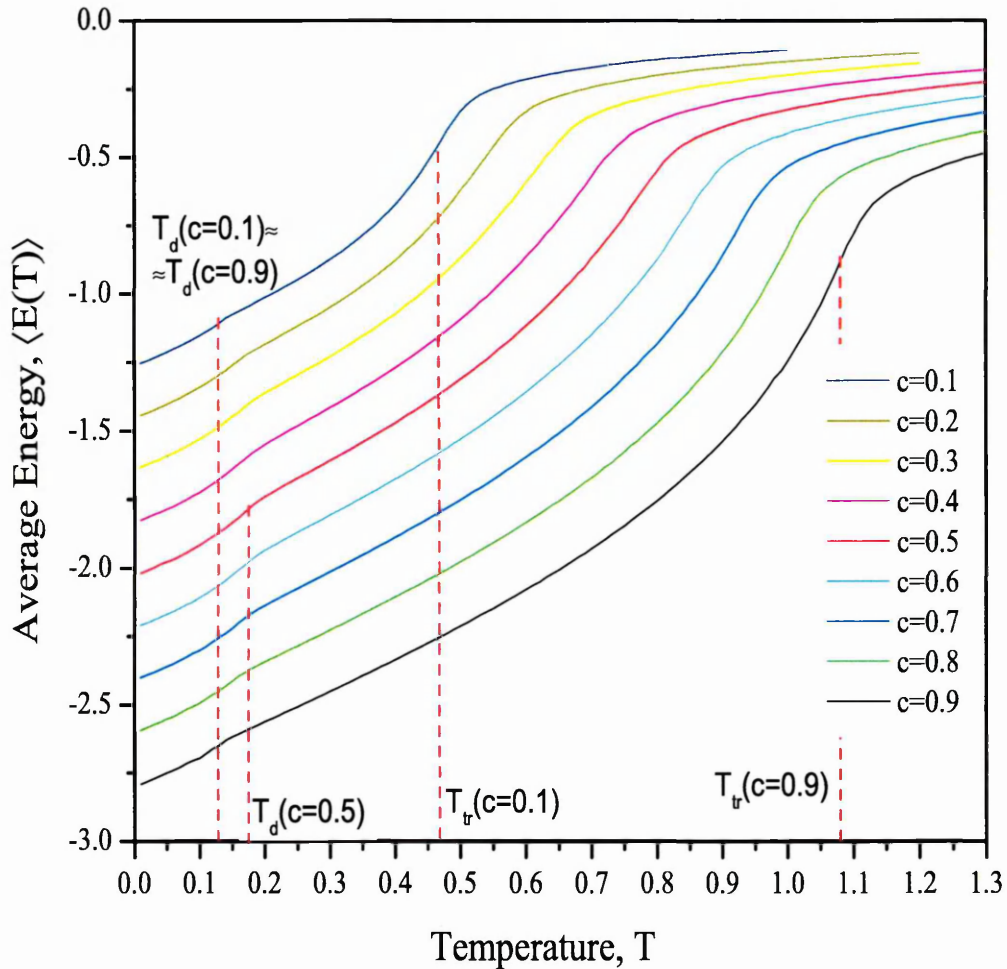


Figure 5.10: Dependence of the average energy $\langle E(T) \rangle$ on the temperature, for the system with $\varepsilon = 0.6$. Various curves represent $\langle E(T) \rangle$, at different concentrations c .

Starting from the highest temperature on the graph, we initially observe the same kind of behaviour as in the previous system. At temperatures $T_{tr}(c)$ the $\langle E(T) \rangle$ curves show gradient discontinuities for all concentrations c . $T_{tr}(c)$ is unique for each concentration and occurs roughly at equal temperature intervals for equal differences

concentration c	Temperature $T_{tr}(c)$	Temperature $T_d(c)$
0.0	0.41 ± 0.01	N/A
0.1	0.47 ± 0.01	0.13 ± 0.01
0.2	0.52 ± 0.01	0.16 ± 0.01
0.3	0.61 ± 0.01	0.17 ± 0.01
0.4	0.70 ± 0.01	0.17 ± 0.01
0.5	0.76 ± 0.01	0.17 ± 0.01
0.6	0.84 ± 0.01	0.16 ± 0.01
0.7	0.92 ± 0.01	0.16 ± 0.01
0.8	1.01 ± 0.01	0.15 ± 0.01
0.9	1.08 ± 0.01	0.12 ± 0.01
1.0	1.15 ± 0.01	N/A

Table 5.4: Table of Temperatures $T_{tr}(c)$ and $T_d(c)$ based on results from the thermal dependence of the energy, $\langle E(T) \rangle$. $T_{tr}(c)$ were derived as a point where the tangent of $\langle E(T) \rangle$ is the steepest.

in the concentration. As the temperature continues to go down, the energy $\langle E \rangle$ decreases in a manner similar to that seen in the system with $\varepsilon = 0.9$, until it reaches another discontinuity temperature, $T_d(c)$. The second deviation, however, is much weaker than the first and the temperature at which it occurs, $T_d(c)$, changes only slightly with the concentration of the system. In Table 5.4 we present the values of both temperatures, $T_{tr}(c)$ and $T_d(c)$ for the set of concentrations. We omit the graph of the correlation function $g_2(r)$ for the current system, as it adds little to the data presented earlier for the system with $\varepsilon = 0.90$ (Fig.5.2).

The dependence of the order parameter on temperature ($\langle P_2(T) \rangle$) for the binary mixture with coupling constant $\varepsilon = 0.60$ is shown in Fig.5.11. From the Figure we see that the system undergoes the isotropic-nematic transition at a temperature $T_{tr}(c)$, which varies with the concentration of the system. The temperature of the transition decreases as the concentration c decreases (Fig.5.11). The value of $T_{tr}(c = 1.0)$ is, of course, the same - 1.18 - as in the previous system, and when the concentration $c \rightarrow 0.0$, the transition temperature of the mixture approaches the transition temperature of the pure system where all the particles are of type B ($T_{IN}^B = \varepsilon^2 T_{IN}^A = 0.36 \cdot 1.18$). Table 5.5 shows the value of $T_{tr}(c)$ for the full set of concentrations. These values are in good agreement with the values of $T_{tr}(c)$ obtained from the energy measurements.

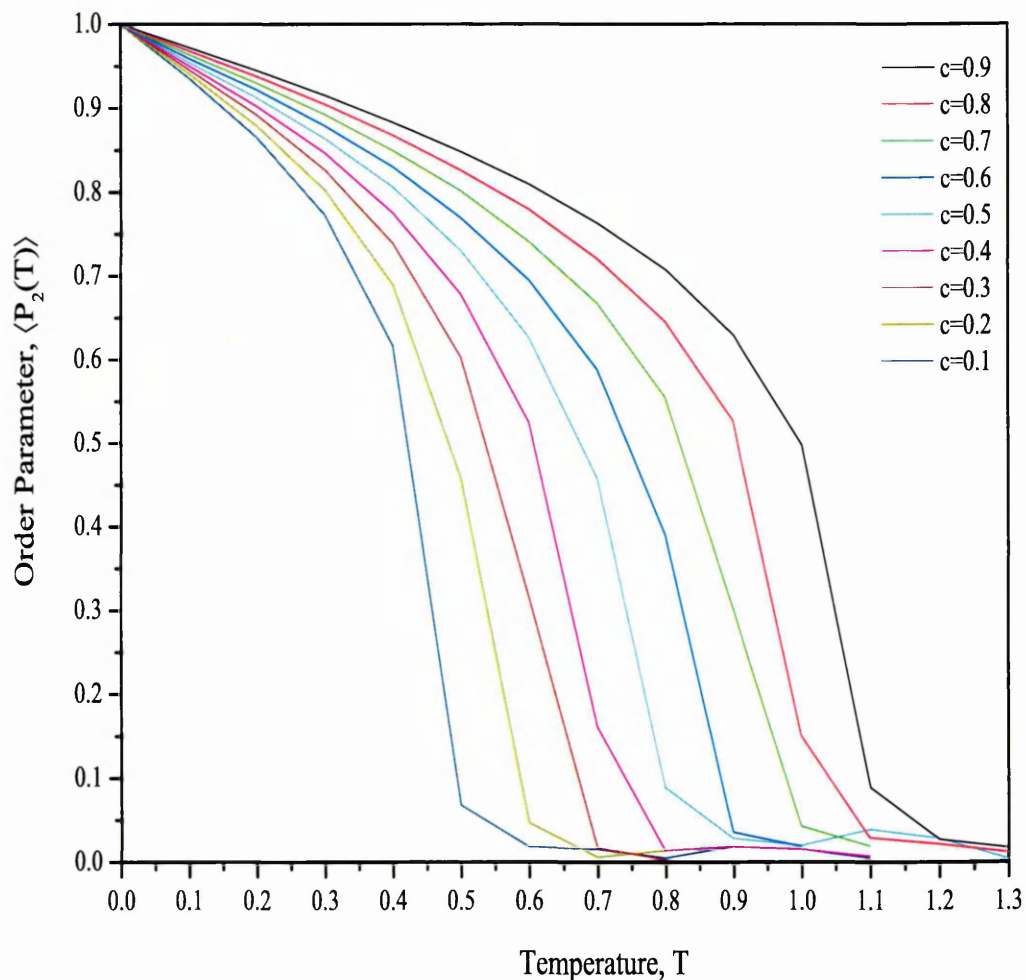


Figure 5.11: The second rank orientational order parameter, $\langle P_2(T) \rangle$. Different set of curves represent different concentrations c . System with $\varepsilon = 0.60$.

The dependence of $\langle P_2(T) \rangle$ taken separately for the two components of the mixture reveals a slight difference in the shape of the two order parameter functions $\langle P_2(T) \rangle^A$ and $\langle P_2(T) \rangle^B$, as was the case in the system with $\varepsilon = 0.90$; and indeed, all the features of the order parameter for A and B components are similar to those in the previous system.

The isotropic-nematic transition occurs at the same temperature for both species, but the shape of $\langle P_2(T) \rangle$ for the two components varies. The order parameter for particles A is always higher than that for particles B at any given temperature in the

nematic phase. This difference in order parameters for particles A and B is greater, however, than that found for particles A and B for the system with $\varepsilon = 0.90$.

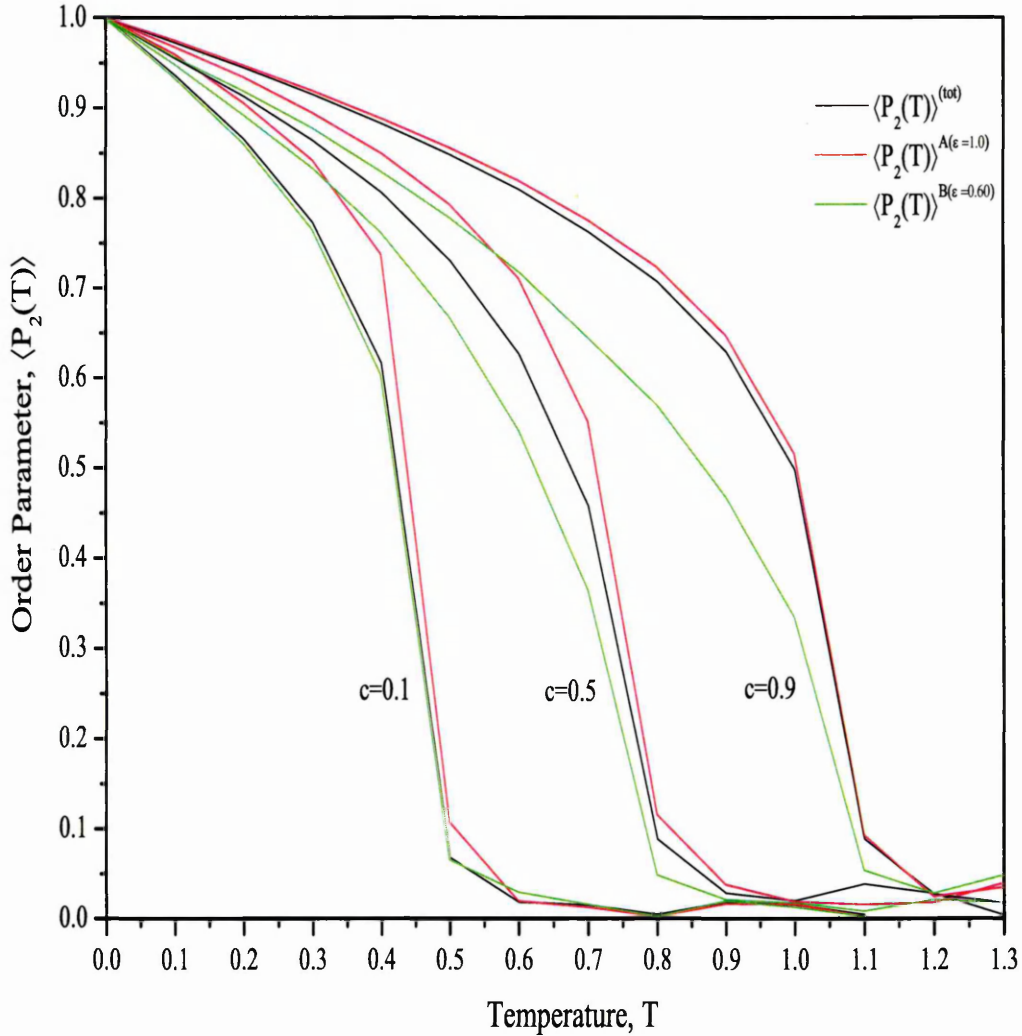


Figure 5.12: The second rank orientational order parameter shown individually for components A and B. Dependence on the temperature. Different curves represent different concentrations c . System with $\varepsilon = 0.60$.

The next observable is the radial distribution function. In Figures 5.13, 5.14 we present the dependence of the short range radial distribution function on temperature $g^{AB}(r = 1, T)$ for the set of concentrations.

Starting from $T \approx 1.3$, the value of $g^{AB}(r = 1)$ slowly and monotonically decreases as the temperature falls. This is true for all concentrations. At a temperature

concentration c	Temperature $T_{tr}(c)$
0.0	0.42 ± 0.05
0.1	0.50 ± 0.05
0.2	0.59 ± 0.05
0.3	0.69 ± 0.05
0.4	0.75 ± 0.05
0.5	0.82 ± 0.05
0.6	0.90 ± 0.05
0.7	0.98 ± 0.05
0.8	1.05 ± 0.05
0.9	1.12 ± 0.05
1.0	1.18 ± 0.05

Table 5.5: Table of Temperatures $T_{tr}(c)$ based on results obtained from $\langle P_2 \rangle$.

$T_{tr}(c)$, the $g^{AB}(r = 1, T)$ curve decreases rapidly by a relatively small value, and this is followed by another slow decline. As in the previous system ($\varepsilon = 0.90$), the value of $T_{tr}(c)$ varies with concentration. From the Figure we see that the function's discontinuity behaviour at $T_{tr}(c)$ is stronger here than it was in the system with $\varepsilon = 0.90$. The slope of the curve after the temperature of discontinuity, $T < T_{tr}(c)$, appears steeper than it was for $\varepsilon = 0.90$.

As the temperature falls still further, the curve continues to decline monotonically after $T_{tr}(c)$, until it reaches another discontinuity in the gradient at a temperature $T_d(c)$. This time the curve decreases sharply to a significantly lower value. The temperature $T_d(c)$ is slightly different for each concentration. $T_d(c)$ is highest at concentrations around $0.4 > c > 0.6$. These temperatures follow the same pattern as in the system with $\varepsilon = 0.90$; however, the system with $\varepsilon = 0.60$ exhibits more dramatic behaviour, in that $T_d(c)$ varies more markedly with the concentration. The values of $T_{tr}(c)$ and $T_d(c)$ for the system with $\varepsilon = 0.60$ for the set of concentrations are presented in Table 5.6. These values are in good agreement with those presented in Table 5.5. They are slightly overestimated in the region of low concentrations and underestimated in the region of high concentrations. Both tables present values higher than that from Table 5.4. The ratio of the values of the decreases in $g^{AB}(r = 1, T)$ which happen at $T_{tr}(c)$ and $T_d(c)$ equals 0.11, for the system with $\varepsilon = 0.60$. This is an order of magnitude higher than that of $\varepsilon = 0.90$.

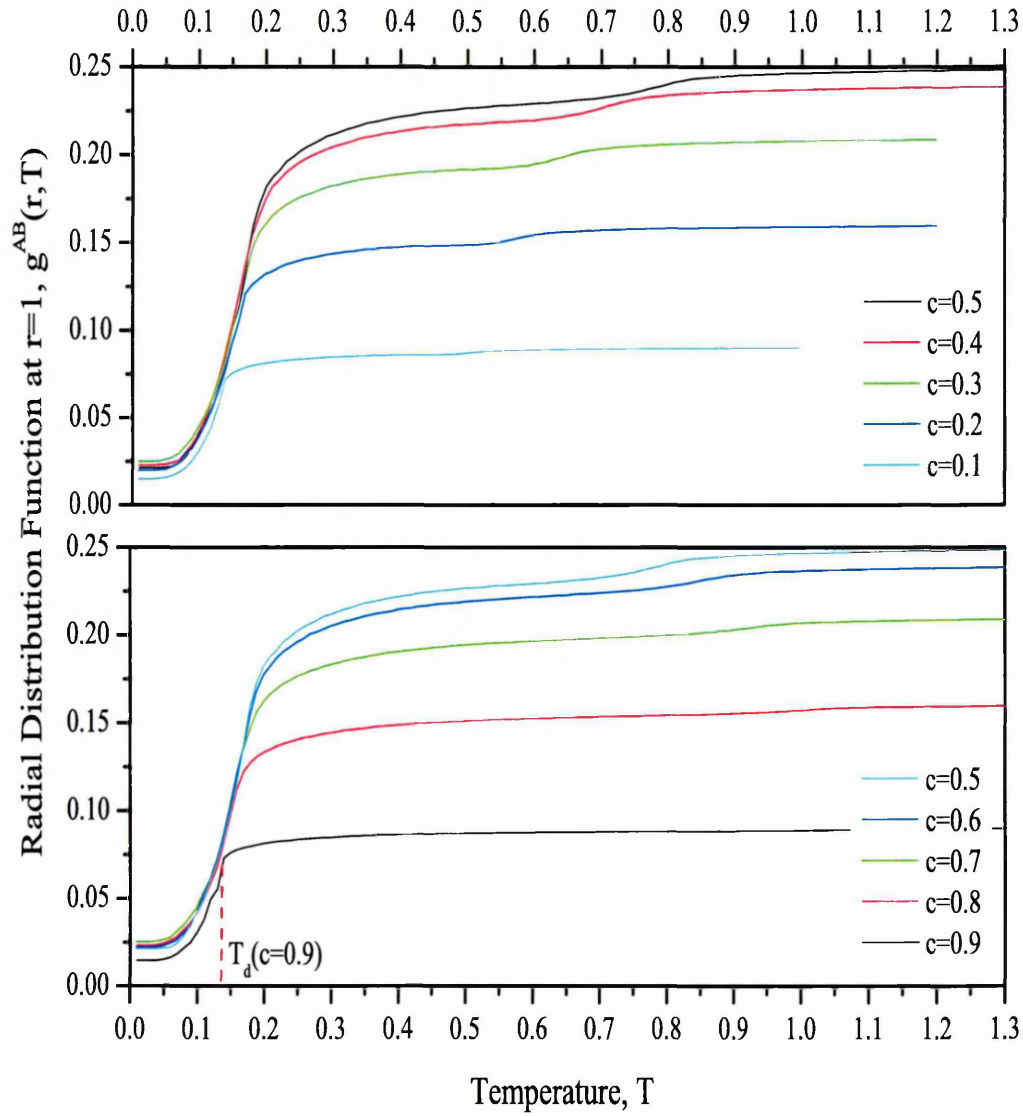


Figure 5.13: The short range radial distribution function dependence on the temperature, $g^{AB}(r = 1)$. Different curves represent different c . System with $\varepsilon = 0.60$.

From the data presented in this section, we have constructed a phase diagram for the system with coupling constant $\varepsilon = 0.6$; this is presented in Figure 5.15. As previously explained, the phase diagram is based on a two-dimensional set of points of different colours. Each colour represents a different phase or structure of the system, the exception being green, which represents phase points at which we were not able unambiguously to determine the phase of the system.

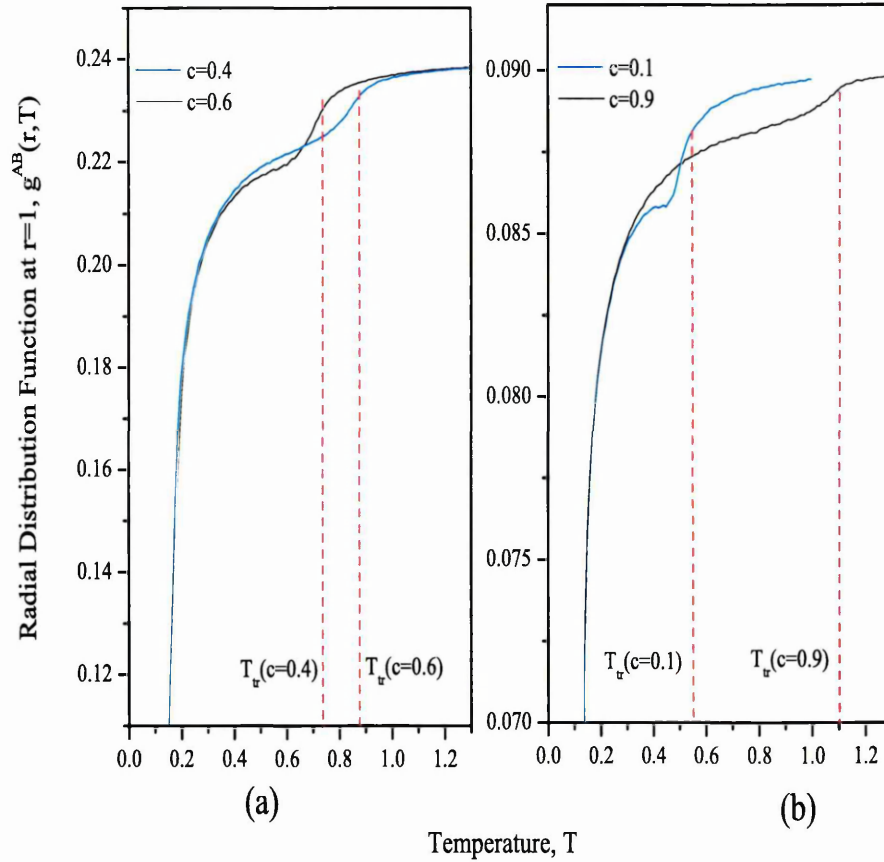


Figure 5.14: Magnified graph of the radial distribution function $g^{AB}(r = 1)$ presented in Fig. 5.13. Different curves represent different concentrations c .

concentration c	Temperature $T_{tr}(c)$	Temperature $T_d(c)$
0.0	N/A	N/A
0.1	0.55 ± 0.02	0.15 ± 0.02
0.2	0.62 ± 0.02	0.19 ± 0.02
0.3	0.67 ± 0.02	0.24 ± 0.02
0.4	0.74 ± 0.02	0.25 ± 0.02
0.5	0.79 ± 0.02	0.25 ± 0.02
0.6	0.88 ± 0.02	0.25 ± 0.02
0.7	0.95 ± 0.02	0.22 ± 0.02
0.8	1.05 ± 0.02	0.19 ± 0.02
0.9	1.10 ± 0.02	0.14 ± 0.02
1.0	N/A	N/A

Table 5.6: Table of temperatures $T_{tr}(c)$ and $T_d(c)$ based on the results obtained from $g^{AB}(r = 1, T)$, $\varepsilon = 0.60$.

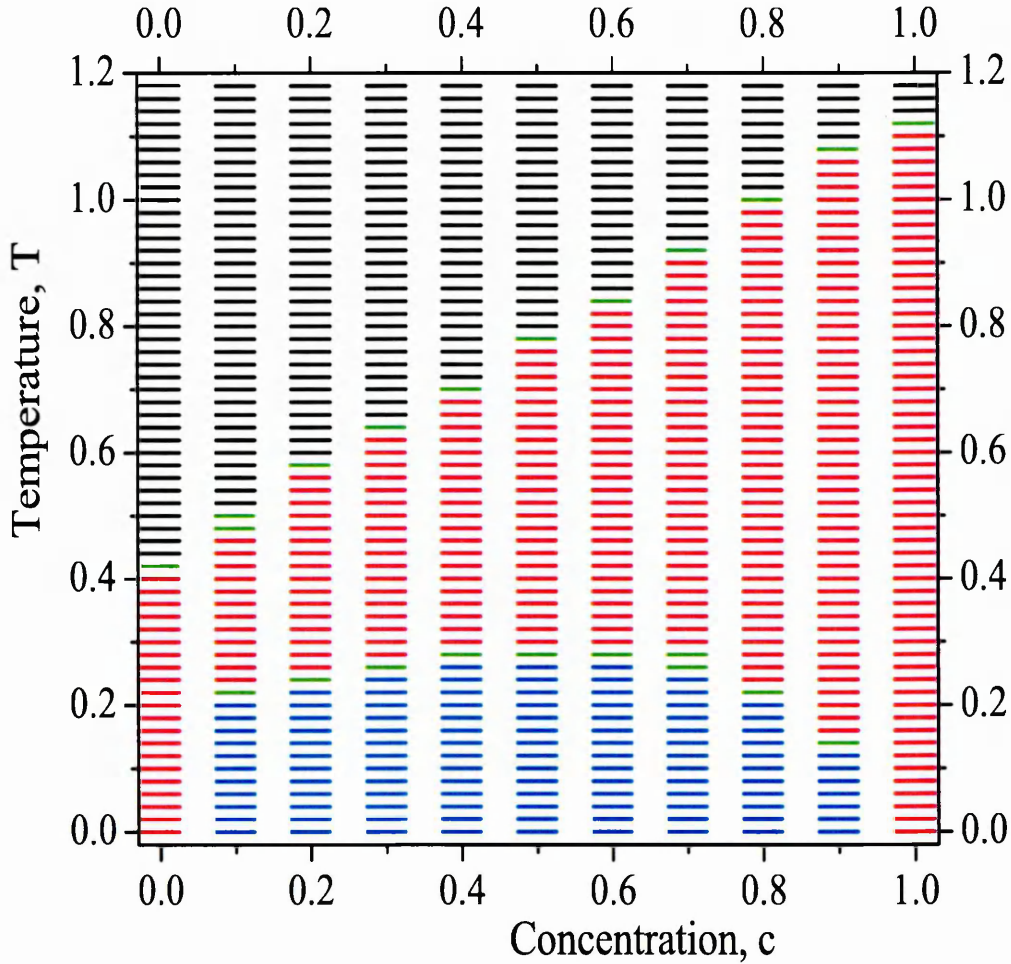


Figure 5.15: The phase diagram for the system with $\varepsilon = 0.6$.

As in the case of the previous system ($\varepsilon = 0.9$), the diagram comprises three areas. The top area, shown in black, represents the isotropic phase. In the region of low concentration this area has extended into the lower temperature region, as compared to the system with $\varepsilon = 0.9$. However, the nematic mixed phase (red) still occupies most of the area of the diagram (Fig. 5.15).

The boundary between the isotropic and the nematic phases (henceforth $T_{IN}(c)$ curve) is very narrow and cannot be resolved using the measured observables. At both ends of the concentration axis the system orders at the I-N transition temperatures of its pure components. As the concentration changes from one extreme to

the other, the $T_{IN}(c)$ curve changes linearly, to a reasonable approximation.

The region at the bottom of the phase diagram, shown in blue, is the area of nematic-nematic phase coexistence. It is highest at concentrations around $c \approx 0.5 \pm 0.1$ and narrows down to vanishing on both sides of the concentration axis. The entire coexistence envelope appears to be asymmetric. It reaches higher values of T in the region of concentrations $0.0 < c < 0.5$, on the left of the diagram (Fig. 5.15).

The behaviour of the system with $\varepsilon = 0.60$ is consistent with that of the system with $\varepsilon = 0.90$. There is a difference, however, in the slope of the $T_{IN}(c)$ curve and in the size of the demixing envelope of N-N coexistence. The asymmetry of the demixing envelope was not seen in the system with $\varepsilon = 0.90$, perhaps due to the much smaller area of N-N phase coexistence. Further discussion of these results will follow in Section 5.4.

5.1.3 System with $\varepsilon = 0.45$

The next system has a coupling constant $\varepsilon = 0.45$ and exhibits phenomena not seen in previous systems. Thus, as this section progresses, we will introduce new parameters and focus on slightly different aspects of the observables introduced previously.

The first observable to be considered in this system is the average energy and its variation with the temperature. In Figure 5.16 we present these data, the various curves in the Figure representing different concentrations c .

Let us start with the highest concentration on the graph, $c = 0.9$, which is represented by the bottom curve (Fig. 5.16). At the highest temperature, the energy $\langle E(T) \rangle$ has a low negative value, which decreases slowly as the temperature falls, until at $T \approx T_{tr}(c)$ it decreases quite rapidly. The energy value then continues to decrease with temperature until it exhibits a second discontinuity at a temperature $T_d(c)$. After this, $\langle E(T) \rangle$ decreases steadily as $T \rightarrow 0$. This pattern is the same as that seen in the previous two cases of $\varepsilon = 0.6$ and $\varepsilon = 0.6$.

When the concentration is decreased to 0.8, however, $\langle E(T) \rangle$ shows three weak but distinct discontinuities which we denote $T_{tr}(c)$, $T_d(c)$ and $T'_{tr}(c)$. Note that $T'_{tr}(c)$

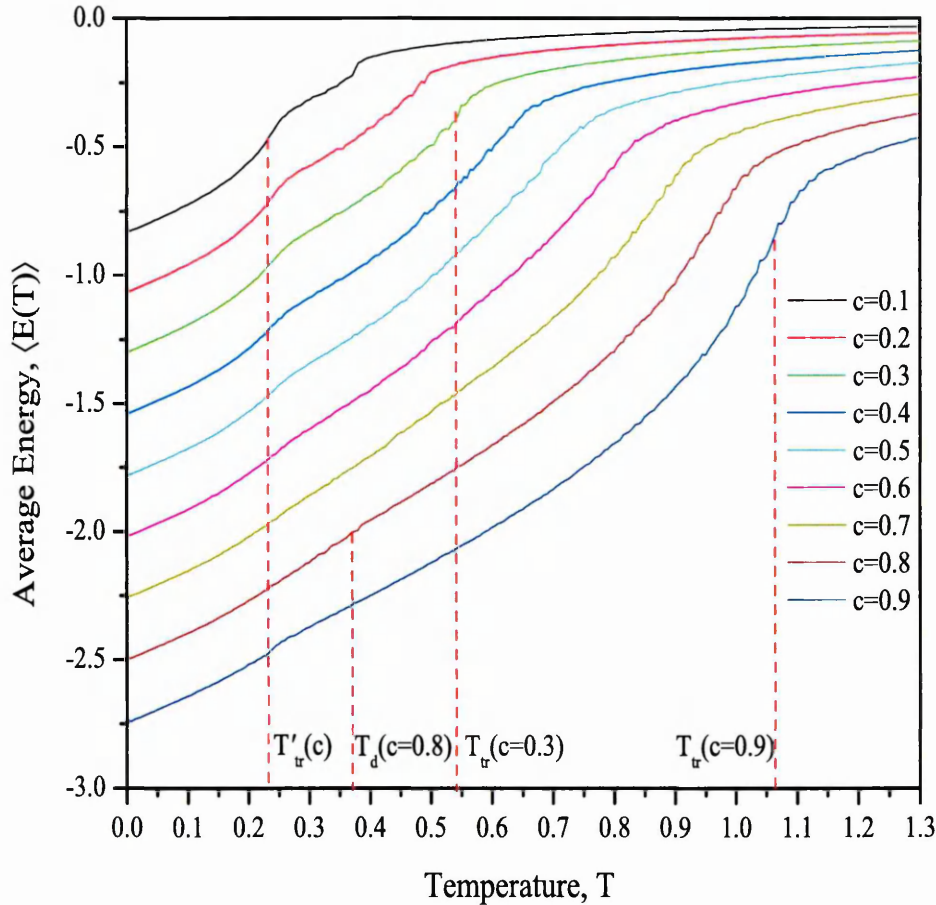


Figure 5.16: The dependence of the average energy on the temperature, $\langle E(T) \rangle$. Different curves represent $\langle E(T) \rangle$ for different concentrations c .

always appears below $T_d(c)$ in Figure 5.16 (see the phase diagram for this system in Figure 5.27). In Figure 5.16, the value of $T'_{tr}(c)$ appears to be around 0.23 and is visible clearly only in differentiated $\langle E(T) \rangle$ (Figure 5.18).

Although two of these three deviations on this curve are weak, such observations were not present at all in the first two systems. Neither is it present at any other concentrations for this system, except for a faint indication in the next two concentrations, $c = 0.7$ and $c = 0.6$. These were revealed by the derivatives of $\langle E(T) \rangle$, but are not seen on original $\langle E(T) \rangle$ curves. The energy dependence for other concentrations ($c < 0.6$) exhibits only two discontinuities in the gradient of $\langle E(T) \rangle$ - $T_{tr}(c)$ (which, as we shall show, coincides with $T_d(c)$) and $T'_{tr}(c)$.

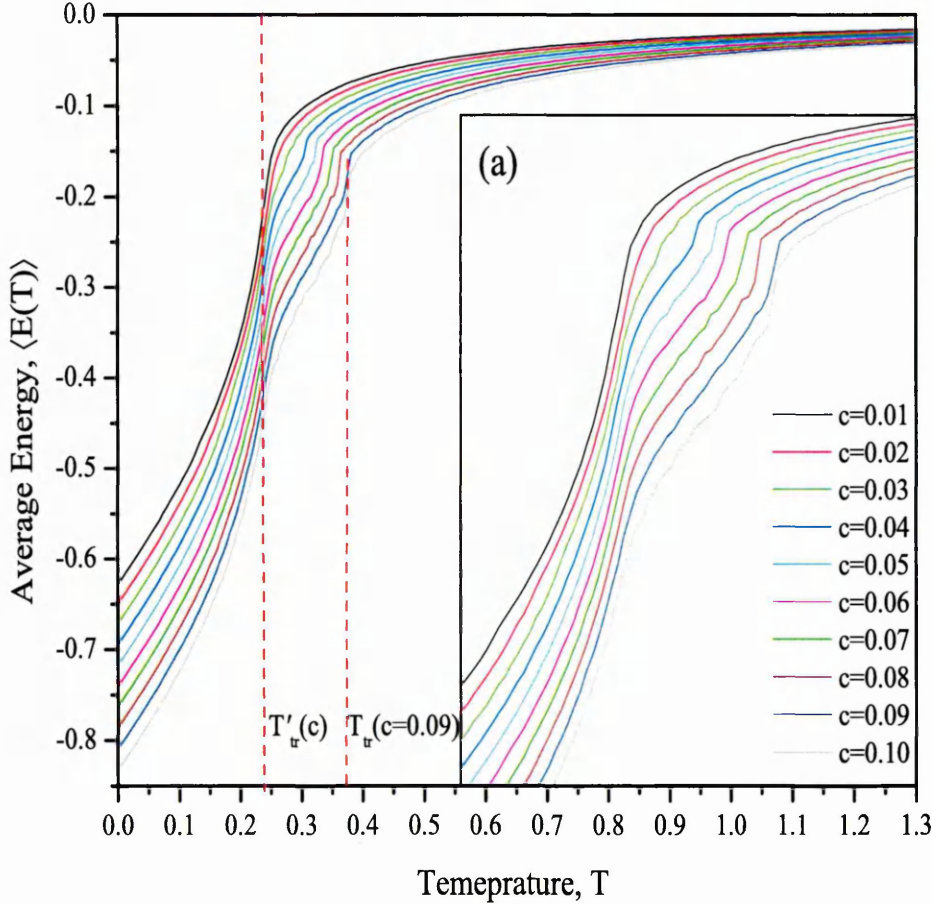


Figure 5.17: The dependence of the average energy on the temperature, $\langle E(T) \rangle$. Different curves represent $\langle E(T) \rangle$ for different concentrations $0 < c < 0.1$.

The highest discontinuity temperature $T_{tr}(c)$, decreases with a reduction in concentration c . $T_{tr}(c)$ is unique for each concentration of the system and takes values which are different from those of the two previous systems for the same concentration. The temperature of the last discontinuity $T'_{tr}(c)$ seems not to depend at all on concentration, although the shape of both deviations $T_{tr}(c)$ and $T'_{tr}(c)$ becomes sharper as the concentration of the system decreases.

Reduction of the concentration causes $T_{tr}(c)$ to move closer to $T'_{tr}(c)$. However, these temperatures do not meet at $c = 0.1$. Thus, in Figure 5.17 we present results for the energy dependence $\langle E(T) \rangle$, but at concentrations $c < 0.1$. From this Figure one can see that the sharp decrease of $\langle E(T) \rangle$ to a very low value still occurs at the same temperature $T'_{tr}(c)$. The discontinuity which occurred at $T_{tr}(c)$ in Figure 5.16 follows

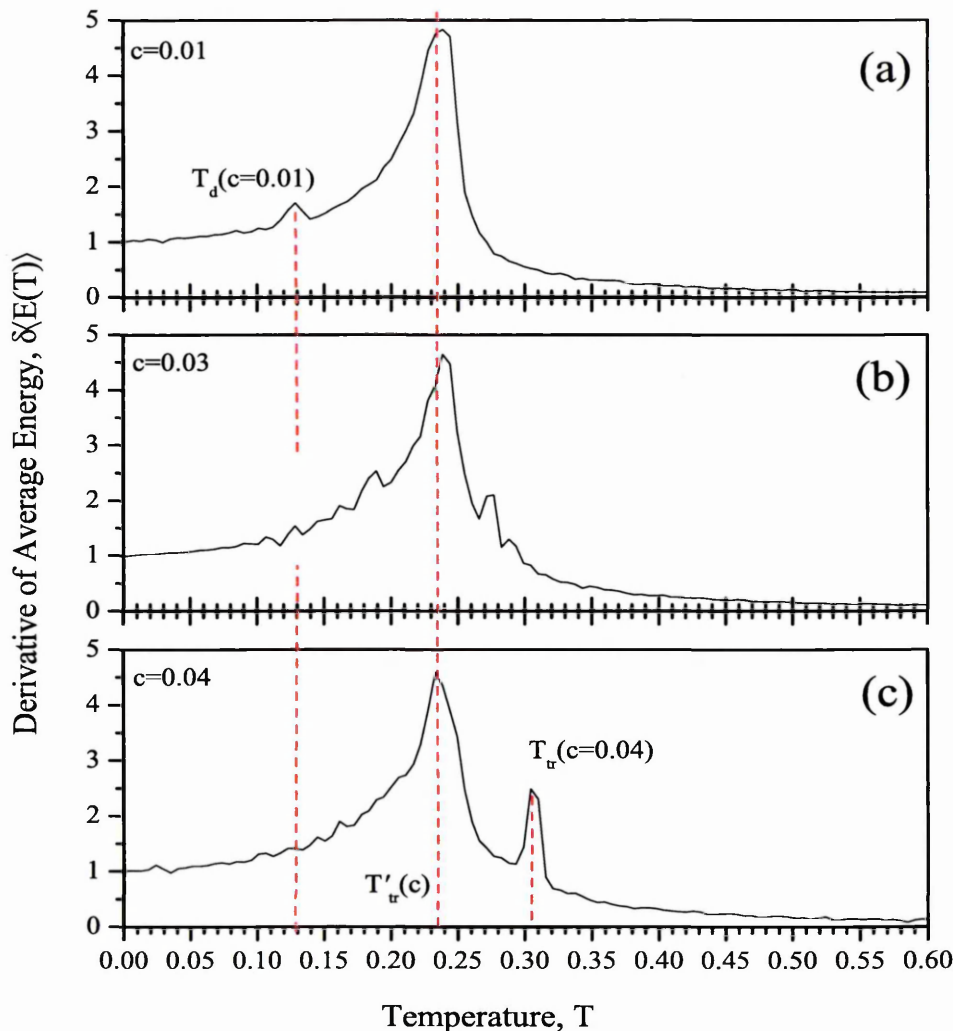


Figure 5.18: The numerical differential of average energy on the temperature, $\langle E(T) \rangle$. Different curves represent $\langle E(T) \rangle$ for different concentrations $0 < c < 0.1$.

the same pattern. The decrease in $T_{tr}(c)$ is virtually linear as the concentration of the system decreases from $c = 0.1$ to $c = 0.04$. At $c = 0.03$ discontinuities $T_{tr}(c)$ and $T'_{tr}(c)$ merge and seem to stay that way as concentration decreases further till $c \rightarrow 0.0$. In other words, the difference between $T_{tr}(c)$ and $T'_{tr}(c)$ disappears and the single transition temperature represents the boundary between mixed isotropic and mixed nematic phases, similar to $T_{tr}(c)$ for high concentrations (Figure 5.27). Figure 5.17(a), magnified and placed with no scale, gives more detailed picture of the behaviour of the $\langle E(T) \rangle$ curve in the region of temperatures $T_{tr}(c)$ and $T'_{tr}(c)$. The derivatives of $\langle E(T) \rangle$ curves from the numerical differentiation for concentrations $c < 0.1$ reveal that $T_{tr}(c)$ continues to decrease after $c = 0.03$ as concentration decreases, while $T'_{tr}(c)$ remains unchanged (Figure 5.18). At concentrations above

concentration c	Temperature $T_{tr}(c)$	Temperature $T_d(c)$	Temperature $T'_{tr}(c)$
0.0	0.23 ± 0.01	N/A	N/A
0.01	0.23 ± 0.01	0.13 ± 0.01	0.23 ± 0.01
0.02	0.23 ± 0.01	0.16 ± 0.01	0.23 ± 0.01
0.03	0.23 ± 0.04	0.3 ± 0.04	0.23 ± 0.01
0.04	0.30 ± 0.01	0.30 ± 0.01	0.23 ± 0.01
0.05	0.32 ± 0.01	0.32 ± 0.01	0.23 ± 0.01
0.06	0.33 ± 0.01	0.33 ± 0.01	0.23 ± 0.01
0.07	0.35 ± 0.01	0.35 ± 0.01	0.23 ± 0.01
0.08	0.36 ± 0.01	0.36 ± 0.01	0.23 ± 0.01
0.09	0.37 ± 0.01	0.37 ± 0.01	0.23 ± 0.01
0.1	0.38 ± 0.01	0.38 ± 0.01	0.23 ± 0.01
0.2	0.49 ± 0.01	0.49 ± 0.01	0.23 ± 0.01
0.3	0.54 ± 0.01	0.54 ± 0.01	0.23 ± 0.01
0.4	0.65 ± 0.01	0.65 ± 0.01	0.23 ± 0.01
0.5	0.68 ± 0.01	0.55 ± 0.01	0.23 ± 0.01
0.6	0.80 ± 0.01	0.49 ± 0.01	0.23 ± 0.01
0.7	0.88 ± 0.01	0.43 ± 0.01	0.23 ± 0.01
0.8	0.96 ± 0.01	0.38 ± 0.01	0.23 ± 0.01
0.9	1.07 ± 0.01	0.24 ± 0.01	0.23 ± 0.01
1.0	1.15 ± 0.01	N/A	N/A

Table 5.7: Table of temperatures $T_{tr}(c)$, $T_d(c)$ and $T'_{tr}(c)$ obtained from the results of $\langle E(T) \rangle$. $T_{tr}(c)$ were derived as a point where the tangent of $\langle E(T) \rangle$ is the steepest.

$c = 0.03$, $T_{tr}(c)$ is clearly higher than $T'_{tr}(c)$ (Figure 5.18.(c)). At the concentration $c = 0.03$, the value of $T_{tr}(c)$ is approximately equal to the value of $T'_{tr}(c)$ and the derivative of $\langle E(T, c = 0.03) \rangle$ does not show two resolvable peaks corresponding to these two discontinuity temperatures (Figure 5.18.(b)). As the concentration passes $c = 0.03$ approaching zero, the discontinuity temperature that we previously denoted $T_{tr}(c)$ decreases to a value lower than that of $T'_{tr}(c)$ (Figure 5.18.(a)). Note, that for reasons that will be clear later, we mark this discontinuity as $T_d(c)$ in the region of concentrations $0 < c < 0.03$. At this stage let us just assert that for concentrations $0.03 \lesssim c \lesssim 0.6$, $T_{tr}(c) \approx T_d(c)$ but for lower concentrations $T_d(c)$ continues to decrease while $T_{tr}(c) \approx T'_{tr}(c)$.

Let us look now at the thermal dependence of the second rank orientational order parameter $\langle P_2(T) \rangle$, obtained from $g_2(r \gg 3)$ for the system with $\varepsilon = 0.45$. As

previously noted the value of the function projected on the ordinate, $\langle P_2 \rangle$, relates to the long range pair correlation function as a square root of $g_2(r \gg 3)$ (Eq.1.11). At the highest temperature, the order parameter is close to zero; then, at $T_{tr}(c)$, it increases rapidly. Then, unlike $\langle P_2(T) \rangle$ of the systems with $\varepsilon = 0.90$ and

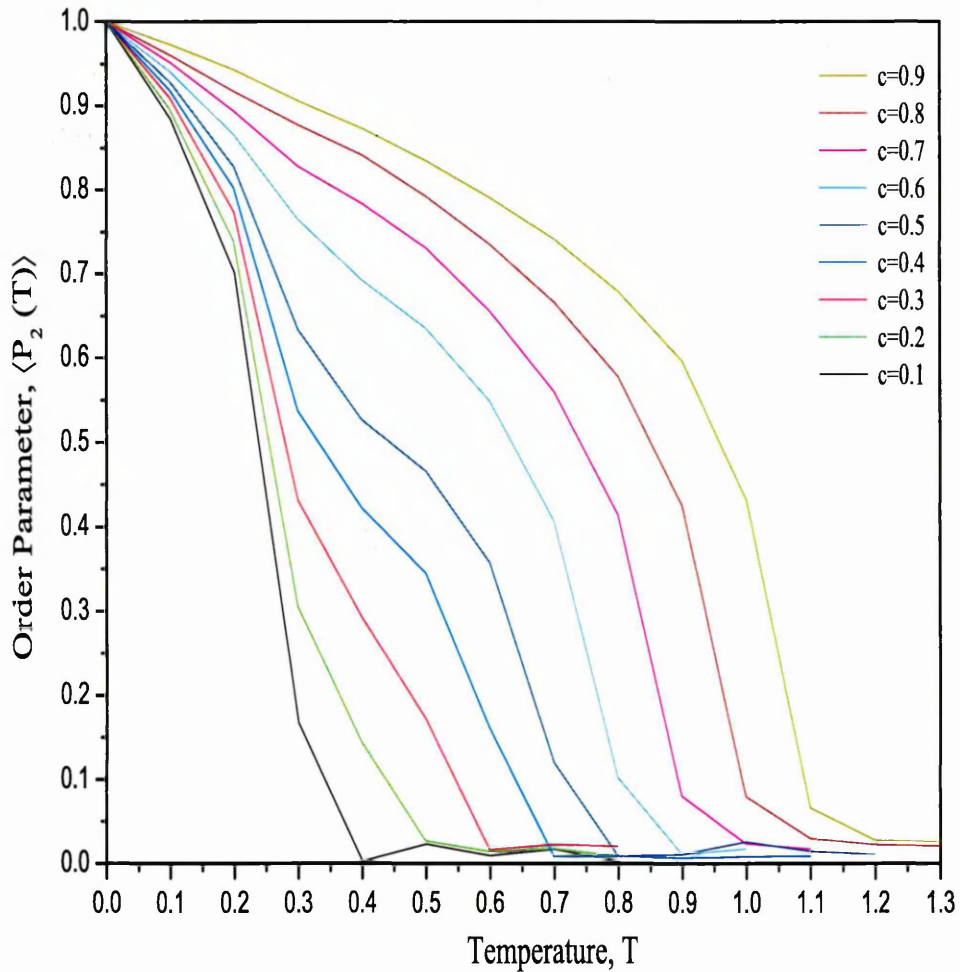


Figure 5.19: The dependence of the second rank orientational order parameter on the temperature, $\langle P_2(T) \rangle$. Different curves represent different concentrations c in the binary system with $\varepsilon=0.45$.

$\varepsilon = 0.60$, its gradient does not decrease monotonically as the temperature decreases, approaching the value of 0. Instead, $\langle P_2(T) \rangle$ approaches a value of ≈ 0.6 as the temperature decreases until, at $T'_{tr}(c)$, it rapidly increases again, approaching $\langle P_2(T) \rangle \rightarrow 1$. This effect is seen at most concentrations, however it is strongest at concentrations around 0.5. The value of $T'_{tr}(c)$ does not seem to vary significantly

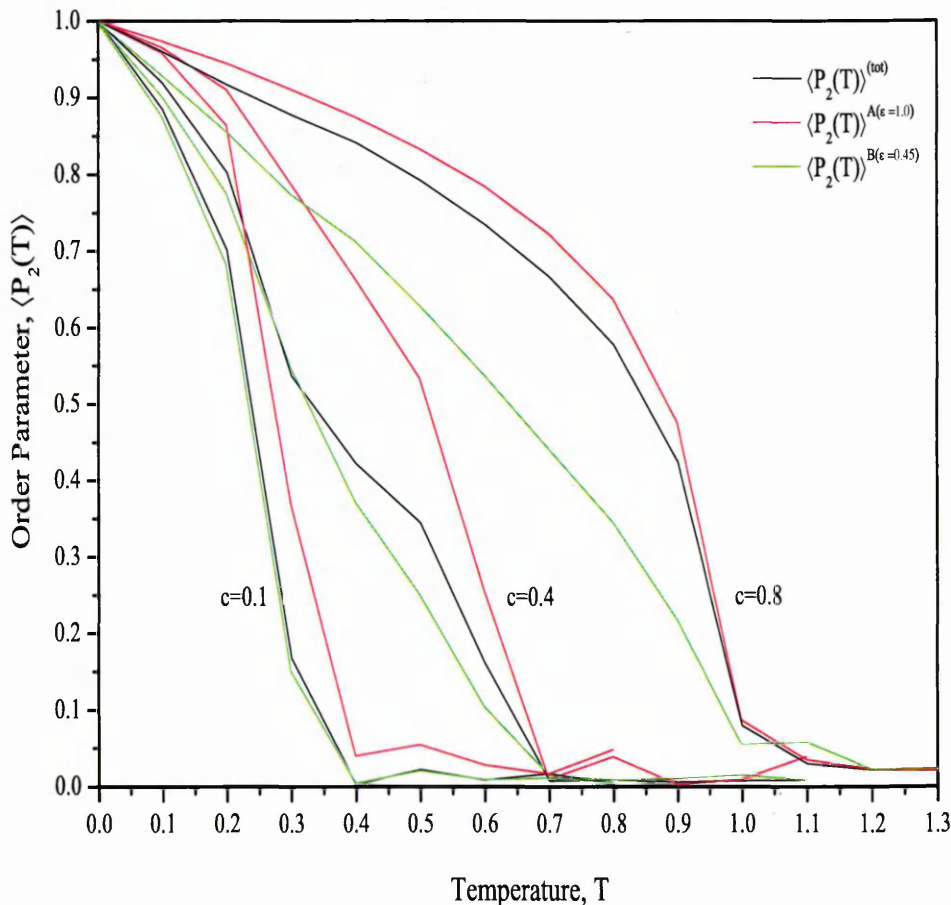


Figure 5.20: The dependence of the second rank orientational order parameter on the temperature, $\langle P_2(T) \rangle$, individually for particles A and B. $\epsilon=0.45$.

with concentration and equals 0.2...0.3. Table 5.8 shows the values for $T_{tr}(c)$ obtained from the order parameter data for the full concentration range. These values of $T_{tr}(c)$ in Table 5.8 agree with those obtained from the energy calculations, presented earlier in this section (Table 5.7).

The shape of $\langle P_2(T) \rangle$ differs significantly from the shape of the order parameter of the systems with $\epsilon = 0.90$ and $\epsilon = 0.60$. This deviation of $\langle P_2(T) \rangle$ from the conventional behaviour is strongest when the two components of the system are in more or less equal proportions.

Let us, therefore, examine individually the order parameters of the components A ($\langle P_2 \rangle^A$) and B ($\langle P_2 \rangle^B$) (Fig.5.20). Though the transition temperature is the same in

concentration c	Temperature $T_{tr}(c)$
0.0	0.24 ± 0.05
0.1	0.35 ± 0.05
0.2	0.48 ± 0.05
0.3	0.55 ± 0.05
0.4	0.68 ± 0.05
0.5	0.72 ± 0.05
0.6	0.83 ± 0.05
0.7	0.92 ± 0.05
0.8	1.01 ± 0.05
0.9	1.12 ± 0.05
1.0	1.18 ± 0.05

Table 5.8: Table of Temperatures $T_{tr}(c)$ based on results obtained from $\langle P_2 \rangle$, $\varepsilon=0.45$.

each case, the shapes of the $\langle P_2(T) \rangle$ curves differ significantly. The increase in the value of $\langle P_2 \rangle^B$ with reduction in temperature is not as rapid as that of $\langle P_2 \rangle^A$. For the temperature $T \approx 0.5$, the difference in $\langle P_2(T) \rangle$ between the two components reaches more than 0.3 for concentration $c = 0.5$. This is the greatest difference observed so far in the three systems investigated. The order parameter of both components reaches 1, as the temperature approaches zero. Figure 5.20 shows that the total value of the order parameter is not simply a superposition of the order parameters of the two components. We will discuss this further in Section 5.4.

The next observable is the radial distribution function ($g^{AB}(r)$). In Figure 5.5 we presented typical behaviour of the radial distribution function ($g^{AB}(r)$) for the unlike particles for the system with $\varepsilon = 0.9$.

As was the case for the results for the system with $\varepsilon = 0.9$, the value of $g^{AB}(r)$ for $\varepsilon = 0.45$ varies with distance r . However, for this lower ε value, changes in $g^{AB}(r)$ extend to greater distances r , as the temperature is decreased. Eventually, when the temperature is low enough, both the short and long range values of the radial distribution function start to decrease (Fig. 5.21).

In Figure 5.22 we present the dependencies of the function on temperature at short ($r^2 = 1$) and long ($r^2 = 64$) ranges for the system with $\varepsilon = 0.45$ and $c = 0.5$. From the Figure we see a feature which is common to both graphs, namely values of $g^{AB}(r)$ at both ranges sharply change their gradient at similar temperature $T_d(c = 0.5) \approx 0.67$ (See Fig. 5.22 and Table 5.9). The short range value of the radial

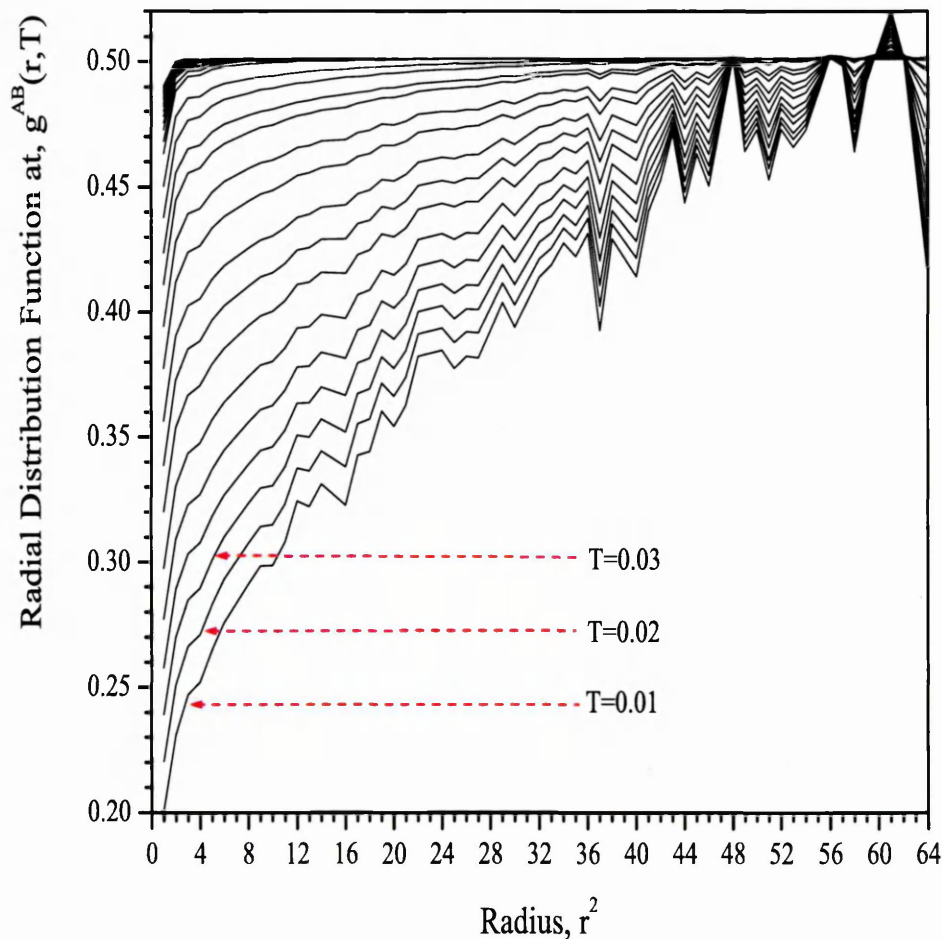


Figure 5.21: Radial Distribution Function $g^{AB}(r)$ for $\varepsilon = 0.45$ and $c = 0.5$. Different curves represent $g^{AB}(r)$ taken at different temperatures.

distribution function experiences a marked decrease while the long range function decreases slightly. Overall, the temperature, at which the value of the function at short range drops by approximately 10% correlates with the temperature at which the long-range function starts to decrease.

Thus, the changes that occur at long range $g^{AB}(r)$ can also be inferred from those that happen at sort range. This is also true for all other systems presented in this chapter. For the rest of this section, therefore, we will present results only from the short range part of the function and omit graphs similar to those shown in Figures 5.21 and 5.22.

In Figure 5.23 we present $g^{AB}(r = 1, T)$ for the set of concentrations. At concentration $c = 0.9$, variations in $g^{AB}(r = 1, T)$ in response to temperature change are negligible at high temperatures. The function seems to have very steady slope throughout a wide region of temperatures until $T_d(c) \approx 0.25$ is reached, when it decreases sharply. Magnification of the graph in the region of high temperatures, however, reveals the presence of a small deviation at $T_{tr}(c) \approx 1.08$ (Figure 5.24(a)). This kind of discontinuity, hardly seen in Figure 5.23($c = 0.9$), is more clearly

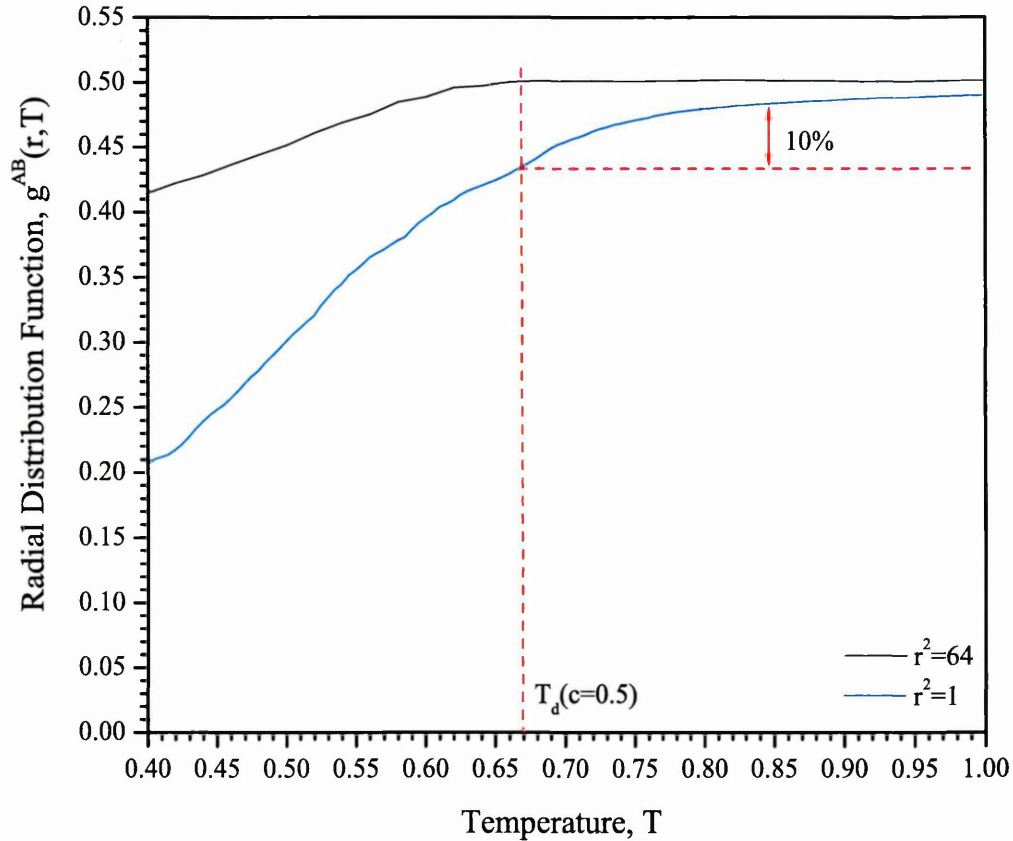


Figure 5.22: Dependence of the radial distribution function $g^{AB}(r)$ on temperature, T , for the system with $\varepsilon = 0.45$ and $c = 0.5$. Different curves represent long and short range. The temperature of 10% decrease of $g^{AB}(r = 1)$ correlates to the temperature, at which the long range $g^{AB}(r)$ starts to decrease.

present for lower concentrations (compare $c = 0.8$ and $c = 0.7$ in Figures 5.23 and 5.24(b),(c)). As we move down in concentration these deviations start to emerge. At $c = 0.8$ the value of $g^{AB}(r = 1, T)$ seems initially to remain unchanged as the temperature decreases, until it reaches $T_{tr}(c) \approx 1.0$, when it starts to decline more steeply (Figure 5.24(b)). This decline continues at fairly steady rate as the tem-

perature continues to decrease, but becomes still more pronounced at $T_d(c) \approx 0.4$ (Figure 5.23). After this, the function levels off to its minimum value as $T \rightarrow 0$, but not without a slight deviation at $T'_{tr}(c) \approx 0.24$, which is hardly seen for this concentration (Figure 5.23). Figure 5.23(a) shows an unscaled magnified picture of such temperature region. The deviation at $T'_{tr}(c)$ becomes more pronounced as concentration decreases. From the Figure 5.23 it is clear that $g^{AB}(r = 1, T)$ for

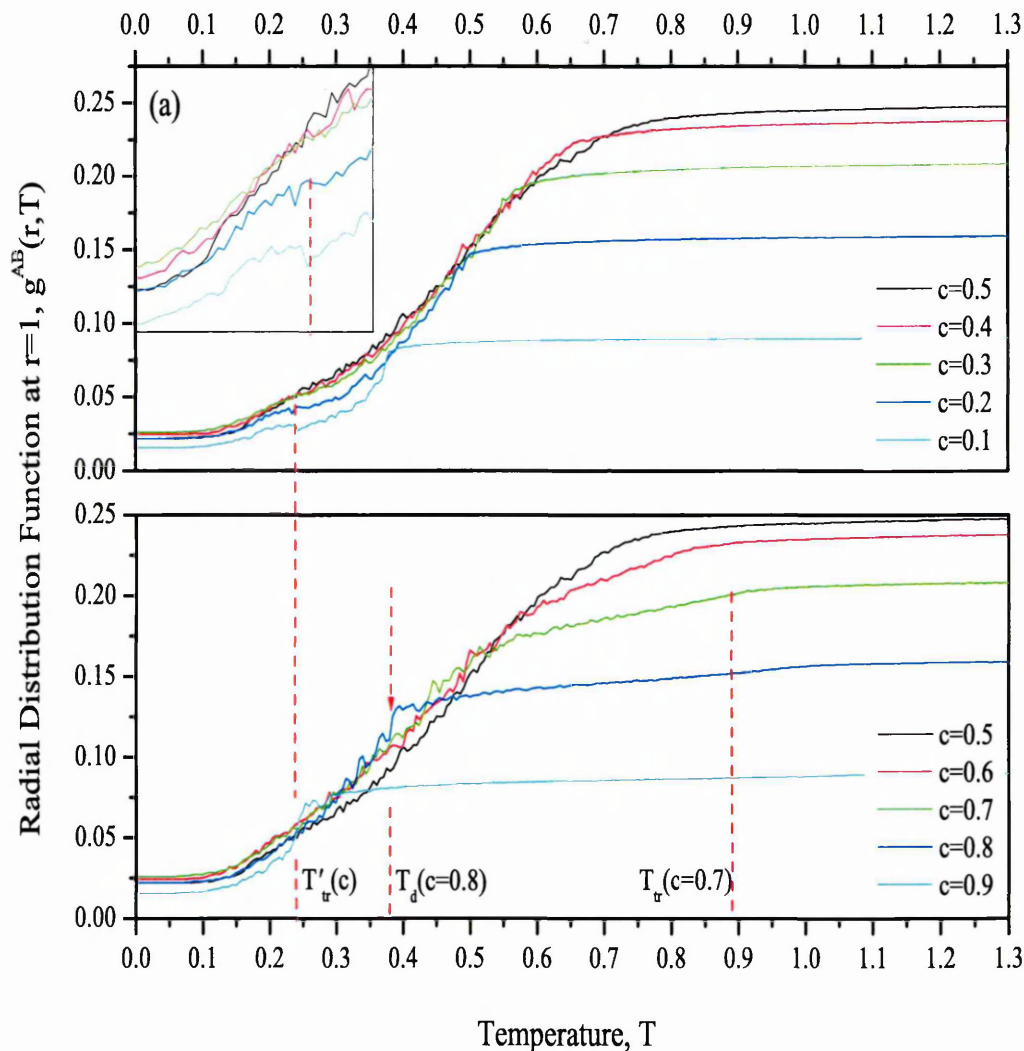


Figure 5.23: The short range radial distribution function dependence on the temperature, $g^{AB}(r = 1)$. Different curves represent different c . System with $\varepsilon = 0.45$.

other concentrations exhibits similar behaviour. As the concentration decreases, temperatures $T_{tr}(c)$ and $T_d(c)$ move closer together until, at $c \approx 0.5$, they meet. As they converge, the slope in the region between $T_{tr}(c)$ and $T_d(c)$ becomes steeper and

eventually vanishes at $c \approx 0.5$. At all concentrations lower than $c \approx 0.5$ there are only two discontinuities present on the $g^{AB}(r = 1, T)$ function: $T_{tr}(c)$ (which is the same as $T_d(c)$) and $T'_{tr}(c)$. Also, when the concentration c in the system decreases, the deviation which occurs at $T'_{tr}(c)$ becomes stronger and $T_{tr}(c)$ moves closer to $T'_{tr}(c)$.

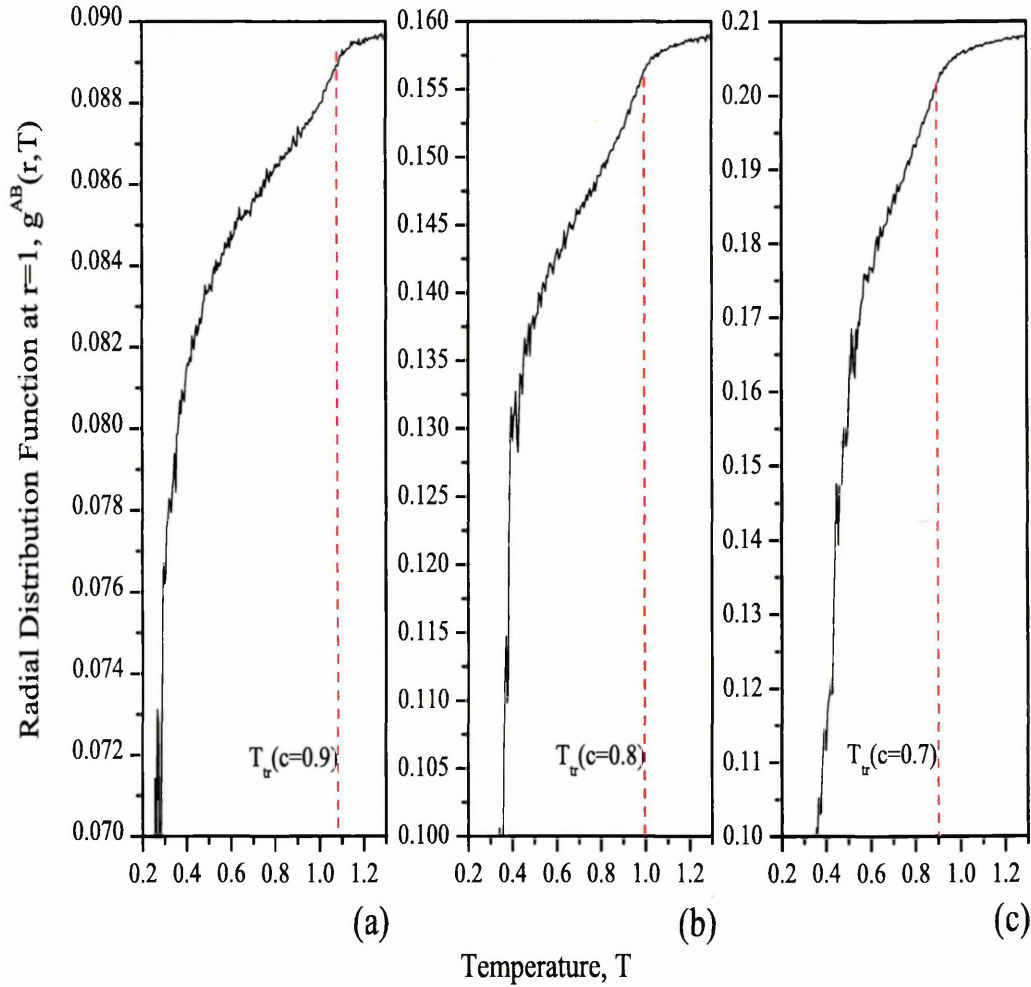


Figure 5.24: Radial Distribution Function $g^{AB}(r)$. Some of the curves from Fig. 5.23 are magnified to show $T_{tr}(c)$.

Figure 5.25 shows the behaviour of $g^{AB}(r = 1, T)$ in the range of concentrations $0.01 \leq c \leq 0.10$. Similar to the results of the thermal behaviour of the average energy, the value of $T_{tr}(0.03 < c \lesssim 0.6)$ ($\approx T_d(0.03 < c \lesssim 0.6)$) is higher than that of $T'_{tr}(c)$. However, as concentration becomes lower than 0.03, the value of $T_d(c)$ decreases to be lower than the value of $T'_{tr}(c)$, while $T_{tr}(c) \approx T'_{tr}(c)$. In Figure 5.25, the behaviour of $g^{AB}(r = 1, T)$ for concentrations higher than 0.03 is similar to

that of the rest of the concentration region, where $T_{tr}(c) \approx T_d(c)$. The behaviour of $g^{AB}(r = 1, T)$ for concentrations lower than 0.03 is similar to that of the region of high concentrations ($0.6 \lesssim c < 1.0$), where $T_{tr}(c)$ precedes $T_d(c)$ as the temperature decreases. The behaviour of $g^{AB}(r = 1, T)$ in the vicinity of $c \approx 0.03$ is unclear. As the temperature decreases, $g^{AB}(r = 1, T)$ curve at $c = 0.03$ decreases sharply at $T \approx 0.28$. Then, at $T \approx 0.24$ it increases sharply, almost regaining its original value, shortly after which it falls again at $T \approx 0.19$. Further discussion on this will follow in Section 5.4. The values of all such temperatures are noted in Table 5.9. The values from the Table are overestimated by the order of 0.1 in the region of $c = 0.5$ as compared to those in Table 5.7 but consistent with them. Discussion of the hump on $g^{AB}(r = 1, T)$ at $T'_{tr}(c)$ will follow in Section 5.4.

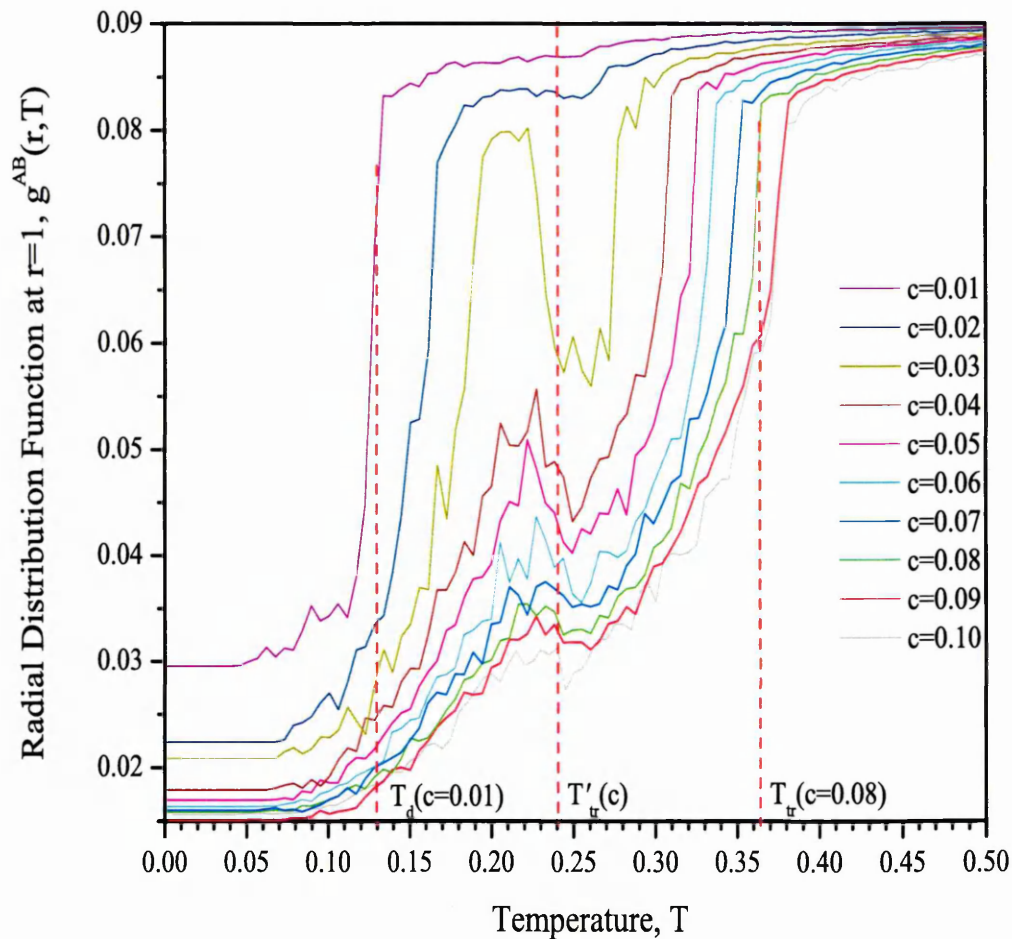


Figure 5.25: Radial Distribution Function $g^{AB}(r)^*$ in the range of $0.01 \leq c \leq 0.10$. Different curves represent different concentrations c . The values of $g^{AB}(r)^*$ were normalised to the value $g^{AB}(r = 1, T = 1.3, c = 0.10)$ for better clarity.

concentration c	Temperature $T_{tr}(c)$	Temperature $T_d(c)$	Temperature $T'_{tr}(c)$
0.0	N/A	N/A	N/A
0.01	0.24 ± 0.02	0.13 ± 0.02	0.24 ± 0.02
0.02	0.24 ± 0.02	0.16 ± 0.02	0.24 ± 0.02
0.03	0.24 ± 0.05	0.24 ± 0.05	0.24 ± 0.02
0.04	0.31 ± 0.02	0.31 ± 0.02	0.24 ± 0.02
0.05	0.33 ± 0.02	0.33 ± 0.02	0.24 ± 0.02
0.06	0.34 ± 0.02	0.34 ± 0.02	0.24 ± 0.02
0.07	0.35 ± 0.02	0.35 ± 0.02	0.24 ± 0.02
0.08	0.36 ± 0.02	0.36 ± 0.02	0.24 ± 0.02
0.09	0.37 ± 0.02	0.37 ± 0.02	0.24 ± 0.02
0.1	0.38 ± 0.02	0.38 ± 0.02	0.24 ± 0.02
0.2	0.47 ± 0.02	0.47 ± 0.02	0.24 ± 0.02
0.3	0.55 ± 0.02	0.55 ± 0.02	0.24 ± 0.02
0.4	0.60 ± 0.02	0.60 ± 0.02	0.24 ± 0.02
0.5	0.67 ± 0.02	0.67 ± 0.02	0.24 ± 0.02
0.6	0.78 ± 0.02	0.53 ± 0.02	0.24 ± 0.02
0.7	0.89 ± 0.02	0.48 ± 0.02	0.24 ± 0.02
0.8	0.97 ± 0.02	0.38 ± 0.02	0.24 ± 0.02
0.9	1.08 ± 0.02	0.25 ± 0.02	0.24 ± 0.02
1.0	N/A	N/A	N/A

Table 5.9: Table of temperatures $T_{tr}(c)$, $T_d(c)$ and $T'_{tr}(c)$ based on results obtained from $g^{AB}(r = 1, T)$.

We come now to the phase diagram for the system with $\varepsilon = 0.45$, based on the results presented above. Figure 5.26 shows qualitatively how various observables contributed to the phase diagram. The feature on $g^{AB}(r = 1, T)$ at the temperature $T'_{tr}(c)$ was especially helpful in identifying the area at the bottom of the phase diagram. To identify the boundary between N and I+N regions we used $g^{AB}(r = 1, T)$ and $\langle P_2(T) \rangle^A$, $\langle P_2(T) \rangle^B$ data, not shown in the Figure in order to not overcrowd it. As previously stated, the phase diagram is based on a set of points of different colours each of which represents a different phase or structure of the system. The green area, however, represents ‘coordinates’ at which we were not able unambiguously to determine the phase of the system.

Three phase areas which were present on the diagrams of previous systems ($\varepsilon = 0.9$ and $\varepsilon = 0.6$) also appear on the current diagram ($\varepsilon = 0.45$). However, the system with $\varepsilon = 0.45$ also exhibits a new region, not present in the other systems described earlier. This region is shown as magenta and represents the isotropic-nematic coex-

istence of the system. This region occupies the area which would otherwise belong to the demixed nematic-nematic coexistence. More precisely, it occupies the top part of the area and pushes the latter down the temperature axis. Due to the steep slope of the boundary between the isotropic and the nematic phase, the isotropic phase occupies more of the diagram, as compared with the systems with $\varepsilon = 0.9$ and $\varepsilon = 0.6$. Thus, the nematic phase (marked in red) becomes even smaller and no longer occupies the greater part of the phase area (Fig. 5.27). Moreover, the nematic-nematic demixing envelope (blue) along with a new, isotropic-nematic coexistence region, separates two distinct regions of mixed nematic.

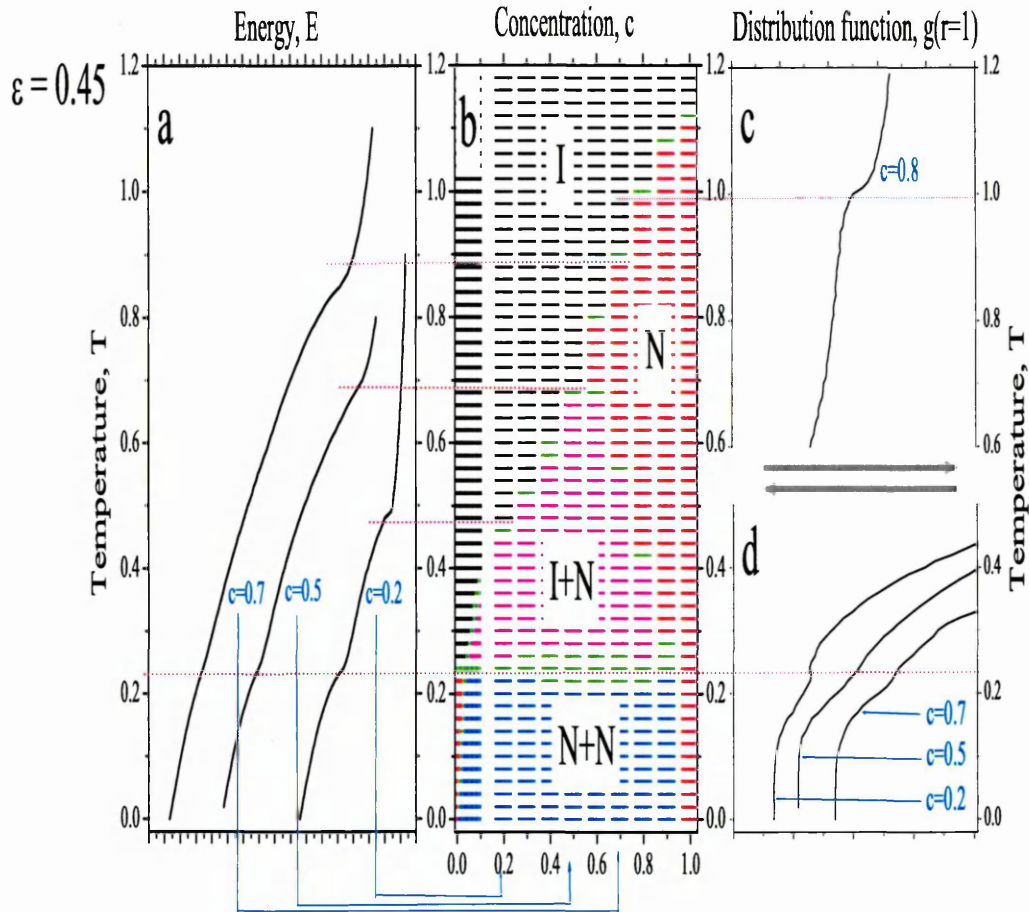
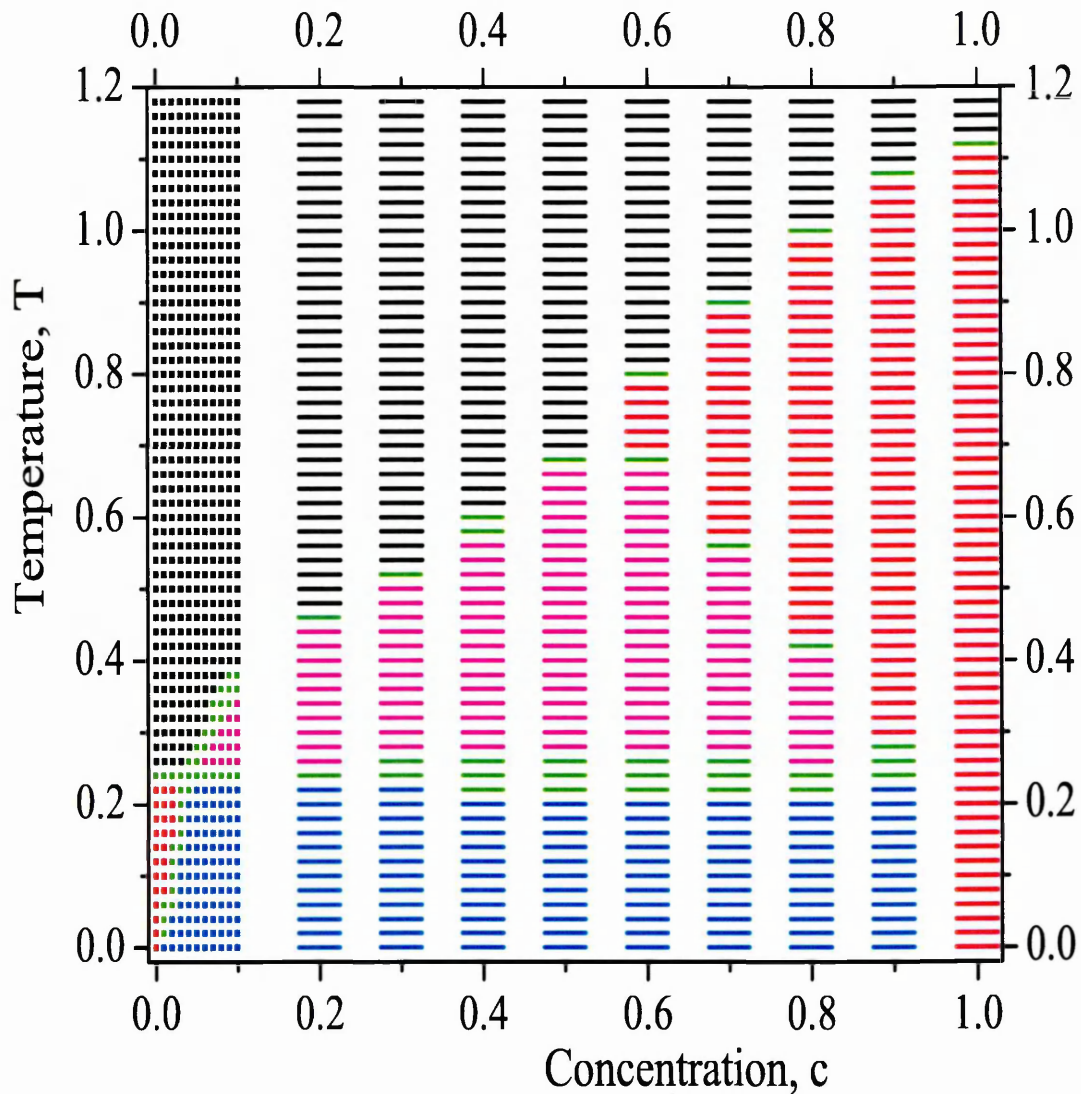


Figure 5.26: Constructing of the phase diagram (b) from $\langle E(T) \rangle$ (a) and $g^{AB}(r = 1, T)$ (c and d) for the system with $\varepsilon = 0.45$

Figure 5.27: Phase diagram. $\varepsilon = 0.45$

Let us consider the boundaries between the various phases, starting with the boundary between the isotropic and the nematic phases. At both ends of the concentration axis, the system undergoes I-N transition at the temperatures of I-N transition of its pure components. As the concentration changes from one extreme to the other, the $T_{IN}(c)$ curve changes linearly within the limits of approximation in the region of concentrations $0.1 \lesssim c \leq 1.0$. In the region of concentrations $0.0 \leq c \lesssim 0.1$,

the boundary deviates at $c_x \approx 0.04$, owing to the crossover with the boundary that separates the new, demixed isotropic-nematic coexistence envelope (magenta) and the demixed nematic-nematic coexistence region (blue). Depending on the concentration, a reduction in the temperature may result in the system changing from the isotropic phase to the nematic phase (on intervals $0.0 \leq c < c_x$ and $0.6 \lesssim c \leq 1.0$); or to the region of isotropic-nematic coexistence ($c_x < c \lesssim 0.5$); or indeed to the region of nematic-nematic coexistence (in the vicinity of c_x).

The boundary between the isotropic-nematic coexistence (magenta) and the nematic-nematic coexistence (blue) regions is practically a straight horizontal line, which appears to lie at the same temperature as the isotropic-nematic transition for $c = 0.0$, $T \approx 0.24$. However, the location of the boundary has a large uncertainty for most of the concentrations (Fig. 5.27).

On decreasing the coupling constant ε from 0.6 to 0.45, therefore, the demixing envelope has been found to spread significantly from the bottom of the phase diagram. In addition, the slope of the boundary between the isotropic and nematic phases has decreased in the region of low concentrations (Figures 5.9, 5.15, 5.27). This has led to the development of a new region of phase space - the isotropic-nematic coexistence region (Figure 5.27). The asymmetry of the demixing envelope is difficult to quantify, owing to its merger with the boundary between the isotropic and nematic phases.

Other than this, the behaviour of the system with $\varepsilon = 0.45$ is consistent with those of the systems with $\varepsilon = 0.90$ and $\varepsilon = 0.60$. Further discussion of these results will be given in Section 5.4.

5.1.4 System with $\varepsilon = 0.3$

The next system to be considered is the mixture with $\varepsilon = 0.3$. The first observable of this system to be examined is the average energy of the system $\langle E \rangle$. In Figure 5.28 we present the dependencies of the energy $\langle E \rangle$ on temperature for various concentrations c .

The behaviour of the $\langle E(T) \rangle$ curves for the system does not differ significantly from that of the system with $\varepsilon = 0.45$. In Figure 5.28 we present the measured $\langle E(T) \rangle$ behaviour for a series of systems with different concentrations c . Starting from

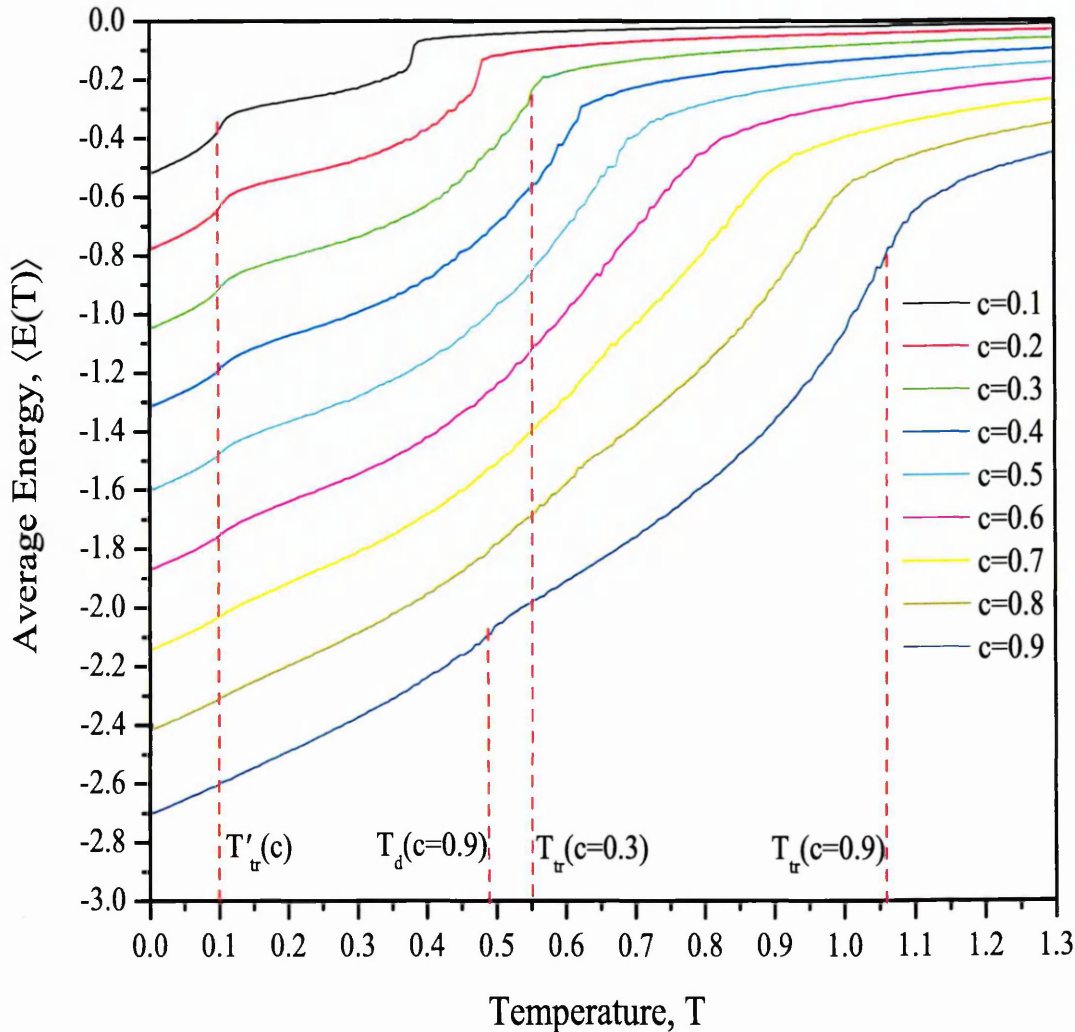


Figure 5.28: The dependence of the average energy on temperature, $\langle E(T) \rangle$. $\varepsilon = 0.3$.

the highest concentration on the graph, $c = 0.9$ (bottom curve in Fig. 5.28), we observe that from the point of highest temperature, the energy $\langle E(T) \rangle$ decreases slowly with reduction of temperature until at $T \approx T_{tr}(c)$ it starts to decrease more rapidly. The energy then continues to decrease; however, the gradient flattens out as the temperature continues to reduce, so that eventually the original slope is restored. As this happens, $\langle E(T) \rangle$ has another gradient discontinuity at $T_d(c)$, after which $\langle E(T) \rangle$ decreases steadily down to $T \rightarrow 0$. The discontinuity at $T'_{tr}(c)$ for

concentration c	Temperature $T_{tr}(c)$	Temperature $T_d(c)$	Temperature $T'_{tr}(c)$
0.0	0.10 ± 0.01	N/A	0.10 ± 0.01
0.1	0.38 ± 0.01	0.38 ± 0.01	0.10 ± 0.01
0.2	0.48 ± 0.01	0.48 ± 0.01	0.10 ± 0.01
0.3	0.55 ± 0.01	0.55 ± 0.01	0.10 ± 0.01
0.4	0.61 ± 0.01	0.61 ± 0.01	0.10 ± 0.01
0.5	0.68 ± 0.01	0.68 ± 0.01	0.10 ± 0.01
0.6	0.72 ± 0.01	0.68 ± 0.04	0.10 ± 0.01
0.7	0.85 ± 0.01	0.63 ± 0.01	0.10 ± 0.01
0.8	0.94 ± 0.01	0.60 ± 0.01	0.10 ± 0.01
0.9	1.06 ± 0.01	0.49 ± 0.01	0.10 ± 0.01
1.0	1.15 ± 0.01	N/A	N/A

Table 5.10: Table of Temperatures $T_{tr}(c)$, $T_d(c)$ and $T'_{tr}(c)$ based on the results of $\langle E(T) \rangle$. $T_{tr}(c)$ were derived as a point where the tangent of $\langle E(T) \rangle$ is the steepest.

this concentration is not noticeable in Figure 5.28, but is seen on the derivative of $\langle E(T) \rangle$. This pattern was seen previously for $\varepsilon = 0.45$ system.

When the concentration is decreased to 0.8 the high-temperature value of $\langle E(T) \rangle$ increases slightly, but remains negative. This value decreases slowly with reduction of temperature in the same manner as that which was noted for the concentration 0.9. The curve has deviation at $T_{tr}(c)$ and $T_d(c)$. Energy then continues to decrease, but the slope changes continuously as the temperature reduces, until it has a third discontinuity at $T'_{tr}(c)$. This phenomenon, where three discontinuities occur on the same curve, was observed in the system with $\varepsilon = 0.45$, and, as found previously, the phenomenon becomes weaker with decrease in concentration. In addition, $T_d(c)$ moves closer to $T_{tr}(c)$ and the two coincide for $c \lesssim 0.6$. The energy dependence for the rest of the concentrations ($c < 0.6$) therefore exhibits only two discontinuities in the gradient of $\langle E(T) \rangle$ at temperatures $T_{tr}(c)$ and $T'_{tr}(c)$. The temperature $T_{tr}(c)$ decreases with reduction of the concentration c . The value of $T_{tr}(c)$ is unique for each concentration of the system and so is the value of $T_d(c)$, whereas the value of $T'_{tr}(c)$ seems to remain unchanged for the entire concentration range at around 0.1. However, the shape of the feature at $T'_{tr}(c)$ becomes sharper as the concentration of the system decreases. This is also true for the discontinuity of $\langle E(T) \rangle$ at $T_{tr}(c)$. All of the temperatures described above are given in Table 5.10.

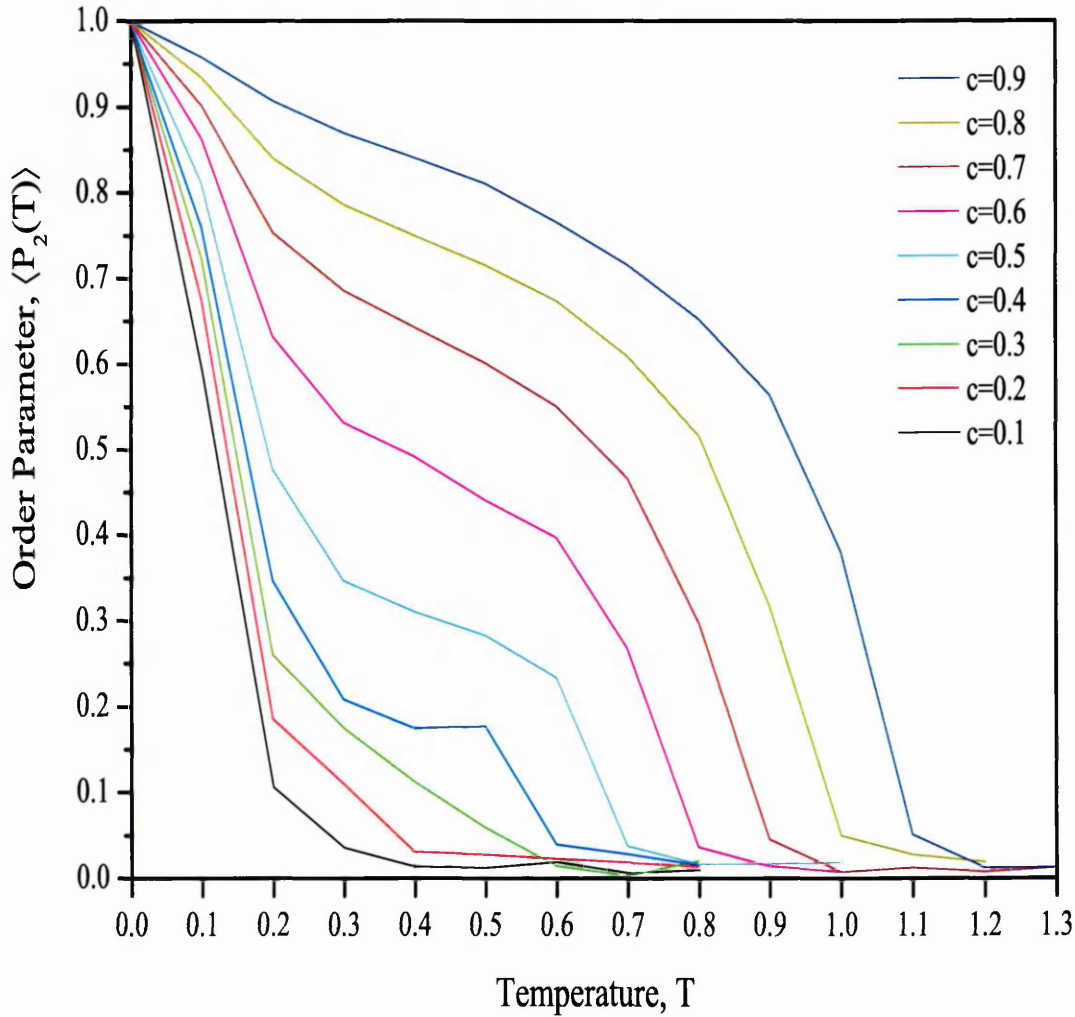


Figure 5.29: The thermal dependence of the second rank orientational order parameter, $\langle P_2(T) \rangle$. Different curves represent different concentration c in the mixture with $\varepsilon=0.3$.

Let us turn next to the thermal dependence of the second rank orientational order parameter $\langle P_2(T) \rangle$, obtained from $g_2(r \gg 3)$ for the system with $\varepsilon = 0.30$ and concentration $c = 0.5$ (Figure 5.29). At the highest temperature, the order parameter is close to zero; then, at $T_{tr}(c)$, it increases rapidly. But unlike $\langle P_2(T) \rangle$ in the systems with $\varepsilon = 0.90$ and $\varepsilon = 0.60$, it does not, as the temperature decreases, increase with monotonic gradient and approach the value of 1.

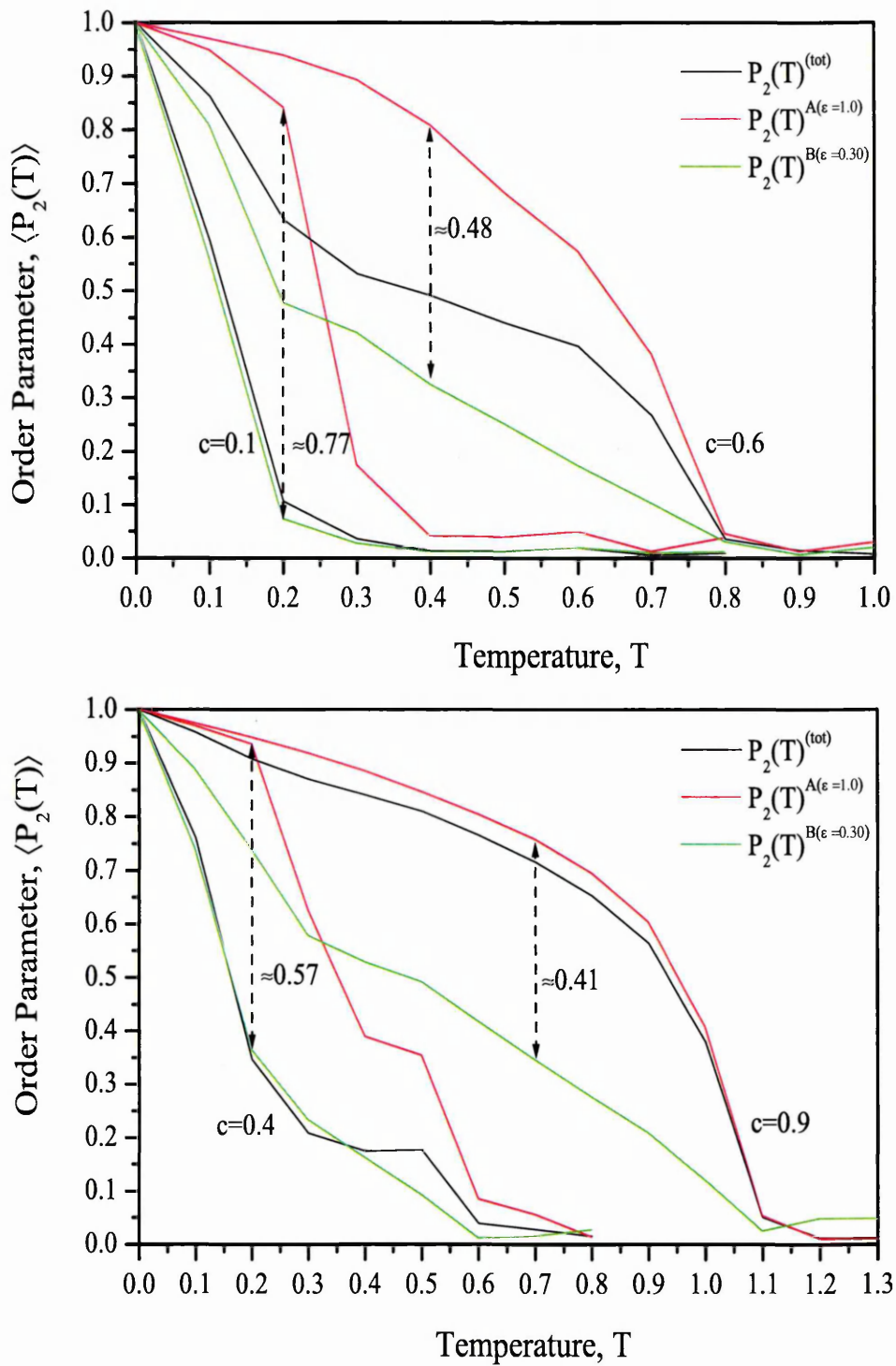


Figure 5.30: Second rank orientational order parameter for A and B separately. Dependence on temperature. Different curves represent different concentration c in the binary mixture with $\epsilon=0.30$. Yes, these dashed arrow lines are parallel to ordinate $\langle P_2(T) \rangle$.

concentration c	Temperature $T_{tr}(c)$	Temperature $T'_{tr}(c)$
0.0	0.11 ± 0.05	0.15 ± 0.05
0.1	0.35 ± 0.05	0.15 ± 0.05
0.2	0.42 ± 0.05	0.15 ± 0.05
0.3	0.55 ± 0.05	0.15 ± 0.05
0.4	0.62 ± 0.05	0.15 ± 0.05
0.5	0.70 ± 0.05	0.15 ± 0.05
0.6	0.80 ± 0.05	0.15 ± 0.05
0.7	0.91 ± 0.05	0.15 ± 0.05
0.8	1.00 ± 0.05	0.15 ± 0.05
0.9	1.10 ± 0.05	0.15 ± 0.05
1.0	1.18 ± 0.05	N/A

Table 5.11: Table of Temperatures $T_{tr}(c)$ and $T'_{tr}(c)$ based on results obtained from $\langle P_2 \rangle$, $\langle P_2 \rangle^A$ and $\langle P_2 \rangle^B$. System with $\varepsilon = 0.30$.

Instead, it approaches $\langle P_2(T) \rangle \approx 0.35$ as the temperature decreases until, at $T'_{tr}(c)$, it rapidly increases again, approaching $\langle P_2(T) \rangle \rightarrow 1$. This effect is seen at most concentrations and was also observed in the system with $\varepsilon = 0.45$. However, the value of $\langle P_2(T) \rangle$ has never previously decreased with the reduction of the temperature (see $\langle P_2(T) \rangle$ for $c = 0.4$ in Figure 5.29). As in the system with $\varepsilon = 0.45$, the value of $T'_{tr}(c)$ does not seem to vary significantly with the concentration and equals 0.1...0.2. Table 5.11 shows values for $T_{tr}(c)$ and $T'_{tr}(c)$ for the set of concentrations. These values of $T_{tr}(c)$ in Table 5.11 agree with the values of $T_{tr}(c)$ obtained from the energy calculations presented earlier in this section (Table 5.10).

Let us now examine individually the order parameters of the components A ($\langle P_2 \rangle^A$) and B ($\langle P_2 \rangle^B$) (Fig.5.30). Though the temperature at which $\langle P_2(T) \rangle$ becomes non-zero is the same in each case, the shapes of the growth of $\langle P_2(T) \rangle$ differ significantly. The initial increase in the value of $\langle P_2(T) \rangle^B$ with the reduction of the temperature is not as great as for $\langle P_2(T) \rangle^A$ and in some cases it does not resemble the typical shape of a second rank order parameter at all. For the temperature $T \approx 0.2$, the difference in $\langle P_2(T) \rangle$ between the two components reaches a value ≈ 0.77 for concentration $c = 0.1$. As concentration increases the difference becomes smaller, but still remains significant. These differences in the values of the order parameter are greater than that seen in the other three systems investigated. If we look closely at $\langle P_2 \rangle^A$ and

$\langle P_2 \rangle^B$ for concentration $c = 0.5$, we notice that in the region of temperatures $0.2 \lesssim T \lesssim 0.4$ the value of the total order parameter is lower than $\langle P_2 \rangle^A$ or $\langle P_2 \rangle^B$. At other temperatures, it is somewhere between the values of the order parameters of the two components. The order parameter of both components reaches 1, as the temperature approaches zero.

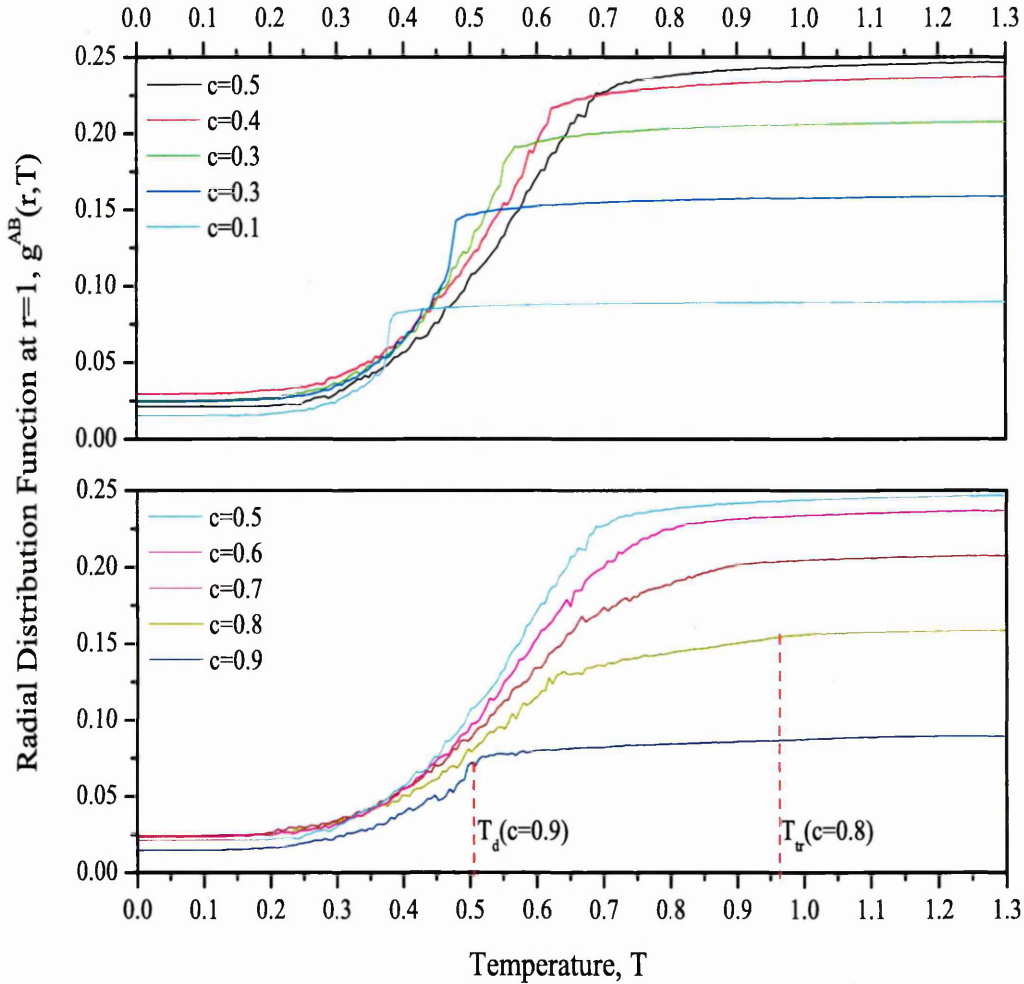


Figure 5.31: The short range radial distribution function dependence on the temperature, $g^{AB}(r = 1)$. Different curves represent different c . System with $\varepsilon = 0.30$.

The next observable to be considered is the radial distribution function ($g^{AB}(r)$). In Figure 5.31 we present $g^{AB}(r = 1, T)$ for the set of concentrations. At concentration $c = 0.9$, $g^{AB}(r = 1, T)$ decreases slowly as the temperature falls. Then, at $T_{tr}(c) \approx 1.04$, there occurs a slight discontinuity in the gradient. With further decrease in temperature, $g^{AB}(r = 1, T)$ maintains a constant slope throughout a wide region

concentration c	Temperature $T_{tr}(c)$	Temperature $T_d(c)$
0.0	N/A	N/A
0.1	0.38 ± 0.02	0.38 ± 0.02
0.2	0.48 ± 0.02	0.48 ± 0.02
0.3	0.55 ± 0.02	0.55 ± 0.02
0.4	0.61 ± 0.02	0.61 ± 0.02
0.5	0.68 ± 0.02	0.68 ± 0.02
0.6	0.75 ± 0.02	0.70 ± 0.05
0.7	0.85 ± 0.02	0.65 ± 0.02
0.8	0.96 ± 0.02	0.61 ± 0.02
0.9	1.07 ± 0.02	0.51 ± 0.02
1.0	N/A	N/A

Table 5.12: Table of Temperatures based on results obtained from $g^{AB}(r = 1, T)$. System with $\varepsilon = 0.30$.

of temperatures until $T_d(c) \approx 0.51$ is reached, when it steepens sharply. At $c = 0.8$ the value of $g^{AB}(r = 1, T)$ remains unchanged as the temperature decreases, until it reaches $T_{tr}(c) \approx 0.96$, when it starts to decline with a steeper slope. The slope remains fairly steady as the temperature continues to decrease. Then, at $T_d(c) \approx 0.61$ the slope of $g^{AB}(r = 1, T)$ becomes suddenly steeper. After that, the function levels off to its minimum value as $T \rightarrow 0$, displaying some nonlinearity at $T'_{tr}(c) \approx 0.20$ (Fig. 5.31).

From the Figure it is clear that $g^{AB}(r = 1, T)$ for other concentrations exhibits similar behaviour. As concentration decreases, temperatures $T_{tr}(c)$ and $T_d(c)$ move closer together until at $c \approx 0.5$ they converge.

At all concentrations lower than $c \approx 0.5$ there are only two discontinuities present on the $g^{AB}(r = 1, T)$ function: $T_{tr}(c)$ and $T'_{tr}(c)$. Also, when the concentration c in the system decreases, the deviation which occurs at $T_{tr}(c)$ ($\equiv T_d(c)$) becomes sharper. The values of all such temperatures are noted in Table 5.12.

The next part of this section looks at the phase diagram for the system with $\varepsilon = 0.30$, based on the results presented above. All four phase areas that were present on the diagram of the previous system ($\varepsilon = 0.45$) are also present on the current diagram ($\varepsilon = 0.30$), although, there are some changes in the relative size or area of various regions. The isotropic-nematic coexistence region (magenta), as it has increased in size, has pushed the demixed nematic-nematic coexistence further down (Fig.

5.32). In addition, the isotropic-nematic coexistence region has broadened slightly and pushed both of the nematic regions (red) aside. The size of the region occupied by the isotropic phase shows no significant variation from that in the system with $\varepsilon = 0.45$.

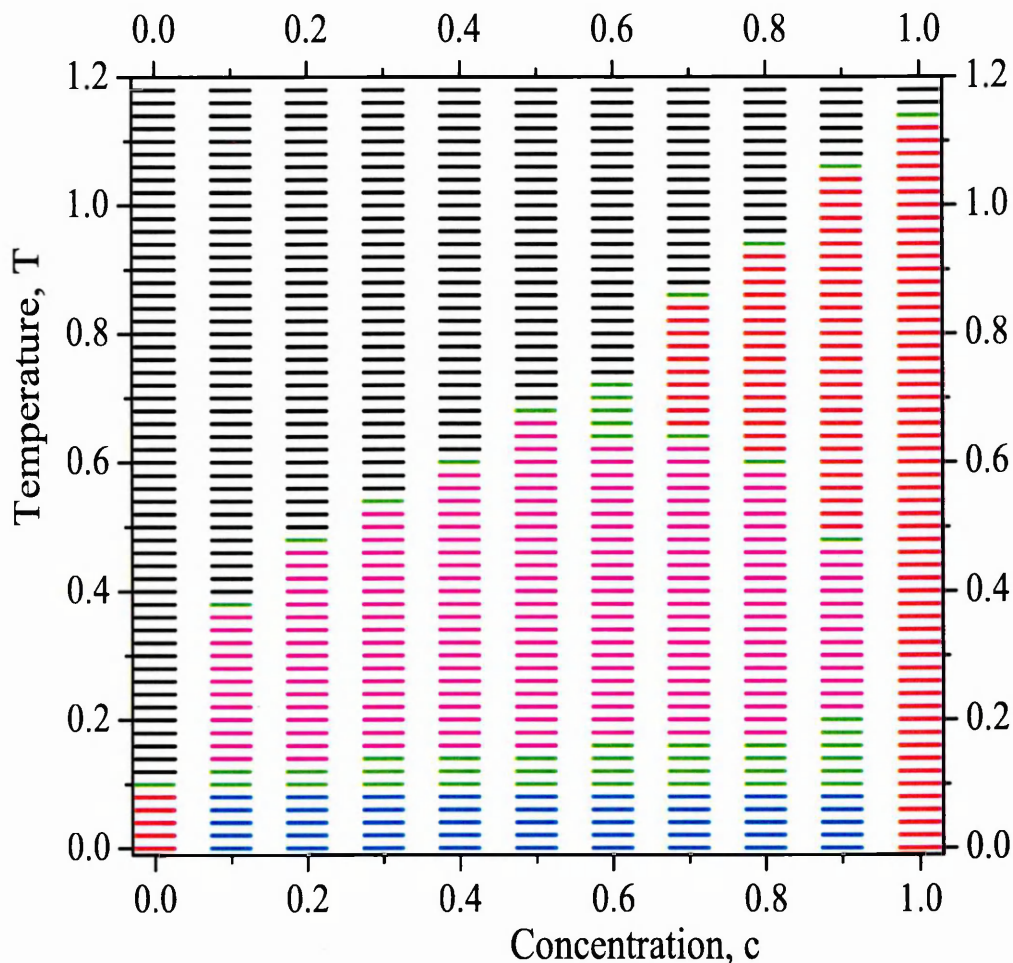


Figure 5.32: Phase diagram. $\varepsilon = 0.3$

Let us consider the boundaries between the various phases. The highest boundary on the temperature scale is that between the isotropic and the nematic phases. The slope of the boundary in the region of concentrations $0.1 \lesssim c \leq 1.0$ is virtually constant. We were unable to resolve the value of c_x ; however, the data from the previous system suggests its presence somewhere in the concentration region $0.0 <$

$c_x < 0.1$. The interpolation of the existing data for the system $\varepsilon = 0.3$ suggests $c_x \approx 0.02$. Depending on the concentration, a reduction in temperature may result in the system changing from the isotropic phase to the nematic phase (on intervals $0.0 \leq c < c_x$ and $0.6 \lesssim c \lesssim 1.0$); or to the region of isotropic-nematic coexistence ($c_x < c \lesssim 0.5$); or indeed to the region of nematic-nematic coexistence (in the vicinity of c_x).

The boundary between isotropic-nematic coexistence (magenta) and the nematic-nematic coexistence (blue) phases is practically a straight horizontal line, which appears to be at the same value T as the isotropic-nematic transition for $c = 0.0$, $T \approx 0.1$. However, the boundary is very indistinct for most concentrations, compared to that of the previous system (Fig. 5.32).

Referring to the phase diagrams presented earlier, as the coupling constant increases from $\varepsilon = 0.9$ to $\varepsilon = 0.6$, the demixing envelope spreads from the bottom of the phase diagram, displacing other phase regions. Then, somewhere between $0.6 \lesssim \varepsilon \lesssim 0.45$, the change in the slope of the boundary between the isotropic and nematic phases was halted and remained constant as ε was decreased to the value of 0.3 (Figures 5.27, 5.32).

Other than this, the behaviour of the system with $\varepsilon = 0.30$ is similar to that of the system with $\varepsilon = 0.45$. Overall, the behaviour of the system with $\varepsilon = 0.30$ is consistent with the behaviour of the systems with $\varepsilon = 0.90$ and $\varepsilon = 0.60$. Discussion of the results presented above will follow in Section 5.4.

5.1.5 System with $\varepsilon = 0.1$

The next system simulated was that with coupling constant $\varepsilon = 0.1$. Let us consider the first observable of this system, average energy $\langle E \rangle$. The behaviour of the $\langle E(T) \rangle$ curves for this system does not differ significantly from those for the systems with $\varepsilon = 0.45$ and $= 0.30$. In Figure 5.33 we present the dependence of the energy on the temperature $\langle E(T) \rangle$ for different concentrations c .

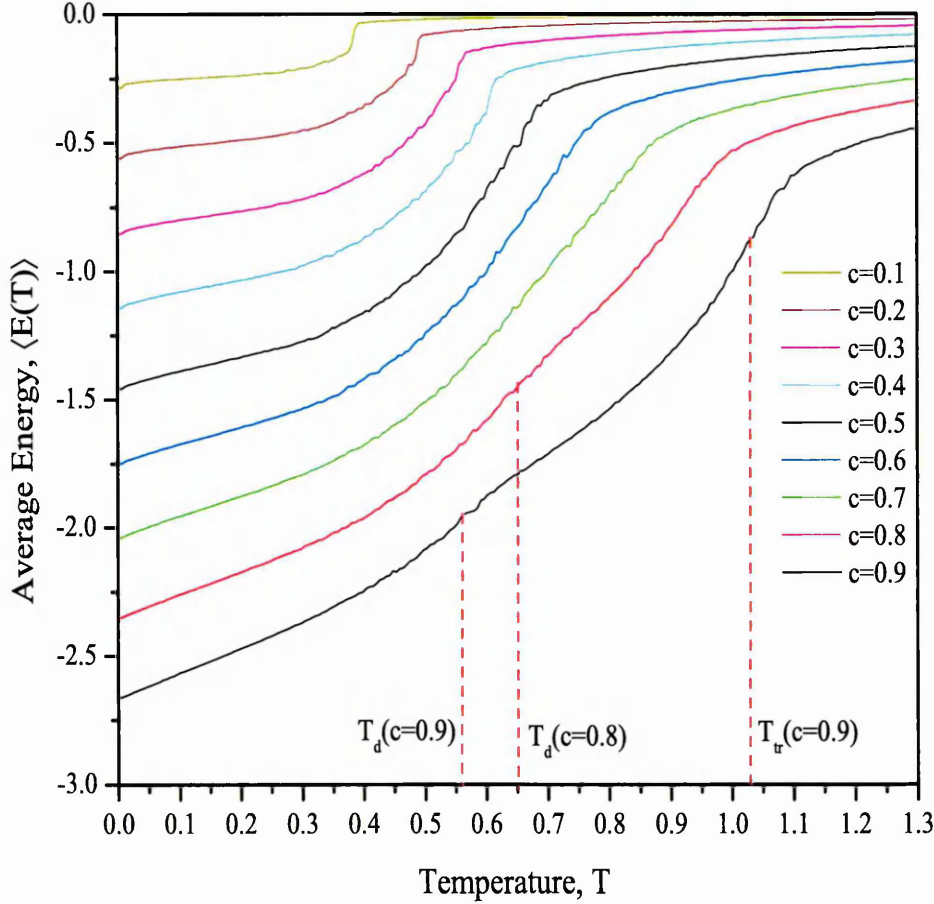


Figure 5.33: Average Energy dependence on temperature, $\langle E(T) \rangle$ for the system with $\varepsilon = 0.10$.

We begin with the highest concentration on the graph, $c = 0.9$ (bottom curve in Fig. 5.33). The energy $\langle E(T) \rangle$ decreases slowly with reduction of temperature until at $T \approx T_{tr}(c)$ it decreases rapidly. The energy then continues to decrease gradually, reducing in steepness as the temperature continues to reduce, until eventually it returns to the original slope. Then at $T_d(c)$, $\langle E(T) \rangle$ decreases sharply again. After this, $\langle E(T) \rangle$ decreases steadily down to $T \rightarrow 0$. As with the previous system, the discontinuity which occurs at $T_d(c)$ eventually fades with decreasing concentration. At the same time, $T_d(c)$ moves closer to $T_{tr}(c)$ and the two coincide at $c \approx 0.6$. At low concentrations we observe a sharper decrease of $\langle E(T) \rangle$ at $T_{tr}(c)$ compared to that of high concentrations. The sharpness of the discontinuity at $T'_{tr}(c)$ also increases as the concentration decreases. The value of $T'_{tr}(c)$ is very low and seems

to be the same for all concentrations. This discontinuity, virtually unnoticeable in Figure 5.33 is clearly seen from the numerical differentiation of the $\langle E(T) \rangle$ curves. The peak of $\frac{d\langle E(T) \rangle}{dT}$ at $T'_{tr}(c)$ does not depend on concentration and is highest at $c = 0.1$. Figure 5.34 shows that $T'_{tr}(c) \approx 0.01$. All the temperatures described above are given in Table 5.13.

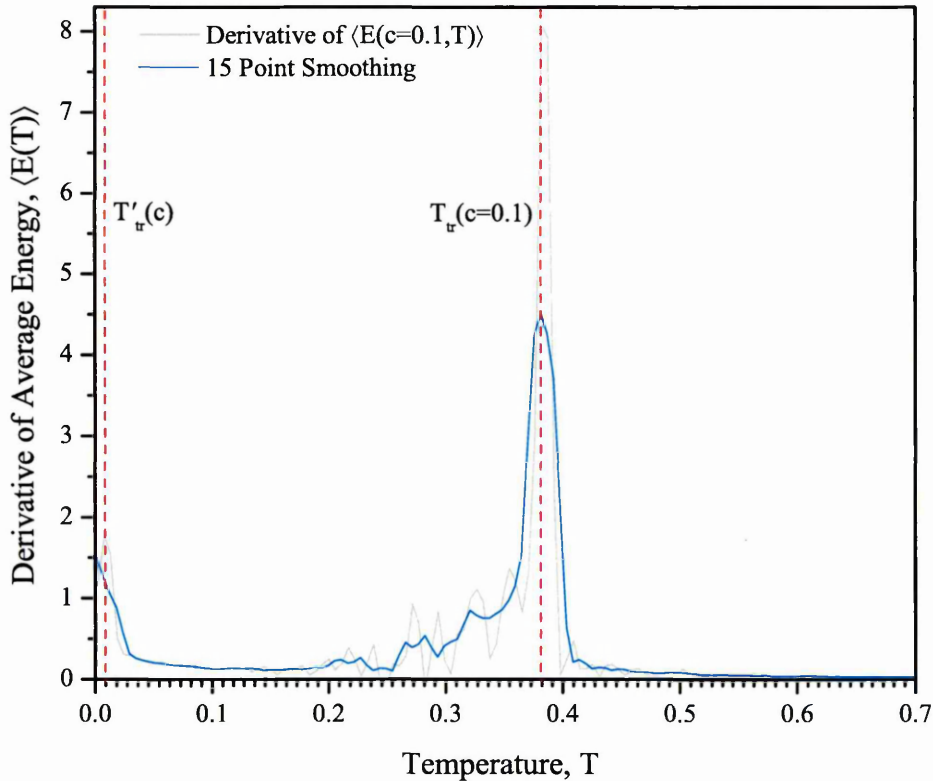


Figure 5.34: The derivative of the average energy function for the concentration $c = 0.1$.

Let us now consider the thermal dependence of the second rank orientational order parameter $\langle P_2(T) \rangle$, obtained from $g_2(r \gg 3)$ for the system with $\varepsilon = 0.10$ (Figure 5.35). For most concentrations, starting from the highest temperature, the order parameter is close to zero. Then, at $T_{tr}(c)$, the value of $\langle P_2(T) \rangle$ increases rapidly and seems to approach, as $T \rightarrow 0.1$, a value between 0 and 1, which is unique for each concentration. At temperatures lower than 0.1 $\langle P_2(T) \rangle$ suddenly increases rapidly again, this time approaching 1 as $T \rightarrow 0.0$. This behaviour is similar to that seen in the two previous systems ($\varepsilon = 0.45$ and $\varepsilon = 0.30$). The temperature of the second increase in $\langle P_2(T) \rangle$, $T'_{tr}(c)$, does not seem to depend on concentration, again as was observed for the systems with $\varepsilon = 0.45$ and $\varepsilon = 0.30$.

concentration c	Temperature $T_{tr}(c)$	Temperature $T_d(c)$	Temperature $T'_{tr}(c)$
0.0	0.01 ± 0.01	<i>N/A</i>	0.01 ± 0.01
0.1	0.38 ± 0.01	0.38 ± 0.01	0.01 ± 0.01
0.2	0.48 ± 0.01	0.48 ± 0.01	0.01 ± 0.01
0.3	0.54 ± 0.01	0.54 ± 0.01	0.01 ± 0.01
0.4	0.59 ± 0.01	0.59 ± 0.01	0.01 ± 0.01
0.5	0.64 ± 0.01	0.64 ± 0.02	0.01 ± 0.01
0.6	0.70 ± 0.01	0.69 ± 0.02	0.01 ± 0.01
0.7	0.82 ± 0.01	0.77 ± 0.05	0.01 ± 0.01
0.8	0.92 ± 0.01	0.65 ± 0.01	0.01 ± 0.01
0.9	1.03 ± 0.01	0.56 ± 0.01	0.01 ± 0.01
1.0	1.15 ± 0.01	<i>N/A</i>	<i>N/A</i>

Table 5.13: Table of Temperatures $T_{tr}(c)$. $T_{tr}(c)$ were derived as a point where the tangent of $\langle E(T) \rangle$ is the steepest.

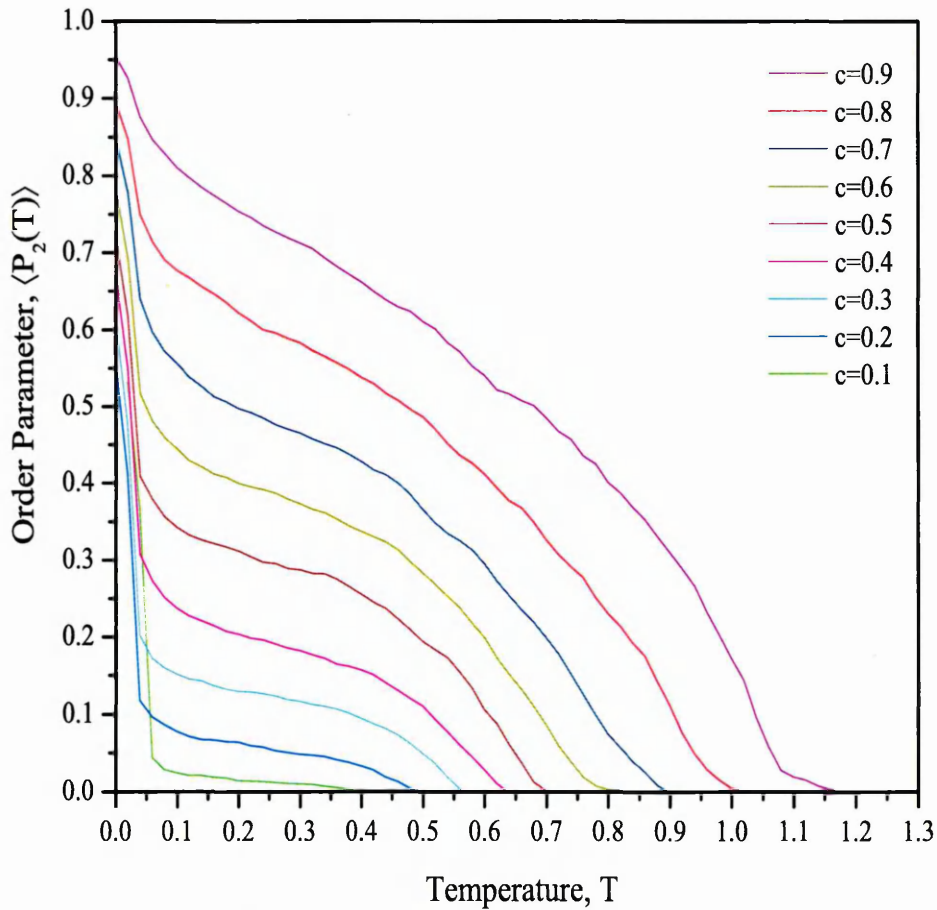


Figure 5.35: Second rank orientational order parameter. Dependence on temperature. Different curves represent different concentration c in the binary mixture. $\varepsilon=0.10$.

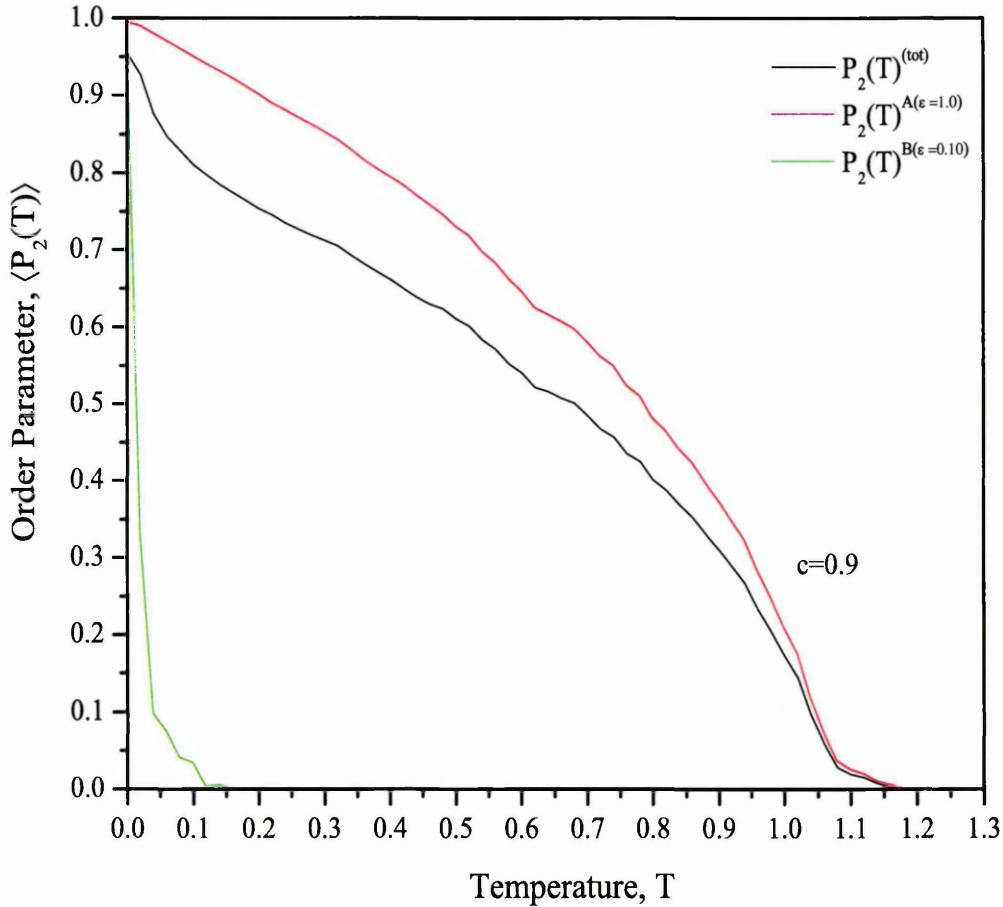


Figure 5.36: Second rank orientational order parameter for component A (red curve) and B (blue curve) separately. Black curve - the order parameter of the whole system. Dependence on temperature for the system with $\epsilon=0.10$ and $c = 0.9$.

The shape of $\langle P_2(T) \rangle$ differs significantly from the shapes of the order parameter curves of the systems with $\epsilon = 0.90$ and $\epsilon = 0.60$ resembling, instead, the shapes of the order parameter curves for the systems with $\epsilon = 0.45$ and $\epsilon = 0.30$. As in the case of the systems with $\epsilon = 0.45$ and $\epsilon = 0.30$, the deviation of $\langle P_2(T) \rangle$ from the conventional behaviour is strongest when the two components of the system are in more or less equal proportions.

Let us now look individually at the order parameters of the components A ($\langle P_2(T) \rangle^A$) and B ($\langle P_2(T) \rangle^B$) (Fig.5.36). The order parameter for component A does not exhibit any unusual behaviour, except slight deviations of $\langle P_2(T) \rangle^A$ in the region of temper-

concentration c	Temperature $T_{tr}(c)$	Temperature $T'_{tr}(c)$
0.0	0.02 ± 0.05	0.04 ± 0.05
0.1	0.40 ± 0.05	0.04 ± 0.05
0.2	0.48 ± 0.05	0.04 ± 0.05
0.3	0.56 ± 0.05	0.04 ± 0.05
0.4	0.64 ± 0.05	0.04 ± 0.05
0.5	0.70 ± 0.05	0.04 ± 0.05
0.6	0.79 ± 0.05	0.04 ± 0.05
0.7	0.90 ± 0.05	0.04 ± 0.05
0.8	0.98 ± 0.05	0.04 ± 0.05
0.9	1.10 ± 0.05	0.04 ± 0.05
1.0	1.18 ± 0.05	0.04 ± 0.05

Table 5.14: Table of Temperatures $T_{tr}(c)$ based on results obtained from $\langle P_2 \rangle$, $\varepsilon=0.10$.

atures $T < T_{tr}(c)$. As the temperature reaches $T_{tr}(c)$, $\langle P_2(T) \rangle^A$ increases rapidly and saturates slowly to the value of 1 as temperature approaches zero. The $\langle P_2(T) \rangle^B$ curves for most concentrations, however stay roughly at zero as the temperature passes $T_{tr}(c)$ and increase rapidly when it reaches $T'_{tr}(c)$. In other words, particles B remain in the isotropic phase whilst particles A form a nematic phase. Explanation and discussion of this will follow in the Section 5.4. Table 5.14 shows the values for $T_{tr}(c)$ and $T'_{tr}(c)$ for the set of concentrations, obtained from the results of the orientational order parameter. These values (Table 5.14) agree with the values of $T_{tr}(c)$ obtained from the energy calculations, presented earlier in this section (Table 5.13).

The next observable is the radial distribution function ($g^{AB}(r)$). In Figure 5.37 we present $g^{AB}(r = 1, T)$ for the full set of concentrations. At the concentration $c = 0.9$ $g^{AB}(r = 1, T)$ decreases slowly as temperature decreases. Then, at $T_{tr}(c) \approx 1.09$, it exhibits a slight discontinuity in the gradient. Further decrease in the temperature causes $g^{AB}(r = 1, T)$ to decrease slightly faster, but it maintains its gradient until $T_d(c) \approx 0.58$ is reached, when it decreases quite sharply. At temperatures below $T_d(c)$ the function asymptotically approaches a non zero value. At $c = 0.8$, $g^{AB}(r = 1, T)$ starts off from a higher value than it does for $c = 0.9$. At high temperatures it remains unchanged as the temperature decreases until, at $T_{tr}(c) \approx 0.93$, it starts to decline with a steady slope. This decline continues at a steady rate as the temperature falls, but becomes suddenly steeper at $T_d(c) \approx 0.68$. After this, the

function levels off as $T \rightarrow 0$. From the Figure, it is clear that $g^{AB}(r = 1, T)$ for other concentrations exhibits similar behaviour. As the concentration is decreased, the temperatures $T_{tr}(c)$ and $T_d(c)$ move closer together until, at $c \approx 0.6$, they meet. The slope in the region between $T_{tr}(c)$ and $T_d(c)$ at concentrations $c \gtrsim 0.6$ becomes steeper with decreasing c and eventually vanishes at $c \approx 0.6$, as $T_{tr}(c)$ and $T_d(c)$ meet. At all concentrations lower than $c \approx 0.6$ there is only one discontinuity present in the gradient of $g^{AB}(r = 1, T)$, at $T_{tr}(c)$. The values of all such temperatures are noted in Table 5.15.

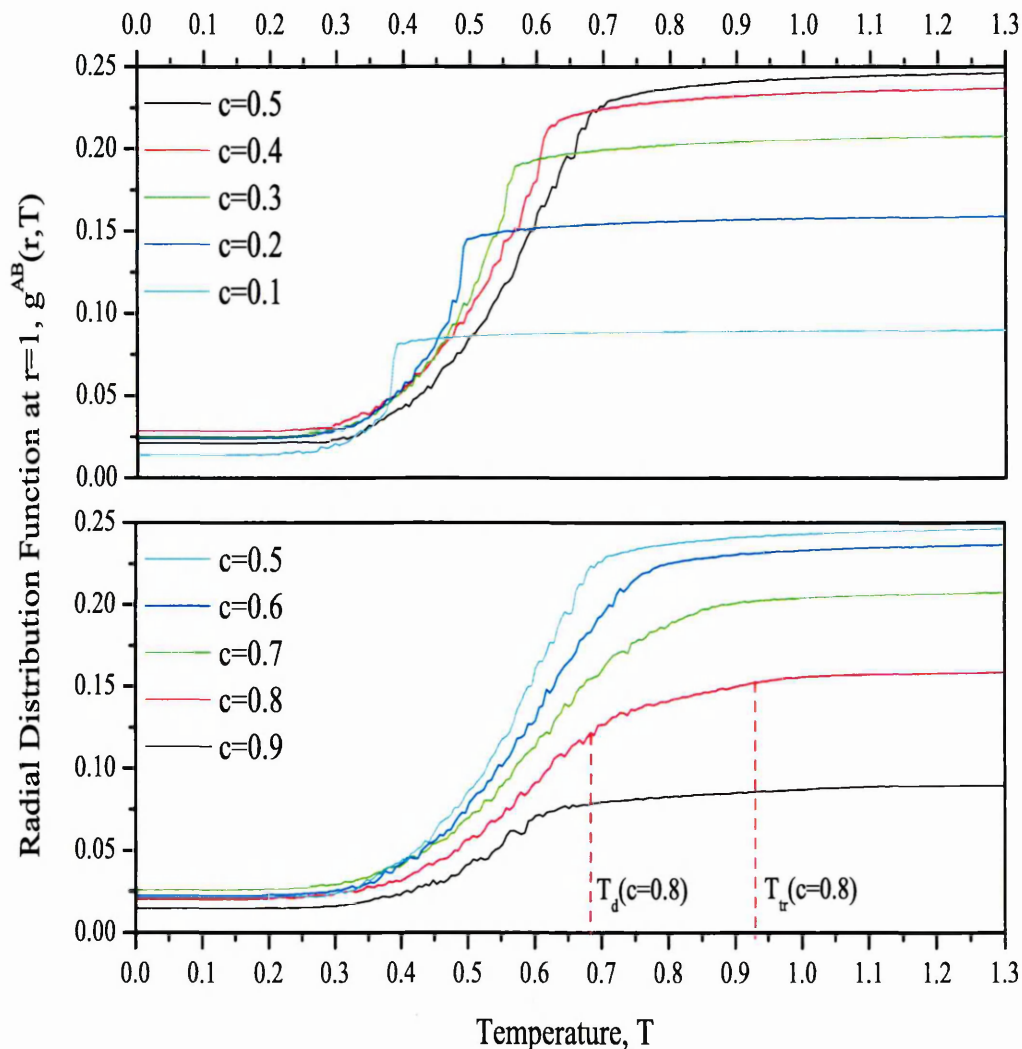


Figure 5.37: The short range radial distribution function dependence on the temperature, $g^{AB}(r = 1)$. Different curves represent different c . System with $\varepsilon = 0.10$.

concentration c	Temperature $T_{tr}(c)$	Temperature $T_d(c)$
0.0	N/A	N/A
0.1	0.39 ± 0.02	0.39 ± 0.02
0.2	0.49 ± 0.02	0.49 ± 0.02
0.3	0.56 ± 0.02	0.56 ± 0.02
0.4	0.61 ± 0.02	0.61 ± 0.02
0.5	0.67 ± 0.02	0.67 ± 0.02
0.6	0.73 ± 0.02	0.69 ± 0.04
0.7	0.83 ± 0.02	0.78 ± 0.05
0.8	0.93 ± 0.02	0.68 ± 0.02
0.9	1.09 ± 0.02	0.58 ± 0.02
1.0	N/A	N/A

Table 5.15: Table of Temperatures based on results obtained from $g^{AB}(r = 1, T)$. System with $\varepsilon = 0.10$.

Next we will consider the phase diagram for the system with $\varepsilon = 0.10$, based on the results presented above. All four phase areas which were present on the diagrams of the two previous systems ($\varepsilon = 0.45$ and $\varepsilon = 0.30$) are also present on the current phase diagram ($\varepsilon = 0.10$). However, the areas occupied by each individual region have been changed compared to those of previous systems. Enlargement of the isotropic-nematic coexistence region (magenta) has pushed the demixed nematic-nematic coexistence (blue) still further down (Fig. 5.38) to make it a very narrow strip at the bottom of the diagram. In addition, the isotropic-nematic coexistence region (magenta) has broadened slightly and encroached on the nematic region (red) on the right-hand side. The small nematic region on the left of the diagram has virtually disappeared. The isotropic phase displays no significant variation in size, as compared with those in the systems with $\varepsilon = 0.45$ and $\varepsilon = 0.30$.

Let us now consider the boundaries between the various phases, starting with the boundary which separates the isotropic from the nematic phase. The slope of the boundary in the region of concentrations $0.1 \lesssim c \leq 1.0$ is virtually constant. Depending on the concentration, a reduction in temperature may result in the isotropic phase changing to the nematic phase (in the vicinity of $c = 0.0$ and on the interval $0.7 \lesssim c \lesssim 1.0$); to the region of isotropic-nematic coexistence ($0.0 < c \lesssim 0.6$); or immediately into the nematic-nematic coexistence region.

The boundary between the isotropic-nematic coexistence (magenta) and the nematic-nematic coexistence (blue) regions is a straight horizontal line, which appears to be at the same temperature as the isotropic-nematic transition for $c = 0.0$, which is $T < 0.02$. However, the boundary is not very distinct for most concentrations, especially in the region of high concentrations (note the large number of green points in Figure 5.38). In other words, the behaviour of the system with $\varepsilon = 0.10$ is similar to that of the system with $\varepsilon = 0.45$ and $\varepsilon = 0.30$. Overall, the behaviour of the system with $\varepsilon = 0.10$ is consistent with the behaviour of the all systems presented in this chapter. Discussion of these results will follow in Section 5.4.

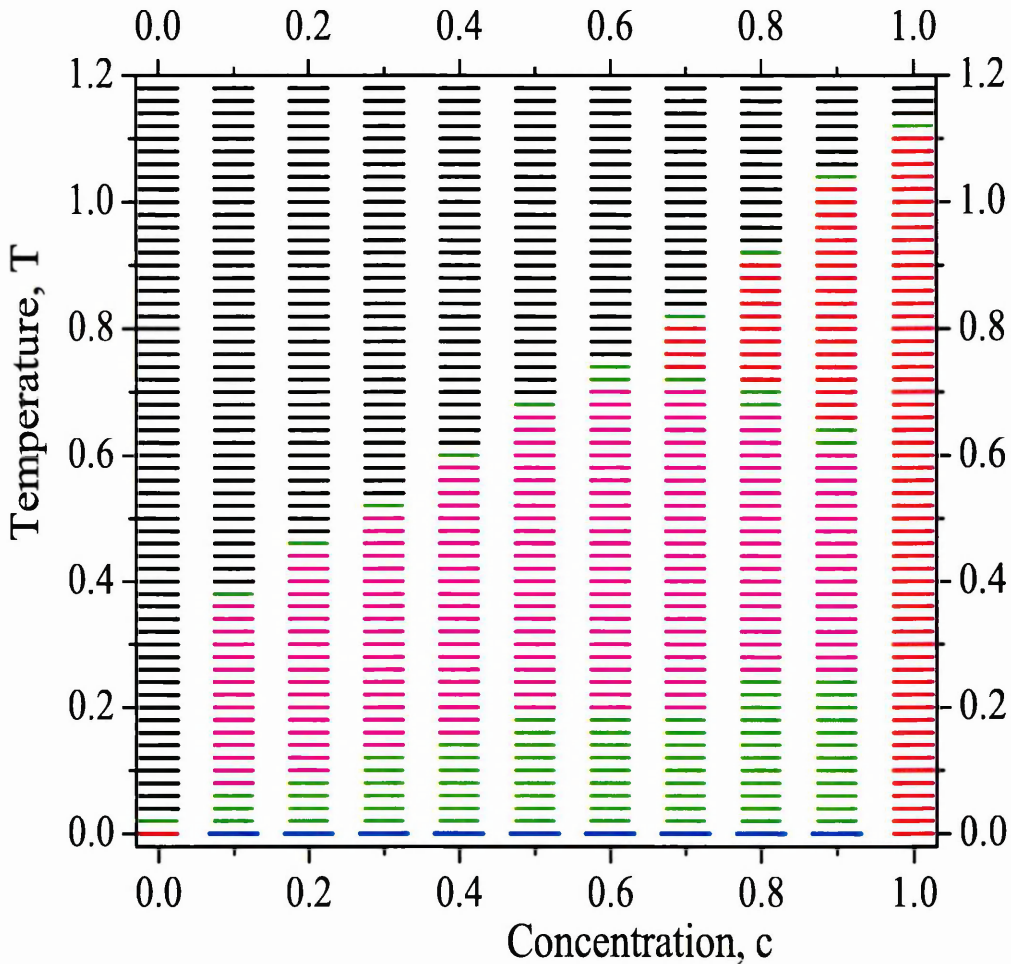


Figure 5.38: Phase diagram. $\varepsilon = 0.1$

5.1.6 System with $\varepsilon = 0.0$

The next and last system to be covered in this chapter has $\varepsilon = 0.00$. This system differs significantly from all systems presented previously. The particles B are absolutely isotropic, which means that they possess spherical symmetry, while the symmetry of particles A is cylindrical. This implies that the orientational order parameter for the B component is always zero. Thus, for example, the highest total order parameter of the perfectly ordered system for the concentration $c = 0.5$ will be equal to 0.5. Bearing this in mind, let us now look at the results, starting from the thermal dependence of the energy for the system $\langle E(T) \rangle$ (Fig. 5.39).

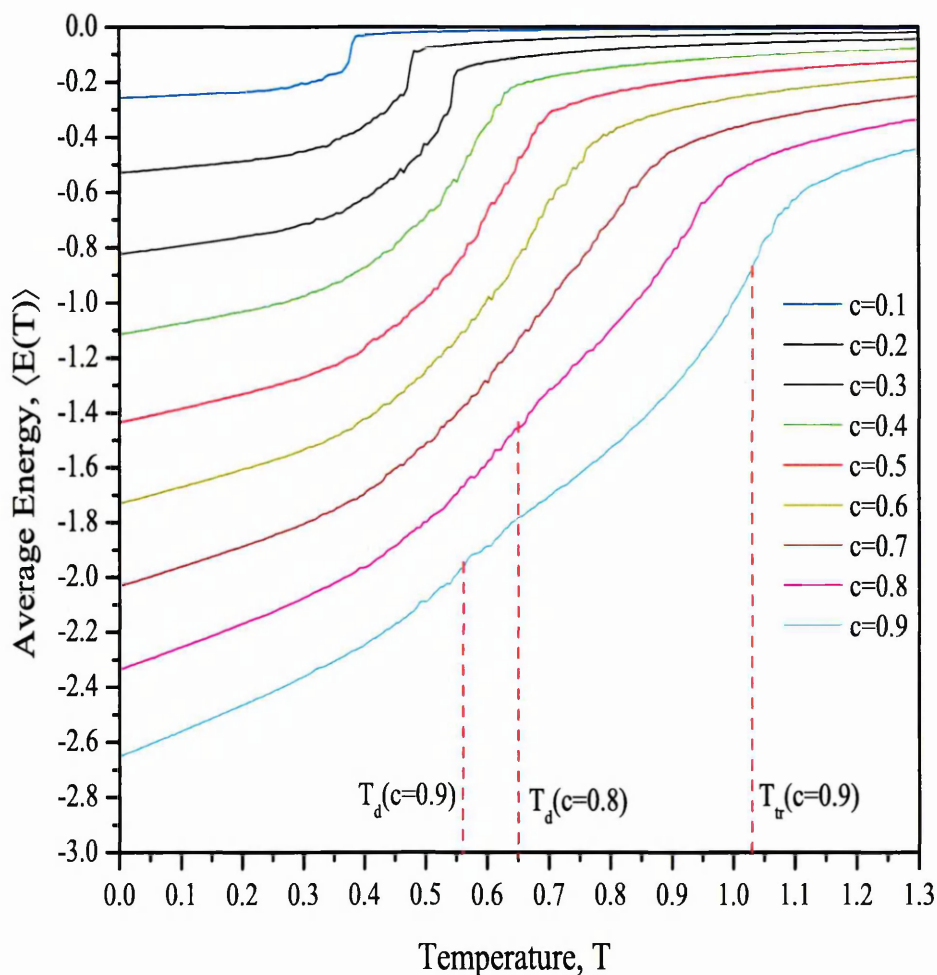


Figure 5.39: Average Energy dependence on temperature, $\langle E(T) \rangle$ for the system with $\varepsilon = 0.00$.

concentration c	Temperature $T_{tr}(c)$	Temperature $T_d(c)$
0.0	0.00 ± 0.01	N/A
0.1	0.38 ± 0.01	0.38 ± 0.01
0.2	0.48 ± 0.01	0.48 ± 0.01
0.3	0.54 ± 0.01	0.54 ± 0.01
0.4	0.59 ± 0.01	0.59 ± 0.01
0.5	0.64 ± 0.01	0.64 ± 0.01
0.6	0.67 ± 0.01	0.65 ± 0.02
0.7	0.79 ± 0.01	0.74 ± 0.05
0.8	0.92 ± 0.01	0.65 ± 0.01
0.9	1.04 ± 0.01	0.56 ± 0.01
1.0	1.15 ± 0.01	N/A

Table 5.16: Table of Temperatures $T_{tr}(c)$ and $T_d(c)$. $T_{tr}(c)$ were derived as a point where the tangent of $\langle E(T) \rangle$ is the steepest.

On the bottom curve ($c = 0.9$) we observe two discontinuities in the gradient of $\langle E(T) \rangle$ at temperatures $T_{tr}(c)$ and $T_d(c)$. With a decrease in the concentration, $T_{tr}(c)$ and $T_d(c)$ move closer and eventually meet at $c \approx 0.7$. As in the previous systems, the discontinuity which occurs at $T_d(c)$ eventually fades with decreasing concentration, vanishing at $c \approx 0.7$ as the temperatures of both deviations move closer. In addition, the sharpness of the deviation which occurs at $T_{tr}(c)$ increases as the concentration decreases. As the temperature falls below $T_d(c)$, in the cases of $c \gtrsim 0.7$, the curve gradually returns to its original slope (i.e. that which it displayed at the highest temperatures). In the case of $c \lesssim 0.7$, the original slope is seen again after the temperature passes below $T_{tr}(c)$. The table of all of the temperatures described above is shown in Table 5.13.

From the Table it is clear that $T_{tr}(c)$ decreases monotonically with decrease in concentration c . Starting from $c = 0.9$, as the concentration decreases the entire curve moves up the energy axis. Also, the shape of the curve changes, being fairly steep at $c = 0.9$ and becoming virtually horizontal as $c \rightarrow 0$. At temperatures above $T_{tr}(c)$, all curves approach a single point ($\langle E \rangle, T \rightarrow \infty$).

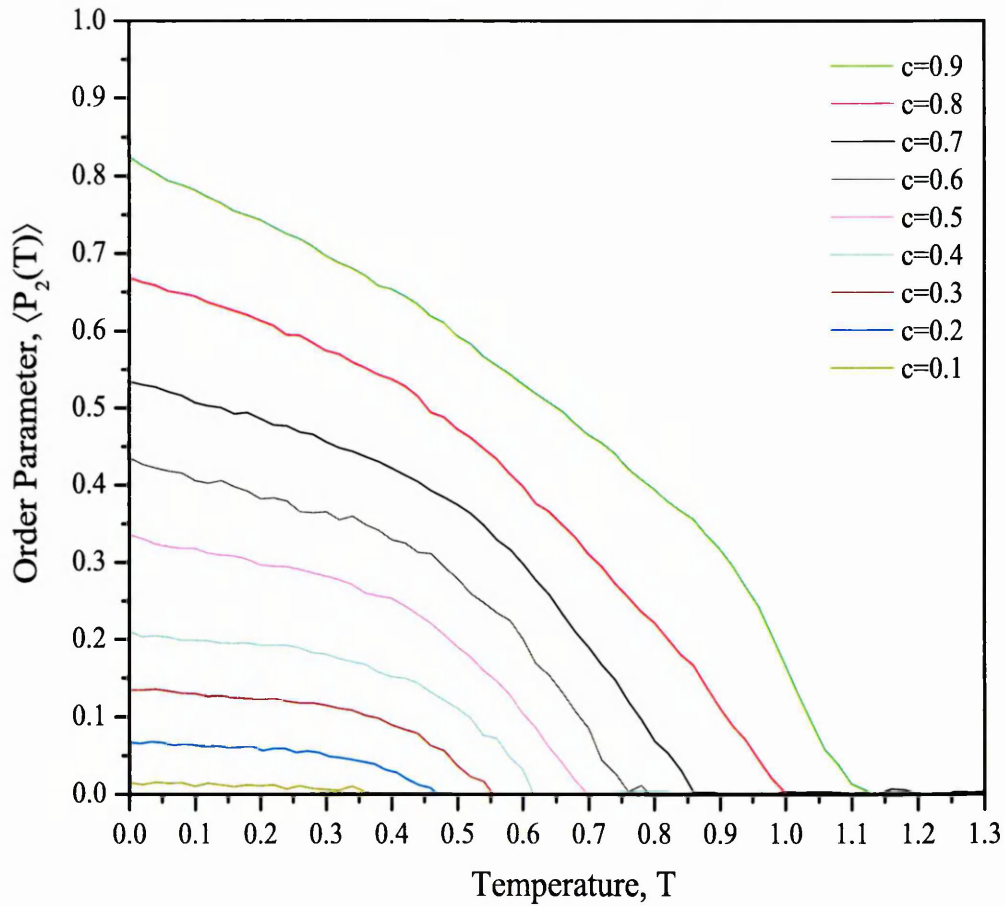


Figure 5.40: Second rank orientational order parameter. Dependence on temperature. Different curves represent different concentration c in the binary mixture. $\varepsilon=0.00$.

Figure 5.40 shows the dependence of the order parameter on temperature ($\langle P_2(T) \rangle$) for the binary mixture with coupling constant $\varepsilon = 0.00$. From the Figure we see that the system undergoes an isotropic-nematic transition at temperature $T_{tr}(c)$, which varies with concentration. From being approximately equal to zero at high temperatures, the function increases rapidly at $T_{tr}(c)$, approaching the value of the order parameter 0.5 as the temperature approaches zero (for $c = 0.5$). For other concentrations, $\langle P_2(T) \rangle$ reaches different values as $T \rightarrow 0.0$. At $c = 0.0$ the value of the order parameter necessarily remains at zero throughout the entire temperature region. As the concentration increases, the value of $\langle P_2(T) \rangle$ increases monotonically and reaches 1 as $c \rightarrow 1.0$ for $T \rightarrow 0.0$. No discontinuities in the curves are observed at temperatures lower than $T_{tr}(c)$. As the temperature falls

concentration c	Temperature $T_{tr}(c)$
0.0	0.00 ± 0.05
0.1	0.40 ± 0.05
0.2	0.48 ± 0.05
0.3	0.55 ± 0.05
0.4	0.62 ± 0.05
0.5	0.70 ± 0.05
0.6	0.79 ± 0.05
0.7	0.86 ± 0.05
0.8	1.00 ± 0.05
0.9	1.11 ± 0.05
1.0	1.18 ± 0.05

Table 5.17: Table of Temperatures $T_{tr}(c)$ based on results obtained from $\langle P_2 \rangle$.

below $T_{tr}(c)$, the order parameter starts to increase rapidly and levels off at non-zero value. The temperature of the transition decreases as the concentration c decreases (Fig.5.40). The value of $T_{tr}(c = 1.0)$ is the same as in all of the previous systems, 1.18, and so when the concentration $c \rightarrow 0.0$, the transition temperature of the mixture approaches zero and vanishes at $c = 0.0$. Table 5.17 shows the value of $T_{tr}(c)$ for the set of concentrations. These values are in good agreement with the values of $T_{tr}(c)$ obtained from the energy measurements. For the binary system with $\varepsilon = 0.00$, the dependence of $T_{tr}(c)$ on concentration is the only characteristic observed from the order parameter function.

The next observable to be considered is the radial distribution function ($g^{AB}(r)$). In Figure 5.41 we present $g^{AB}(r = 1, T)$ for the full set of concentrations. At concentration $c = 0.9$, $g^{AB}(r = 1, T)$ decreases slowly as the temperature decreases. Then, at $T_{tr}(c) \approx 1.07$, the slope changes. With further decrease in temperature, $g^{AB}(r = 1, T)$ decreases almost linearly until at $T_d(c) \approx 0.58$ it decreases sharply, levelling off to a constant value at $T \lesssim 0.25$. At $c = 0.8$, the value of $g^{AB}(r = 1, T)$ decreases slowly as the temperature decreases until it reaches $T_{tr}(c) \approx 0.93$, when it starts to decline more steeply. The slope remains fairly steady as the temperature continues to fall; then, at $T_d(c) \approx 0.68$ it suddenly becomes steeper. Subsequently, the function levels off to its minimum value as $T \rightarrow 0$. From the Figure it is clear that

$g^{AB}(r=1, T)$ exhibits similar behaviour at other concentrations. As concentration decreases, the temperatures $T_{tr}(c)$ and $T_d(c)$ move closer, and as they do so the slope in the region between them becomes steeper until at $c \approx 0.6$, they meet. At all concentrations lower than $c \approx 0.6$, there is only one discontinuity present on the $g^{AB}(r=1, T)$ function; that at $T_{tr}(c)$. When the concentration of the system decreases, this discontinuity becomes sharper. The values of all the temperatures studied are presented in Table 5.18. The results are consistent with the data obtained from the energy (Table 5.16) and order parameter (Table 5.17) calculations.

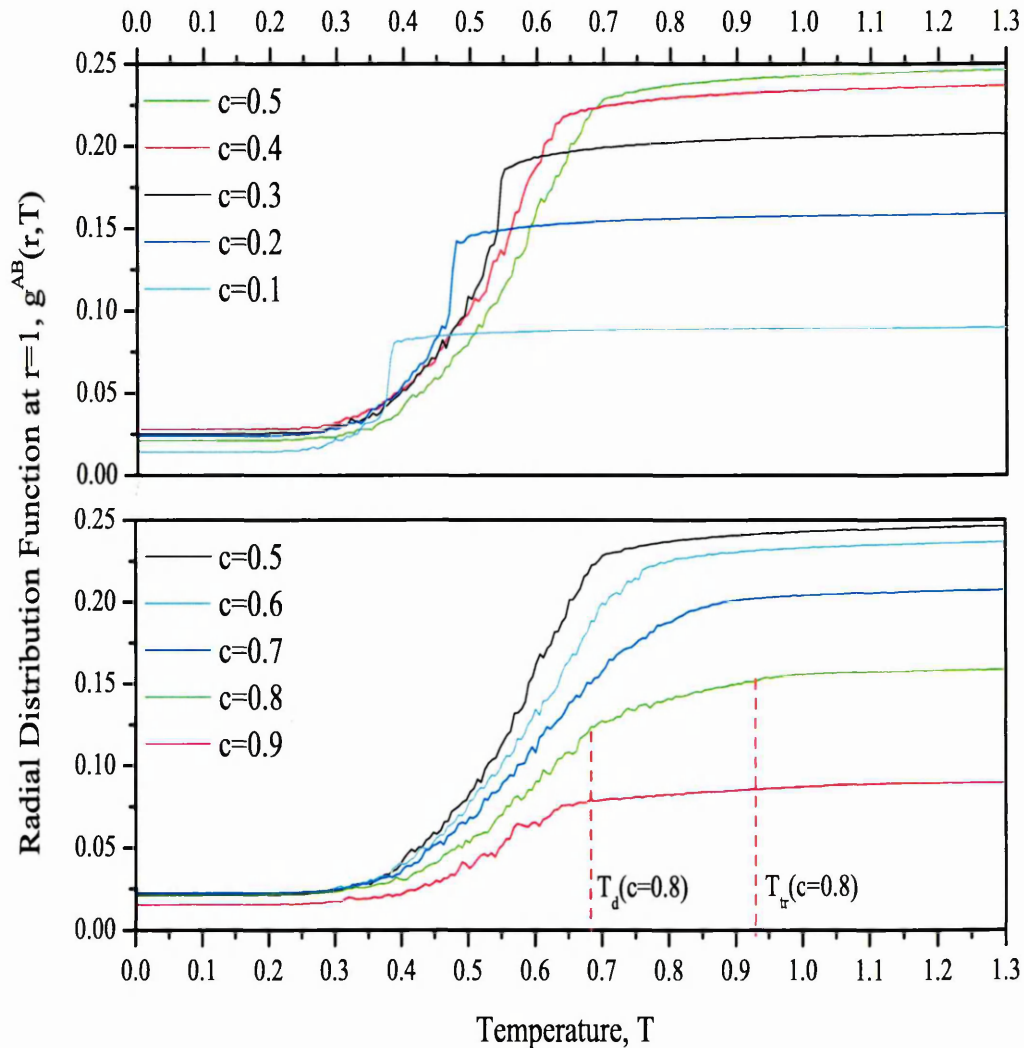


Figure 5.41: Short range radial distribution function $g^{AB}(r)$ for $\varepsilon = 0.0$ system.

concentration c	Temperature $T_{tr}(c)$	Temperature $T_{tr}(c)$
0.0	N/A	N/A
0.1	0.40 ± 0.02	0.39 ± 0.02
0.2	0.50 ± 0.02	0.49 ± 0.02
0.3	0.56 ± 0.02	0.56 ± 0.02
0.4	0.61 ± 0.02	0.61 ± 0.02
0.5	0.67 ± 0.02	0.67 ± 0.02
0.6	0.73 ± 0.04	0.73 ± 0.04
0.7	0.83 ± 0.02	0.78 ± 0.05
0.8	0.93 ± 0.02	0.68 ± 0.02
0.9	1.07 ± 0.02	0.58 ± 0.02
1.0	N/A	N/A

Table 5.18: Table of Temperatures based on results obtained from $g^{AB}(r = 1, T)$.

Let us now look at the phase diagram obtained from the results just discussed (Fig. 6.31). Two regions which were present on the phase diagrams for the three previous systems (those with $\varepsilon = 0.45$, $\varepsilon = 0.30$ and $\varepsilon = 0.10$) do not appear on the phase diagram for the system with $\varepsilon = 0.00$. These are nematic-nematic coexistence region (marked in blue) and the small nematic region on the left of the diagram (red). It has already been observed, in analysing earlier phase diagrams, that these regions diminished in size as the coupling constant was decreased; the system with $\varepsilon = 0.00$ cannot exhibit these phases at all. The size of the isotropic phase region did not change significantly from that for the previous three systems.

Let us consider the boundaries between the various phases, starting with the boundary which separates the isotropic from the demixed isotropic-nematic coexistence envelope. The slope of the boundary in the region of concentrations $0.1 \lesssim c \leq 1.0$ shows hardly any change. Depending on the concentration, with a reduction in temperature the system can change from the isotropic phase to the nematic phase (on the interval $0.7 \lesssim c \lesssim 1.0$) or to the phase of isotropic-nematic coexistence (for all other concentrations).

In all other ways, the behaviour of the system with $\varepsilon = 0.00$ is similar to that of the systems with $\varepsilon = 0.45$, $\varepsilon = 0.30$ and $\varepsilon = 0.10$. Overall, the behaviour of the system with $\varepsilon = 0.00$ is consistent with the behaviour of the systems with $\varepsilon = 0.90$ to $\varepsilon = 0.60$. Discussion of the results presented above will follow in Section 5.4.

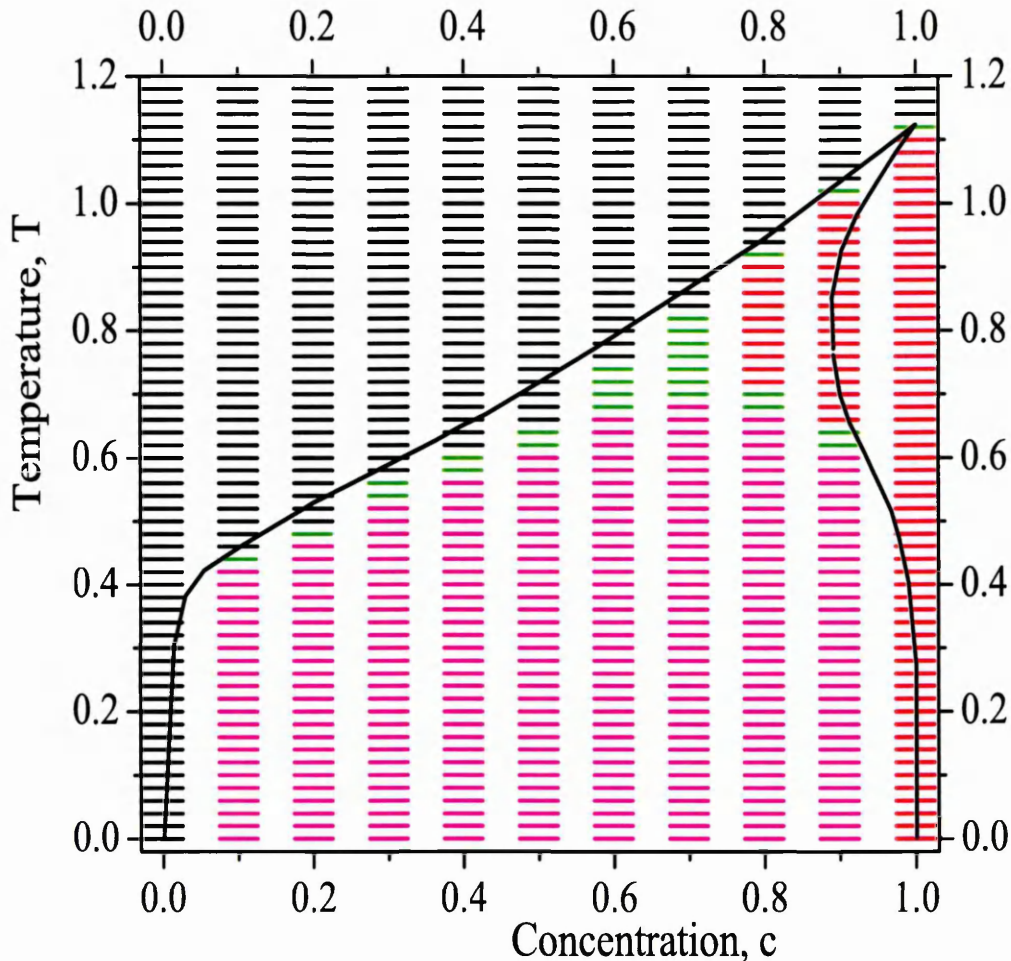


Figure 5.42: Phase diagram. $\varepsilon = 0.0$. Solid lines represent theoretical calculations of the phase boundaries for this system [177] (see also Figure 6.31 and Section 6.5.1).

5.2 Phase Diagram Visualizer

Having presented a series of $T - c$ phase diagrams from $NcVT$ Ensemble results, and realizing the amount of data to be reviewed by the reader, we have constructed an interactive computer application that allows one to view the changing form of the phase diagram dynamically, as ε changes (Appendix A). To do this, the data presented in this chapter were used to construct phase diagrams for values of $\varepsilon = 0.0, 0.1, 0.3, 0.45, 0.6, 0.9$. Data for other values of ε were then generated using an animation morphing technique. The horizontal slide bar at the bottom of the viewing

panel provides for a smooth change of ε . Tick boxes on the bottom right allow the user to toggle various phase regions in and out of invisible mode. The button " T/T^* ", located on the bottom left, provides two scalings for the temperature and T,c coordinates on the bottom right reflect the position of the pointer on the phase diagram. The application allows the viewer to concentrate on a particular area of study without being distracted by changing focus from one figure to another. The only computer requirement for the application is an installed browser which includes a Flash plug-in or Flash viewer application. Most modern PCs have this installed.

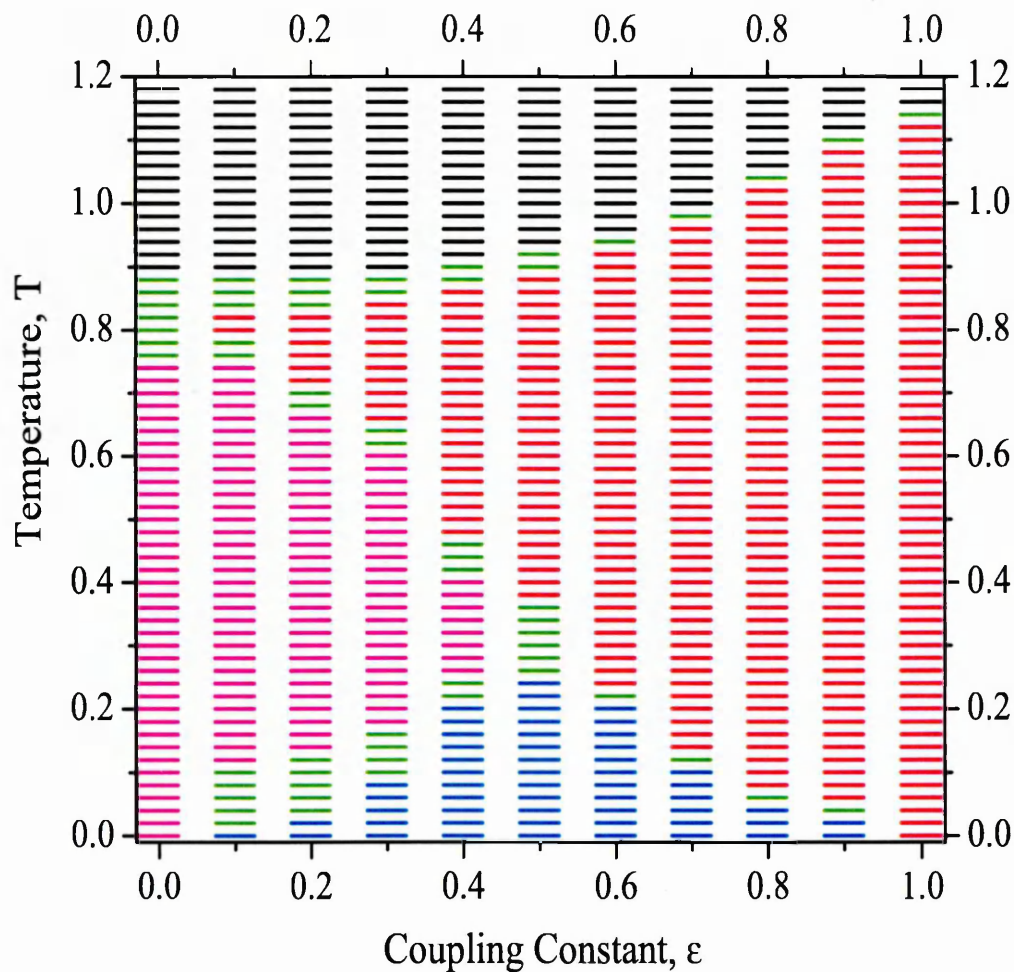
5.3 Results for systems with varying c

In Section 5.1 we presented the results for the binary systems in the form of phase diagrams showing concentration versus temperature (Figures 5.9, 5.15, 5.27, 5.32, 5.38 and 6.31). From these Figures we have seen that phase boundaries are altered as the coupling constant ε changes. We now present the corresponding phase diagrams viewed from the alternative constant concentration perspective.

5.3.1 System with $c = 0.7$.

In the system with $c = 0.7$, the more anisotropic particles (A) are predominant (Fig. 5.43). The isotropic-nematic transition temperature in such a system decreases monotonically as ε decreases, the isotropic phase occupying the top left corner of the diagram. $T_{tr}(c)$ reaches $T \approx 0.82$ when the value of the coupling constant reaches zero.

The boundary which separates mixed phases from demixed ones increases its T value as ε decreases and levels off to $T \approx 0.68$ as $\varepsilon \rightarrow 0$. However, since this value is close to the isotropic-nematic boundary in this region of ε , it is difficult to determine whether these two boundaries meet (green points). On the left hand side of the diagram ($\varepsilon \lesssim 0.45$), there is another boundary separating the two demixed phases, the isotropic-nematic coexistence and the nematic-nematic coexistence. This boundary is highest in the centre of the diagram and decreases monotonically as ε decreases, eventually vanishing at $\varepsilon = 0.0$.

Figure 5.43: Phase diagram. $c = 0.7$

5.3.2 System with $c = 0.5$.

In the next system ($c = 0.5$), there are equal numbers of particles A and particles B (Fig. 5.44). The behaviour of the isotropic-nematic transition temperature in this system is similar to the that in previous system ($c = 0.7$). The temperature decreases monotonically as ε decreases, the isotropic phase again residing in the top left corner. However, the region occupied by the isotropic phase is larger than that in the system with $c = 0.7$. This is because the boundary levels off to the lower value $T \approx 0.64$ as the value of the coupling constant reaches zero. The isotropic phase expands at the expense of phases which are beneath it. As a result, the nematic

region phase decreases and the isotropic-nematic boundary line joins with another line at $\varepsilon \approx 0.45$; this second line is the boundary which separates mixed phases from demixed ones. Both boundaries move closer to a third line, which separates isotropic-nematic from nematic-nematic coexistence and which has not changed from the previous case.

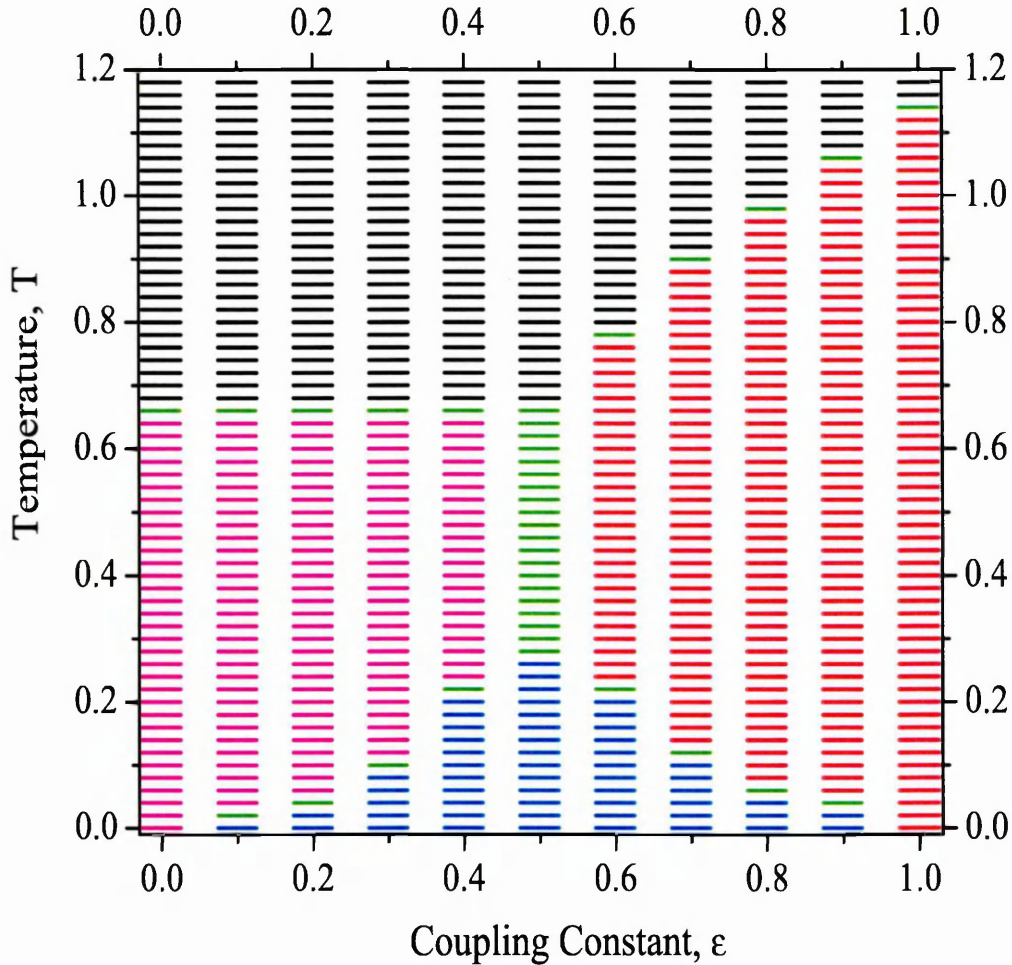
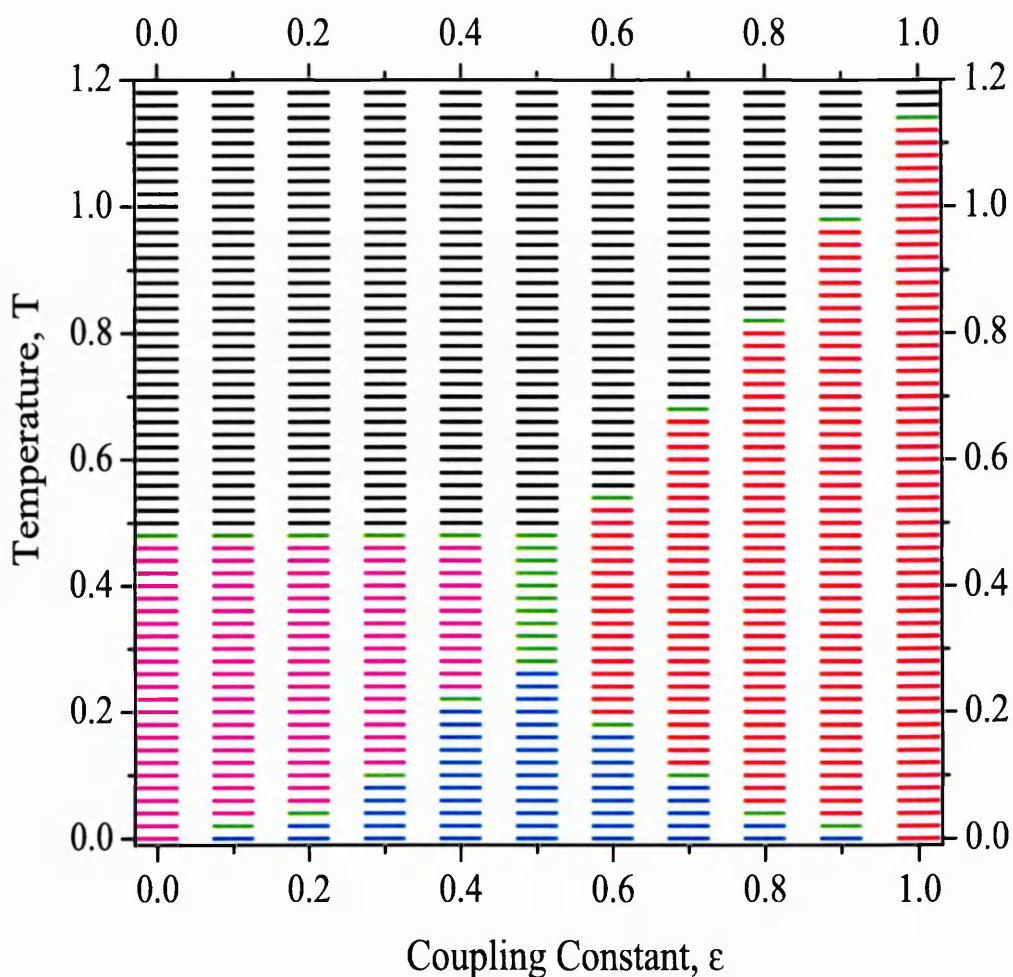


Figure 5.44: Phase diagram. $c = 0.5$

5.3.3 System with $c = 0.2$

In the next system ($c = 0.2$) particles B outnumber particles A (Fig. 5.45). The behaviour of the isotropic-nematic transition temperature in this system repeats that of the previous one. The temperature decreases monotonically as ε decreases

and approaches $T \approx 0.48$ as $\varepsilon \rightarrow 0.0$. The isotropic phase now occupies even more space on the phase diagram and has the largest area on it. The isotropic-nematic boundary line joins with another line at $\varepsilon \approx 0.45$. The boundary which separates mixed phases from demixed ones has not changed. Both isotropic-nematic and mixed-demixed boundaries have moved closer to the third line which separates isotropic-nematic from nematic-nematic coexistence. As concentration changes, the isotropic phase grows depressing other phases. The boundary which separates mixed phases from demixed is not influenced to any great extent by the isotropic-nematic boundary in the region $\varepsilon \gtrsim 0.45$. The isotropic-nematic boundary also has no effect on the third line.

Figure 5.45: Phase diagram. $c = 0.2$

5.4 Interpretation and Discussion

In nature, most processes happen, and their observables are measured, at constant temperature and pressure averaged over a period of time. However, in any statistical ensemble such as the canonical ensemble, it must be clearly understood what the measured observables represent and what is the thermodynamic potential of the given ensemble.

$$\mathcal{F} = U - TS \quad (5.1)$$

The thermodynamic potential of the NcVT - Ensemble (canonical) is the Helmholtz free energy \mathcal{F} (Equation 5.1). Thus, statistics for all the values of this ensemble must be taken in the vicinity of the minimum of the Helmholtz free energy, known as the equilibrium state of the system. To obtain the free energy-like function we have used energy probability histograms $\mathcal{P}(E)$, calculated by the method mentioned in Chapter 4. These same energy histograms, averaged in the NcVT-Ensemble, give the average values of the energy in the system, the results of which were presented in Section 5.1. The distribution of the maximum in $\mathcal{P}(E)$ is known to be Gaussian [186] if the system is in equilibrium and not close to any phase transition.

We will show that the temperature and the nature of the transition can be related to the deviation of the $\langle E(T) \rangle$ curves, presented in Section 5.1, which correlate with the positions of the corresponding maxima of $\mathcal{P}(E)$. We will compare and discuss these in the light of other results from Section 5.1 such as $\langle P_2(T) \rangle$, $g(r)$ etc.

We start this section, therefore, with an overview of the thermal dependence of the average energy of the system. Let us look at some of the energy histograms for the system with various coupling constants and concentrations. One can deduce from the interaction potentials (Section 4.2, Equation 4.6) that a reduction of temperature in the system will reduce the position of the maximum of the $\mathcal{P}(E)$ function from a higher value of energy corresponding to the disordered (isotropic) phase to a lower value in the ordered (nematic) phase. From the average energy graphs (Figures 5.1, 5.10, 5.16, 5.28, 5.33, 5.39) it is clear that the reduction of temperature moves the maximum of the energy distribution to lower values. The value of the average energy represents the position of the peak of $\mathcal{P}(E)$ when far from the transition. Equation

5.1 shows that if temperature is reduced, then so is the effect of entropy. This means that the free energy minimum moves to a lower energy value, closer to the potential energy value.

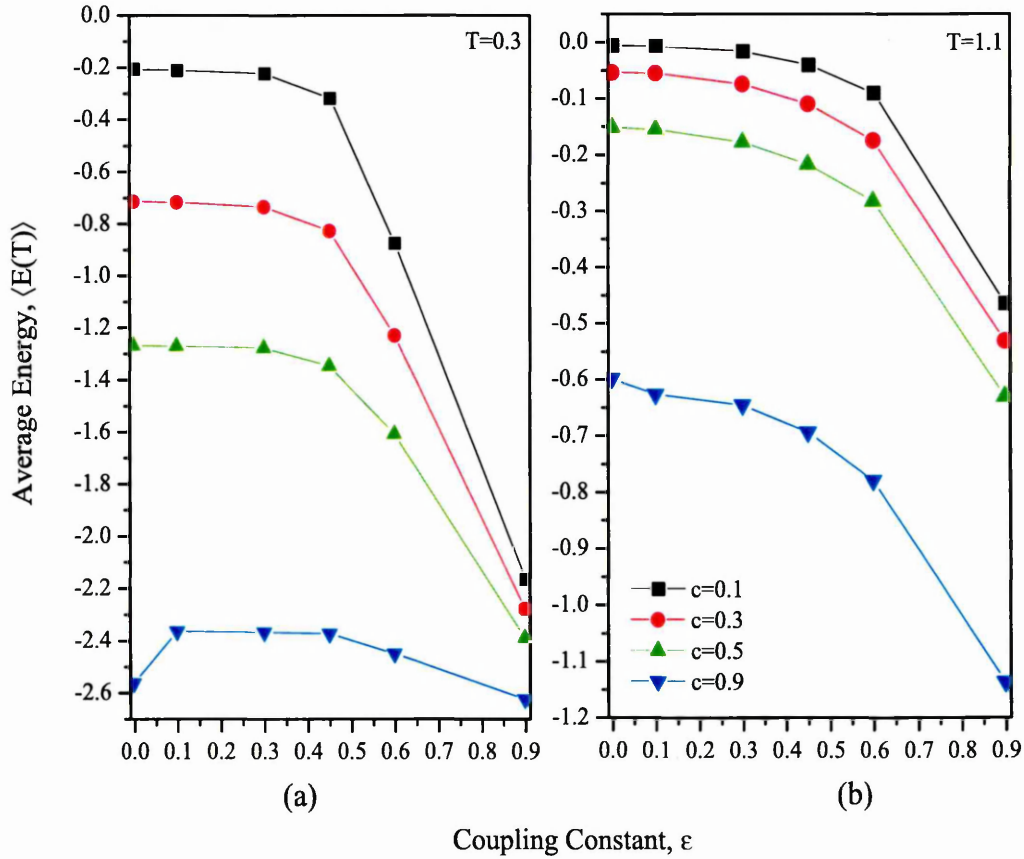


Figure 5.46: Energy dependence on ϵ for $T=0.3$ and $T=1.1$. Dependencies are shown for concentrations $c\{0.1;0.3;0.5;0.9\}$.

On the other hand, the results also show that reduction of the coupling constant moves the maximum to a higher energy value for the same values of T and c . In Figure 5.46, as an example, we assemble a few $\langle E(\epsilon) \rangle$ graphs taken at different T and c .

This behaviour can be explained by the form of the interaction potential (Equation 4.10) and its contribution to the Boltzmann factor in Equation 4.2. From the analytical view of the interaction potential we can deduce that the increase in ϵ moves the energy to a lower value.

Moreover, for the unlike interactions the contribution of the temperature and the coupling constant in the exponent of the Boltzmann factor is $\sim \varepsilon T^{-1}$, which is effectively one constant. This means that if all interactions are linearly dependent on ε , then reducing ε has the same effect as increasing T .

The movement of the position of the $\mathcal{P}(E)$ maximum to a lower energy value is also seen when the concentration of the mixture c is increased, at constant T and ε (Figure 5.47, and Figures 5.1, 5.10, 5.16, 5.28, 5.33, 5.39). The higher the concentration of more anisotropic particles A in the system, the more frequent the coupling of particles with coefficient 1 (rather than ε or ε^2). Thus, the negative contribution of the interaction potential to the total energy is more significant, and it is this which makes the energy peak move to the region of lower energy values. In Figure 5.47 we deliberately selected such T and ε as would ensure that the system exhibited the same phase at all values of c . In a case such as this, the dependence of the position of the $\langle \mathcal{P}(E) \rangle$ maximum on concentration appears to be linear; more generally, it is proportional to $\sim -\frac{c\varepsilon^2}{T}$ in such regions.

However, the dependence of the average energy value $\langle E(T) \rangle$ on temperature T cannot be described analytically for all values of the ‘coordinates’. As we showed in Section 5.1, the energy function displays a number of discontinuities in its gradient. Several factors play significant roles in governing the behaviour of $\langle E(T) \rangle$. Firstly, as discussed above, the coupling constant ε contributes to the total energy as the direct coefficient in the interaction potential (Eq. 4.6).

Secondly, the value of the second term in Equation 4.6, namely $P_2(\cos \phi_{ij})$ is also related to the free energy through the entropy in Equation 5.1. ε influences acceptance of the moves, and this leads to changes in the orientations of particles, with a consequent change the value of the $P_2(\cos \phi_{ij})$ term in the interaction potential. Also, however, the ordering of the particles decreases entropy. All of this affects the free energy minimum. Usually there is only one minimum of free energy for each value of the temperature. But sometimes, in very narrow regions of T , the energy changes abruptly, owing to the value of the free energy being equal for two phases of different symmetry - disordered and ordered orientationally. This is the transition temperature, $T_{tr}(c)$. The transition temperature also changes with change of ε at constant c (Figures 5.43-5.45).

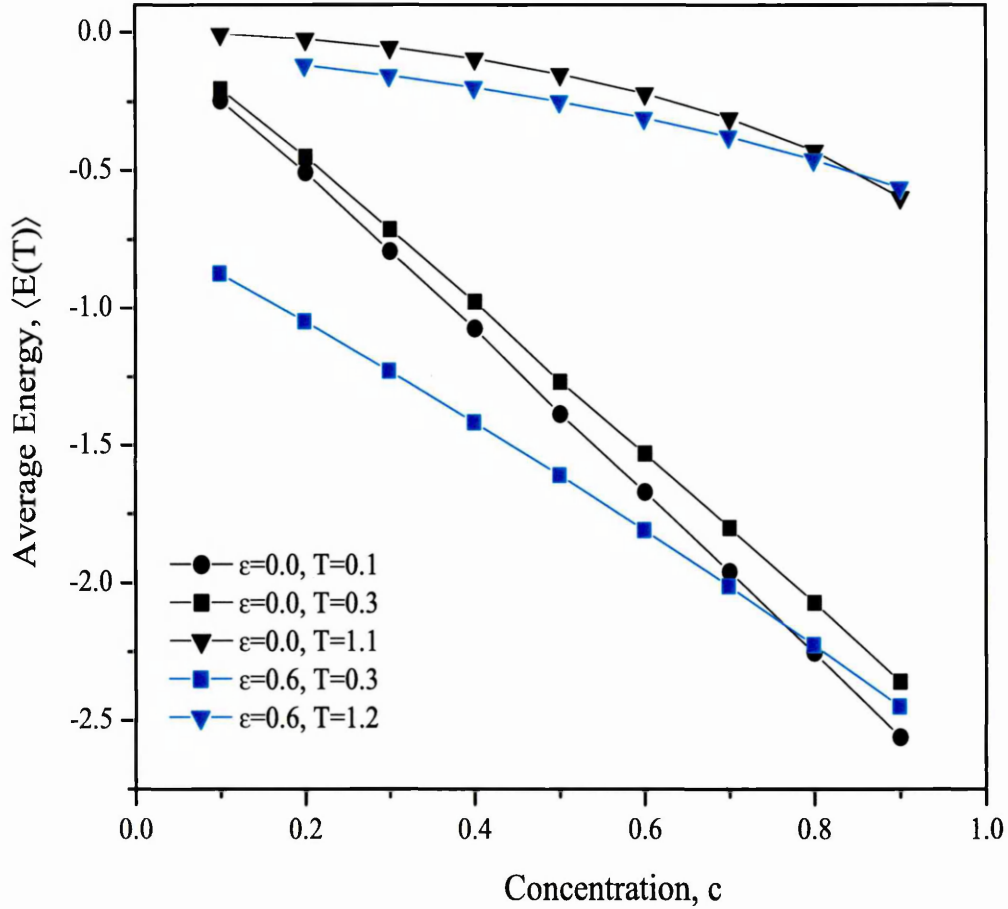


Figure 5.47: Energy dependence on c for various $T\{0.1; 0.3; 1.1; 1.2\}$ and $\epsilon\{0.0; 0.6\}$.

Thirdly, the system consists of two types of particle which are allowed to move within the simulation box. The long and the short range distribution functions of the system, which are dictated by the interaction potential, indicate entropic changes to the free energy. We can illustrate this by a simple example. The local energy for some interactions depends linearly on ϵ (A-B interaction), for some on ϵ^2 (B-B interaction), or for others does not depend on ϵ at all, as is the case for A-A interactions. Therefore, the total energy of the system is different in the cases of homogeneous and demixed configurations. Thus the system's tendency to phase separate increases as the U term in Equation 5.1 becomes more significant. As is shown in Figures 5.10, 5.16, 5.28, 5.33, 5.39, at temperatures above and below $T_d(c)$ the system exhibits homogeneous and demixed configurations respectively. In these two regimes the slope of $\langle E(T) \rangle$ is different.

Fourthly, at certain values of ε and c we observed competition (or co-operation) of other effects - the nematic-isotropic transition and the demixing. We will presently argue that this phenomenon is due to nematic-order-driven phase separation. The results for $\langle P_2(T) \rangle$ and $g^{AB}(r)$ show that for certain ε and c , the system undergoes the nematic-isotropic transition at the same temperature as it demixes ($T_{tr}(c) = T_d(c)$). This may result in the system moving from the homogeneous isotropic phase to the coexistence either of two nematic phases or of the nematic and isotropic phases, depending on the concentration c .

When the system has moved into the coexistence region of demixed isotropic and nematic phases, the isotropic part undergoes the I-N transition at $T'_{tr}(c)$ when the temperature is decreased further. The $g^{AB}(r)$ data reveal that the coexisting isotropic and nematic phases consist mostly of components (B) and (A) respectively. This can be treated as a perturbation of the usual isotropic-nematic transition for a single component system of component B. The perturbation arises from the additional factor that the preferred orientation of the particles in the B-rich phase is influenced by the orientation at the interface separating it from the A-rich phase. The results from $P_2^A(T)$ and $P_2^B(T)$ show that when there is a high concentration of B particles, the transition temperature $T'_{tr}(c)$ approaches that of the single component system analogue.

As a result of the processes described above, the system exhibits six 'transitions' from one phase region to another. These are:

$$I \xrightarrow{\textcircled{1}} N \xrightarrow{\textcircled{3}} N + N$$

$$I \xrightarrow{\textcircled{1}} N \xrightarrow{\textcircled{5}} I + N \xrightarrow{\textcircled{4}} N + N$$

$$I \xrightarrow{\textcircled{2}} I + N \xrightarrow{\textcircled{4}} N + N$$

$$I \xrightarrow{\textcircled{6}} N + N$$

The arrows represent decreasing temperature. As we have shown in this Chapter, all sharp changes in the energy of the system occur at one of the three temperatures $T_{tr}(c)$, $T_d(c)$ and $T'_{tr}(c)$. We turn now to consideration of the behaviour of the system in the vicinity of these temperatures; the discussion will cover the isotropic-nematic transition of the homogeneous system ($\textcircled{1}$); the two-component demixing ($\textcircled{3}$ $\textcircled{5}$); the nematic order-driven demixing ($\textcircled{2}$ $\textcircled{6}$); and the isotropic-nematic transition of particles B ($\textcircled{4}$).

5.4.1 The isotropic-nematic transition of the homogeneous system at $T_{tr}(c)$.

As the temperature of the isotropic homogeneous system decreases, the first temperature of discontinuity which occurs in the system is always the isotropic-nematic transition temperature $T_{tr}(c)$. This transition can be seen throughout the entire range of ε . In systems with $\varepsilon > 0.6$ it appears as a single first-order transition, not coupled with any other processes such as demixing, throughout the entire concentration range; in systems with $\varepsilon \lesssim 0.6$, it occurs at high concentrations. Thus we begin with discussion of such homogeneous transitions (①). Let us look at the average energy dependence on the temperature in the vicinity of $T_{tr}(c)$ (①). The slopes of the $\langle E(T) \rangle$ curves below ($T < T_{tr}(c)$) and above ($T > T_{tr}(c)$) the transition are different. The results of the order parameter for all systems investigated relate this discontinuity temperature in the gradient of $\langle E(T) \rangle$ to the change in the orientational order $P_2(T)$. At $T_{tr}(c)$ the system moves from the isotropic phase (spherical symmetry) to the nematic phase (cylindrical symmetry) as the temperature falls. The radial distribution function does not show any changes at long range, but minor restructuring occurs at short range as $T_{tr}(c)$ is reached (Figures 5.7, 5.13, 5.23, 5.31, 5.37, 5.41). In Section 5.4.5 we consider further the short range structural reorganisation and its influence on $T_{tr}(c)$. All of this indicates a first-order transition. Thus, according to [7,8,186] we expect to see two minima on the energy histograms $\mathcal{P}(E)$.

For this purpose we will discuss two concentrations representing two systems with very different behaviour, namely $c = 1.0$ and $c = 0.5$. Initially, we will look at the single component system in order to exclude any effects due to the mixture and, thus, be able to examine the behaviour of $\mathcal{P}(E)$ due to the transition alone. We will then consider the system with $\varepsilon = 0.8$ at $c = 0.5$ and discuss how the introduction of another anisotropic component affects the shape of the distribution.

Let us look first at $\mathcal{P}(E)$ for the single component system ($c = 1.0$) in the vicinity of the isotropic-nematic transition (Figure 5.48). The distributions $T = 1.123$ and $T = 1.126$ were measured from long runs ($\tau = 3,000,000$) in the vicinity of the isotropic-nematic transition. The rest were calculated using the histogram reweighting technique [175,183] to obtain $\mathcal{P}(E)$ at temperature $T = 1.1244$ (see Section 4.4.4). At the highest temperature in the Figure, which is some distance from the

transition, the distribution of $\mathcal{P}(E)$ seems to be Gaussian. In this case the projection of the peak on the energy axis corresponds to the value $\langle E(T) \rangle$. As the temperature decreases, the shape of $\langle \mathcal{P}(E) \rangle_{NCVT}$ deviates from its Gaussian form and the average energy value is lower compared to the projection of the peak-point of $\langle \mathcal{P}(E) \rangle_{NCVT}$ on the E-axis (Figure 5.48). As a result, we observe a dramatic decrease in the $\langle E(T) \rangle$ curve in the vicinity of $T_{tr}(c)$ as the temperature decreases.

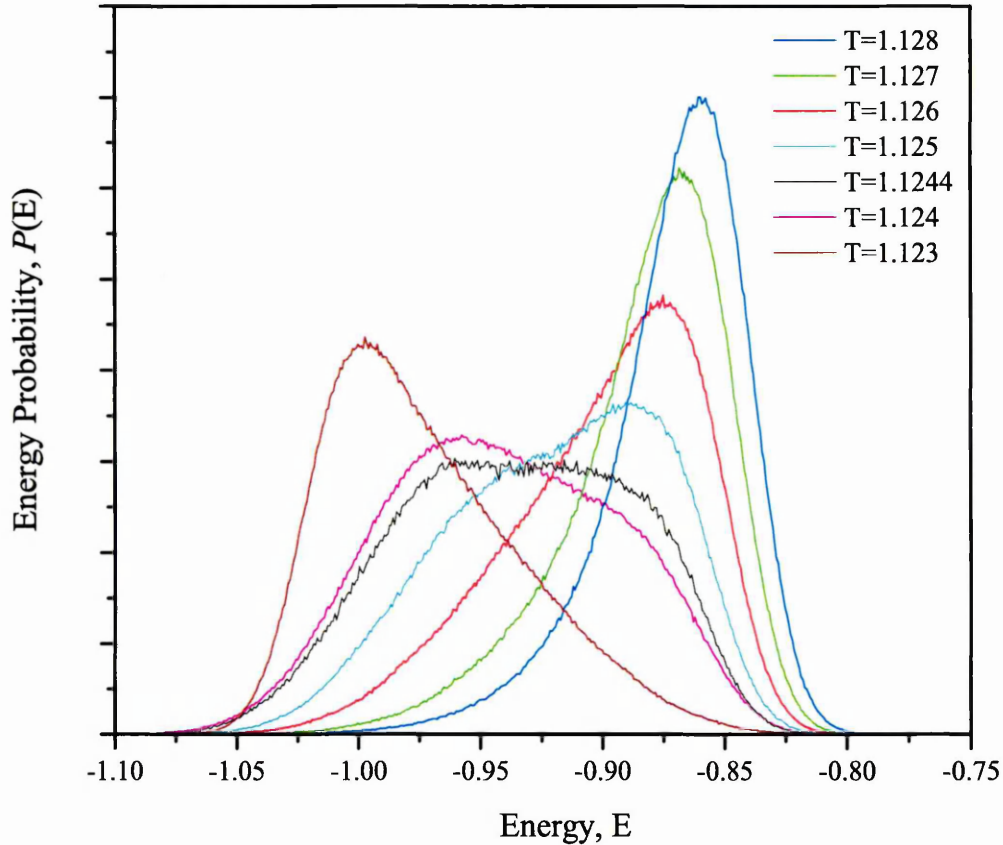


Figure 5.48: Energy histograms taken at a set of temperatures close to I-N transition. Single component system, size 24^3 .

The distortion of the distribution from the Gaussian is caused by the development of another maximum. As we look at the distribution $\langle \mathcal{P}(E) \rangle_{NCVT}$ we find that the decrease in E projected from the peak of the distribution slows down with decrease in temperature. As this peak slows down, a second peak emerges with a lower energy value than that of the first. Then, the magnitude of both peaks changes quickly as

the temperature decreases. As the original peak diminishes, the new peak starts to move more quickly to lower values as the temperature decreases. However, as we see from Figures 5.1, 5.10, 5.16, 5.28, 5.33, 5.39, for most values of ε and c the second peak (that which correlates with $\langle E(T) \rangle$), continues to decrease relatively quickly with decrease in temperature, as the transition region is left.

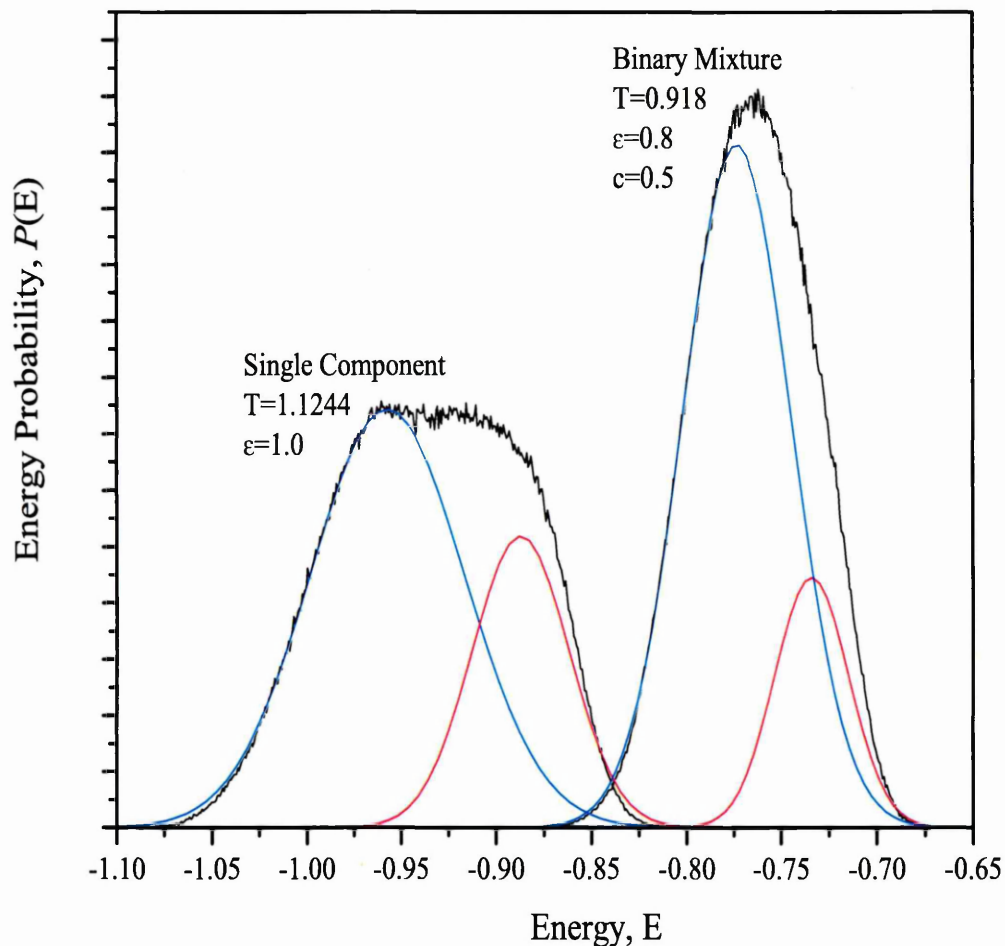


Figure 5.49: Energy histograms for mixture and single component system in the vicinity of I-N transition (black curves). Each histogram was fitted with two Gaussians that represent isotropic (red curves) and nematic (blue curves) phases.

The presence of two maxima in the system at $c = 1.0$ indicates a first-order transition. The results from Figures 5.1, 5.10, 5.16, 5.28, 5.33, 5.39 and previously acquired knowledge all indicate that this should also be the case for the binary mixture (i.e. $0.0 < c < 1.0$). In Figure 5.49 we present $\mathcal{P}(E)$ for both, $c = 1.0$ and

$c = 0.5$ (system with $\varepsilon = 0.8$). As can be seen from the Figure, the energy and the temperature at which both maxima are seen (transition temperature) are different in the case of $c = 1.0$ and $c = 0.5$. At $c = 1.0$ the shape of the distribution unambiguously suggests the presence of multiple maxima (black curve in Fig.5.49). Further analysis of the distribution allows resolution of two maxima, one for the isotropic phase with a higher energy value (red curve) and one for the nematic phase with a lower energy value (blue curve). At $c = 0.5$, while it is still possible to identify both maxima numerically, they are located closer to each other, so that their presence is not obvious to the casual observer.

Owing to the lower ε in the system with $c = 0.5$, the entire picture shifts to less negative energy values. This rescales the energy values of the distributions and, hence, the distance between the peaks. However, even after this rescaling the distance between the peaks in the system with $c = 0.5$ is approximately half that found with $c = 1.0$. The average energy for the system with $c = 1.0$ is $\langle E(T)^{c=1.0} \rangle \approx -0.93$ and for that with $c = 0.5$, $\langle E(T)^{c=0.5} \rangle \approx -0.74$. In the case of a well mixed system the relation between these values is as follows:

$$\langle E(T)^{c=0.5} \rangle \approx \langle E(T)^{c=1.0} \rangle \cdot \varepsilon \approx -0.93 \cdot 0.8 \approx -0.74$$

In the case of a demixed system, the relation between these values reads as:

$$\langle E(T)^{c=0.5} \rangle \approx \frac{\langle E(T)^{c=1.0} \rangle \cdot \varepsilon^2}{2} + \frac{\langle E(T)^{c=1.0} \rangle}{2} + \mathcal{O}_{surface} \approx \frac{-0.93 \cdot (0.64+1)}{2} \approx -0.76$$

where $\mathcal{O}_{surface}$, the energy at the interface, is assumed negligible. From the radial distribution function we conclude that system should be well mixed in both of I-N transitions considered here, thus the rescaling coefficient should be 0.8. In fact, the energy differences between the two peaks of $\mathcal{P}(E, c = 1.0)$ and $\mathcal{P}(E, c = 0.5)$ are 0.08 and 0.03 respectively. Rescaling those suggests that the difference between the two peaks for $c = 0.5$ should be around 0.064, more than twice the measured value, 0.03. We found no evidence from the literature that the addition of a solvent to a mesogen would change the order of the phase transition; nor does previous knowledge of the phase transition point to such a conclusion. The presence of two peaks shows that the transition is still first order; however, it is becoming weaker. Thus the binary mixture should, perhaps, be viewed in terms of impurities and their effect on the strength of the transition.

5.4.2 Two component demixing at $T_d(c)$

Let us move now to another significant temperature, $T_d(c)$ - the temperature of separation of the two types of particle (③⑤). In Figures 5.1 and 5.10, the separation at $T_d(c)$ occurs throughout the entire range of concentrations c (see also phase diagrams, Figures 5.9, 5.15). However, as the coupling constant decreases ($\varepsilon < 0.6$), $T_d(c)$ and $T_{tr}(c)$ meet in a region of concentrations that is specific for each system with a different value of ε (Figures 5.16, 5.28, 5.33, 5.39). Thus, demixing, not induced by other processes, occurs only within a certain range of c . For example, in the system with $\varepsilon = 0.45$ it occurs at concentrations $c \gtrsim 0.6$ and $c \lesssim 0.04$ (Figure 5.16). Here we will concentrate on such processes (③⑤).

The results from the radial distribution function of the unlike particles show that, at temperatures below $T_{tr}(c)$ for the concentrations c and coupling constants ε described above, we observe a homogeneous phase (Figure 5.6). It is only at significantly low temperatures ($T_d(c)$) that the system undergoes demixing, separating into two phases. The order parameters for particles A and particles B, considered separately, both show that at the temperatures immediately below $T_{tr}(c)$ the homogeneous system exhibits a nematic phase. As the temperature reaches $T_d(c)$, the phase-separated system exists either as two coexisting nematic phases or as coexisting isotropic (particle B rich) and nematic (particle A rich) phases. The latter occurs only in systems for which the $T_{tr}(c)$ and $T_d(c)$ lines meet (i.e. those with $\varepsilon < 0.6$).

The results for the average energy dependencies on temperature for most values of ε show a change in the slope at $T_d(c)$ (systems with $\varepsilon = 0.6; 0.45; 0.3; 0.1; 0.0$ in Figures 5.10, 5.16, 5.28, 5.33, 5.39). From the appearance of the interaction potential of the binary mixture it is clear that the energy of the interaction between identical, more anisotropic, particles is more negative than that of unlike particles as the order parameter approaches 1.0. Thus the system separates particles A from particles B in order to maximize the number of these strong interactions. So, as the temperature in the system decreases, the entropy term yields to the potential energy in the system (Eq. 5.1) and the system starts to demix at $T_d(c)$. This results in a steeper change in $\langle E(T) \rangle$ at temperatures lower than $T_d(c)$.

When the difference in anisotropy of the particles is small (for example, the system with $\varepsilon = 0.9$), the average energy dependencies do not exhibit dramatic changes (Figure 5.1). However, the radial distribution function results do still show demixing at very low temperatures, of the order 0.02 (Table 5.3). As the difference in anisotropic coupling of the two components increases, the relevant potential energy-term becomes increasingly significant and, as various results show, the $T_d(c)$ temperature increases as ε decreases.

5.4.3 Cooperative ordering and demixing.

First let us explain the title of this section. In the case of the processes involved in this discussion, it is difficult to say which induces which. Let us consider the system at a temperature just above $T_{tr}(c)$ at any concentration and with any coupling constant within the region of nematic order-driven demixing. On the one hand, ε is low enough for the system to prefer the demixed configuration to the homogeneous one, but on the other, the P_2 -term in the interaction potential is close to zero. As soon as the order parameter of the system increases (at the isotropic-nematic transition) the system phase separates to a preferred configuration, in which a subset of the particles yield a significant P_2 -term thus the term ‘nematic order-driven demixing’ could be used. On the other hand, if demixing were not allowed, the transition temperature $T_{tr}(c)$ would decrease linearly with concentration c (Equation 5.2), and would, thus, occur at a much lower temperature than $T_{tr}(c)$. Therefore, we might just as appropriately have called the process ‘demixing induced isotropic-nematic transition’, since it is the free energy which ultimately drives all processes. However, a practical expedient has been adopted regarding terminology, leaving to the realm of metaphysics the question of who drives the free energy. Let us concentrate now on the particular characteristics of systems which undergo nematic induced demixing.

As $T_{tr}(c)$ meets $T_d(c)$, we observe a sharpening of the discontinuity in the gradient of $\langle E(T) \rangle$. At certain concentrations it is much sharper than that of the isotropic-nematic transition of the single component system. This might appear inconsistent with the observation made earlier, namely that the introduction of another component to the pure system weakens the strength of the transition; thus, the discontinuity in the gradient of $\langle E(T) \rangle$ ought to be less sharp, as was the case for all the

non-induced isotropic-nematic transitions discussed earlier. Instead, results from the energy histograms show a sharp jump in the peak of the distribution as the temperature passes $T_{tr}(c)$. From the fact that we were not able to find the temperature at which both peaks could be seen, we conclude that there is a large free energy barrier between them which does not allow the system to jump from one configuration to another within the lifetime of the simulation. This suggests the possibility of hysteresis effects, although, none were found in practice.

On the other hand, results for the $\langle P_2 \rangle$ data of the individual components show that as the system undergoes an induced transition at $T_{tr}(c)$, the order parameter of particles A increases sharply, whilst that of particles B increases less dramatically for some systems (Figures 5.20, 5.30) and remains close to zero for others (Figure 5.36). The radial distribution functions at all ranges for these systems show a dramatic change at $T_{tr}(c)$, which demonstrates the phase separation. We will discuss this issue further in Section 5.4.5. Let us just note that the reason for the sharpening of the discontinuity must lie in the co-operation of the two processes, orientational ordering and demixing.

5.4.4 Entering N+N coexistence at $T'_{tr}(c)$

The effect seen at the final transition temperature, $T'_{tr}(c)$, is present only in systems with $\varepsilon \lesssim 0.45$. It is observed in the $\langle E(T) \rangle$ dependencies and in the $\langle P_2(T) \rangle$ and $g^{AB}(r=1, T)$ functions and varies with both concentration c and coupling constant ε . This temperature relates to the transition of the B-rich isotropic phase to the B-rich nematic phase. In other words, $T'_{tr}(c)$ defines the boundary between isotropic-nematic coexistence and nematic-nematic coexistence regions on the phase diagram.

Let us look first at the thermal dependence of the average energy of the system $\langle E(T) \rangle$ (Figures 5.16, 5.28, 5.33). The striking evidence that $T'_{tr}(c)$ is practically independent of c indicates that the transition happens in what is virtually a single component subsystem. This must be so, because otherwise the influence of the component A would change with c . The thermal behaviour of the $g^{AB}(r \gg 1, T)$ function shows that the system is equally well demixed before and after $T'_{tr}(c)$. However, the sharpness of the discontinuity becomes weaker as the concentration increases, and practically disappears as the concentration approaches a value close

to 1.0. The results for the order parameters for the two components individually reveal that the subsystem containing particles B exhibits the isotropic-nematic transition at temperature $T'_{tr}(c)$. The energy distribution histograms reveal a widening of the distribution as it moves towards the transition, similar to that on Figures 5.48 and 5.49. The concentration changes the effective system size of the particle-B-rich subsystem. For the reasons presented earlier in the discussion, we therefore expect the two peaks on the histogram to merge, and this is in fact exactly what happens, as the concentration increases. To comment further on this, let us discuss the results obtained for the order parameter.

In systems with a high value of ε , the order parameter rapidly increases and continues to increase with a steady gradient until, on approaching zero temperature, it levels off to the value of 1.0. However, in a situation where part of the system stays in the isotropic phase after $T_{tr}(c)$, the order parameter should approach a value different from that of the homogeneous system or, at least, distorted behaviour of the function should be seen. In Figure 5.19 some non-monotonic behaviour of the order parameter gradient is observed. As in the case of the homogeneous system, the transition temperature $T_{tr}(c)$ changes with concentration c , and $P_2(T)$ rapidly increases below $T_{tr}(c)$. However, at lower temperatures, unusual deviation of the shape of the curve is seen. This deviation is strongest at $c \approx 0.4$ (for the system with $\varepsilon = 0.45$). The second rapid increase of $P_2(T)$ is induced by the isotropic-nematic transition of the B rich phase as we have seen in Figure 5.20.

This also explains the change in the steepness of the discontinuity of the $\langle E(T) \rangle$ curve with the change in concentration, discussed earlier. At low concentrations, the droplet of particles-B-rich phase is large and the contribution of the particles at the edge of the drop is negligible compared to that of the bulk. Therefore, the isotropic-nematic transition at $T'_{tr}(c)$ is similar, in terms of energetic behaviour, to that seen in the homogeneous system at $T_{tr}(c)$. It differs only by virtue of the energetic ‘noise’ produced by the rest of the bulk outside the isotropic drop (which is in a nematic phase and continuously reduces its energy as the temperature falls). This explains the similarity in steepness between this transition and that of the homogeneous system. However, as the concentration increases, the size of the droplet of the isotropic, B-rich, phase decreases. Similarly, the relative contribution of the particles on the surface of the drop increases, making it more difficult to determine the transition temperature $T'_{tr}(c)$ at large c . However, this is not the only obstacle to

accurate calculation of $T'_{tr}(c)$. The transition temperature for the pure B particles of $\varepsilon = 0.45$ is $T'_{IN}(\varepsilon = 0.45) \approx 0.23$. Figure 5.20 clearly shows, however, that $T'_{tr}(c)$ is higher than this at high concentrations. We believe that the explanation for this is that the ordering of the less anisotropic particles (B) is induced by the 'field' of the more anisotropic particles (A) on the interface of the particles-B-rich drop and vice versa. As the diameter of the isotropic droplet comes close to the orientational correlation length of the particles in the drop, while at the same time the configuration of the rest of the system before and after the transition remains unchanged, the order parameter of the B particles starts to increase continuously and this reduces the discontinuity in the gradient of the $\langle E(T) \rangle$ curve at $T'_{tr}(c)$. Thus the size of the ambiguous green area on the phase diagram which relates to this transition, increases in the region of high concentrations (Figures 5.27, 5.32, 5.38).

As we have seen previously, the behaviour of $\langle P_2(T) \rangle$ becomes even more dramatic in systems with $\varepsilon < 0.45$ (Figures 5.29, 5.30 for $\varepsilon = 0.30$; Figures 5.35, 5.36 for $\varepsilon = 0.10$);. In the system with $\varepsilon = 0.30$, for some concentrations the order parameter even decreases slightly as the temperature decreases ($c = 0.4$, Fig.5.29). The smaller the value of ε , the greater the effect of the B-rich isotropic drop on the ordering of the particle-A-rich nematic bulk. At temperatures close to $T'_{tr}(c)$, the order parameter for particles A exhibits a slight deviation from its conventional behaviour; this could be the result of two competing processes. On the one hand, the nematic ordering of the particles A induces para-nematic ordering in the isotropic B-rich drop; while on the other, the isotropic particles B perturb the orientational order of the particles A, decreasing their order parameter. After the transition, however, both phases possess nematic symmetry, which enhances the order parameter of both components.

However, the problem of the configuration of the drop in a bulk with a different orientational symmetry (isotropic drop in a nematic bulk or vice versa) is similar to the problem of anisotropic particles in slab geometry. This kind of configuration has always been known to reduce the strength of the transition, not to enhance it. The possible explanation follows from the results of the radial distribution function of the unlike particles at distance $r = 1$. The short range function is known to reveal structural changes on the smaller scale, which are unnoticeable at long range. In the part of ε - c - T space under consideration, the $g(r = 1)^{AB}(T)$ curve at temperatures close to $T'_{tr}(c)$ exhibits a slight, but definite, increase as the temperature is decreased

past $T'_{tr}(c)$. This could be driven by a change in the shape of the particle B rich drop. This change would not affect the appearance of the distribution function at long range and would change the function only slightly at short range, because of the relatively small size of the drop.

Summarising this section we would like to stress the following. The isotropic-nematic transition of the B-rich phase results in nematic-nematic coexistence below $T'_{tr}(c)$. This temperature does not depend on the concentration c , but on the coupling constant ε . However the system concentration does affect the accuracy with which $T'_{tr}(c)$ can be determined. This transition is seen only in the systems which exhibit the cooperative transition described in Section 5.4.3.

5.4.5 Summary, phase diagrams, expectations, hypothesis

In Figures 5.9, 5.15, 5.27, 5.32, 5.38 and 6.31 we have presented phase diagrams for selected values of ε . As phase diagrams are the summary of the results presented earlier, so the summary of this discussion will be built around discussion of the phase diagrams. We will start with the simplest case (the system with $\varepsilon = 0.9$, Fig. 5.9) and proceed to systems with lesser values of ε , referring to earlier discussions, in a way analogous to that in which we presented the results in this Chapter.

Let us comment on the I-N curve first. At either end of the concentration axis the system exhibits its most extreme features. On one side is a single component system with $\varepsilon = 1.0$ and I-N transition temperature $T_{IN}^{\varepsilon=1.0} = 1.125$. On the other side is a single component system with $\varepsilon = 0.9$ and I-N transition temperature $T_{IN}^{\varepsilon=0.9} = T_{IN}^{\varepsilon=1.0} \cdot \varepsilon^2 = 1.125 \cdot 0.9^2$. In the cases in between, the $T_{IN}(c)$ curve seems to exhibit simple linear dependence:

$$T^{NI} = c(T_{NI}^{\varepsilon=1.0} - T_{NI}^{\varepsilon=0.9}) + T_{NI}^{\varepsilon=0.9} \quad (5.2)$$

Humphries *et al* [25] studied the rod-sphere mixture system and derived similar dependence in their theoretical predictions. However, problems arise when the system is allowed to demix. In the case of the system currently under discussion ($\varepsilon = 0.9$), there is no demixing present near the I-N transition. Thus, Equation 5.2 aptly describes the behaviour of the $T_{IN}(c)$ curve. Although there is an area in Figure 5.9 where it was impossible to determine the phase of the system (points marked in

green), this area cannot with certainty be used as a guide to the I+N coexistence strip, which is expected in the vicinity of the I-N transition. The evidence for such a coexistence strip has been found elsewhere [178], as described in Chapters 2 and 3, as well as in the investigations presented in the next Chapter.

With a decrease of ε to 0.6, we can anticipate several features of the system. The first is that the I-N transition temperature would decrease on the side of low concentration ($c \rightarrow 0$) and the $T_{IN}(c)$ dependence would change monotonically, following Equation 5.2. The second is that a N+N coexistence envelope would possibly increase. As the difference in coupling strengths becomes larger, the energy difference between the mixed and demixed configurations also grows. This would encourage the system to demix at higher temperatures. There are uncertainties, however, about the shape of the N+N coexistence envelope. Let us look at the measured phase diagram (Figure 5.15) and compare it with what was expected. The T_{IN} curve changes virtually linearly with concentration. The demixing envelope increases in size with the highest temperature of demixing being $T \approx 0.26$. The envelope itself appears to be slightly asymmetric about $c = 0.5$.

A number of factors may influence the temperature of demixing at different concentrations (i.e. the shape of the envelope). Let us examine the role of the potential energy in this phenomenon. Both types of particle have cylindrical symmetry and order parameter close to 1 for both phase regions throughout the entire concentration range. For the sake of argument we assume $P_2 = 1$. Since both types occupy the same volume, in cases of low and high concentration (for example $c = 0.1$ and $c = 0.9$) it is the difference in coupling and the concentration ratio which influence the demixing temperature the most, and not the orientational entropy or the entropy which relates to excluded volume in the system.

To understand this in more detail, let us write down the potential energies of four different configurations and compare their contributions to the processes described. Configuration one-D is a drop of more anisotropic particles A in a bulk of less anisotropic particles B ($c = 0.1$). Configuration one-M is a well mixed version of configuration one-D. Respectively, configurations two-D and two-M are demixed and mixed states for $c = 0.9$. Geometrically, configurations one and two are identical. Let us first calculate the potential energy for the two demixed configurations, by splitting each into three parts: the energy of the particles in the bulk U^{bulk} , the

energy of the particles on the surface U^{surf} , and finally, the energy of the particles in the drop U^{drop} . Altogether, they comprise the total energy of the system U^{tot} (Equation.5.3)

$$U^{tot} = U^{bulk} + U^{surf} + U^{drop} \quad (5.3)$$

Let us recall that we ignore the contribution of orientational changes to the total potential energy for simplicity. In both configurations the surface energies are equal. However, let us point out that this dependence is not proportional to that of a sphere, $\sim c^{\frac{2}{3}}$, although it is very close. The investigated system and, hence, its spatial dependence is discretised so that there can be a number of concentrations that result in the same surface area of the drop, and, thus, the same value of U^{surf} . For this reason we simplify the geometry of the surface of the drop in the system by assuming that it is always cubic. As concentration increases, the surface of the drop develops complex forms, but it always approaches a cube every time $(cN)^{\frac{2}{3}}$ returns to a whole number, where N is a total number of particles in the system. Thus, the dependence of the surface area on c will always approach $6(cN)^{\frac{2}{3}}$. Therefore the potential energy associated with interactions on the surface is given by Equation 5.4.

$$U^{surf} = - \left(6 \cdot (cN)^{\frac{2}{3}} \right) \cdot \varepsilon_B \quad (5.4)$$

where c in Equation 5.4 is always the concentration of the component with a lower ratio.

The difference in concentration between configurations one and two ensures that their bulk energies differ the most, compared to other two energy components. The bulk energy is proportional to concentration $c_1 = c = 0.1$ (for configuration one) or $c_2 = 1 - c = 0.9$ (for configuration two) and to the square of the coupling constant ε_B^2 or $\varepsilon_A^2 = 1$ respectively. In the case of configuration one, the bulk energy for the system is given by

$$U_{1D}^{bulk} = - \left(3 \cdot (1 - c) \cdot N - \frac{6 \cdot (cN)^{\frac{2}{3}}}{2} \right) \cdot \varepsilon_B^2 \quad (5.5)$$

The last term in the large brackets takes account of bulk interactions absent due to the surface. In the case of configuration two the potential energy associated with the bulk reads:

$$U_{2D}^{bulk} = - \left(3 \cdot (1 - c) \cdot N - \frac{6 \cdot (cN)^{\frac{2}{3}}}{2} \right) \cdot \varepsilon_A^2 \quad (5.6)$$

Equivalently, the energies for the drops in the two configurations are given by

$$U_{1D}^{drop} = - \left(3 \cdot c \cdot N - \frac{6 \cdot (cN)^{\frac{2}{3}}}{2} \right) \cdot \varepsilon_A^2 \quad (5.7)$$

$$U_{2D}^{drop} = - \left(3 \cdot c \cdot N - \frac{6 \cdot (cN)^{\frac{2}{3}}}{2} \right) \cdot \varepsilon_B^2 \quad (5.8)$$

Now, if we combine the energies for both configurations (Equation. 5.3), we find that the energy for configuration one is higher than that for configuration two, which is supported by results presented in Figure 5.10 (page 70). Moreover, the total energy for configuration one will always be higher than that for configuration two, as long as configuration one relates to the lower concentration of the more anisotropic type of particles A (Equation 5.9).

$$U_{1D}^{bulk} + U^{surf} + U_{1D}^{drop} = U_{1D}^{tot} > U_{2D}^{tot} = U_{2D}^{bulk} + U^{surf} + U_{2D}^{drop} \quad (5.9)$$

Let us now calculate the energy of mixed configurations. Configuration one-M is a well mixed system with 10% of more anisotropic particles A ($c = 0.1$), while configuration two-M is a well mixed system with 10% of less anisotropic particles B ($(1 - c) = 0.9$). Owing to the unequal ratio of the two components, the system will inevitably form single component clusters or a network of the species with higher concentration ratio or a network. In any case, the potential energy of the system U^{tot} , in its ideal configuration (most mixed), can be divided into two parts. One is the energy of the pure component clusters or network or indeed a bulk, U^{pure} and the other is the energy of well mixed clusters U^{mix} (Equation 5.10).

$$U^{tot} = U^{pure} + U^{mix} \quad (5.10)$$

The latter can be considered as the surface energy, introduced in configurations one-D and two-D, and as in case with demixed system, $U_{1M}^{mix} = U_{2M}^{mix} = U^{mix}$ (Equation 5.11). However, U^{mix} is linearly proportional to the concentration, unlike U^{surf} (Equation 5.4).

$$U_{1M}^{mix} = U_{2M}^{mix} = -6 \cdot c \cdot N \cdot \varepsilon_B \quad (5.11)$$

The former, U^{pure} , however has the same form as U^{bulk} , with the remaining number of interactions being proportional to ε_B^2 (for configuration one) or ε_A^2 (for configuration

two). Please compare Equations 5.12 and 5.13 for the mixed system with Equations 5.5 and 5.6 for the demixed system.

$$U_{1M}^{pure} = -(3N - 6 \cdot c \cdot N) \cdot \varepsilon_B^2 = 3(N - 2 \cdot c \cdot N) \cdot \varepsilon_B^2 \quad (5.12)$$

$$U_{2M}^{pure} = -(3N - 6 \cdot c \cdot N) \cdot \varepsilon_A^2 = 3(N - 2 \cdot c \cdot N) \cdot \varepsilon_A^2 \quad (5.13)$$

Here, $3N$ is the total number of interactions in the system, while $6 \cdot c \cdot N$ is the number of interaction between unlike particles.

Please note that, using such division of the potential energy for the system with $c = 0.5$, in mixed configuration $U^{pure} = 0$, owing to all interactions being assumed mixed; and in the demixed configuration the surface energy is changed, owing to the geometry of the system (Equation 5.14).

$$U_{c=0.5}^{surf} = - \left(2 \cdot N^{\frac{2}{3}} \right) \cdot \varepsilon_B \quad (5.14)$$

As concentration reaches equal proportions for both types of particles, the surface changes from being cubic to lamellar with the surface area being equal to two sides of the simulation box, hence the change. As system size increases, the critical concentration at which geometry of the droplet changes from cubic to prism and then to lamellar, also changes. Thus, the phase diagram should change with system size. However, this effect is diminished by the small contribution of U^{surf} to the total potential energy. Analysis of Equations 5.4-5.8 shows that $|U^{surf}| \ll |U^{drop} + U^{bulk}|$.

Now, with the energies of the four configurations found, let us assume that the boundary of the nematic coexistence envelope is symmetrical. Let us also imagine a phase diagram with two points which lie on the N+N boundary and which correspond to $c = 0.1$ and $c = 0.9$ and a fixed temperature T . Let us now examine the energy difference for $c = 0.1$ and $c = 0.9$ between mixed and demixed configurations in the system with $\varepsilon = 0.6$. For $N = 16 \times 16 \times 16$ the values of the energy are:

$$U_{1M}^{tot} \approx -5014 \quad > \quad U_{1D}^{tot} \approx -5184 \quad \Delta U_1^{tot} = U_{1M}^{tot} - U_{1D}^{tot} \approx 170 \quad (5.15)$$

$$U_{2M}^{tot} \approx -11305 \quad > \quad U_{2D}^{tot} \approx -11475 \quad \Delta U_2^{tot} = U_{2M}^{tot} - U_{2D}^{tot} \approx 170 \quad (5.16)$$

As one could expect, in both cases the total energy of the demixed configuration is lower than that of the mixed one. Therefore, at any temperature point the system with $c = 0.1$ and $c = 0.9$ would favour the demixed state to the mixed one, as far as

the potential energy is concerned. What is surprising is that the energy difference in the two cases is strikingly equal. Therefore, for both concentrations there is a virtually identical inclination to undergo demixing. This means that the demixing envelope presented on the phase diagrams should be symmetrical, if the potential energy and the entropy associated with the orientation of the particles is not present. Figures 5.50 and 5.51 show that it is not the conveniently chosen value of ε in Equations 5.15 and 5.16, which leads to such results. In Figure 5.50, we present the

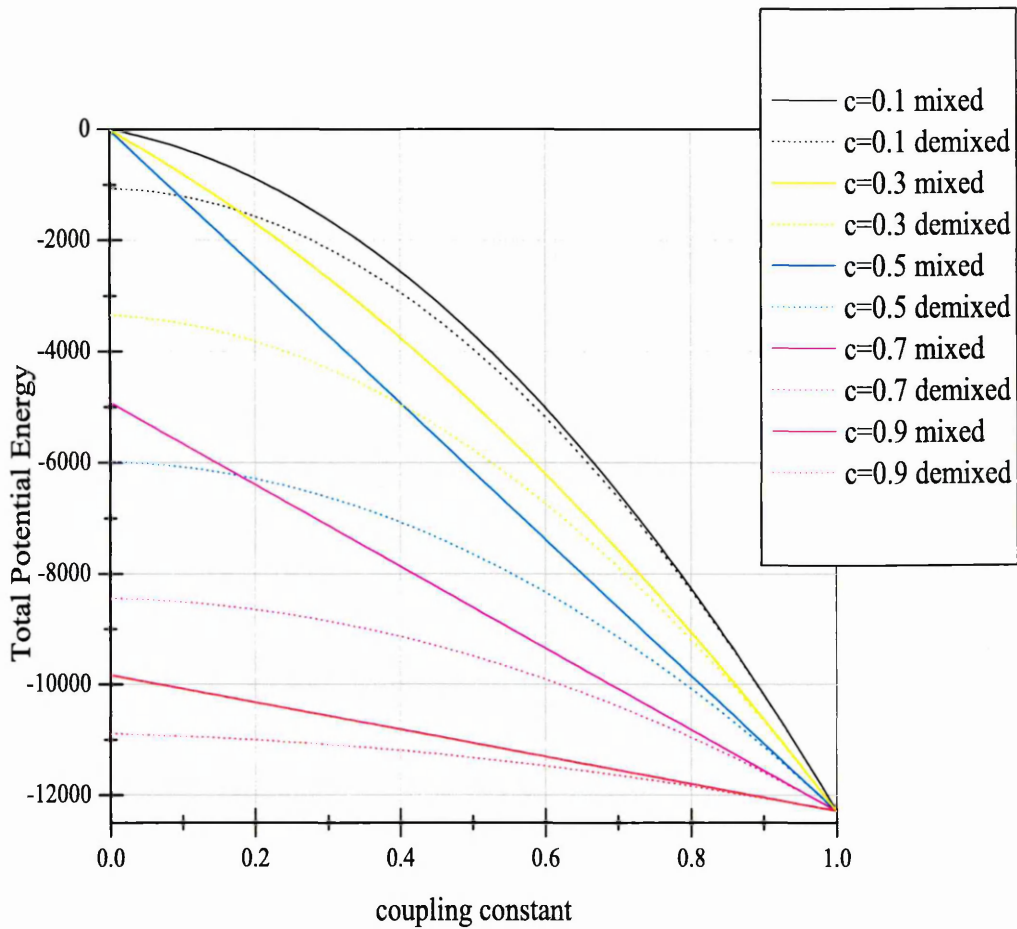


Figure 5.50: The dependence of the potential energy U_M and U_D on coupling constant ε for the range of concentrations c .

dependencies of both U_M and U_D on coupling constant ε . According to the Figure, the energy gap is largest at concentrations around $c = 0.5$. Also, as ε decreases the energy gap between mixed and demixed configurations increases significantly. This means that the potential energy associated with structural changes in the system

contributes greatly to the size of the demixing envelope. It is also seen from Figure 5.51, which also shows that the energy gap at $c = 0.5$ increases more rapidly with decrease of ε , how similar the energy gap is for any pair of concentrations c and $(1 - c)$.

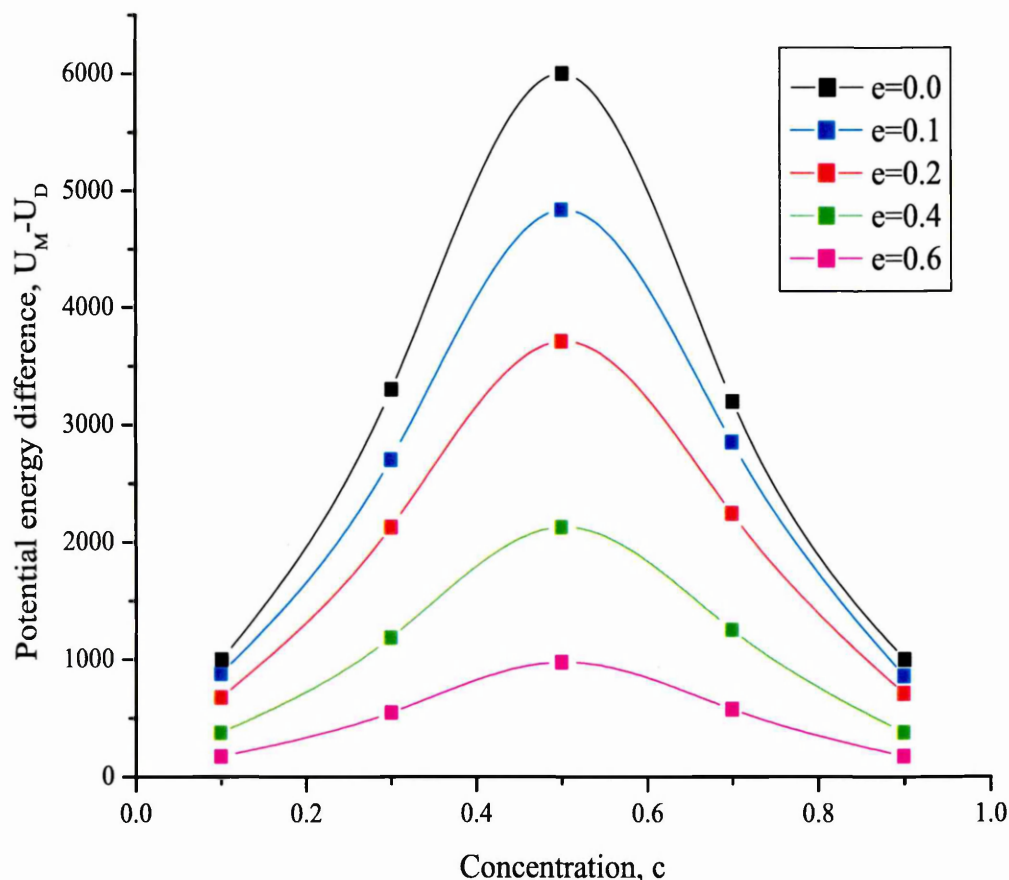


Figure 5.51: The dependence of the energy difference $\Delta U = U_M - U_D$ on concentration c for the range of coupling constants ε .

Figures 5.50 and 5.51 bring us to the conclusion that the asymmetry of the demixing envelope is solely the effect of the anisotropic properties of the system. On the one hand the value of the order parameter is always lower for the lower concentrations, since the system would contain a higher proportion of less anisotropic particles. This causes the potential energy gap between mixed and demixed states to increase more rapidly in configuration one. On the other hand, the entropy associated with the particle orientation will be higher for configuration one for the same reason - it is a less ordered system.

From Figure 5.51 it is clear that the demixing envelope will tend to grow with decrease of ε , encroaching on the phase diagram from the bottom, subject to the constraints imposed by curve. Now, applying Equations 5.2 and 5.3-5.14, one could speculate about the slope of the $T_{IN}(c)$ curve and on the size and shape of the demixing envelope as ε decreases further. Equipped with the phase diagrams of systems with $\varepsilon = 0.9$ and $\varepsilon = 0.6$, one could also predict the merger of these two phase boundaries. Uncertainty, however, arises when the $T_{IN}(c)$ curve meets the boundaries of the coexistence envelope: the demixing envelope and the $T_{IN}(c)$ curve would, presumably, affect the position of each other's boundaries. But let us first abstract from the limits of what we already know from the results. In Figure 5.52(b) we present an 'unrealistic' extrapolation of the phase diagram for the system with $\varepsilon = 0.45$ (black lines), based on the behaviour of two systems with $\varepsilon = 0.6$ and $\varepsilon = 0.9$. In the Figure we define several regions within the coexistence envelope where the prediction of coexisting phases might become problematic. Let us consider the highest portion of the coexistence envelope which lies in the isotropic phase (shaded area in Figure 5.52(b)). This isotropic-isotropic coexistence region has been seen experimentally in several cases [20] (Figure 2.3), and has been predicted by the Flory Huggins and the Maier-Saupe theories [123]. As represented in Figure 5.52(b), this area presents an obvious inconsistency with the basic rules of constructing a phase diagram, but fortunately the entire shaded area as depicted is not possible in the present model. The key parameter driving the phase separation of the two types is the coupling constant which is hidden in the interaction potential along with the angle dependent term $P_2(\cos \phi_{ij})$ (Equation 4.6). In the isotropic phase, $P_2(\cos \phi_{ij}) \rightarrow 0$ and, therefore, ε has a very little influence on the demixing. Thus, there is no demixing possible in the system while it stays in the isotropic phase. However, as soon as $P_2(\cos \phi_{ij}) \neq 0$ and continues to rise, the system begins to be able to demix. None the less, we cannot rule out this region completely from our predictions. The system with parameters in the middle of the shaded area always contains the possibility of being in either, on the one hand, the demixed isotropic (particles-B-rich) and nematic (particles-A-rich) phase coexistence or, on the other, the homogeneous isotropic phase. The only certainty is that we cannot observe I+I coexistence in the system, for the reasons stated above. Therefore we do not expect to see the I+I region on the phase diagram at all, but there may be distortions of the $T_{IN}(c)$ curve caused by the presence of the demixing envelope. The remaining area of the coexistence envelope is split horizontally, as is shown by the dashed line

in Figure 5.52(a). This line passes through the I-N transition temperature of the B-rich component, and represents the boundary of N+N demixing.

Before we comment further on this, let us consider the measured phase diagram for the system with $\varepsilon = 0.45$, which is shown in Figure 5.27 and faded image of which is included in Figure 5.52(b) for convenience. As is expected, the $T_{IN}(c)$ curve is sloped, meeting the transition temperature of the pure component B as $c \rightarrow 0$. The $T_{IN}(c)$ curve is still close to having linear dependence for most concentrations. It deviates slightly from this, however, in the region where the $T_{IN}(c)$ curve meets the coexistence envelope. In the region of low concentrations ($c \lesssim 0.1$), $T_{IN}(c)$ exhibits a significant change in its behaviour, although as $c \rightarrow 0$ it approaches the transition temperature $T_{NI}^{\varepsilon=0.45} = T_{NI}^{\varepsilon=1.0} \cdot 0.45^2$ as expected. A phenomenon perhaps more interesting and unexpected can be observed on the $T_{IN}(c)$ curve at $0.5 \lesssim c \lesssim 1.0$ in Figure 5.27. Although there is no evidence of demixing or any other obvious cause, the measured curve appears to be slightly higher than that predicted by our extrapolation (Figure 5.52(a)) and by the work of Humpries *et al* [25]. This phenomenon may be related to the change in the short range radial distribution function, which we showed in Figure 5.24 (page 89). Except for this distortion to the $T_{IN}(c)$ curve, the observed phase diagram supports our predictions regarding the shaded area of the coexistence envelope, i.e. there is no demixing in the isotropic phase. Predictions about the horizontal line at approximately $T_{NI}^{\varepsilon=0.45}$, which separates the demixing envelope into two phase coexistence regions, are also consistent with the obtained results. However, the boundary between these two regions is somewhat blurred (Figure 5.27), for the reasons discussed earlier.

In the area of low concentrations ($c \lesssim 0.1$), we obtained points for the phase diagram, which were taken at smaller concentration intervals. This was done to clarify the small region of nematic phase stability (Figure 5.52(b)). On the measured phase diagram (Figure 5.27), there is a cross-point, where the near-horizontal line for the B-rich I-N transition crosses the boundary of the demixing envelope (point *C* in Figure 5.52(b)). When the concentration is lower than point *C*, the more anisotropic particles (A) do not have much influence on the behaviour of the B-rich system. As a result, the system undergoes this transition virtually at temperature $T_{NI}^{\varepsilon=0.45}$. At lower temperatures, the system then demixes according to the rules described earlier (Equations 5.3-5.14). Alternatively, when the concentration is higher than the point *C*, the ratio of anisotropic particles (A) is sufficient for the system to demix first,

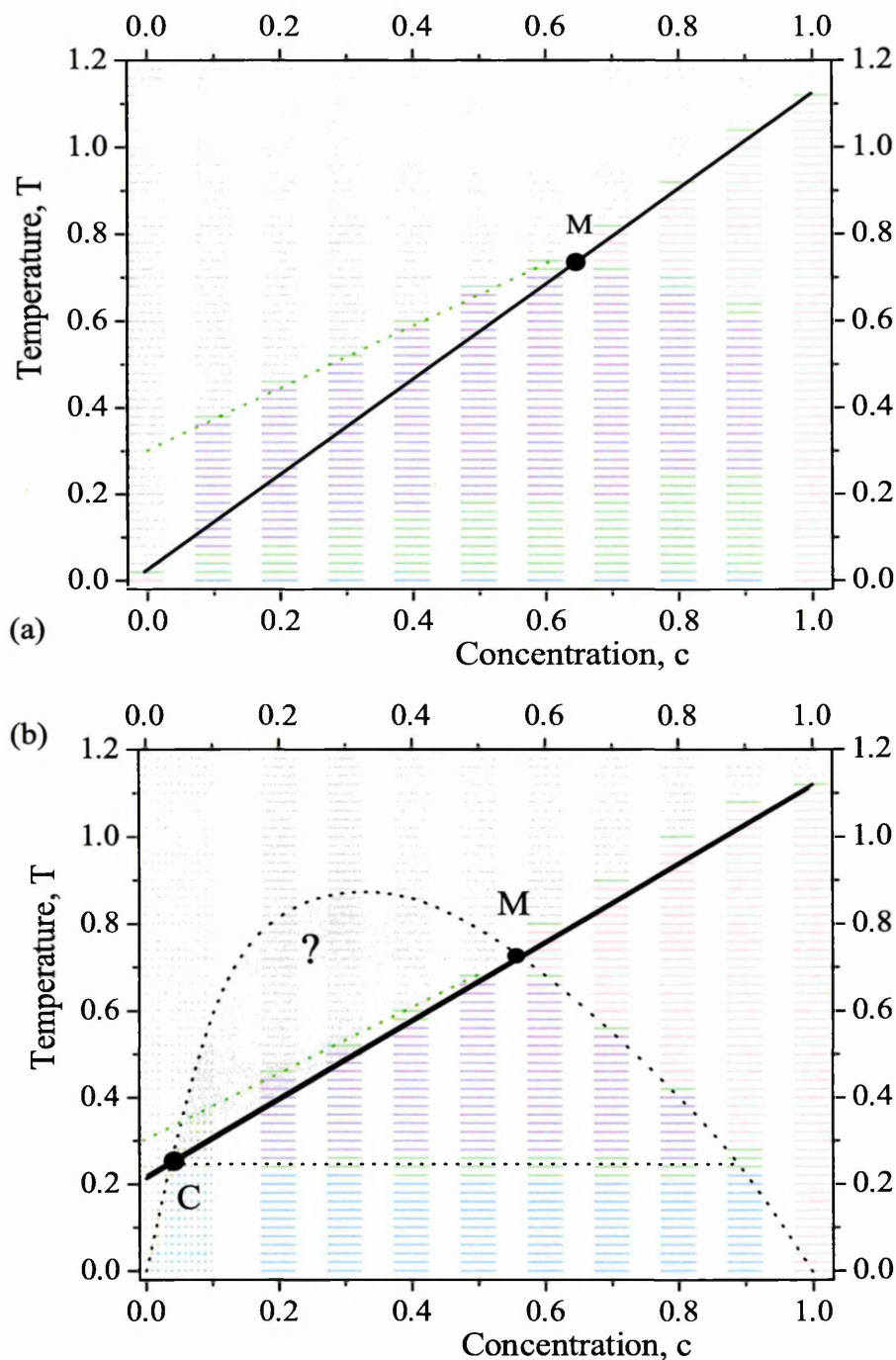


Figure 5.52: Phase diagrams for the system with $\varepsilon = 0.10$ (a) and $\varepsilon = 0.45$ (b). The black solid line represents the $T_{IN}(c)$ unaffected by the N+N envelope. The black dashed curve is the speculated demixing envelope unaffected by the I-N transition. The black dashed horizontal line represents the boundary between I+N and N+N regions. The green dashed line shows the slope of the measured $T_{IN}(c)$ curve in the region to the left of point M .

only at lower temperature, does the B-rich isotropic phase in the already demixed system undergo the I-N phase transition described in previous paragraphs. Closer to the point C we observe ambiguities between these transitions, shown as green points on the diagram (Figure 5.27).

The three remaining systems, with coupling constants $\varepsilon = 0.30$, $\varepsilon = 0.1$, and $\varepsilon = 0.0$, exhibit similar behaviour to the system with $\varepsilon = 0.45$. If we compare the phase diagrams of all four systems (Figures 5.27, 5.32, 5.38, and 6.31) we can deduce the following. The $T_{IN}(c)$ curve is virtually the same in all four cases. The slope of the curve remains at the same level for all systems with $\varepsilon < 0.45$ (Figure 5.52(a)). At approximately $c \lesssim 0.05$, the $T_{IN}(c)$ curve changes dramatically, approaching T_{IN}^ε as $c \rightarrow 0$ for all systems with $\varepsilon < 0.45$. In other words, if we denote the ε value at which the demixing envelope merges with the $T_{IN}(c)$ curve as ε_{coup} , the slope of the $T_{IN}(c)$ curve remains unchanged for all lower values $\varepsilon < \varepsilon_{coup}$. As a consequence, the measured $T_{IN}(c)$ curve to the left of point M deviates increasingly from the predicted solid line as ε decreases, since the $T_{IN}(c)$ curve remains almost in the same place regardless of the value of ε (Figures 5.52(a),(b)).

In addition to the simulations already presented in this Chapter, we investigated the system at a number of other values of ε to determine the value of ε_{coup} . From these we found the value of ε_{coup} to be somewhere between 0.50 and 0.55. Also, we studied the slope of the $T_{IN}(c)$ curve and its behaviour before and after the coupling. As was mentioned before, the slope of the $T_{IN}(c)$ curve remains virtually unchanged after it meets the demixing envelope (green dashed line). Therefore, it may be that the value of this slope could be related to the value of ε at which the coupling of the $T_{IN}(c)$ curve and the demixing envelope occurs. Taking into account that it is the part of the $T_{IN}(c)$ curve on the left of the point M which is affected by the demixing envelope, we extrapolate this slope to the temperature axis and find that it crosses the $c = 0$ abscissa at $T \approx 0.30$ (green dashed lines in Figures 5.52(a),(b)). This temperature corresponds to the I-N transition temperature of the pure component with $\varepsilon \approx \sqrt{\frac{0.30}{T_{NI}^\varepsilon - 1.0}} \approx 0.52$, which is consistent with the value found for ε_{coup} .

To conclude this discussion, we would like to say a little more about the system with $\varepsilon = 0.0$. This particular case merits individual investigation. The system with $\varepsilon = 0.0$ represents a mixture of particles with different symmetries, whereas all other cases involve particles of the same symmetry. From Figure 6.31 we see only three re-

gions. The region that is missing is N+N coexistence, which must necessarily vanish as $\varepsilon \rightarrow 0.0$. We can see also that, except for a small nematic island existing at high concentrations and high temperatures, the system exists either as a homogeneous isotropic phase or as coexisting isotropic and nematic phases. This is consistent with previous simulation results and the molecular field theory [177]. Although this binary mixture of particles with spherical and cylindrical symmetries is the simplest nematogen mixture, molecular field theory predicts that it will exhibit an intriguing phase behaviour. For example, for the highest concentrations ($c \gtrsim 0.8$), the phase sequence is predicted to be: isotropic, I+N coexistence region, nematic, and re-entrant I+N coexistence regions [177,179]. Below this concentration, however, the I+N coexistence region which forms from the isotropic phase is predicted to be stable at all lower temperatures. It is difficult to test these predictions experimentally, since most real systems crystallise before the coexistence region can be formed for the required concentrations. However, there have been attempts to test the molecular field theory of the re-entrant I+N coexistence region by a computer simulation study [177]. To discuss the results presented in Figure 6.31 and compare them with [177] we must keep in mind the following. The accuracy of the position of the phase boundaries in the vicinity of the transition temperatures (namely, I-region versus I+N coexistence region) is very poor, owing to the weakening of the first-order I-N transition by the binary mixture. The problem with the approaches described above is that they do not involve direct measurements of the free energy function, which governs phase equilibria. An important advancement in such calculations is the finite-size scaling technique described by Lee and Kosterlitz [187,188], which allows to calculate phase boundaries more accurately. This approach was applied to the Lebwohl-Lasher Model by Zhang *et al* [173]. However, even using such techniques, the re-entrant phase behaviour could not be supported with certainty, either in [177], or in our simulations (Figure 6.31). This ambiguity is partly due to the measurement methods involved, and partly to the effect of isotropic dilutant on the strength of the transition, as discussed in the previous paragraph. Nevertheless, from the P_2 data and general information on the first-order transition, we can conclude that the green area in Figure 6.31 represents I+N coexistence; the observed behaviour may be due either to the sole effect of the transition, or to the combined effects of the transition and demixing.

The results discussed in this chapter represent an extensive investigation of the Lebwohl-Lasher model and give a good overview of its phase behaviour. Although the possible re-entrance of the I+N coexistence region was demonstrated using a range of different approaches, further study of the system is required, in which the coexistence regions can be clearly defined. In next Chapter we will discuss the phenomenon of phase re-entrance further in the light of simulations performed in an alternative ensemble.

Chapter 6

Results And Discussion.

Bi-Dispersed System. $N\Delta\mu VT$.

In this Chapter we present and discuss the results of the phase coexistence behaviour of binary system, obtained by performing Monte Carlo simulations on the Lebwohl-Lasher lattice model in the Semi-Grand Canonical Ensemble ($N\Delta\mu VT$). The rationale of this ensemble was discussed in Section 4.1.2. The model basis is similar to that presented in the previous Chapter and is described in Chapter 4.

For consistency with the results presented earlier, we used for most calculations a system in which the cubic simulation box consisted of sixteen sites on each of its sides (i.e. a system size of $16 \times 16 \times 16$ particles). All results presented in this Chapter were obtained using this size unless otherwise stated. The correlation length of run for the given system was estimated to be around 5,000 run steps, which approximately is the same as the number of run steps required for the system to equilibrate. Therefore, for the calculation of the average preferred concentration $\langle c(\Delta\mu) \rangle_{N\Delta\mu VT}$, runs with 20,000 steps per point were performed, allowing an additional 5,000 steps for equilibration (see Section 4.4.5). Generally, this number was also adequate for the calculation of the second-rank order parameter $\langle P_2(\Delta\mu) \rangle_{N\Delta\mu VT}$, used to identify nematic ordering, although it had to be doubled at low T. Phase boundaries were determined using the $\langle c(\Delta\mu) \rangle_{N\Delta\mu VT}$ and $\mathcal{P}(c)_{\Delta\mu=const}$ data. For the calculation of concentration histograms $\mathcal{P}(c)_{\Delta\mu=const}$, the number of steps per point was increased to 3,000,000. The temperature step for most runs was $\Delta T = 0.1$ or $\Delta T = 0.05$, except for certain systems where ΔT was reduced to 0.01 in a certain temperature

range. The step of chemical potential difference for most calculations was at least $\delta\Delta\mu = 0.0005$. The concentration histograms $\mathcal{P}(c)_{\Delta\mu=const}$ were calculated for specific temperature and chemical potential difference values (usually in the vicinity of the transition), guided by $\langle c(\Delta\mu) \rangle_{N\Delta\mu VT}$ calculations.

In Section 6.1 we give the system evaluation and explain how the phase diagrams, presented in subsequent sections, were constructed. In the next three Sections we present results for eight binary systems with coupling constants $\varepsilon = 0.9, 0.6, 0.55, 0.53, 0.52, 0.50, 0.45, 0.0$. The lower the coupling constant ε , the less anisotropic is one of the components of the binary mixture in the system. The systems with different coupling constants were grouped according to the topographies of their two phase coexistence regions I+N and N+N. In Section 6.2 we present results for the systems with coupling constants $\varepsilon = 0.9, 0.6, 0.55$. In these systems the two coexistence regions are widely separated from each other. In Section 6.3 we present results for another three binary systems with coupling constants $\varepsilon = 0.53, 0.52, 0.50$. These systems exhibit the two coexistence regions as they merge. In Section 6.4 we present results for the remaining two binary systems with coupling constants $\varepsilon = 0.45, 0.0$. Both of these systems exhibit a single coexistence region.

The results presented for each system are divided into three main parts. In the first part, we present calculations of the average preferred concentration and its dependence on temperature T and chemical potential difference $\Delta\mu$, $\langle c(T, \Delta\mu) \rangle_{N\Delta\mu VT}$. In the second part we present the results of the second-rank orientational order parameter $\langle P_2 \rangle_{N\Delta\mu VT}$ and its dependence on temperature T and chemical potential difference $\Delta\mu$, $\langle P_2(T, \Delta\mu) \rangle_{N\Delta\mu VT}$. In the third and final part, we present the phase diagram of the system, which is based on the results presented previously.

In Section 6.5 of this Chapter we discuss the results presented in sections 6.1-6.4 and present additional results to clarify some particular characteristics of the behaviour of the system, which have emerged from the results presented in sections 6.1-6.4. The discussion in Section 6.5 proceeds in the following order. First in this section we make general comments on $\langle c(T, \Delta\mu) \rangle_{N\Delta\mu VT}$ isotherms, presented in earlier sections of the Chapter 6. These are discussed in terms of theoretical Van der Waals loops [189, 190], hysteresis effect, etc. Then, the coexistence boundaries of phase diagrams are discussed in three parts, starting with $T_{IN}(c_1, c_2)$ coexistence region (Section 6.5.1), then nematic-nematic coexistence region (Section 6.5.2) followed by the discussion of

single coexistence region, coupled from previous two (Section 6.5.3). In Section 6.5.4 we present alternative view of the phase behaviour. Discussion is based around ε - T phase diagrams. The Chapter concludes with summary of the discussion of NcVT and $N\Delta\mu VT$ data (Section 6.5.5)

Since all observables presented in this Chapter were obtained at constant $N\Delta\mu VT$, we omit the index ($N\Delta\mu VT$) in our notation. In this Chapter, the more anisotropic particles are indexed as particles A and the less anisotropic particles, as particles B. In all the systems covered in this Chapter, only the anisotropy of particles B is subject to change.

6.1 System Evaluation And Introduction To The Results

In the Semi-Grand Canonical Ensemble, its thermodynamic function, grand potential Ω , has a unique minimum for any value of $\Delta\mu$ and there is no $\Delta\mu$ that corresponds to an area of coexistence. This makes it very sensitive to phase boundaries: a slight change of $\Delta\mu$ can prompt the state point to move rapidly from one minimum to another, as the system undergoes a transition from one phase to another. However, owing to the size of the system, concentration fluctuations can cause the system to oscillate from one minimum to another and back again in a single simulation with $\Delta\mu = \text{const}$. Therefore, in the vicinity of a narrow coexistence region, concentration histograms can show two peaks, corresponding to two preferred concentrations. These concentration values provide the coordinates for the coexistence boundaries on the phase diagram for a given temperature (Figure 6.1(a)). The phase diagram in this case was plotted against the same two parameters as for the NcVT Ensemble (Chapter 5). However, the underlying approach adopted in this Chapter determines phase boundaries by scanning the concentration indirectly (e.g. by changing $\Delta\mu$), so that the concentration is not fixed, as was the case in the Canonical Ensemble. The determining of phase boundaries using this different approach will enable us to check the results against those obtained by means of the NcVT Ensemble, and to clarify ambiguous areas of the phase diagrams based on those calculations.

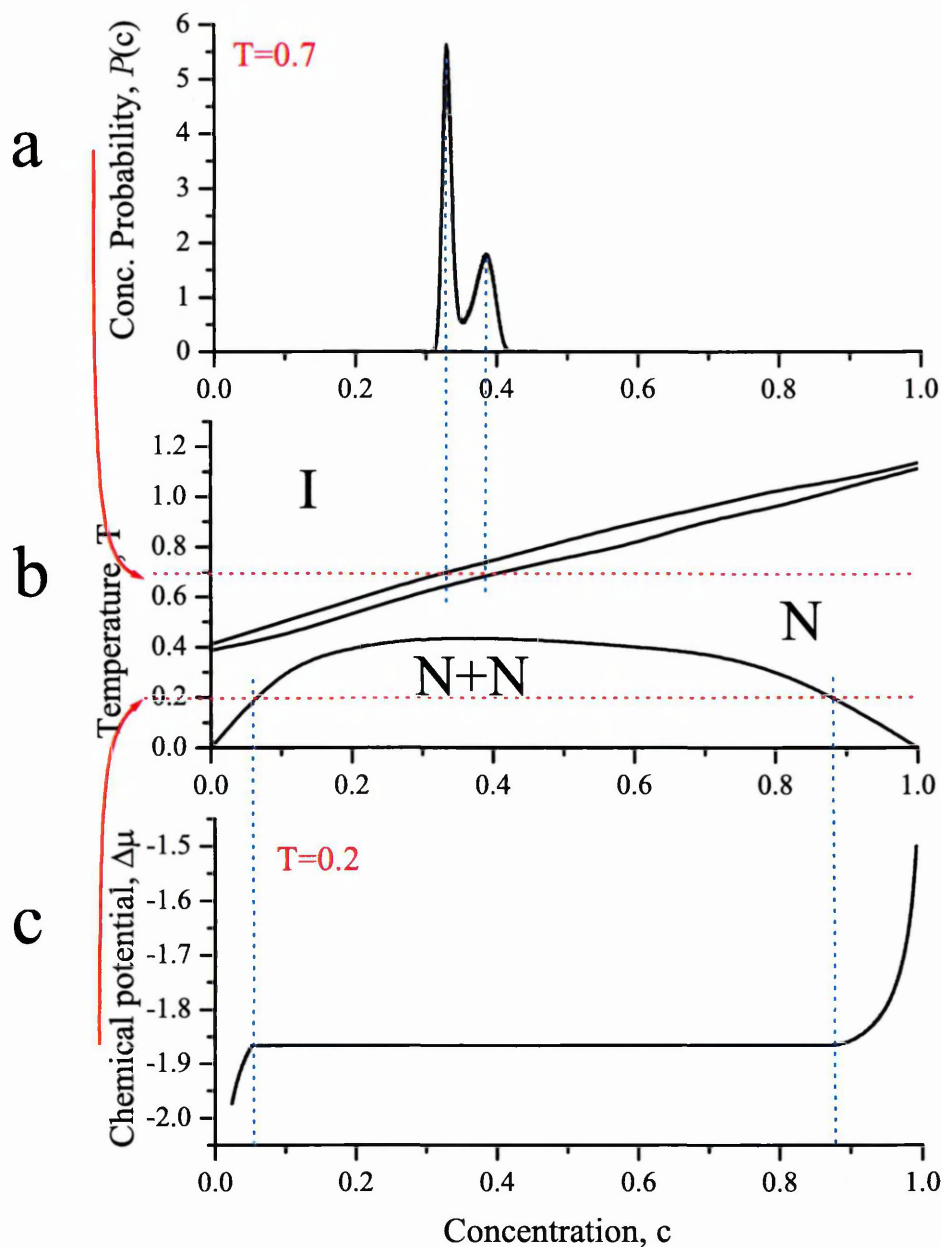


Figure 6.1: Construction of a phase diagram using $\langle c(\Delta\mu) \rangle$ and $\mathcal{P}(c)$ data.

According to the literature [178], there is in the $N\Delta\mu VT$ ensemble a value of $\Delta\mu_{coex}$ at which two probability peaks on the concentration histogram can be observed, if in fact coexistence region exists for the given set of parameters (T, ε) . As was mentioned earlier, the positions of these two peaks give the coordinates of the coexistence boundary for the given T and ε . A difficulty arises, however, when one aims to find such a value of $\Delta\mu_{coex}$, which exists in a very narrow region of $\Delta\mu$. As we

will show in subsequent sections, for low values of T and ε the accuracy to which $\Delta\mu_{coex}$ is required is approximately 0.005, while the range of $\Delta\mu$ required to cover the concentration space 1 to 0 is of the order of 2.0. To search the space of such magnitude (at least 4000 $\Delta\mu$ -points for each value of T and ε , allowing $\sigma = 3,000,000$ steps for each point for good statistics) is an inordinately time-consuming procedure. With the reduction of σ the number by one order, the double-peak feature cannot be resolved. It is also pointless measuring $\mathcal{P}(c)$ away from the coexistence as the distribution is of single Gaussian form. In order to utilize our efforts we used significantly shorter runs (σ in the order of 20,000 steps per point); this procedure gives limited results as far as the concentration histograms are concerned, but yields a satisfactory estimation of the concentration dependence on $\Delta\mu$. The dependence $\langle c(\Delta\mu) \rangle$ is then plotted.

At a high constant temperature, $\langle c(\Delta\mu) \rangle$ exhibits a gradient discontinuity at $\Delta\mu_{coex}$ (similar to that shown in Figure 6.3(b)). $\Delta\mu_{coex}$ was determined from the maximum of $\frac{d\langle c(\Delta\mu) \rangle}{d\Delta\mu}$ (similar to that shown in Figure 6.3(a)). Then, a simulation with a large number of steps was performed to identify the two preferred concentrations (c_1 and c_2) for a constant value of $\Delta\mu = \Delta\mu_{coex}$ from the two peaks in the measured distribution $\mathcal{P}(c)_{\Delta\mu}$ (Figure 6.2). To check the credibility of the method and of the model as a whole, we attempted to replicate the results from the work of Polson and Burnell [178]. The paper does not explain how the specific value of $\Delta\mu_{coex}$ was determined; nor does it give the value $\Delta\mu_{coex}$ at which two peaks were observed. However, it specifies the temperature $T \approx 0.6738$ (assuming $T_{NI}^{(B)} = 1.123$ in [178]) and the coupling constant $\varepsilon \approx 0.632456$ (equivalent to that in [178], $\varepsilon_{AA}/\varepsilon_{BB} = 0.4$, $\gamma_{AA} = \gamma_{BB}$, $T/T_{NI}^{(B)} = 0.6$, $L = 25$). Their results for this set of parameters were $c_1 \approx 0.33$ and $c_2 \approx 0.39$. In Figure 6.2 we present a concentration histogram for the system with $\varepsilon = 0.632456$, $T = 0.6738$, and $\Delta\mu_{coex} = -0.9900$. The value of $\Delta\mu_{coex}$ was determined as $\max(\frac{d\langle c(\Delta\mu) \rangle}{d\Delta\mu})$. From the Figure we note peak concentrations that are in good agreement with data from [178]. Any deviation in the concentration values might be result of original value of $T_{NI}^{(B)} \neq 1.123$ in [178].

However, this method was shortly abandoned, owing to still demanding requirements of the computational power available. Instead, another criterion was used to determine c_1 and c_2 (Figure 6.3). The concentration values were determined as cross-points of a vertical line ($\Delta\mu_{coex}$) and two lines tangent to the two slopes of the $\langle c(\Delta\mu) \rangle$ on the both sides from the vertical line. The coordinate for the vertical line

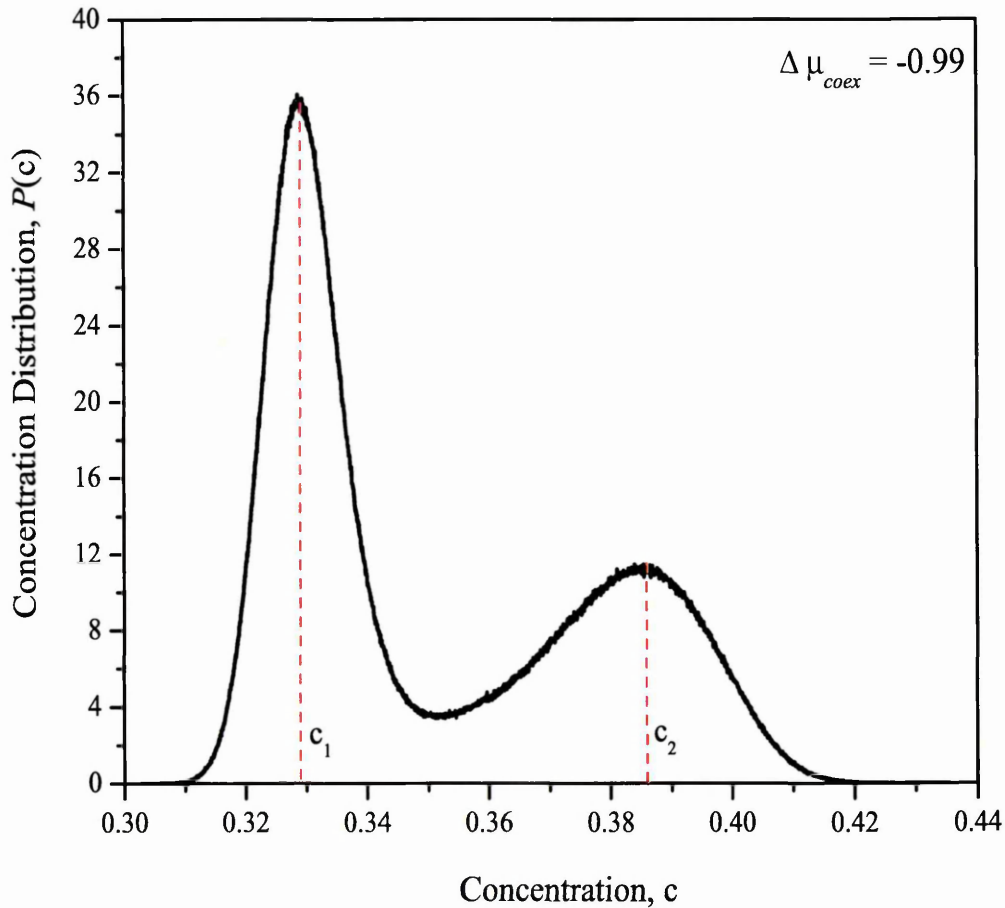


Figure 6.2: Distribution of the preferred concentration for the system with $\varepsilon = 0.632456$, $T = 0.6738$, $L = 25$. 3,000,000 steps. Distribution values were normalized to set the area under the curve to be 1. Two peaks are observed for $\Delta\mu = -0.99$. The positions of the two peaks are $c_1 \approx 0.329$ and $c_2 \approx 0.386$.

was still given by the position of the maximum of $\frac{d\langle c(\Delta\mu) \rangle}{d\Delta\mu}$. Figure 6.3 shows the feasibility of such a method, comparing obtained values of c_1 and c_2 with these obtained using histogram distribution (Figure 6.2). The nature of $\mathcal{P}(c)_{\Delta\mu}$ distribution is such that the Gaussian changes its position continuously until at certain range of $\Delta\mu$ two Gaussians at two different positions (c_1 and c_2) start to change their height relatively rapidly, so that discontinuity on the $\langle c(\Delta\mu) \rangle$ curve occurs. Thus, it is acceptable to use the cross-points shown in Figure 6.3, as they approximately represent c_1 and c_2 , which otherwise could be obtained from the concentration histograms.

For low temperatures the discontinuity is very abrupt. We were thus able to determine the two preferred concentrations directly from the $\langle c(\Delta\mu) \rangle$ dependence, c_1 and c_2 (Figure 6.1(c)). These concentrations relate to the values of $\Delta\mu_1$ and $\Delta\mu_2$, which

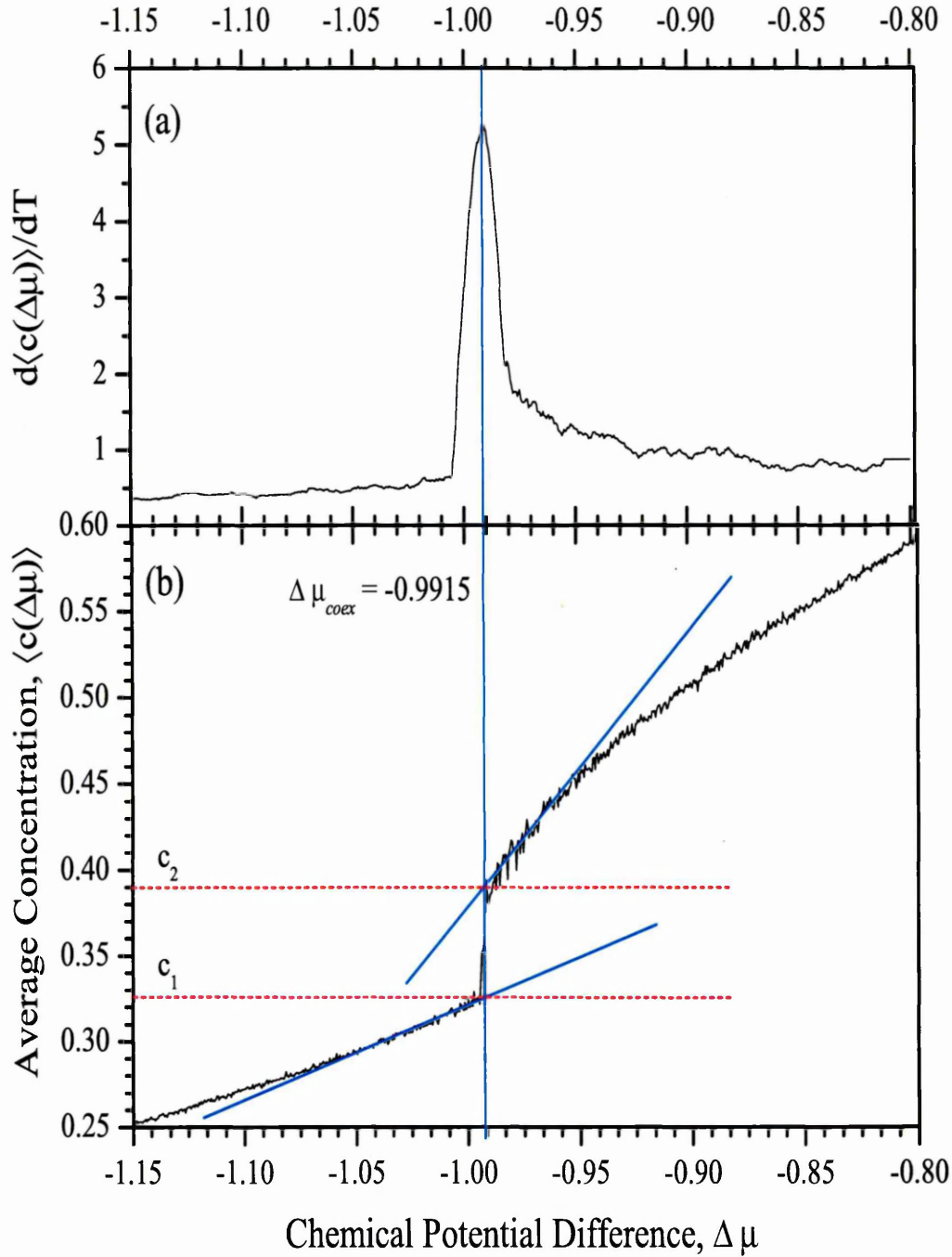


Figure 6.3: (b) Two preferred concentrations determined as cross-points of the vertical line ($\Delta\mu_{coex} = -0.9915$) and tangents to the slopes of the $\langle c(\Delta\mu)\rangle$ curve on both sides of the discontinuity. System with $\varepsilon = 0.632456$, $T = 0.6738$, $L = 24$, 1,500 steps. (a) $\Delta\mu_{coex}$ is determined as a maximum of the numerical differential of the $\langle c(\Delta\mu)\rangle$ curve, along with smoothing ± 20 points.

are close to $\Delta\mu_{coex}$. For convenience, we note these $\Delta\mu_1$ and $\Delta\mu_2$ as one point, $\Delta\mu_{coex} = \frac{\Delta\mu_2 + \Delta\mu_1}{2}$, and set values $\Delta\mu_2 \leq \Delta\mu_1$, $c_2 > c_1$. From these, we can deduce the coexistence boundaries (Fig.6.1(b)).

Therefore we conclude this section with the following. Using the constant $N\Delta\mu VT$ -Ensemble we can resolve concentration probability distribution $\mathcal{P}(c)$ at a range of temperatures (Fig.6.1(a)). From these, we can deduce the coexistence boundaries on the phase diagram (Fig.6.1(b)) for a coexistence region that is narrow enough. The peaks of $\mathcal{P}(c)$ histograms show ‘exact’ boundaries of coexistence for isotropic and nematic phases, c_1 and c_2 (Figures 6.1(a) and 6.2). These concentrations found to be in good agreement with those obtained by more efficient approach shown in Figure 6.3. These results are consistent with other works [178]. When the energy barrier between the two peaks becomes too high or distance between peaks too large, c_1 and c_2 were estimated directly from $\langle c(\Delta\mu) \rangle$ curve as points of sharp discontinuity in the curve (Fig.6.1(c)). In the latter case, the hysteresis effect becomes more evident and should be taken into account when determining coexistence boundaries (will be discussed in Section 6.5). Using these we constructed phase diagrams as it is shown in Figure 6.1. As has been explained at the beginning of this Chapter and in Chapter 4, $\langle c(\Delta\mu) \rangle$ does not reveal the mesophases of the system for given parameters. Thus, in Sections 6.2-6.4 we also present results of the dependence of the second-rank orientational order parameter on $\Delta\mu$ as an auxiliary observable.

6.2 Systems with $\varepsilon = 0.90$, $\varepsilon = 0.60$, $\varepsilon = 0.55$

The first system investigated is the binary system with coupling constant $\varepsilon = 0.9$. As was shown in the previous Chapter, this system is the closest to its single component equivalent.

The first observable to be presented is the average preferred concentration of the mixture $\langle c(\Delta\mu) \rangle$ and its behaviour with a change of the chemical potential difference $\Delta\mu$. In Figure 6.4 we present such dependencies taken at different temperatures in the range $0 < T < 0.2$.

At the lowest temperature on the graph, $T = 0.01$, the value of the concentration approaches 1 and remains unchanged as $\Delta\mu$ decreases from its highest value until

$\Delta\mu \approx -0.545$. Then, the concentration decreases rapidly over a short range of $\Delta\mu$ ($-0.545 \gtrsim \Delta\mu \gtrsim -0.590$) with a maximum gradient at $\Delta\mu \approx -0.570$. Between $\Delta\mu_1 \approx -0.585$ and $\Delta\mu_2 \approx -0.560$, the value of c decreases dramatically, with the corresponding values of concentration being $c_1 \approx 0.013$ and $c_2 \approx 0.978$ respectively.

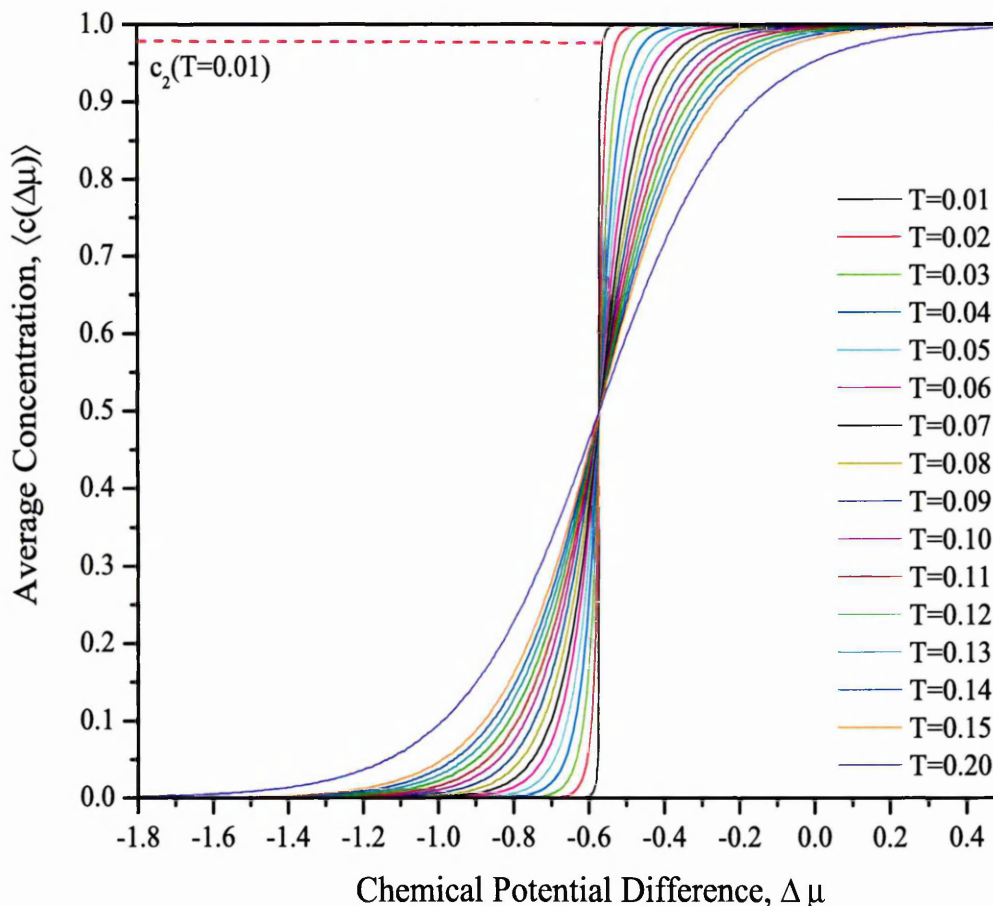


Figure 6.4: Dependence of the preferred concentration on $\Delta\mu$. $\varepsilon=0.90$. Different curves represent runs at different temperatures in the range $0 < T < 0.1$.

As the temperature is increased further, the $c(\Delta\mu)$ curve becomes continuous at $T \approx 0.04$. For temperatures $T > 0.1$, the $\langle c(\Delta\mu) \rangle$ curve takes on a more linear shape as the temperature increases. In Figure 6.5 we present the $\langle c(\Delta\mu) \rangle$ data for the range of temperatures $0.1 \leq T \leq 0.9$. According to the results presented in the previous Chapter, one would expect to see a discontinuity in the gradient of $\langle c(\Delta\mu) \rangle$

in the range of temperatures $0.93 \lesssim T \lesssim 1.15$. Thus we present another graph of $\langle c(\Delta\mu) \rangle$ curves taken in that region of temperatures (Figure 6.6).

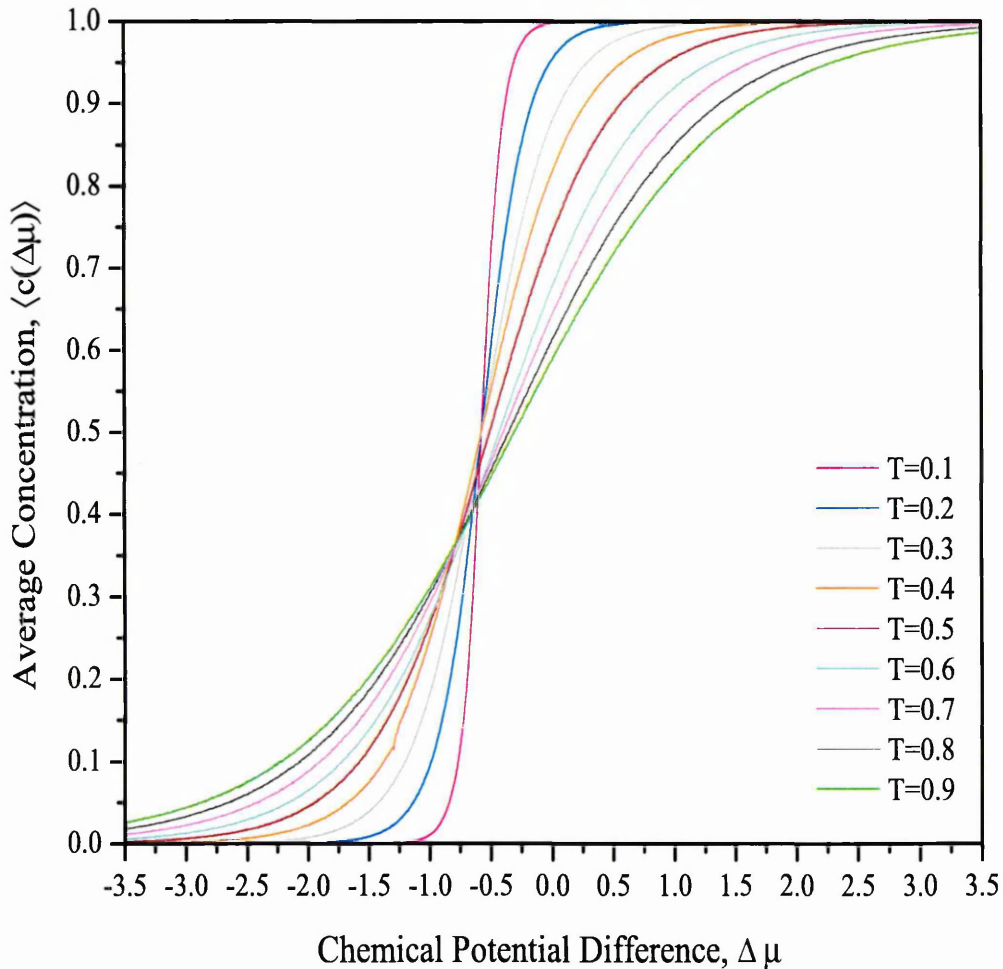


Figure 6.5: Dependence of the preferred concentration on $\Delta\mu$. $\varepsilon=0.90$. Different curves represent runs at different temperatures.

For these temperatures no discontinuities are apparent on $\langle c(\Delta\mu) \rangle$ isotherm for a wide range of T . For this reason we performed another set of simulations at constant $\Delta\mu$. In such a method, the thermal dependence of the preferred concentration ($\langle c(T)_{\Delta\mu=const} \rangle$) is expected to exhibit a discontinuity at $c_1(T)$ and $c_2(T)$. This method can be more sensitive than that of constant temperature, since the state point moves by a different path (Section 6.5). In Figure 6.7 we present such $\langle c(T) \rangle$ curves, measured at different values of $\Delta\mu$.

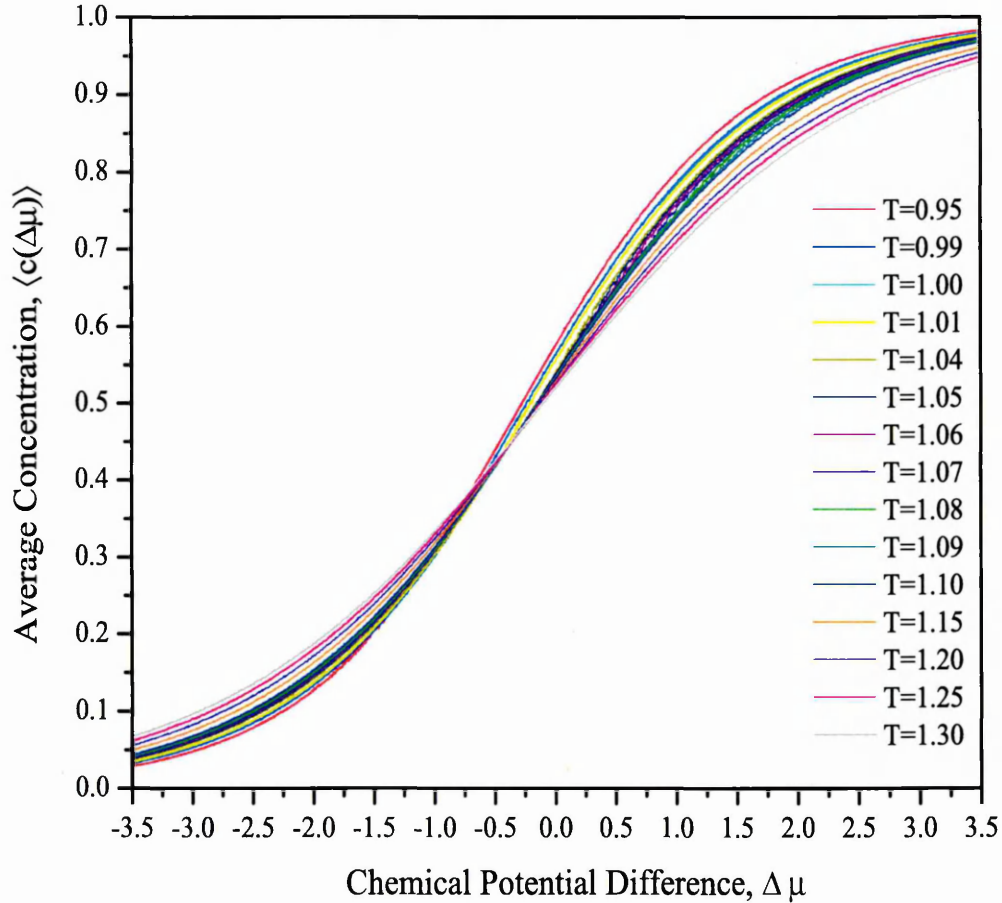


Figure 6.6: Dependence of the preferred concentration on $\Delta\mu$. $\varepsilon=0.90$. Different curves represent runs at different temperatures.

The next Figure (6.8) shows the dependence of the preferred orientational order parameter on $\Delta\mu$. This observable changes its value relatively sharply at $\Delta\mu_{coex}$, which then allows estimation of the approximate concentration (from Figure 6.6) at which the ordering transition occurs for a given temperature.

For temperatures $T \lesssim 0.91$ the order parameter changes continuously from non-zero value to another, lower, non-zero value as $\Delta\mu$ decreases. For the small range of temperatures $0.92 \lesssim T \lesssim 1.12$ the order parameter changes from a non-zero value to a close-to-zero value as $\Delta\mu$ decreases. The change in order is greatest at temperatures around $T \approx 1.02 \pm 0.06$. The isotropic-nematic coexistence region is believed to be at its widest in this range of temperatures (Section 6.5.1), however

we were not able to determine c_1 and c_2 from the $\langle c(\Delta\mu) \rangle$ data or unambiguously determine the position of c_2 from the $\langle c(\Delta\mu) \rangle$, as was shown earlier. We will discuss this isotropic-nematic coexistence region further in the beginning of Section 6.5 and Section 6.5.1.

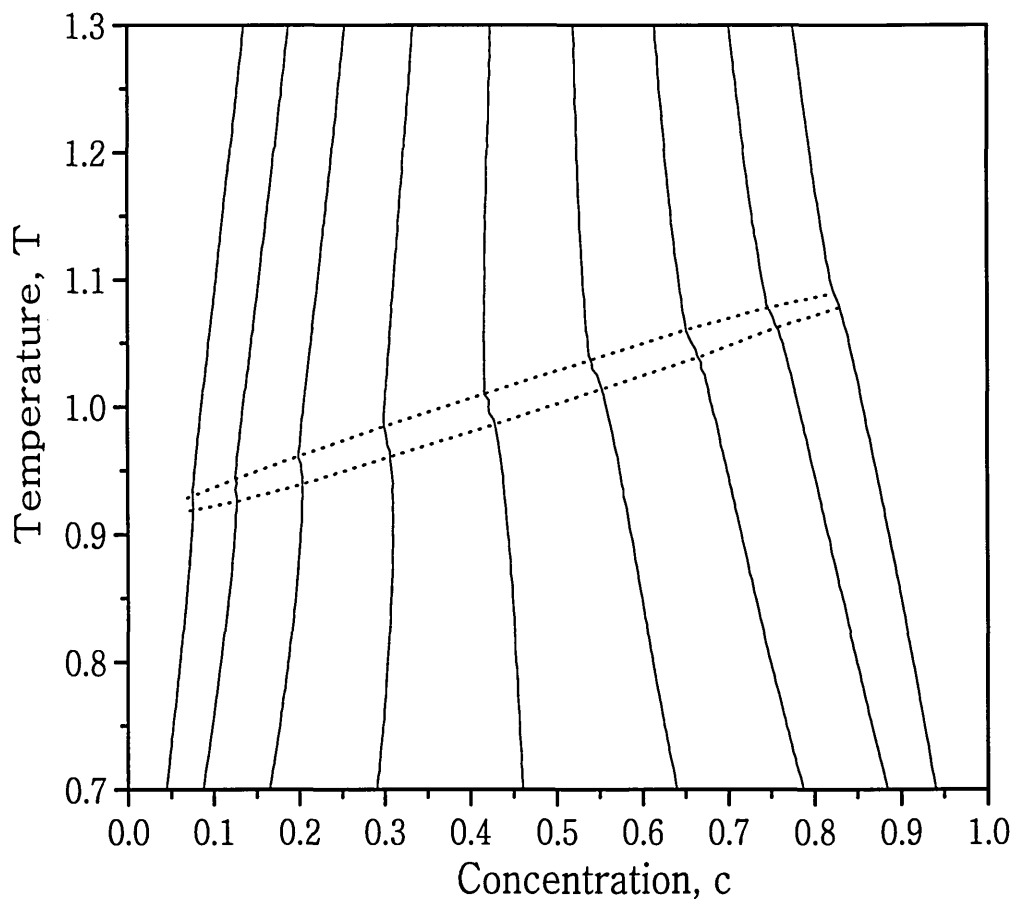


Figure 6.7: Dependence of the preferred concentration on T . $\varepsilon=0.90$. Different curves represent runs at different chemical potential difference $\Delta\mu = \text{const}$.

From the data presented above we were able to construct an approximate phase diagram (blue-filled circles in Figure 6.9). Black-filled squares represent data from the NcVT Ensemble discussed in the previous Chapter. A comparison and discussion of the two sets of results will be presented in Section 6.5.

Let us comment first of all on the isotropic-nematic transition ($T_{IN}(c)$). It is assumed that the system undergoes an I-N transition at the temperatures of its pure

components at both ends of the concentration axis ($c = 0.0$ and $c = 1.0$), i.e. $T_{IN}(c = 0.0) \approx 0.93$ and $T_{IN}(c = 1.0) \approx 1.15$ (the temperatures from the average energy data of NcVT Ensemble (page 59), higher than that, predicted in [177], taking into account the system size), $T_{IN}(c = 0.0) \approx 0.93$ and $T_{IN}(c = 1.0) \approx 1.15$. The

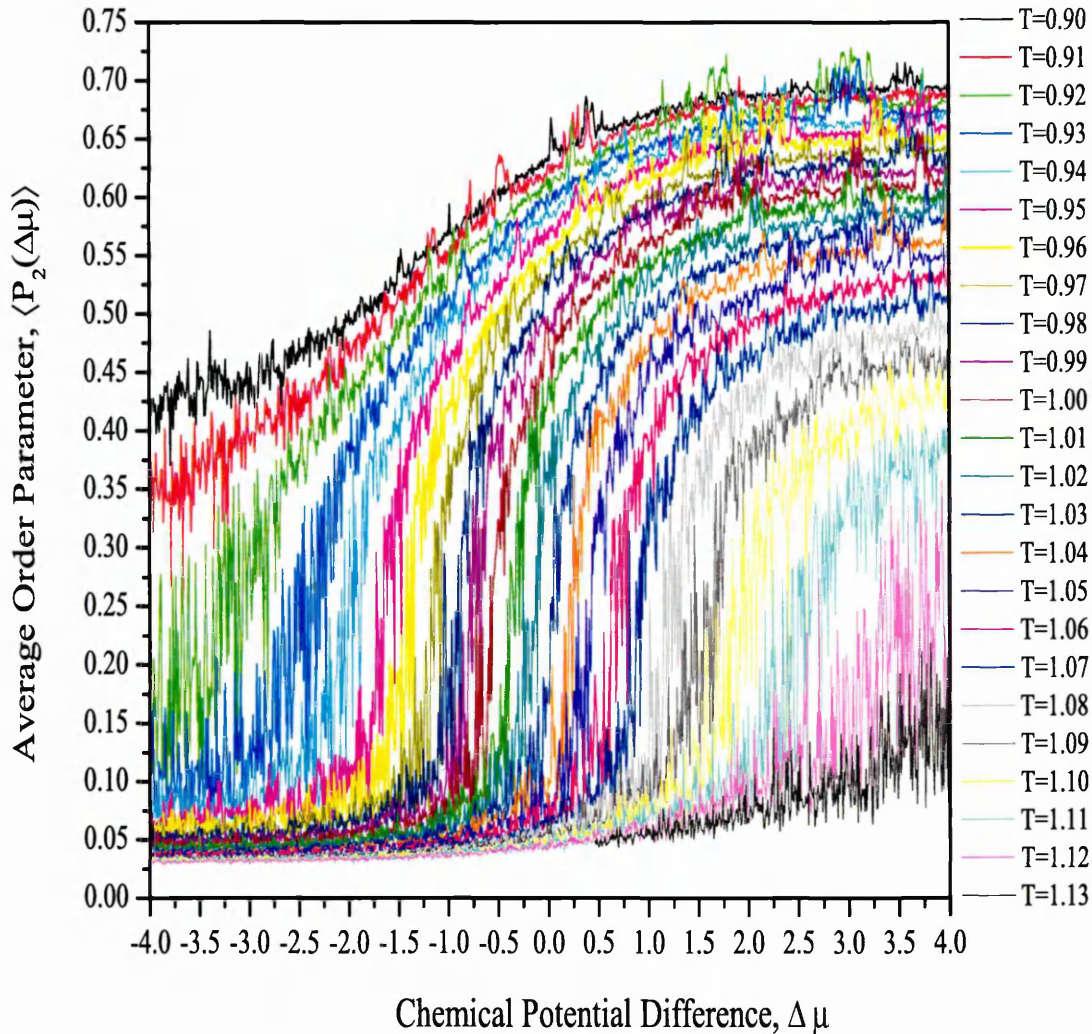


Figure 6.8: Dependence of the preferred concentration on $\Delta\mu$. $\varepsilon=0.90$. Different curves represent runs at different temperatures.

$N\Delta\mu VT$ order parameter data (Figure 6.8) agree on these values within ± 0.01 . Below $T_{IN}(c = 0.0)$ the order parameter is high and above $T_{IN}(c = 1.0)$ it remains close to zero throughout the entire concentration range. At concentrations in between, the dependence of the $T_{IN}(c)$ is approximately linear in both ensembles (NcVT and

$N\Delta\mu VT$). The system undergoes an I-N transition at all concentrations, however the coexistence boundaries remain unclear.

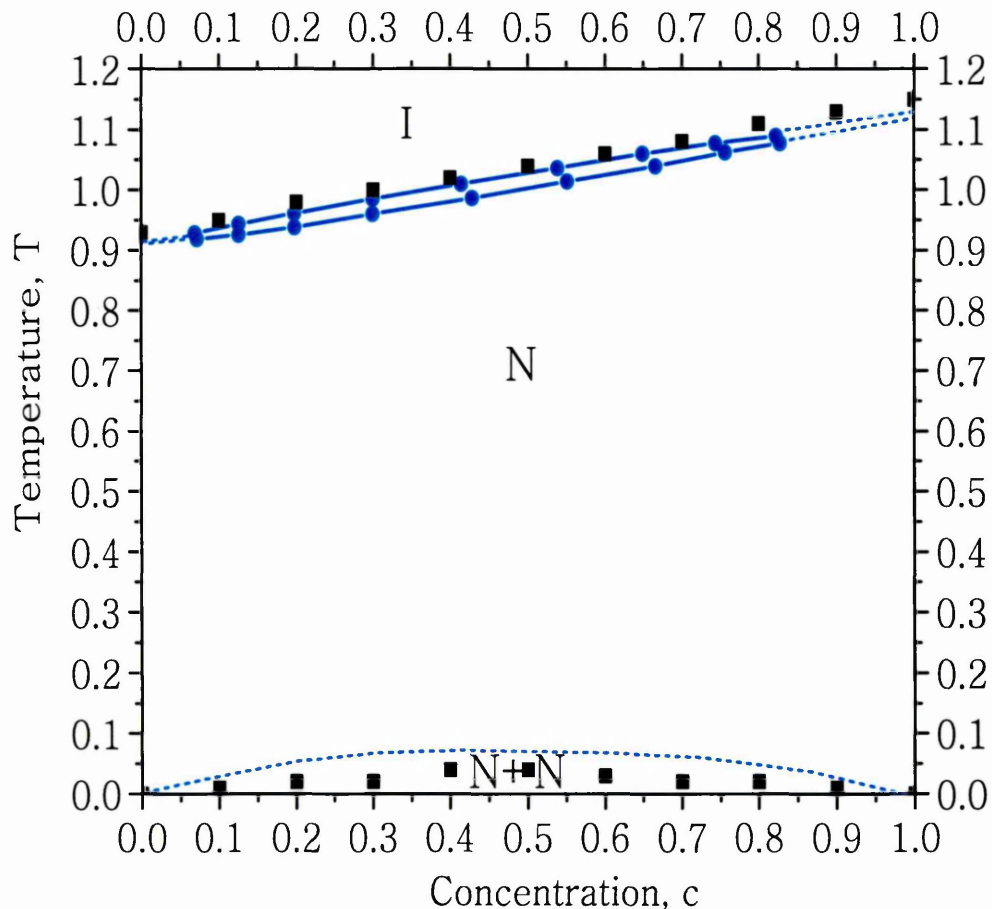


Figure 6.9: Phase diagram for the system with $\varepsilon=0.90$. Blue filled circles represent the data points obtained from $N\Delta\mu VT$ Ensemble (Figure 6.7). Filled black squares represent the data points obtained from $NcVT$ Ensemble. Dotted line represents approximation based on the data obtained from both ensembles.

At considerably lower temperatures we observe a coexistence region. This corresponds to the demixed system in which two nematic phases, each rich in one of the two components of the mixture, coexist. This area of the phase diagram is very small and does not extend for temperatures greater than $T \approx 0.06$.

The phase diagram is found to comprise four areas. In the region of high temperatures the top part of the diagram is divided by the $T_{IN}(c)$ coexistence region (with undetermined boundaries) into isotropic (above $T_{IN}(c)$) and nematic (below $T_{IN}(c)$)

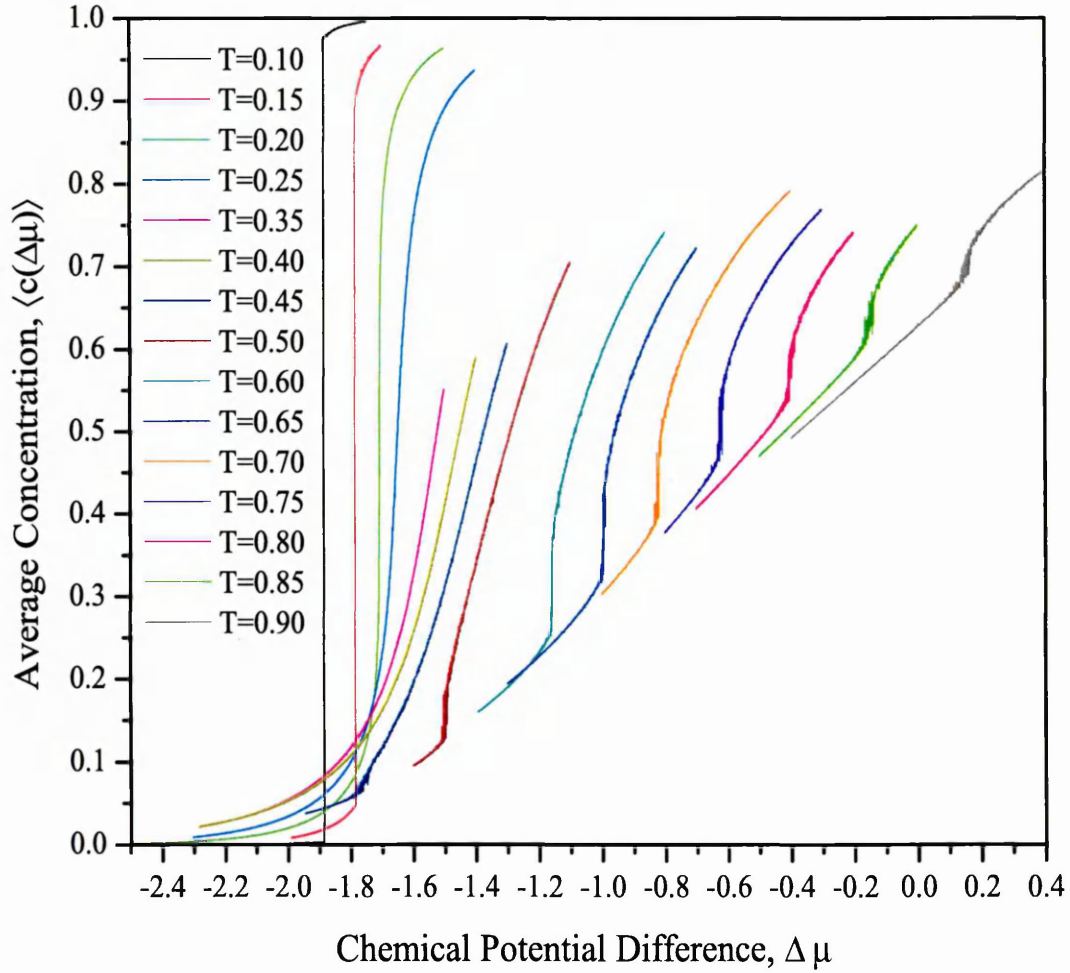


Figure 6.10: Dependence of the preferred concentration on $\Delta\mu$. $\varepsilon=0.60$. Different curves represent runs at different temperatures.

phases. The nematic region extends down to low temperatures where it meets the nematic-nematic coexistence region. The nematic-phase region in the middle occupies most of the phase space considered (Fig. 6.9).

The behaviour found here for the system with $\varepsilon = 0.90$ is therefore consistent with that obtained using the NcVT Ensemble.

We move now to the system with the coupling constant $\varepsilon = 0.6$. The behaviour of the $\langle c(\Delta\mu) \rangle$ curves for this system differs significantly from that for the system with $\varepsilon = 0.9$. There are new features not previously seen, the first of which is that

T	$\Delta\mu_{coex}$	c_1	c_2	Δc
0.1	-1.885 ± 0.005	0.00 ± 0.01	0.98 ± 0.01	0.98 ± 0.02
0.15	-1.783 ± 0.005	0.04 ± 0.01	0.91 ± 0.01	0.87 ± 0.02
0.2	-1.705 ± 0.005	0.33 ± 0.01	0.68 ± 0.01	0.35 ± 0.02
0.25	-1.647 ± 0.005	N/A	N/A	N/A
0.3-0.4	N/A	N/A	N/A	N/A
0.45	-1.759 ± 0.005	0.06 ± 0.01	0.08 ± 0.01	0.02 ± 0.02
0.5	-1.498 ± 0.005	0.12 ± 0.01	0.18 ± 0.01	0.06 ± 0.02
0.6	-1.159 ± 0.005	0.24 ± 0.01	0.39 ± 0.01	0.15 ± 0.02
0.65	-0.995 ± 0.005	0.32 ± 0.01	0.51 ± 0.01	0.19 ± 0.02
0.7	-0.822 ± 0.005	0.39 ± 0.01	0.57 ± 0.01	0.18 ± 0.02
0.75	-0.625 ± 0.005	0.47 ± 0.01	0.60 ± 0.01	0.13 ± 0.02
0.8	-0.397 ± 0.005	0.54 ± 0.01	0.64 ± 0.01	0.10 ± 0.02
0.85	-0.145 ± 0.005	0.61 ± 0.01	0.66 ± 0.01	0.05 ± 0.02
0.9	0.156 ± 0.005	0.68 ± 0.01	0.72 ± 0.01	0.04 ± 0.02

Table 6.1: Table of coexistence concentrations (c_1 and c_2), their difference (Δc), the corresponding chemical potential difference ($\Delta\mu_{coex}$) as a function of temperature (T). The system with $\varepsilon = 0.6$. Criteria of defining these were set out in Section 6.1.

curves taken at different temperatures vary not only in their slopes, but also in the position at which the slope is steepest on the $\Delta\mu$ axis. The second novel feature is that gradient discontinuities in the $\langle c(\Delta\mu) \rangle$ curves occur over a larger range of temperature values.

Let us consider the curve taken at the highest temperature on the graph, $T = 0.9$. Starting from the highest value of $\Delta\mu$, the preferred concentration of the system is high (for example, for $\Delta\mu = 0.40$, $c \approx 0.817$). As $\Delta\mu$ falls the concentration of the system decreases continuously. Then, at $\Delta\mu_{coex} \approx 0.156$, the concentration changes quite rapidly with change in $\Delta\mu$, after which the gradient changes and the concentration reverts to approximately linear behaviour. In the vicinity of these rapid changes ($\Delta\mu_{coex} \approx 0.156$), the system seems to have two preferred concentrations for the same value of $\Delta\mu$. As the temperature decreases, the discontinuity in $\langle c(\Delta\mu) \rangle$ shifts to progressively lower values of $\Delta\mu$. This discontinuity relates to the narrow coexistence concentrations, equivalent to these occurring at temperature $T = 0.9$. The difference between these concentrations varies with the temperature, but overall they both move towards lower values as the temperature decreases.

Initially, as the temperature is decreased, the distance between the two preferred concentrations $\Delta c = c_2 - c_1$ increases, reaching its maximum value at $T \approx 0.6$.

Then Δc decreases and eventually vanishes as the temperature approaches 0.4. For the interval of temperatures $0.25 \lesssim T \lesssim 0.4$, the slope of the $\langle c(\Delta\mu) \rangle$ curve is finite from $c = 1.0$ to $c = 0.0$ as $\Delta\mu$ decreases.

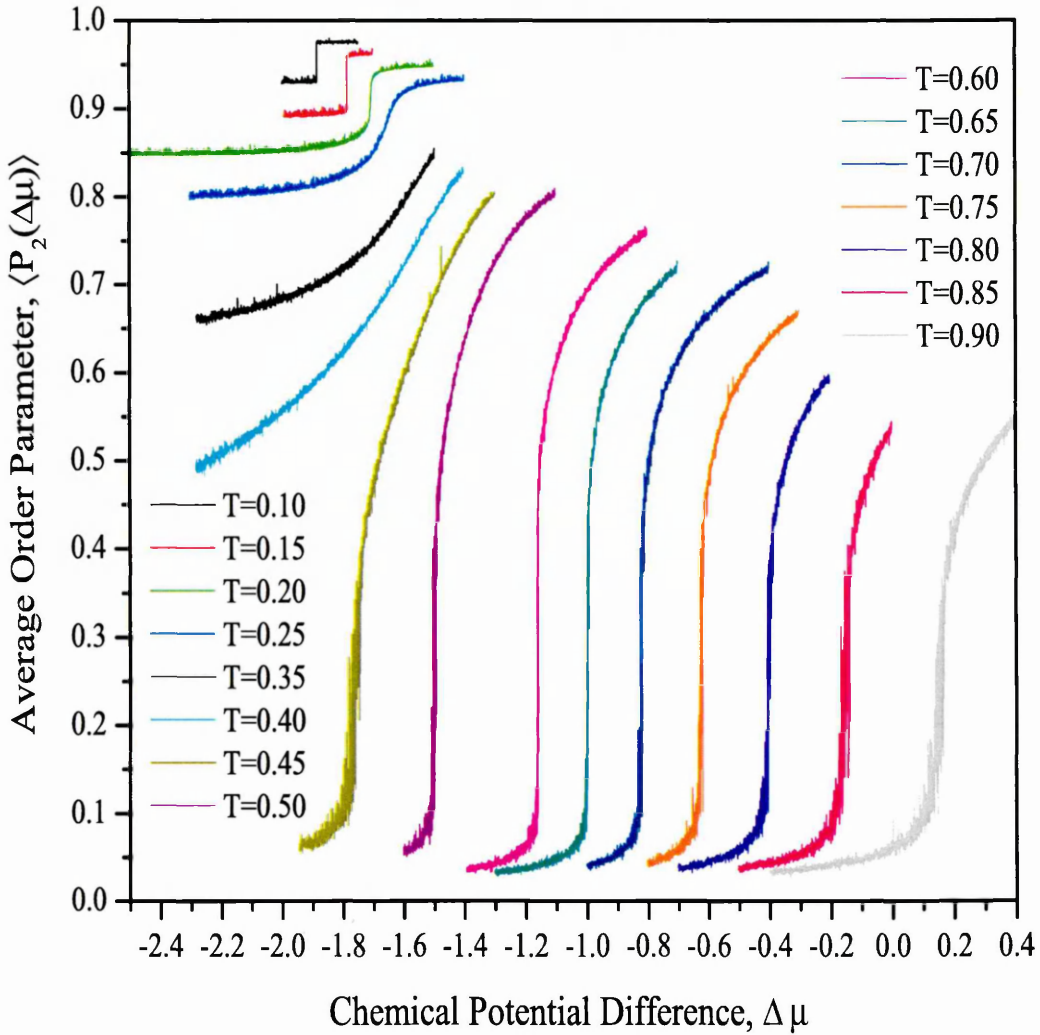


Figure 6.11: Order Parameter dependence on $\Delta\mu$ for the system with $\varepsilon=0.60$.

The discontinuity in the $\langle c(\Delta\mu) \rangle$ curve reappears with a further decrease in the temperature at $T \approx 0.2$. However, the difference between the two preferred concentrations, Δc , is much greater than that observed for higher temperatures. As $T \rightarrow 0.0$ the distance between the two preferred concentrations Δc grows, with $c_1 \rightarrow 1.0$ and $c_2 \rightarrow 0.0$. The values of these concentrations are presented in Table 6.1.

The variation of the order parameter with $\Delta\mu$ is shown in Figure 6.11. The different curves represent the order parameter for different temperatures. Let us consider the

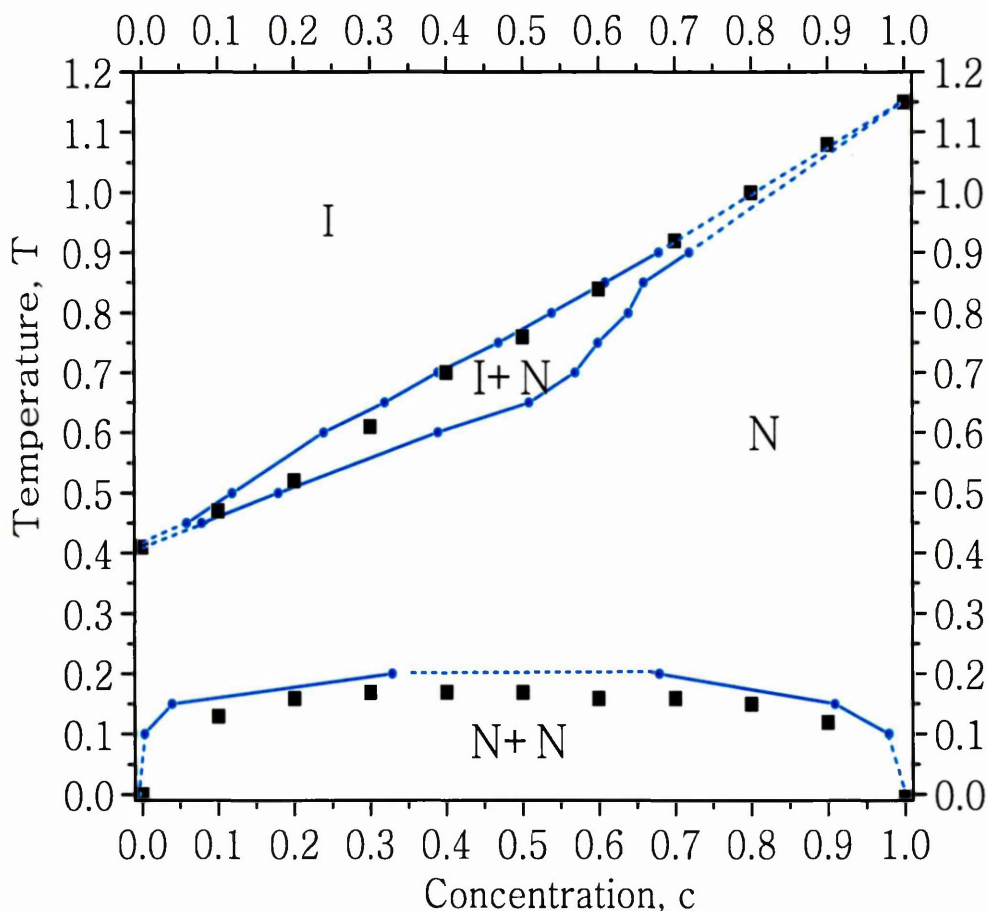


Figure 6.12: Phase diagram for the system with $\varepsilon=0.60$. Blue filled circles represent the data points obtained from $N\Delta\mu VT$ Ensemble. Filled black squares represent the data points obtained from $NcVT$ Ensemble. Dotted line represents approximation based on data obtained from both ensembles.

curve taken at the highest temperature on the graph, $T = 0.9$. Starting from the highest $\Delta\mu$, the preferred order parameter of the system is high, corresponding to the nematic phase (for example for $\Delta\mu = 0.40$ $\langle P_2 \rangle \approx 0.548$). As $\Delta\mu$ falls, the order parameter of the system decreases with a steady gradient. Then, at $\Delta\mu \approx 0.156$, as the concentration curve shown in Figure 6.10 decreases rapidly, so $\langle P_2(\Delta\mu) \rangle$ changes quite rapidly, approaching zero. For temperatures in the range $0.45 \lesssim T \lesssim 0.9$, the order parameter similarly changes rapidly from a non zero to a close-to-zero

value at the previously identified $\Delta\mu_{coex}(T)$ values. At temperatures in the range $0.25 \lesssim T \lesssim 0.40$ the value of $\langle P_2(\Delta\mu) \rangle$ decreases continuously with decrease in $\Delta\mu$, but remains non-zero throughout the entire range of $\Delta\mu$. At temperatures $T \lesssim 0.20$, the order parameter changes rapidly from one non-zero value to another, lower, non-zero value as $\Delta\mu$ decreases.

From the data presented above we were able to construct the phase diagram (blue-filled circles) shown in Figure 6.12. The black-filled squares in this figure represent equivalent data from the NcVT Ensemble discussed in the previous Chapter. A comparison of the two sets of results will be presented in Section 6.5.

Let us comment first of all on the isotropic-nematic coexistence region ($T_{IN}(c_1, c_2)$ region). It is assumed that the system undergoes an I-N transition at the temperatures of its pure components at both ends of the concentration axis, i.e. $T_{IN}(c = 0.0) \approx 0.41$ and $T_{IN}(c = 1.0) \approx 1.15$ (from NcVT Ensemble). At intermediate concentrations, the variation of $T_{IN}(c_1, c_2)$ is approximately linear. The system undergoes an I-N transition at all concentrations. The order parameter data for this system indicate the presence of the isotropic and nematic phases, respectively, above and below the $T_{IN}(c_1, c_2)$ region. The $c(\Delta\mu)$ data indicate that the system is homogeneous at temperatures above and below the transition throughout the entire concentration range. The region is wider in the middle of the diagram and narrows towards concentrations $c = 0.0$ and $c = 1.0$.

However, at considerably lower temperatures we observe another coexistence region. This corresponds to the demixed system in which two nematic phases, each rich in one of the two components of the mixture, coexist. This area of the phase diagram remains relatively small, but its shape appears to be slightly asymmetric, c_1 on the left of the diagram being further from the centre than c_2 on the right (Fig. 6.12).

The diagram comprises four areas. In the region of low concentration at the top of the diagram the isotropic phase has extended into a lower temperature region, as compared to the system with $\varepsilon = 0.9$. However, the nematic mixed phase still occupies most of the phase space considered (Fig. 6.12) with the narrow lens-shaped region (isotropic-nematic coexistence) separating this phase from the isotropic phase above. The bottom part of the diagram contains an increased nematic-nematic coexistence region. The behaviour of the system with $\varepsilon = 0.60$ is consistent with

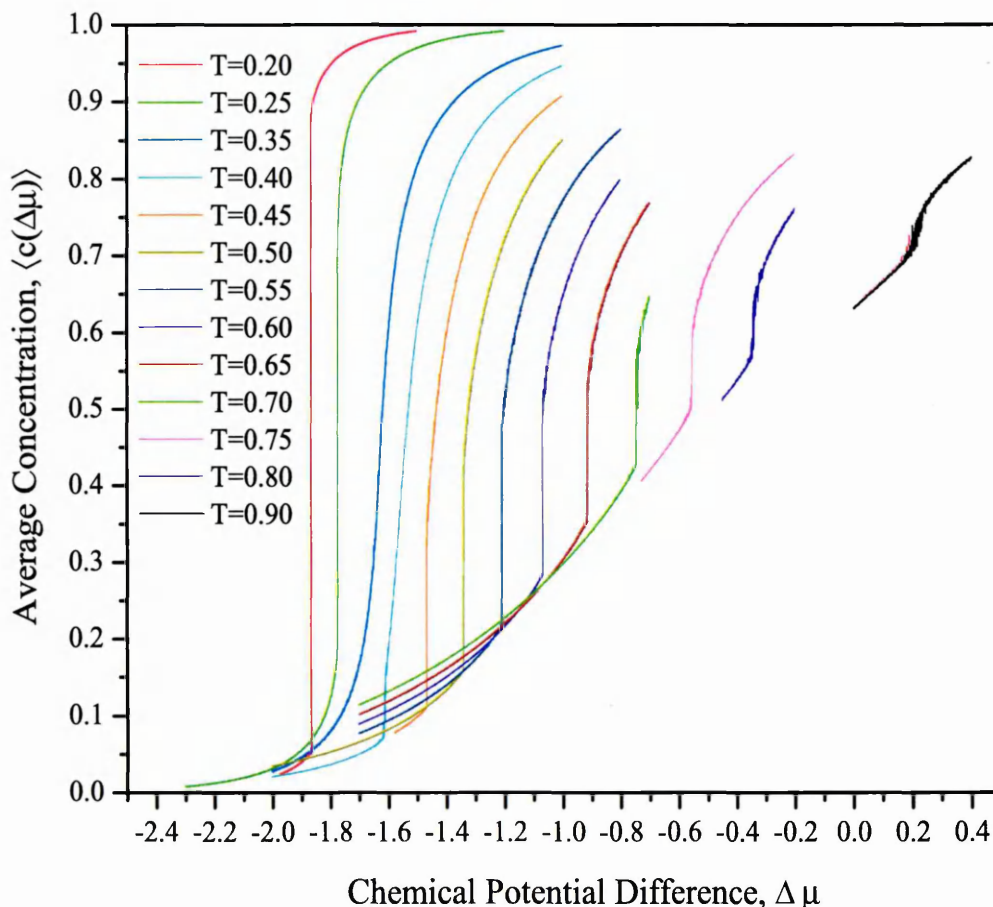


Figure 6.13: Dependence of the preferred concentration on $\Delta\mu$. $\varepsilon=0.55$. Different curves represent runs at different temperatures.

that found for the system with $\varepsilon = 0.90$, the differences, however, being the size of the demixing envelope of N+N coexistence and the fact that the I-N coexistence region, not seen in the system with $\varepsilon = 0.90$, became clearly evident in the system with $\varepsilon = 0.60$.

We move now to the system with the coupling constant $\varepsilon = 0.55$. In Fig.6.13 we present the $\langle c(\Delta\mu) \rangle$ curves obtained at various temperatures for this system.

The behaviour of the $\langle c(\Delta\mu) \rangle$ curves for this system differs only slightly from that for the system with $\varepsilon = 0.6$, the values of $\Delta\mu_{coex}$ for high temperature system being at slightly higher values of $\Delta\mu$. Starting from the highest temperature on the graph, $T = 0.9$, the preferred concentration of the system for $\Delta\mu = -0.40$ is

T	$\Delta\mu_{coex}$	c_1	c_2	Δc
0.2	-1.862 ± 0.005	0.05 ± 0.01	0.89 ± 0.01	0.84 ± 0.02
0.25	-1.770 ± 0.005	0.19 ± 0.01	0.78 ± 0.01	0.59 ± 0.02
0.35	-1.628 ± 0.005	<i>N/A</i>	<i>N/A</i>	<i>N/A</i>
0.40	-1.610 ± 0.005	0.07 ± 0.01	0.15 ± 0.01	0.08 ± 0.02
0.45	-1.463 ± 0.005	0.11 ± 0.01	0.37 ± 0.01	0.26 ± 0.02
0.5	-1.339 ± 0.005	0.16 ± 0.01	0.44 ± 0.01	0.28 ± 0.02
0.55	-1.206 ± 0.005	0.21 ± 0.01	0.48 ± 0.01	0.27 ± 0.02
0.6	-1.071 ± 0.005	0.28 ± 0.01	0.52 ± 0.01	0.24 ± 0.02
0.65	-0.914 ± 0.005	0.35 ± 0.01	0.54 ± 0.01	0.19 ± 0.02
0.7	-0.743 ± 0.005	0.42 ± 0.01	0.57 ± 0.01	0.15 ± 0.02
0.75	-0.555 ± 0.005	0.49 ± 0.01	0.61 ± 0.01	0.12 ± 0.02
0.8	-0.339 ± 0.005	0.57 ± 0.01	0.67 ± 0.01	0.10 ± 0.02
0.9	0.218 ± 0.005	0.70 ± 0.01	0.75 ± 0.01	0.05 ± 0.02

Table 6.2: Table of coexistence concentrations (c_1 and c_2), their difference (Δc), the corresponding chemical potential difference ($\Delta\mu_{coex}$) as a function of temperature (T). The system with $\varepsilon = 0.55$. Criteria of defining these were set out in Section 6.1.

$c \approx 0.828$. As $\Delta\mu$ decreases, the concentration of the system falls continuously until, at $\Delta\mu \approx 0.218$, the $\langle c(\Delta\mu) \rangle$ curve exhibits a discontinuity in its gradient with preferred concentrations $c_1 \approx 0.718$ and $c_2 \approx 0.746$. At lower temperatures this discontinuity becomes more marked. At $T = 0.7$, for example, the curve changes abruptly from $c_2 \approx 0.557$ to $c_1 \approx 0.425$ at $\Delta\mu_{coex} \approx 0.745$.

As the temperature continues to decrease, the discontinuity in the $\langle c(\Delta\mu) \rangle$ curve occurs at successively lower values of $\Delta\mu$. The two preferred concentrations, which correspond to each discontinuity $\Delta\mu_{coex}(T)$, are different for each temperature. The difference Δc between these concentrations varies with the temperature, but overall both concentration values decrease as the temperature decreases. Initially, as the temperature is decreased, Δc increases, approaching its maximum value of $\Delta c \approx 0.283$ at temperature $T = 0.5$. Δc then decreases and eventually vanishes as the temperature approaches 0.35. In the interval of temperatures $0.30 \lesssim T \lesssim 0.35$, the slope of the $\langle c(\Delta\mu) \rangle$ curve remains finite from $c = 1.0$ to $c = 0.0$ as $\Delta\mu$ decreases.

The discontinuity in $\langle c(\Delta\mu) \rangle$ appears again at temperature $T \approx 0.25$, with the difference between the two preferred concentrations being $\Delta c = 0.622$. As $T \rightarrow 0.0$ Δc grows, and approaches its maximum ($\Delta c = 1.0$).

This behaviour is generally the same as that shown in Figure 6.10 for the system with $\varepsilon = 0.60$. We observe a small values for Δc at high temperatures and larger ones at low temperatures. As in the previous cases, there are temperatures at which no discontinuity is found across the entire $\Delta\mu$ region. However, the range of these temperatures is smaller than that found previously ($0.3 \lesssim T \lesssim 0.34$). The high temperature discontinuity follows the tendency observed in previous systems. The concentrations relating to $\Delta\mu_{coex}(T)$ depend more strongly on the changes in temperature, compared with those for systems with higher ε . In addition, in the region of temperatures $0.4 \lesssim T \lesssim 0.7$ the width Δc increases to a greater extent, compared to the previous system. These concentrations are set out in Table 6.2.

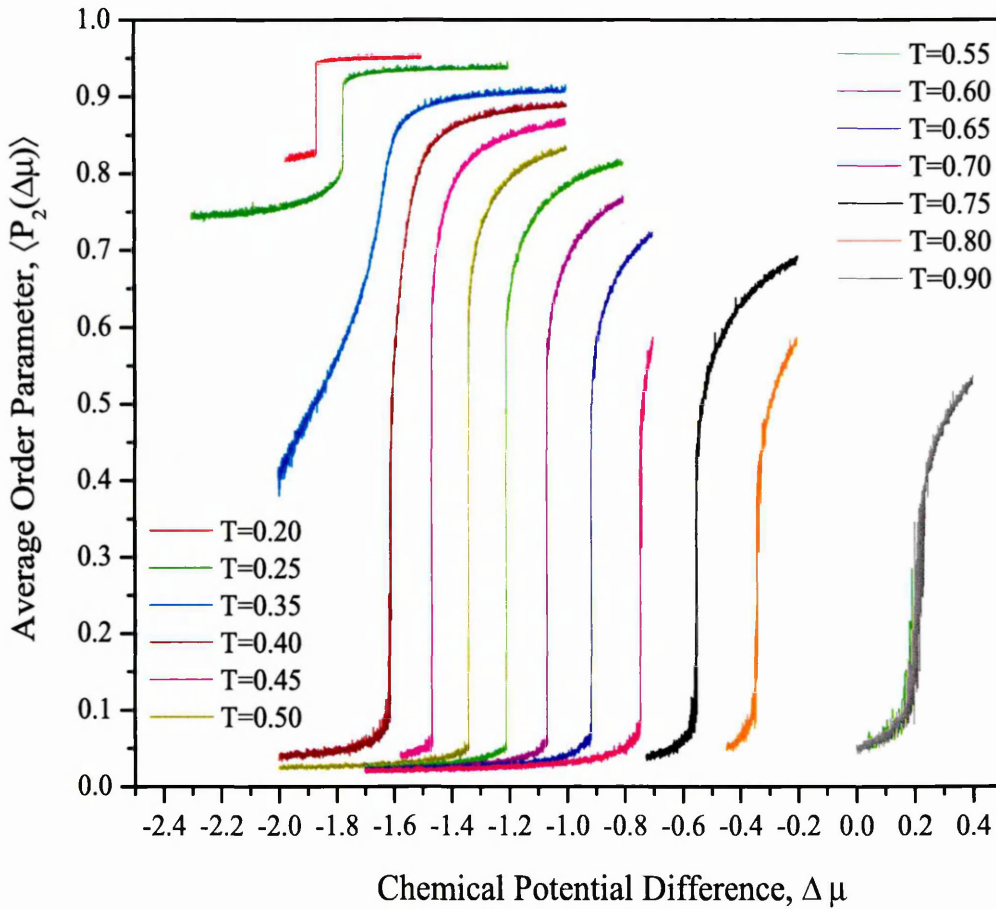


Figure 6.14: Dependence of the preferred order parameter on $\Delta\mu$. $\varepsilon=0.55$.

The order parameter dependence on $\Delta\mu$ and T is shown in Figure 6.14. Let us consider the curve taken at the highest temperature on the graph, $T = 0.9$. Starting from the highest $\Delta\mu$, the preferred order parameter of the system is high, indicating

the nematic phase (for example for $\Delta\mu = 0.40$, $\langle P_2(\Delta\mu) \rangle \approx 0.536$). As $\Delta\mu$ falls, the order parameter decreases with a steady gradient. Then, at $\Delta\mu \approx 0.218$, $\langle P_2(\Delta\mu) \rangle$ changes quite rapidly and approaches zero. In the vicinity of $\Delta\mu \approx 0.218$ further analysis shows that the system has two preferred order parameters, corresponding to the nematic and isotropic phases for c_2 and c_1 respectively.

For temperatures in the range $0.40 \lesssim T \lesssim 0.9$, the order parameter changes rapidly from a non-zero to zero value at $\Delta\mu_{coex}(T)$. At temperatures around $T \approx 0.35$ the value of $\langle P_2(\Delta\mu) \rangle$ decreases rapidly at first from approximately 0.86 to 0.7, and then decreases continuously with $\Delta\mu$. At temperatures $T \lesssim 0.25$ the order parameter changes rapidly from one non-zero value to another, lower, non-zero value as $\Delta\mu$ decreases.

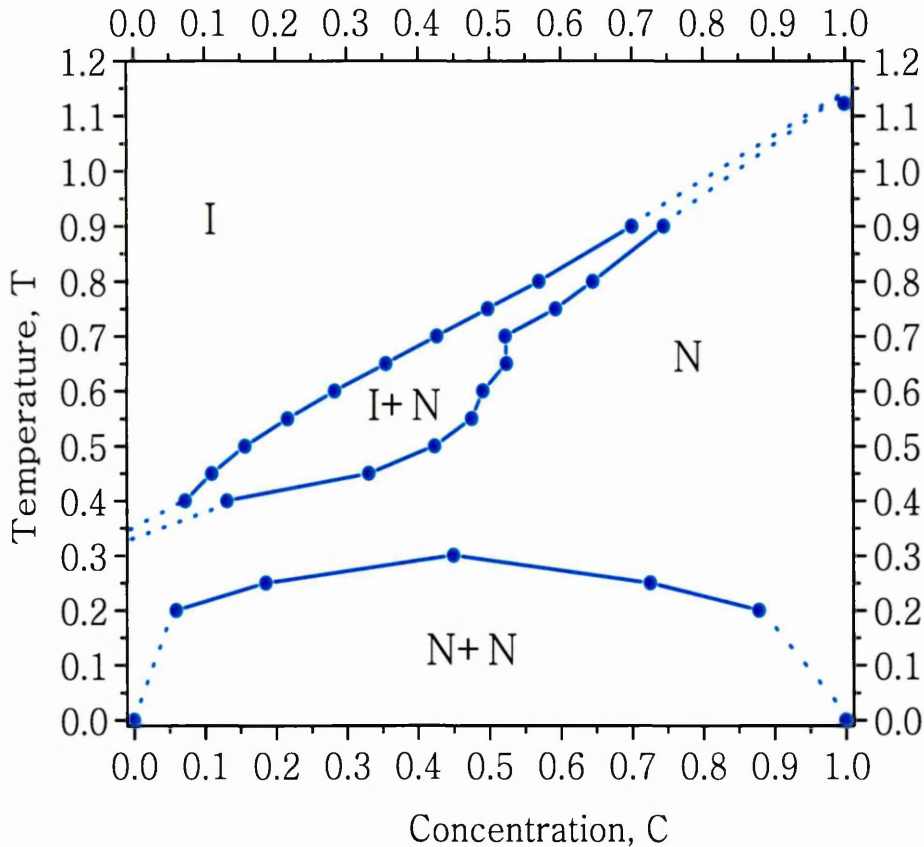


Figure 6.15: Phase diagram for the system with $\varepsilon=0.55$. Blue filled circles represent the data points obtained from $N\Delta\mu VT$ Ensemble. Dotted line represents approximation based on the data obtained from both ensembles.

From the data presented above we have constructed the phase diagram shown in Figure 6.15. Let us start with the isotropic-nematic coexistence region ($T_{IN}(c_1, c_2)$ region). At both ends of the concentration axis ($c = 0.0$ and $c = 1.0$), the system

exhibits an I-N transition at the temperatures $T_{IN}(c = 0.0) \approx 0.35$ and $T_{IN}(c = 1.0) \approx 1.15$ (these are taken from the energy calculations of the previous chapter). At concentrations other than $c = 0.0$ and $c = 1.0$, the upper boundary of the $T_{IN}(c_1, c_2)$ region varies approximately linearly with c . The lower boundary of the $T_{IN}(c_1, c_2)$ region extends in the area of low concentrations, creating a bulge in the coexistence envelope in the middle of the diagram. The $\langle c(\Delta\mu) \rangle$ data indicate nevertheless that the system is homogeneous at temperatures above and below the transition ($T_{IN}(c_1, c_2)$) throughout the entire concentration range.

Another region, which we observe at considerably lower temperatures - the coexistence of the two nematic phases - has increased significance when compared with the system with $\varepsilon = 0.6$. Again, a slight asymmetry is apparent in the coexistence boundaries of this region.

As in the case of the previous system ($\varepsilon = 0.6$), the diagram comprises four regions. In the region of low concentration on the top of the diagram the isotropic phase has extended further into the lower temperature region, as compared to the previous system. The nematic-nematic coexistence region in the bottom of the diagram has also increased in size. As a result, the nematic phase in the middle of the diagram now occupies approximately the same area as the isotropic phase (Fig. 6.15). The nematic and the isotropic phases are separated by the region of the isotropic-nematic coexistence region, which has now become distorted for $0.15 < c < 0.5$.

6.3 System with $\varepsilon = 0.53$, $\varepsilon = 0.52$, $\varepsilon = 0.50$

According to the predictions set out in the previous Chapter, we would expect to see a merger of the two coexistence regions at $\varepsilon \approx 0.52$. The results for systems with $\varepsilon = 0.90$, $\varepsilon = 0.60$ and $\varepsilon = 0.55$ show that the range of temperatures for which there is no phase coexistence for any concentration decreases with the decrease of ε . For this reason, we made more detailed measurements in the region between $\varepsilon = 0.55$ and $\varepsilon = 0.45$, investigating systems with $\varepsilon = 0.53$, $\varepsilon = 0.52$, $\varepsilon = 0.50$.

Following the same procedure as that adopted in the previous section, we consider first the dependence of the average concentration of the mixture with $\varepsilon = 0.53$ on the chemical potential difference $\langle c(\Delta\mu) \rangle$ (Figure 6.16).

The behaviour of $\langle c(\Delta\mu) \rangle$ curves for the system differs only slightly from that observed for the system with $\varepsilon = 0.55$. For each temperature there is a unique value of $\Delta\mu_{coex}(T)$ and two preferred concentrations $c_1(T)$ and $c_2(T)$. As the tempera-

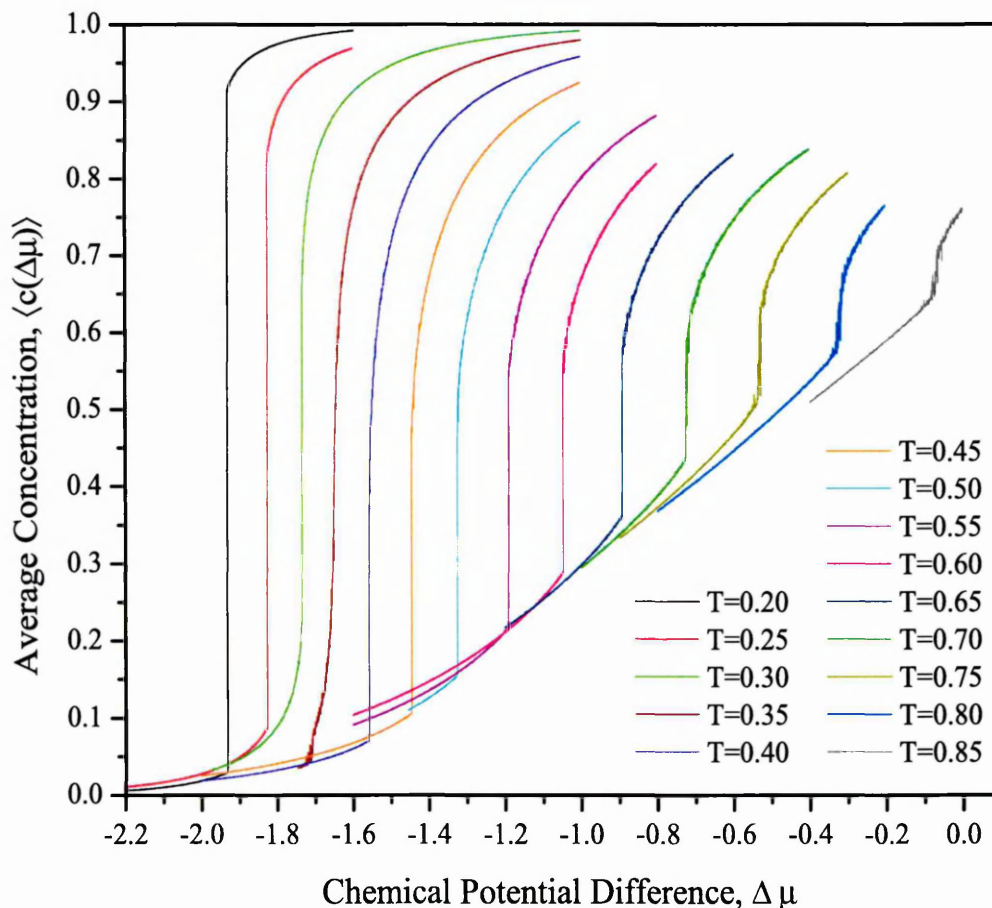


Figure 6.16: Dependence of the preferred concentration on $\Delta\mu$. $\varepsilon=0.53$. Different curves represent runs at different temperatures.

ture decreases the distance between the two preferred concentrations Δc increases, reaching its maximum value of $\Delta c \approx 0.46$ at temperature $T = 0.45$. Then Δc decreases and eventually vanishes as the temperature decreases shortly below 0.35 (Figure 6.17, Table 6.3). This system is unlike the previous two systems ($\varepsilon = 0.60$ and $\varepsilon = 0.55$), in that there is no temperature at which the $\langle c(\Delta\mu) \rangle$ curve changes continuously from $c = 1.0$ to $c = 0.0$ as $\Delta\mu$ decreases. Instead, in the temperature interval $0.33 < T < 0.36$, the $\langle c(\Delta\mu) \rangle$ curve experiences two discontinuities as $\Delta\mu$ changes.

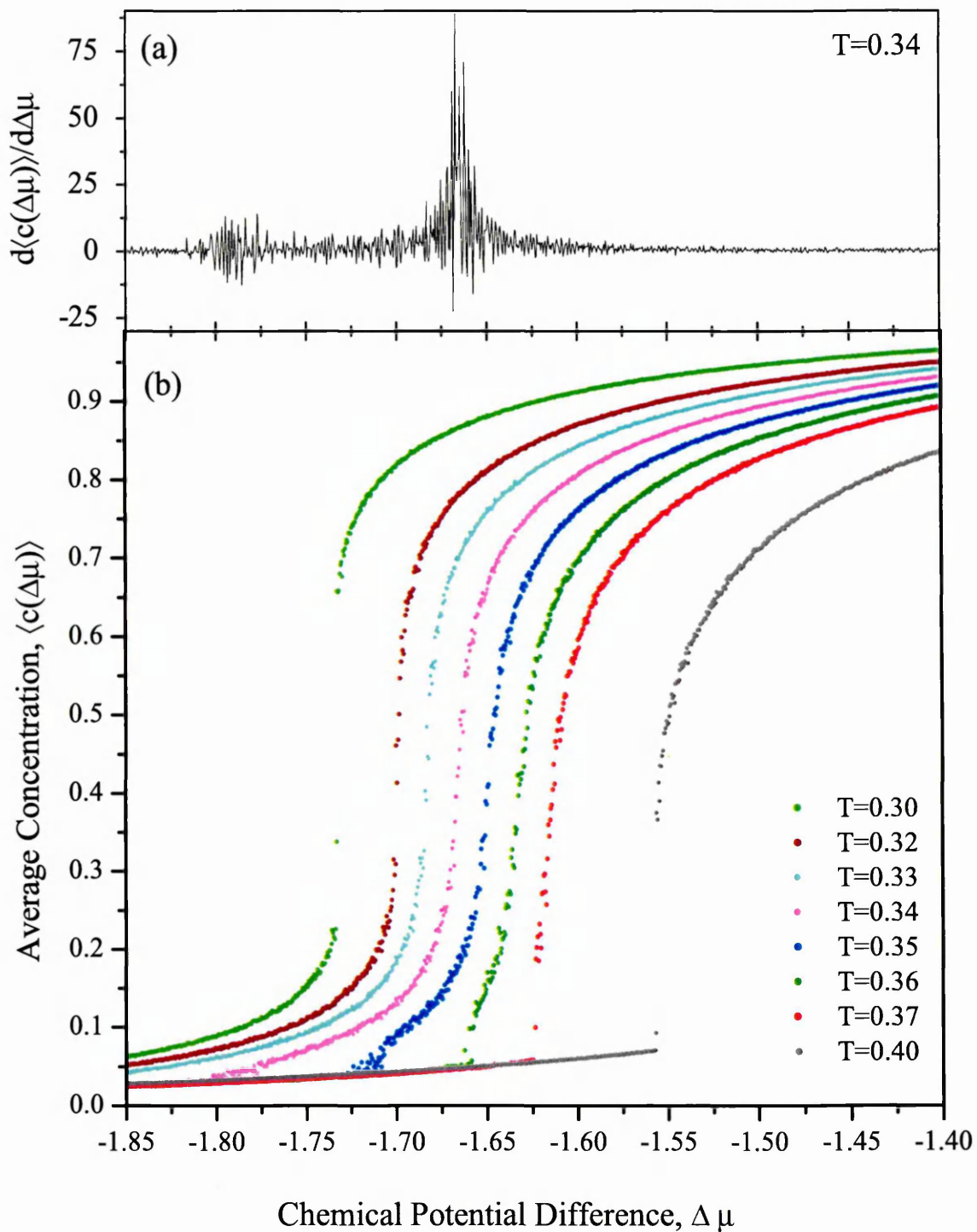


Figure 6.17: Dependence of the preferred concentration on $\Delta\mu$ for temperatures $0.30 \leq T \leq 0.40$ (b). Numerical differential of the $\langle c(\Delta\mu)\rangle$ curve at $T = 0.34$ (a). System with $\varepsilon = 0.53$.

T	c_1	c_2	c'_1	c'_2	Δc	$\Delta c'$
0.30	0.20 ± 0.01	0.67 ± 0.01	N/A	N/A	0.47 ± 0.02	N/A
0.32	0.32 ± 0.01	0.55 ± 0.01	N/A	N/A	0.23 ± 0.02	N/A
0.33	0.32 ± 0.01	0.50 ± 0.01	N/A	N/A	0.18 ± 0.02	N/A
0.34	0.35 ± 0.01	0.45 ± 0.01	0.03 ± 0.01	0.04 ± 0.01	0.10 ± 0.02	0.01 ± 0.02
0.35	0.40 ± 0.01	0.40 ± 0.01	0.04 ± 0.01	0.07 ± 0.01	0.00 ± 0.02	0.03 ± 0.02
0.36	N/A	N/A	0.05 ± 0.01	0.11 ± 0.01	N/A	0.06 ± 0.02
0.37	N/A	N/A	0.05 ± 0.01	0.19 ± 0.01	N/A	0.14 ± 0.02
0.40	N/A	N/A	0.06 ± 0.01	0.49 ± 0.01	N/A	0.43 ± 0.02

Table 6.3: Table of concentrations c_1 , c_2 and c'_1 , c'_2 and their difference (Δc and $\Delta c'$) that occur at single temperature (T). Data reflect Figure 6.17(b) for the system with $\varepsilon = 0.53$. Criteria of defining these were set out in Section 6.1.

T	$\Delta\mu_{coex}$	c_1	c_2	Δc
0.2	-1.930 ± 0.005	0.02 ± 0.01	0.92 ± 0.01	0.90 ± 0.02
0.25	-1.825 ± 0.005	0.08 ± 0.01	0.83 ± 0.01	0.75 ± 0.02
0.30	-1.734 ± 0.005	0.20 ± 0.01	0.67 ± 0.01	0.47 ± 0.02
0.40	-1.558 ± 0.005	0.06 ± 0.01	0.49 ± 0.01	0.43 ± 0.02
0.45	-1.443 ± 0.005	0.10 ± 0.01	0.56 ± 0.01	0.46 ± 0.02
0.5	-1.323 ± 0.005	0.15 ± 0.01	0.58 ± 0.01	0.43 ± 0.02
0.55	-1.186 ± 0.005	0.21 ± 0.01	0.58 ± 0.01	0.37 ± 0.02
0.6	-1.045 ± 0.005	0.28 ± 0.01	0.57 ± 0.01	0.29 ± 0.02
0.65	-0.891 ± 0.005	0.36 ± 0.01	0.58 ± 0.01	0.22 ± 0.02
0.7	-0.752 ± 0.005	0.43 ± 0.01	0.59 ± 0.01	0.16 ± 0.02
0.75	-0.530 ± 0.005	0.50 ± 0.01	0.64 ± 0.01	0.14 ± 0.02
0.8	-0.316 ± 0.005	0.56 ± 0.01	0.66 ± 0.01	0.10 ± 0.02
0.85	-0.067 ± 0.005	0.65 ± 0.01	0.71 ± 0.01	0.06 ± 0.02

Table 6.4: Table of two preferred concentrations (c_1 and c_2) and their difference (Δc) that occur at unique value of the chemical potential difference ($\Delta\mu_{coex}$) for any given temperature (T). The system with $\varepsilon = 0.53$. Criteria of defining these were set out in Section 6.1.

This feature can be seen more clearly in the results for these temperatures presented in Figure 6.17(b). The curve at $T = 0.34$ suggests a presence of the two discontinuities: one at $\Delta\mu_{coex} \approx -1.667$ with corresponding concentrations $c_1 \approx 0.35$, $c_2 \approx 0.45$ and another at $\Delta\mu_{coex} \approx -1.791$ with corresponding concentrations $c'_1 \approx 0.03$, $c'_2 \approx 0.04$ (Figure 6.17(b)). Numerical differentiation shows the location of these two discontinuities more clearly (Figure 6.17(a)). Any change in the temperature results in the disappearance of one of these discontinuities (Figure 6.17, Table 6.3).

Below $T = 0.34$ there is only one discontinuity in the gradient of $\langle c \rangle(\Delta\mu)$ present. As temperature decreases further the distance between two preferred concentrations Δc for that discontinuity becomes larger and approaches its maximum of $\Delta c = 1.0$ as $T \rightarrow 0.0$. The table of all remaining concentrations is presented in Table 6.4.

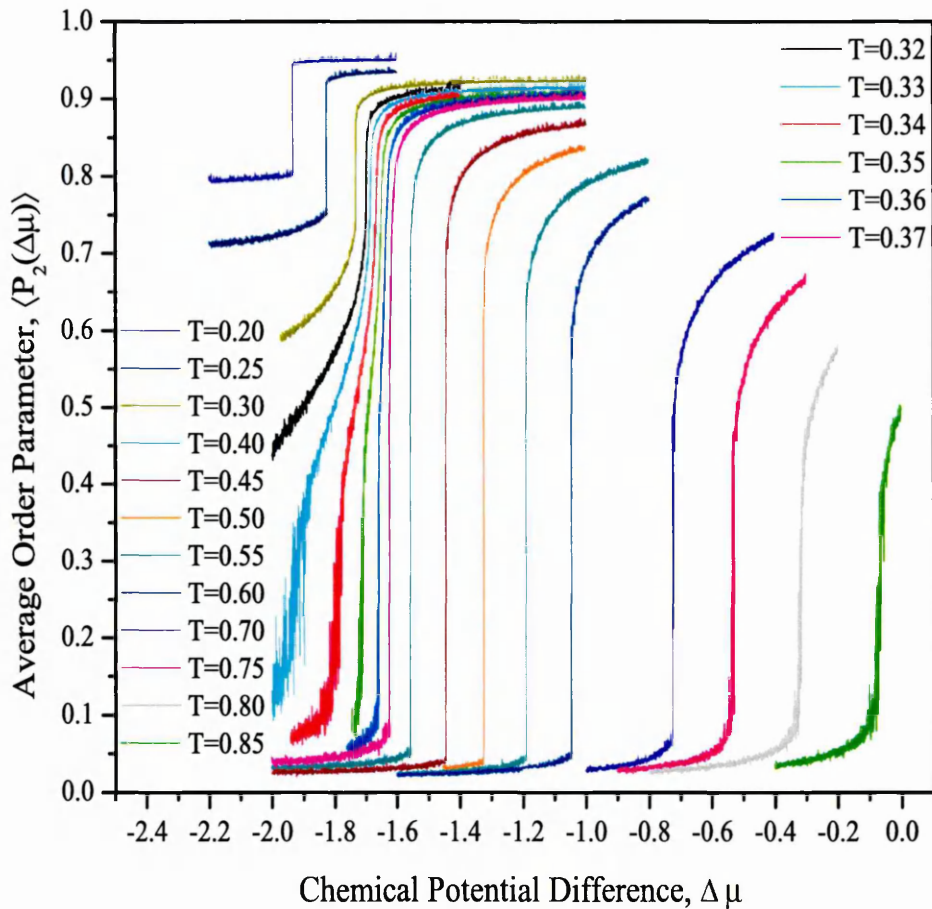


Figure 6.18: Dependence of the preferred Order Parameter on $\Delta\mu$. $\varepsilon=0.53$.

The corresponding $\langle P_2(\Delta\mu) \rangle$ data are shown in Figure 6.18, different curves representing the order parameter variation for different temperatures. For temperatures in the range $0.37 \lesssim T \lesssim 0.9$, the order parameter changes rapidly from a non-zero to a zero value at $\Delta\mu_{coex}(T)$. The differences between values of $\langle P_2(\Delta\mu) \rangle$ on both sides of $\Delta\mu_{coex}(T)$ are higher than those found for the system with $\varepsilon = 0.55$. At

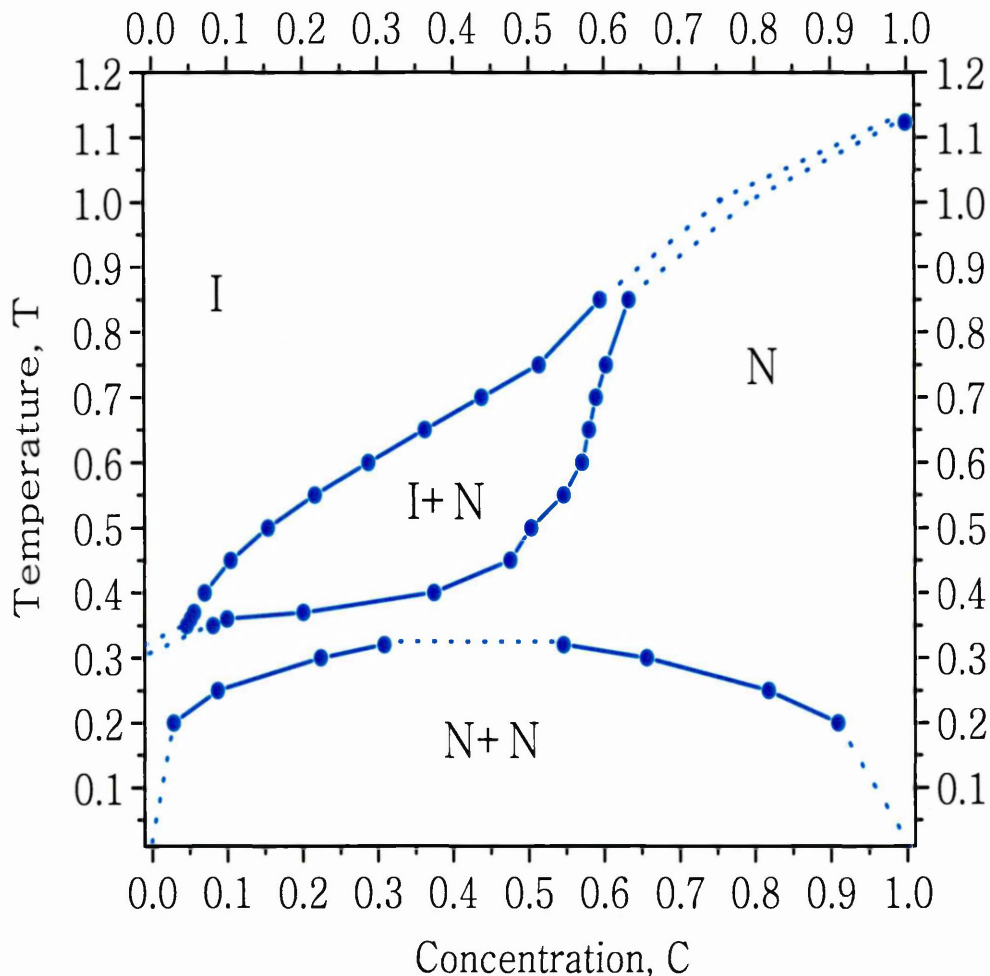


Figure 6.19: Phase diagram for the system with $\varepsilon=0.53$. Blue filled circles represent the data points obtained from $N\Delta\mu VT$ Ensemble. Dotted line represents approximation based on the data obtained from both ensembles.

temperatures below $T \approx 0.37$ the value of $\langle P_2(\Delta\mu) \rangle$ decreases rapidly twice. First it decreases sharply from a high positive to a slightly lower, positive value as $\Delta\mu$ decreases. Then it decreases steadily for a short while, which is followed by another

rapid decrease to a close-to-zero value. This double decrease is more clearly seen at $T \approx 0.35$, $T \approx 0.34$, $T \approx 0.33$. At temperatures $T \lesssim 0.25$ the order parameter changes rapidly from one non-zero value to another, lower, non-zero value as $\Delta\mu$ decreases.

The phase diagram, constructed from the data presented above, is shown in Figure 6.19. For all concentrations the dependence of $T_{IN}(c_1, c_2)$ is approximately linear at its boundary with the isotropic phase (c_1). The system still undergoes an I-

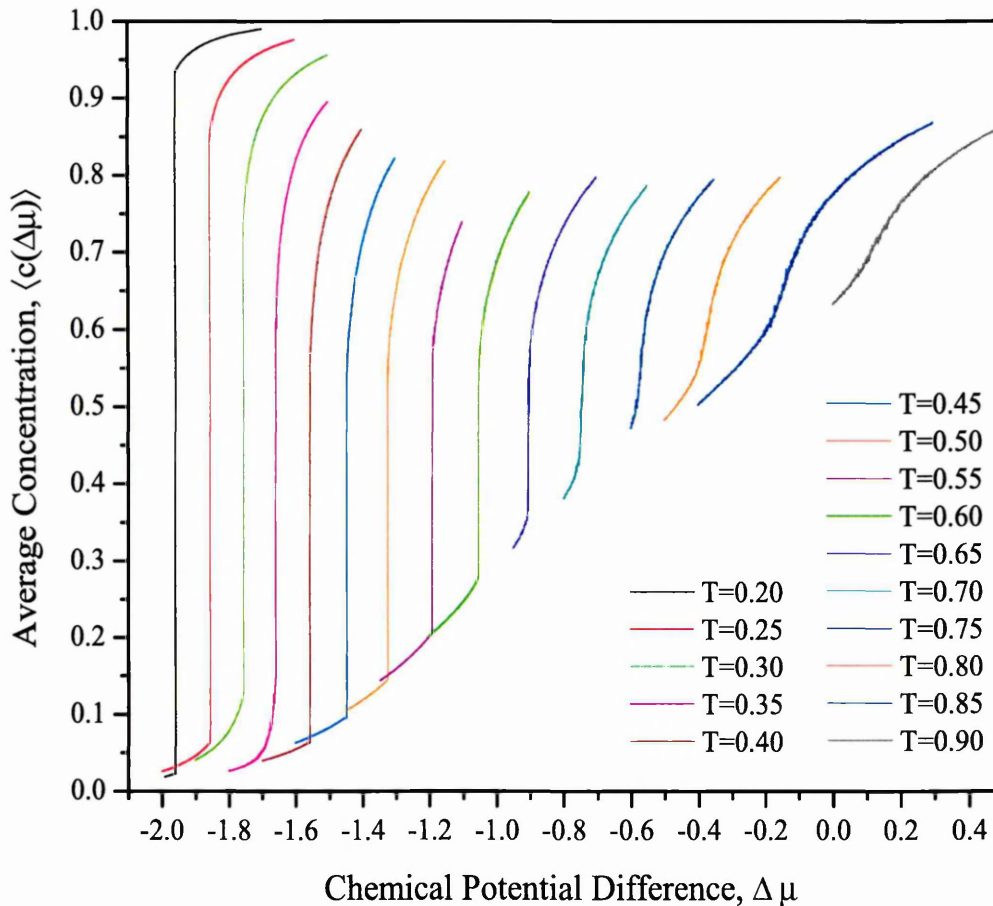


Figure 6.20: Dependence of the preferred concentration on $\Delta\mu$. $\varepsilon=0.52$. Different curves represent runs at different temperatures.

N transition at all concentrations; however, there is now a very fine bottleneck in the nematic region, separating two coexistence regions. This is due to the lower boundary of the $T_{IN}(c_1, c_2)$ region which extends to even lower temperatures in the

area of low concentrations. Another coexistence region, which we observe at slightly lower temperatures - representing the demixed coexistence of the two nematic phases - has risen slightly as compared to the system with $\varepsilon = 0.55$. It is highest at concentrations around and less than $c \approx 0.5$ but changes down to zero on both limits of the concentration axis. The asymmetry of this coexistence envelope leads it to lean slightly towards the widened $T_{IN}(c_1, c_2)$ region. As was the case in the

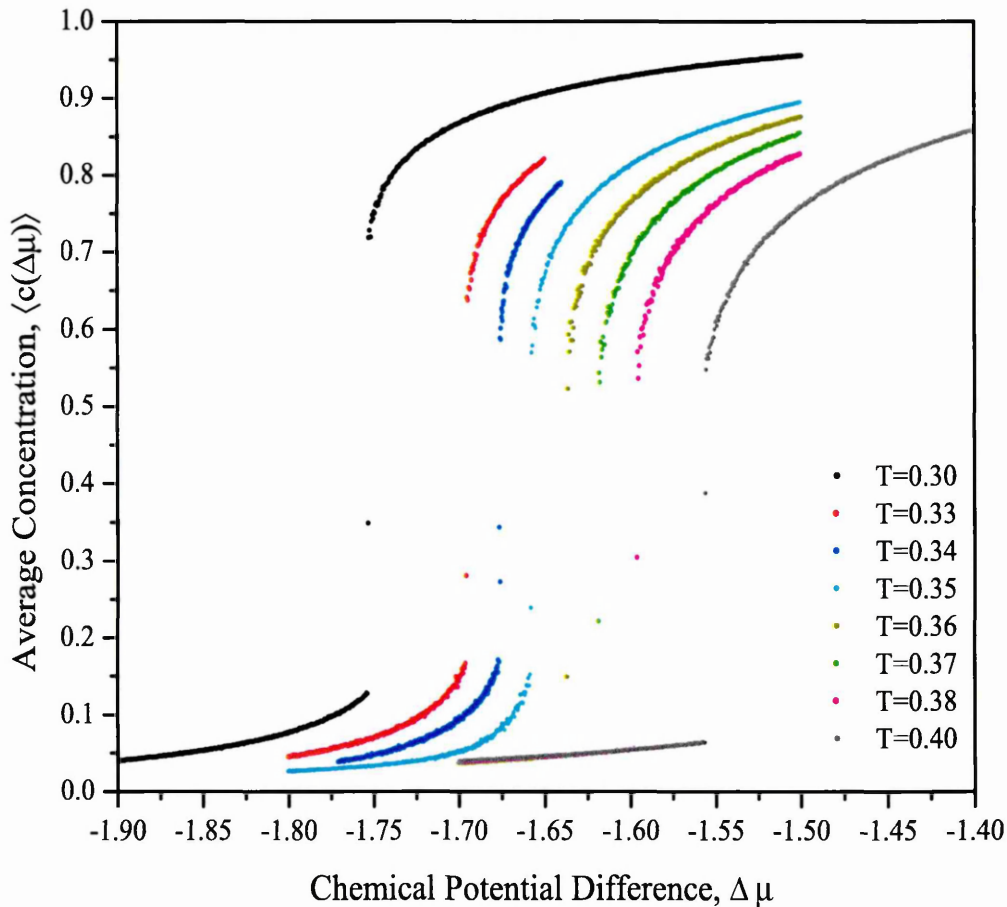


Figure 6.21: Dependence of the preferred concentration on $\Delta\mu$. $\varepsilon=0.52$. A set of simulation runs for the temperature range $0.30 < T < 0.40$.

previous systems, this phase diagram also comprises four regions. In the region of low concentration on the top of the diagram the isotropic phase has extended further into the lower temperature region, as compared to the system with $\varepsilon = 0.55$. The nematic-nematic coexistence region at the bottom of the diagram has also increased in size. The nematic phase in the middle of the diagram still occupies an area similar

in size to that of the isotropic phase (Fig. 6.19), however this region has shrunk somewhat compared with that of the previous system (Fig. 6.15). The nematic and the isotropic phases are separated by the increasingly distorted isotropic-nematic coexistence region.

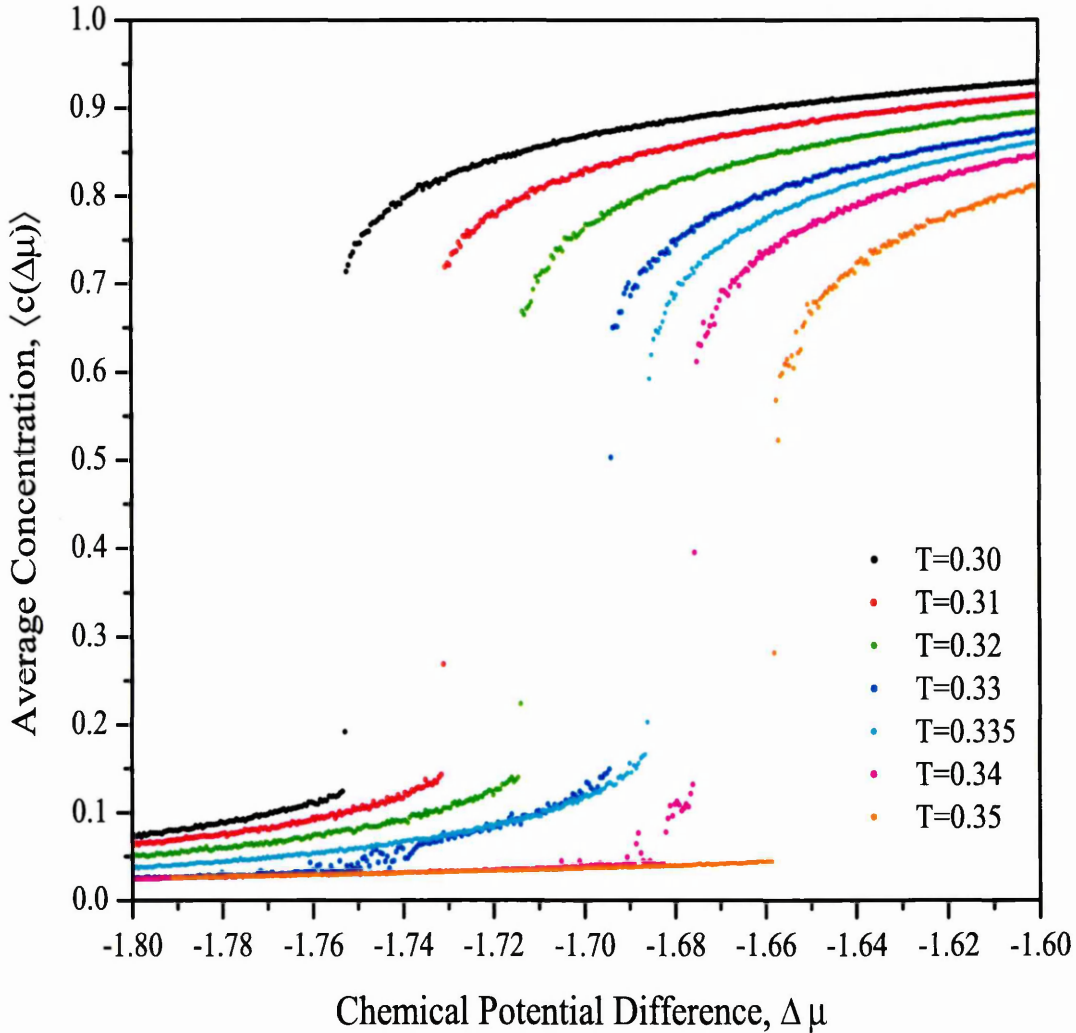


Figure 6.22: Dependence of the preferred concentration on $\Delta\mu$. $\varepsilon=0.52$. A set of short simulation runs for the temperature range $0.30 < T < 0.35$.

The behaviour of the system with $\varepsilon = 0.53$ is consistent with that of the previous systems. There is a difference, however, in the sizes of all regions, the nematic phase region having shrunk and all other regions expanded.

T	$\Delta\mu_{coex}$	c_1	c_2	Δc
0.20	-1.959 ± 0.005	0.02 ± 0.01	0.93 ± 0.01	0.91 ± 0.02
0.25	-1.854 ± 0.005	0.06 ± 0.01	0.85 ± 0.01	0.79 ± 0.02
0.30	-1.753 ± 0.005	0.12 ± 0.01	0.75 ± 0.01	0.63 ± 0.02
0.33	-1.694 ± 0.005	0.16 ± 0.01	0.71 ± 0.01	0.55 ± 0.02
0.34	-1.676 ± 0.005	0.15 ± 0.01	0.66 ± 0.01	0.51 ± 0.02
0.35	-1.657 ± 0.005	0.14 ± 0.01	0.64 ± 0.01	0.50 ± 0.02
0.40	-1.556 ± 0.005	0.06 ± 0.01	0.58 ± 0.01	0.52 ± 0.02
0.45	-1.445 ± 0.005	0.10 ± 0.01	0.55 ± 0.01	0.45 ± 0.02
0.50	-1.323 ± 0.005	0.14 ± 0.01	0.59 ± 0.01	0.45 ± 0.02
0.55	-1.193 ± 0.005	0.20 ± 0.01	0.58 ± 0.01	0.38 ± 0.02
0.60	-1.052 ± 0.005	0.28 ± 0.01	0.57 ± 0.01	0.29 ± 0.02
0.65	-0.905 ± 0.005	0.35 ± 0.01	0.57 ± 0.01	0.22 ± 0.02
0.70	-0.742 ± 0.005	0.46 ± 0.01	0.55 ± 0.01	0.09 ± 0.02
0.75	-0.569 ± 0.005	0.53 ± 0.01	0.56 ± 0.01	0.02 ± 0.02
0.80	-0.365 ± 0.005	0.61 ± 0.01	0.62 ± 0.01	0.01 ± 0.02

Table 6.5: Table of two preferred concentrations (c_1 and c_2) and their difference (Δc) that occur at unique value of the chemical potential difference ($\Delta\mu_{coex}$) for any given temperature (T). The system with $\varepsilon = 0.52$. Criteria of defining these were set out in Section 6.1.

We move now to the system with $\varepsilon = 0.52$. Let us look at the dependence of the average concentration for this system on the chemical potential difference $\langle c(\Delta\mu) \rangle$ (Figure 6.20). The overall behaviour of the $\langle c(\Delta\mu) \rangle$ curves for the system differs slightly from that observed in the previous system. For each temperature there is a unique value of $\Delta\mu_{coex}(T)$ and two preferred concentrations $c_1(T)$ and $c_2(T)$. As the temperature decreases, the distance between the two preferred concentrations Δc increases continuously, until at $T \approx 0.35$ it decreases slightly. After this, Δc goes on to increase continuously as $T \rightarrow 0.0$. This system differs from those examined previously, in that no $\langle c(\Delta\mu, T) \rangle$ curve was found which changed continuously from $c = 1.0$ to $c = 0.0$ as $\Delta\mu$ was decreased; nor was any temperature noted at which the $\langle c(\Delta\mu) \rangle$ curve experienced two discontinuities on the full range of $\Delta\mu$. Throughout the entire temperature region there was always one discontinuity to be observed on the $\langle c(\Delta\mu) \rangle$ curve (Figures 6.20,6.21).

There is some ambiguity, however, in the region of temperatures around $T = 0.34\dots 0.35$, where the dependence of c_1 on T showed non-monotonic behaviour ($T = 0.30\dots 0.35$ in Table 6.5). As temperature decreases from high value approaching $T \approx 0.35$, the value of c_1 continuously decreases. Then at $T \approx 0.35$, c_1 increases

sharply until $T \approx 0.33$, after which $c_1 \rightarrow 0.0$ with further decrease of T . In addition to this, in the range $\Delta\mu < \Delta\mu_{coex}$, on the left from the abrupt change, the dependence of the $\langle c(\Delta\mu) \rangle$ curves for temperatures immediately above $T = 0.35$ is virtually linear, but for temperatures $T \lesssim 0.35$ the curve changes with a steep gradient. All this points to a difference between the part of the coexistence boundary (represented by c_1) below $T \approx 0.35$ and above it.

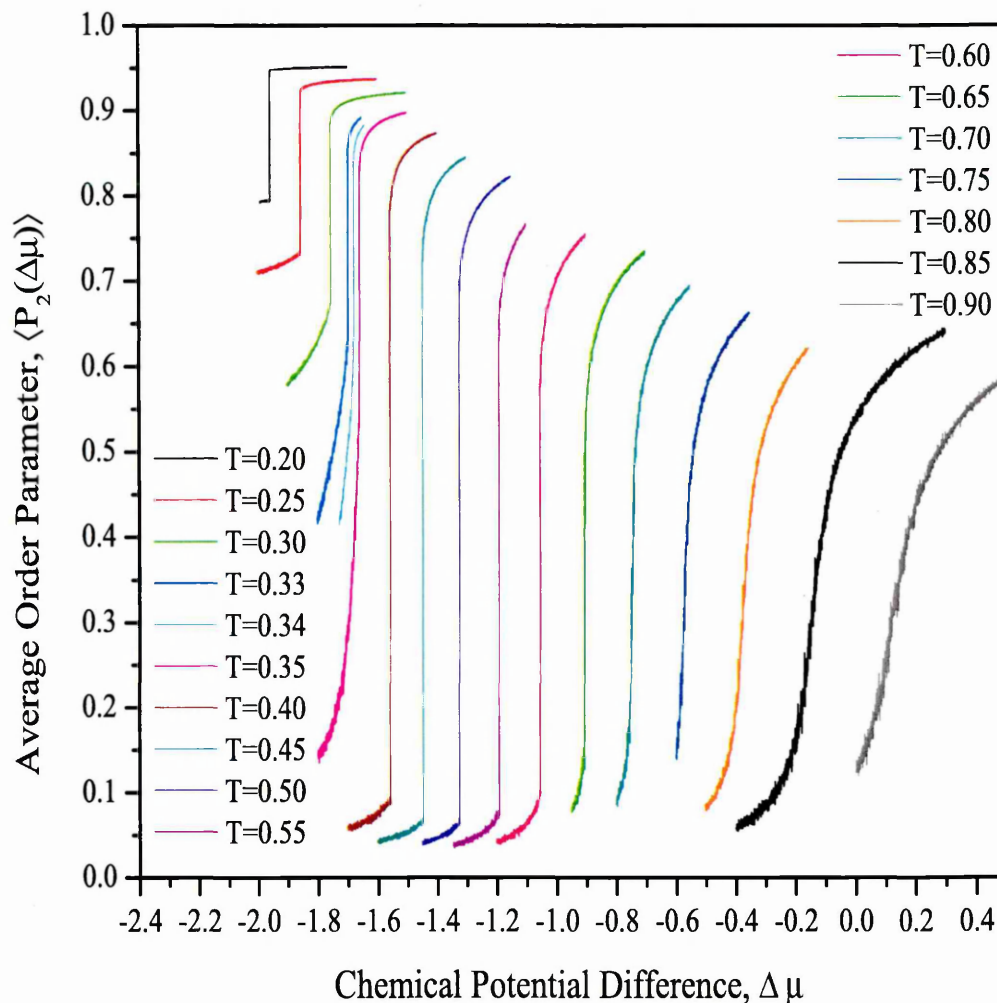


Figure 6.23: Dependence of the preferred Order Parameter on $\Delta\mu$. $\varepsilon=0.52$.

In Figure 6.22 we present the results for the same temperatures as in Figure 6.21, but obtained using shorter runs ($\sigma = 7,000$ steps per point as compared with 20,000

steps previously). From the Figure we now see the area of ambiguity from a slightly different perspective. At temperatures $T = 0.33; 0.34$, we observe two discontinuities, while at $T = 0.335$ we observe only one. A short run often does not allow the system to equilibrate and the system sticks in a metastable state or state with a low energetic barrier between other, more energetically favourable states. We will discuss this further in Section 6.5.

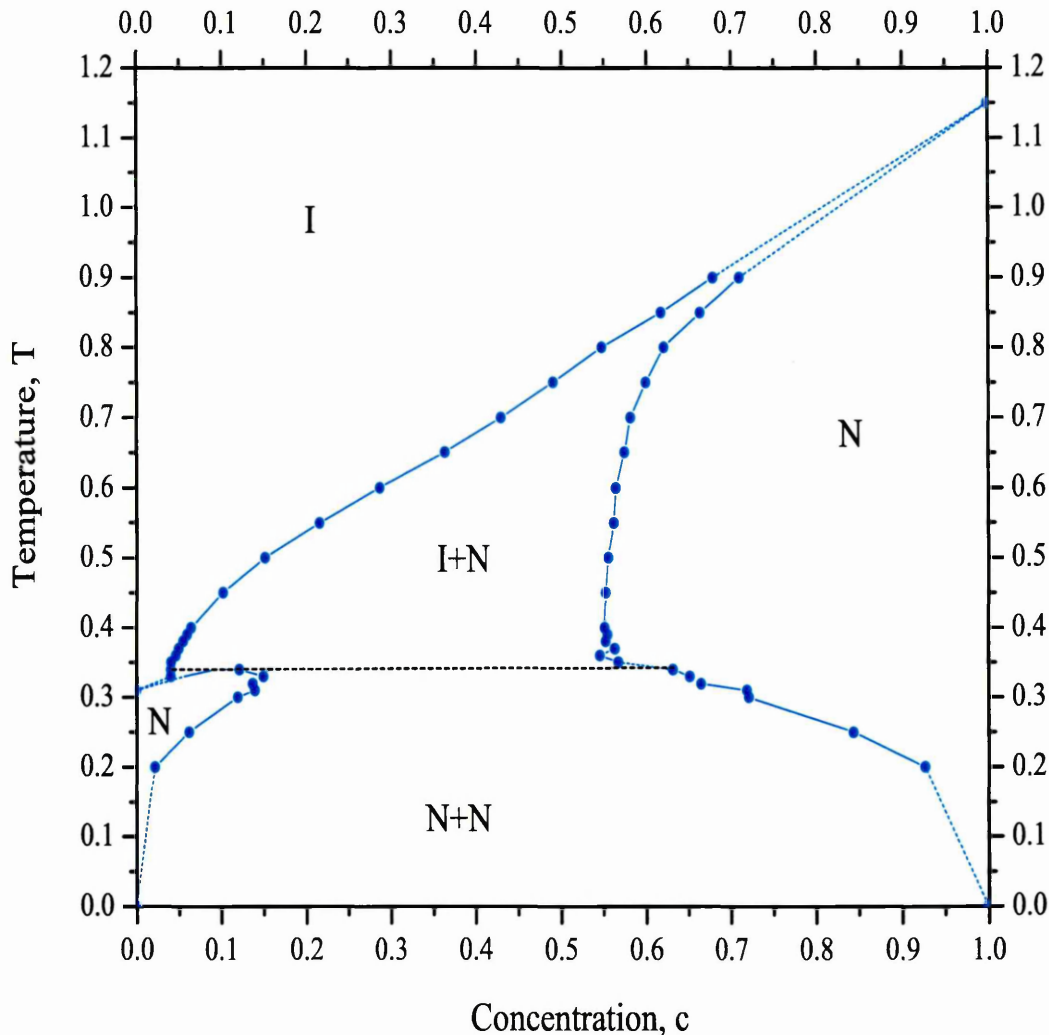


Figure 6.24: Phase diagram for the system with $\varepsilon=0.52$. Blue filled circles represent the data points obtained from $N\Delta\mu VT$ Ensemble. Blue dotted line represents approximation based on the data obtained from both ensembles. Black dotted line represents the approximated boundary between I+N and N+N regions based on the $\langle P_2(\Delta\mu) \rangle$ data and knowledge from $NcVT$ data.

As was the case for systems investigated previously, the distance between the two coexisting concentrations Δc becomes greatest and approaches $\Delta c = 1.0$, as $T \rightarrow 0.0$. These concentration values are presented in Table 6.5.

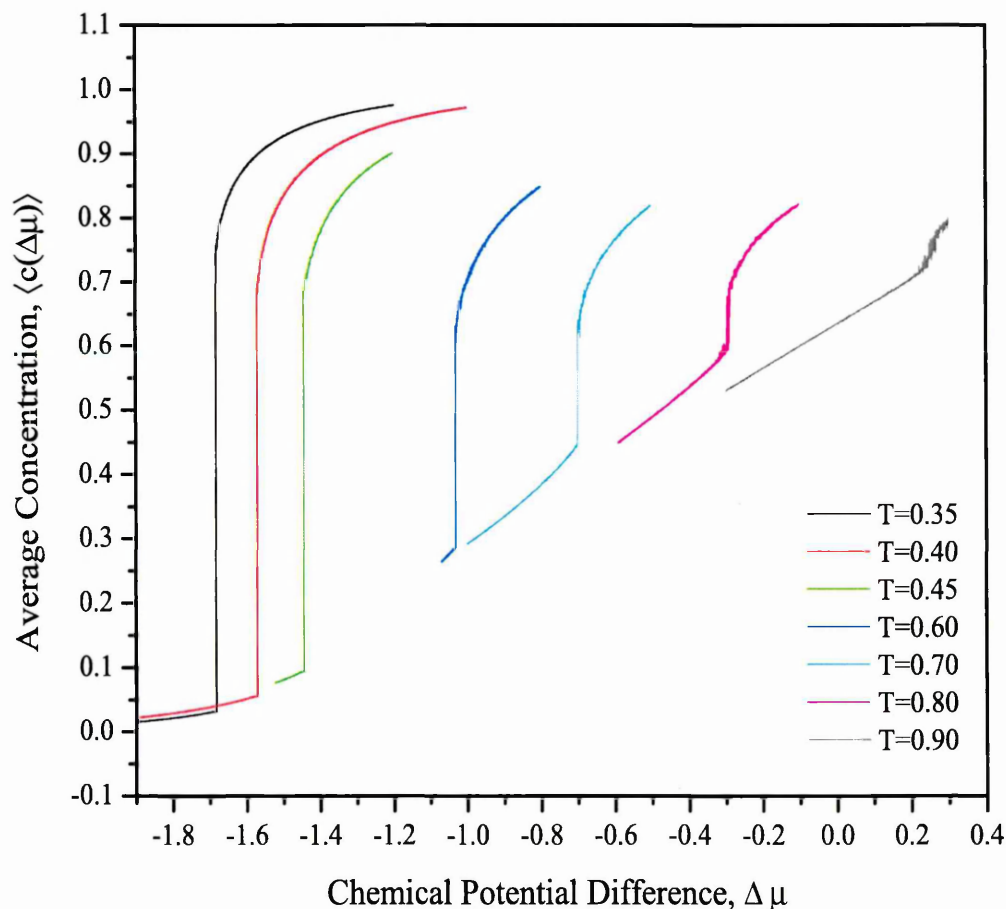


Figure 6.25: Dependence of the preferred concentration on $\Delta\mu$. $\varepsilon=0.50$. Different curves represent runs at different temperatures.

The values of the preferred order parameters for a given $\Delta\mu$ are shown in Figure 6.23. The different curves represent the order parameter for different temperatures. For temperatures $T \gtrsim 0.65$, as $\Delta\mu$ decreases the order parameter changes from a high to a close-to-zero value; the change is not abrupt, but the discontinuity is plainly evident. For temperatures in the range $0.40 \lesssim T \lesssim 0.65$ the order parameter changes abruptly from a high, to a close-to-zero value, at $\Delta\mu_{coex}(T)$. The difference between the values of $\langle P_2(\Delta\mu) \rangle$ on the two sides of $\Delta\mu_{coex}(T)$ is most marked at temperatures around $T \approx 0.40$. In the range of temperatures $0.33 \lesssim T \lesssim 0.35$ the order parameter

T	$\Delta\mu_{coex}$	c_1	c_2	Δc
0.35	-1.683 ± 0.005	0.03 ± 0.01	0.79 ± 0.01	0.76 ± 0.02
0.40	-1.572 ± 0.005	0.05 ± 0.01	0.72 ± 0.01	0.67 ± 0.02
0.45	-1.444 ± 0.005	0.09 ± 0.01	0.71 ± 0.01	0.62 ± 0.02
0.6	-1.027 ± 0.005	0.28 ± 0.01	0.65 ± 0.01	0.37 ± 0.02
0.7	-0.700 ± 0.005	0.44 ± 0.01	0.64 ± 0.01	0.20 ± 0.02
0.8	-0.288 ± 0.005	0.59 ± 0.01	0.71 ± 0.01	0.12 ± 0.02
0.9	0.258 ± 0.005	0.72 ± 0.01	0.76 ± 0.01	0.04 ± 0.02

Table 6.6: Table of two preferred concentrations (c_1 and c_2) and their difference (Δc) that occur at unique value of the chemical potential difference ($\Delta\mu_{coex}$) for any given temperature (T). The system with $\varepsilon = 0.50$. Criteria of defining these were set out in Section 6.1.

falls rapidly at $\Delta\mu_{coex}(T)$ to a non-zero value, after which it continuously decreases to a close-to-zero value, as $\Delta\mu_{coex}(T)$ decreases. At temperatures $T \lesssim 0.30$ the order parameter changes rapidly from one non-zero value to another, lower, non-zero value as $\Delta\mu$ decreases.

We present the phase diagram that is most consistent with the data obtained in Figure 6.24. The upper portion of the region of low concentration (the isotropic phase) has extended slightly further into the lower temperature region, as compared to the system with $\varepsilon = 0.53$. The top boundary of $T_{IN}(c_1, c_2)$ (c_1) has changed only slightly as compared to the previous system. At concentrations between $c = 0.1$ and $c = 1.0$, its dependence is approximately linear. The lower border of $T_{IN}(c_1, c_2)$ region, however has extended into the area of lower temperatures and is coupled with the nematic-nematic coexistence region, which has also expanded. Δc for this single coexistence region now increases continuously with the decrease in temperature until $T \approx 0.34$, when its width Δc decreases sharply to 80% of its value. With a further decrease in temperature, Δc quickly restores to a maximum value and increases to 1 as $T \rightarrow 0$.

This results in the division of the nematic phase into two, in the areas of low and high concentrations, creating respectively B-rich and A-rich nematic phases. The boundaries of the B-rich nematic region are rather ambiguous, however - this will be discussed in Section 6.5.3. The total area of the two nematic regions is decreased slightly, compared to that of the previous system, owing to the expansion of the $T_{IN}(c_1, c_2)$ and demixing regions in that area. The order parameter data suggest a

horizontal line, which divides the single coexistence region (formed by the merging of two regions, as observed previously) into isotropic-nematic coexistence above the line and nematic-nematic coexistence below.

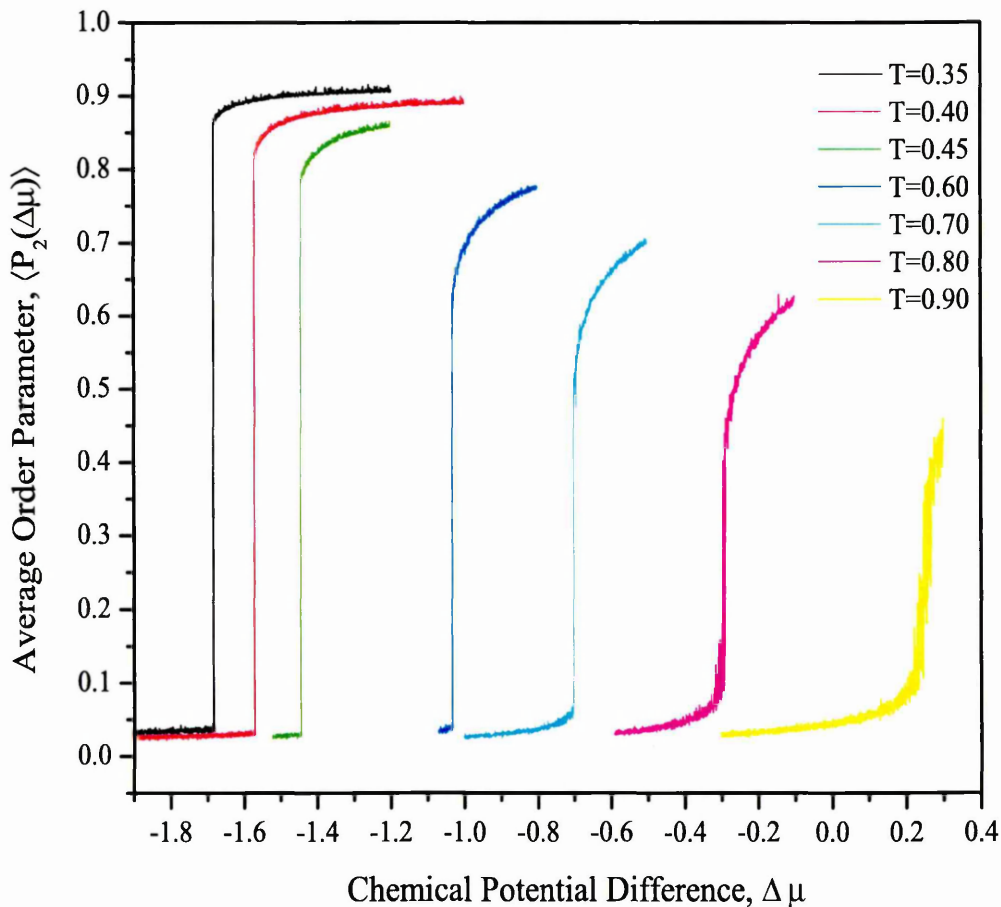


Figure 6.26: Dependence of the preferred Order Parameter on $\Delta\mu$. $\varepsilon=0.50$.

The behaviour of the system with $\varepsilon = 0.52$ is consistent with that of the systems presented earlier. There are features, however, not seen previously. The first is the coupling of the two coexistence regions and their assumed division into isotropic-nematic and nematic-nematic coexistence regions.

The next system investigated differs by the virtue of the coupling constant, $\varepsilon = 0.50$. Let us look at the dependence of the average concentration for this system on the chemical potential difference $\langle c(\Delta\mu) \rangle$ (Figure 6.25).

Overall, the behaviour of $\langle c(\Delta\mu) \rangle$ curves for the system does not differ from the previous system, except that they display no ambiguity. For each temperature there is a unique value of $\Delta\mu_{coex}(T)$ and two preferred concentrations $c_1(T)$ and $c_2(T)$. As the temperature decreases, the distance between the two preferred concentrations Δc increases continuously as $T \rightarrow 0.0$. There is no temperature at which the $\langle c(\Delta\mu) \rangle$ curve changes continuously from $c = 1.0$ to $c = 0.0$ as $\Delta\mu$ decreases, nor is there a temperature at which the $\langle c(\Delta\mu) \rangle$ curve experiences two discontinuities on the full range of $\Delta\mu$. Throughout the entire temperature region there is only one discontinuity on the $\langle c(\Delta\mu) \rangle$ curve.

The values of the preferred order parameters for a given $\Delta\mu$ are shown in Figure 6.26. Different curves represent the order parameter for different temperatures. Throughout the entire temperature range the order parameter changes its value from high non-zero to close-to-zero. For all of these temperatures the order parameter changes sharply at $\Delta\mu_{coex}(T)$.

The phase diagram constructed from the data presented above is shown in Figure 6.27. The diagram comprises three areas, owing to the merger of $T_{IN}(c_1, c_2)$ and demixing regions, plus additional area as a result of division of the coupled single coexistence area with a horizontal line. The upper portion of the region of low concentration (the isotropic phase) seems to remain the same, as compared to the system with $\varepsilon = 0.52$. At concentrations between $c = 0.1$ and $c = 1.0$, the dependence of $T_{IN}(c_1, c_2)$ is approximately linear on its boundary with isotropic phase (c_1). On entering the coexistence region $T_{IN}(c_1, c_2)$, the system stays demixed as $T \rightarrow 0.0$ for a wide range of concentrations ($0.0 < c \lesssim 0.64$). In the area of high concentrations ($0.64 \lesssim c < 1.0$), the system enters a homogeneous nematic phase shortly after it enters the I+N coexistence region ($T_{IN}(c_1, c_2)$) as the temperature decreases. As the temperature continues to fall the system demixes forming either I+N or N+N coexistence, depending on concentration (the concentration threshold is determined by the point of crossover between the horizontal line and the coexistence boundary (c_2)). After entering I+N coexistence the system moves to N+N coexistence region as the temperature decreases. The horizontal line lies in the region of temperatures $0.28 < T < 0.30$ (according to Figure 6.26). The values of $\langle P_2(\Delta\mu) \rangle$ that correspond to concentrations on the right-hand and the left-hand side of the coexistence boundaries indicate respectively the nematic and isotropic order for temperatures $T > 0.30$. In the region $T < 0.28$ the $\langle P_2(\Delta\mu) \rangle$ data indicates a nematic order on

both sides of the coexistence region. This agrees well with the predictions discussed in Section 5.4.4. The nematic region on the right-hand side of the diagram is slightly diminished, when compared with that of previous system, owing to the continuous expansion of the single coexistence region in that area. The behaviour of the sys-

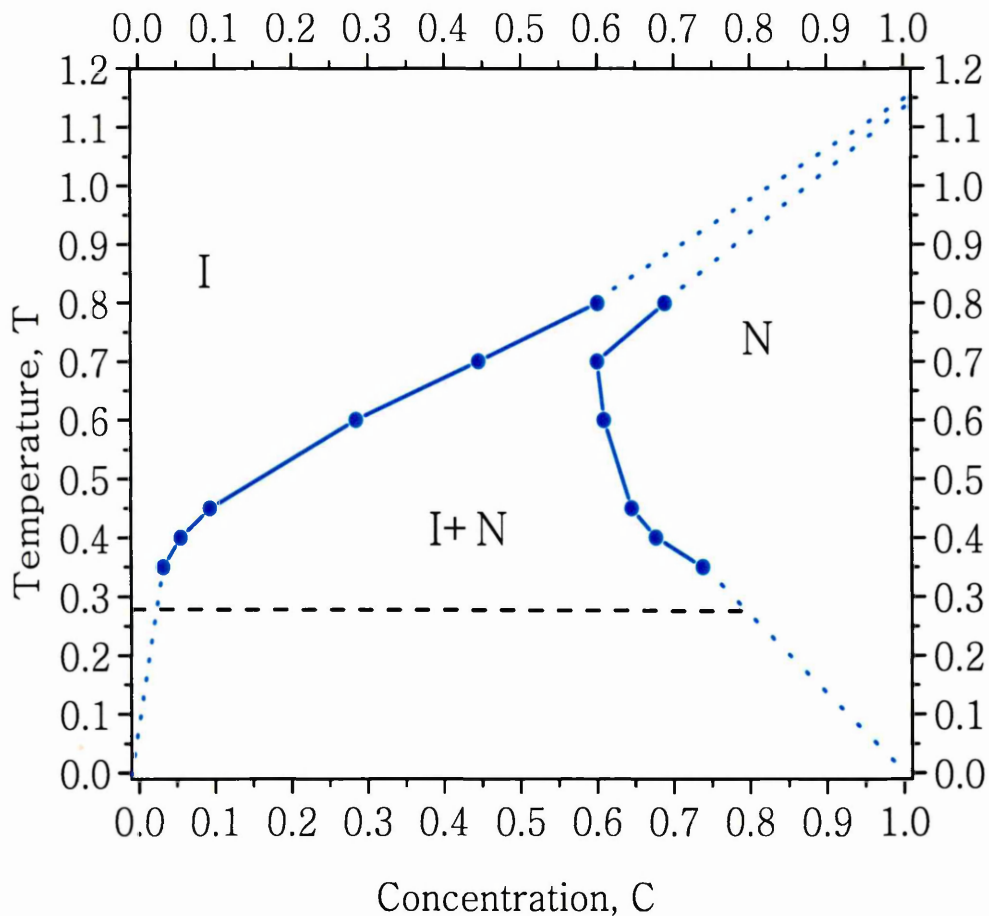


Figure 6.27: Phase diagram for the system with $\varepsilon=0.50$. Blue filled circles represent the data points obtained from $N\Delta\mu VT$ Ensemble. Blue dotted line represents approximation based on the data obtained from both ensembles. Black dotted line represents the approximated boundary between I+N and N+N regions based on the knowledge from $NcVT$ data.

tem with $\varepsilon = 0.50$ is consistent with that of the systems, presented earlier. There is a difference, however, in the size and shape of the $T_{IN}(c_1, c_2)$ and N+N coexistence regions, as they have coupled in a single region (compared to the systems with $\varepsilon = 0.90$, $\varepsilon = 0.60$, $\varepsilon = 0.55$, and $\varepsilon = 0.53$) and B-rich nematic phase decreased significantly (compared to the system with $\varepsilon = 0.52$). Further discussion of these results will follow in Section 6.5.3.

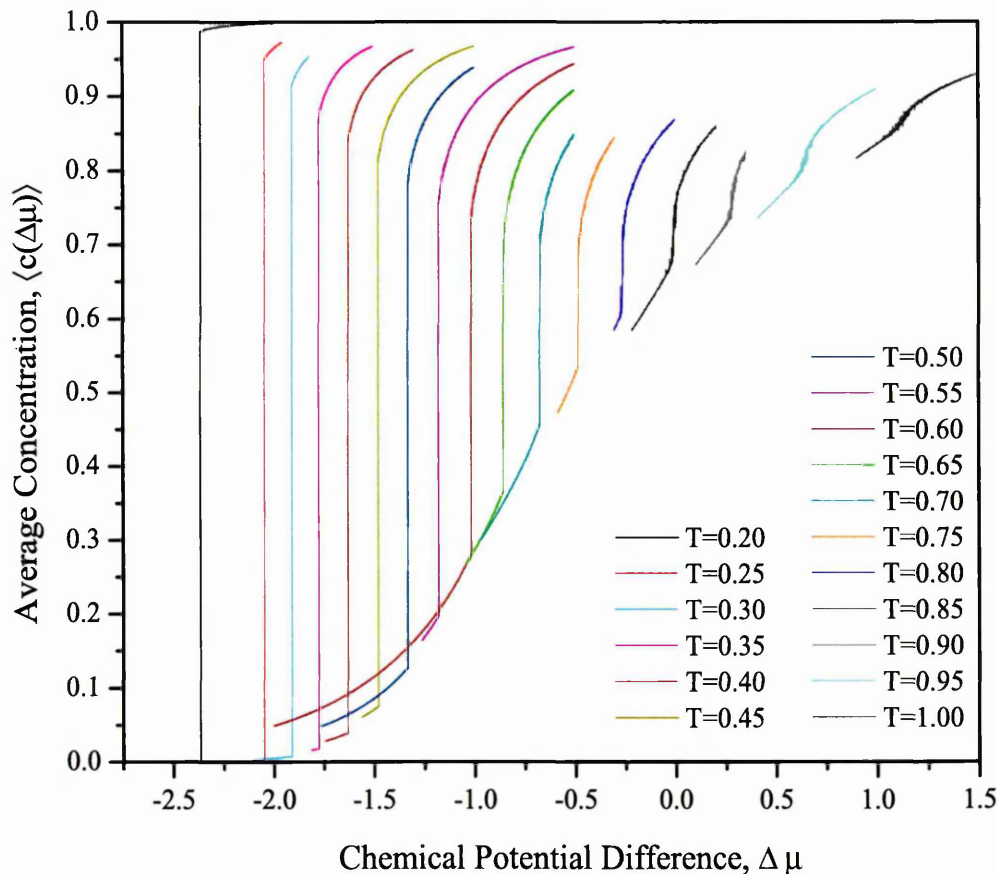


Figure 6.28: Dependence of the preferred concentration on $\Delta\mu$. $\varepsilon = 0.45$. Different curves represent runs at different temperatures.

6.4 System with $\varepsilon = 0.45$, $\varepsilon = 0.00$

The first system in this section is the binary system with coupling constant $\varepsilon = 0.45$. The first observable for this system which we present is the preferred average concentration of the mixture $\langle c(\Delta\mu) \rangle$ (Figure 6.28); once again, various curves represent the system at different temperatures.

Overall, the behaviour of the $\langle c(\Delta\mu) \rangle$ curves for the system does not differ from the previous two systems, except that ambiguity was detected in $\langle c(\Delta\mu) \rangle$ curves in the region of low concentration, compared to the $\varepsilon = 0.52$ system. For each temperature there is a unique value of $\Delta\mu_{coex}(T)$ and two preferred concentrations $c_1(T)$ and $c_2(T)$. As the temperature decreases, the distance between the two preferred concentrations Δc increases continuously as $T \rightarrow 0.0$.

T	$\Delta\mu_{coex}$	c_1	c_2	Δc
0.2	-2.363 ± 0.005	0.00 ± 0.01	0.99 ± 0.01	0.99 ± 0.02
0.25	-2.036 ± 0.005	0.00 ± 0.01	0.95 ± 0.01	0.95 ± 0.02
0.3	-1.907 ± 0.005	0.01 ± 0.01	0.92 ± 0.01	0.91 ± 0.02
0.35	-1.903 ± 0.005	0.02 ± 0.01	0.87 ± 0.01	0.85 ± 0.02
0.40	-1.625 ± 0.005	0.03 ± 0.01	0.85 ± 0.01	0.82 ± 0.02
0.45	-1.472 ± 0.005	0.07 ± 0.01	0.83 ± 0.01	0.76 ± 0.02
0.5	-1.332 ± 0.005	0.12 ± 0.01	0.79 ± 0.01	0.67 ± 0.02
0.55	-1.189 ± 0.005	0.20 ± 0.01	0.76 ± 0.01	0.56 ± 0.02
0.6	-1.015 ± 0.005	0.27 ± 0.01	0.75 ± 0.01	0.48 ± 0.02
0.65	-0.856 ± 0.005	0.35 ± 0.01	0.72 ± 0.01	0.37 ± 0.02
0.7	-0.685 ± 0.005	0.45 ± 0.01	0.71 ± 0.01	0.26 ± 0.02
0.75	-0.482 ± 0.005	0.53 ± 0.01	0.71 ± 0.01	0.18 ± 0.02
0.8	-0.261 ± 0.005	0.61 ± 0.01	0.73 ± 0.01	0.12 ± 0.02
0.85	-0.011 ± 0.005	0.67 ± 0.01	0.77 ± 0.01	0.10 ± 0.02
0.9	0.286 ± 0.005	0.74 ± 0.01	0.79 ± 0.01	0.05 ± 0.02
0.95	0.652 ± 0.005	0.80 ± 0.01	0.85 ± 0.01	0.05 ± 0.02
1.00	1.127 ± 0.005	0.86 ± 0.01	0.87 ± 0.01	0.01 ± 0.02

Table 6.7: Table of two preferred concentrations (c_1 and c_2) and their difference (Δc) that occur at unique value of the chemical potential difference ($\Delta\mu_{coex}$) for any given temperature (T). The system with $\varepsilon = 0.45$. Criteria of defining these were set out in Section 6.1.

There is no temperature at which the $\langle c(\Delta\mu) \rangle$ curve changes continuously from $c = 1.0$ to $c = 0.0$ as $\Delta\mu$ decreases, nor is there a temperature at which the $\langle c(\Delta\mu) \rangle$ curve experiences two discontinuities on the full range of $\Delta\mu$. Throughout the entire temperature region, there is only one discontinuity on the curve.

The values of the preferred order parameters for a given $\Delta\mu$ for the system with $\varepsilon = 0.45$ are very similar to those for the system $\varepsilon = 0.50$ shown in Figure 6.26. Throughout the investigated temperature range the order parameter changes its value from high non-zero to close-to-zero in the region of temperatures $T > 0.25$. In the range $T < 0.20$ the order parameter changes its value from high non-zero to low non-zero value. As in the case of previous systems, using $\langle P_2(\Delta\mu) \rangle$ data we were able to identify phases on opposite sides of the coexistence boundaries, and these are shown in the phase diagram constructed from the data presented above (Figure 6.29). As in the previous system, the diagram comprises three areas, owing to the merger of the two coexistence regions. One more region can be determined

from the division of the single coexistence region into I+N and N+N coexistence regions, based on data from $NcVT$ Ensemble. The isotropic phase (upper region on the diagram) remained approximately unchanged, as compared to the systems with $\varepsilon = 0.52$ and $\varepsilon = 0.50$. At concentrations between $c = 0.1$ and $c = 1.0$, the

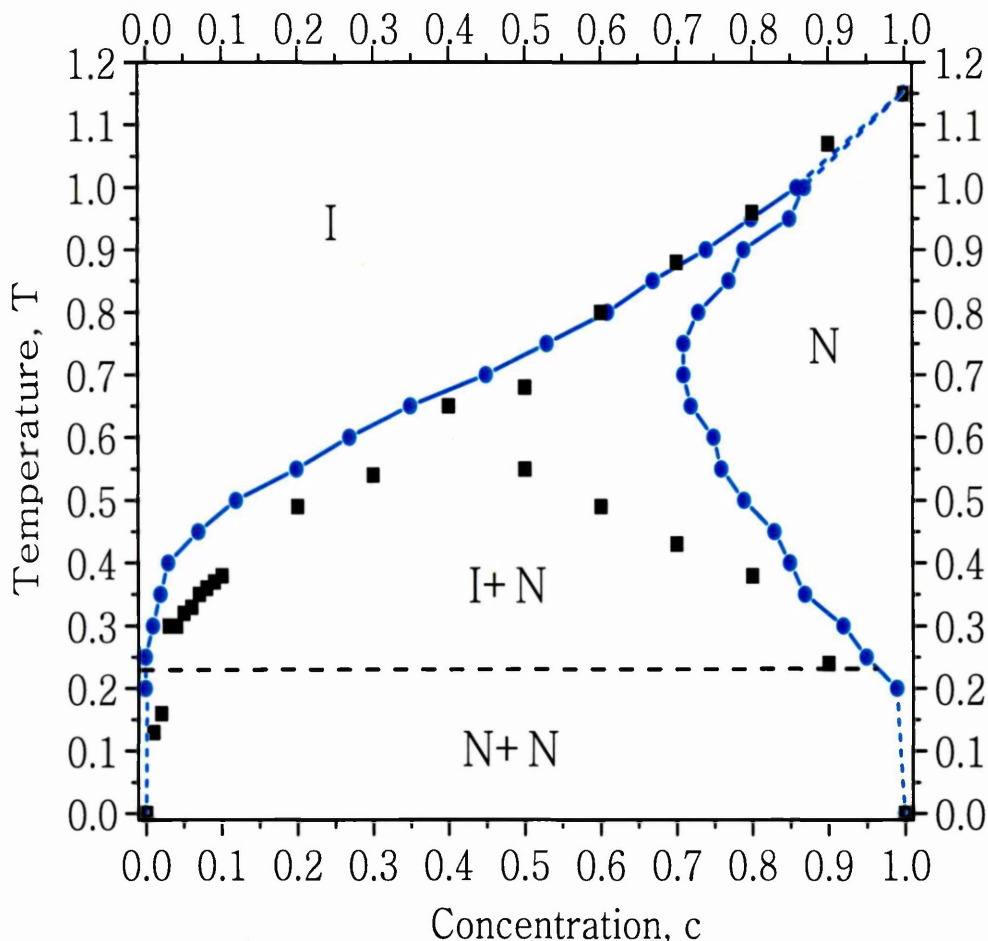


Figure 6.29: Phase diagram for the system with $\varepsilon=0.45$. Blue filled circles represent the data points obtained from $N\Delta\mu VT$ Ensemble. Blue dotted line represents approximation based on the data obtained from both ensembles. Black dotted line represents the approximated boundary between I+N and N+N regions based on the knowledge from $NcVT$ data. Black filled squares represent the data from $NcVT$ Ensemble.

dependence of $T_{IN}(c_1, c_2)$ is approximately linear on its boundary with the isotropic phase (c_1). For low concentrations ($c \lesssim 0.1$), the curve decreases sharply with a decrease of concentration and approaches zero at $c \rightarrow 0.0$. Having moved from the isotropic phase into the coexistence region, the system remains there as $T \rightarrow 0.0$

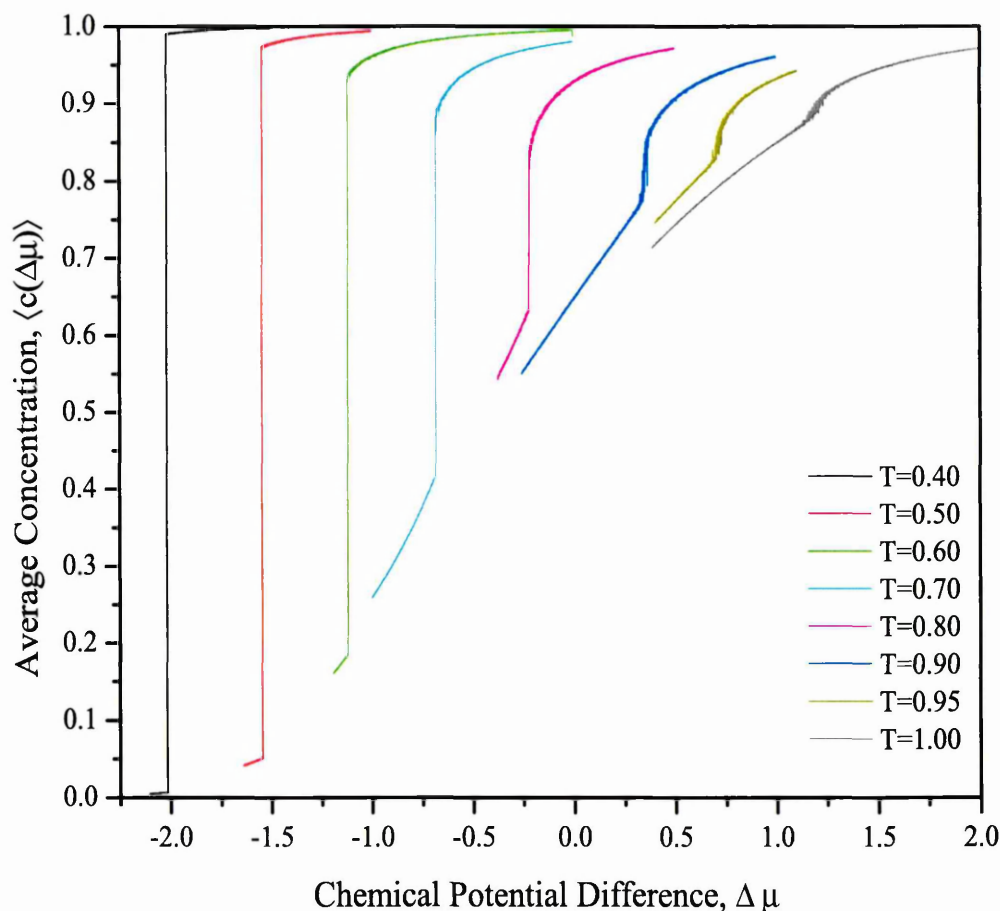


Figure 6.30: Dependence of the preferred concentration on $\Delta\mu$. $\varepsilon=0.0$. Different curves represent runs at different temperatures.

for the range of concentrations ($0.0 < c \lesssim 0.71$) wider than that for the previous systems. In the area of high concentrations ($c \gtrsim 0.71$) the system undergoes the first order isotropic-nematic transition (with relatively narrow I+N coexistence region), after which the system re-enters into the coexistence region as the temperature decreases. The width of the coexistence at the isotropic-nematic transition at high temperatures and the type of the coexistence (I+N or N+N) that the system enters at low temperatures depends on the concentration.

The area of the nematic region on the right-hand side of the diagram decreased slightly, compared to that in the previous system, owing to the continuous expansion of the merged $T_{IN}(c_1, c_2)$ and demixing regions in that area. We were not able to

T	$\Delta\mu_{coex}$	c_1	c_2	Δc
0.4	-2.014 ± 0.005	0.01 ± 0.01	0.99 ± 0.01	0.98 ± 0.02
0.5	-1.536 ± 0.005	0.05 ± 0.01	0.97 ± 0.01	0.92 ± 0.02
0.6	-1.112 ± 0.005	0.18 ± 0.01	0.94 ± 0.01	0.76 ± 0.02
0.7	-0.679 ± 0.005	0.41 ± 0.01	0.89 ± 0.01	0.48 ± 0.02
0.8	-0.215 ± 0.005	0.63 ± 0.01	0.84 ± 0.01	0.21 ± 0.02
0.9	0.351 ± 0.005	0.77 ± 0.01	0.85 ± 0.01	0.08 ± 0.02
0.95	0.716 ± 0.005	0.83 ± 0.01	0.88 ± 0.01	0.05 ± 0.02
1.00	1.193 ± 0.005	0.89 ± 0.01	0.91 ± 0.01	0.02 ± 0.02

Table 6.8: Table of two preferred concentrations (c_1 and c_2) and their difference (Δc) that occur at unique value of the chemical potential difference ($\Delta\mu_{coex}$) for any given temperature (T). The system with $\varepsilon = 0.00$. Criteria of defining these were set out in Section 6.1.

resolve the nematic region on the left-hand side of the diagram, as it exists only at very low concentrations ($c < 0.01$) and temperatures $T \lesssim 0.29$ (based on the data from the NcVT Ensemble).

The behaviour of the system with $\varepsilon = 0.45$ is similar to system with $\varepsilon = 0.50$ and consistent with the results for the rest of the systems presented in this chapter. There is a difference, however, in the size of the merged coexistence region, which has increased. The assumed horizontal line, inferred from the NcVT data, moved to the lower temperature. Overall, the NcVT data for the rest of the boundaries (black squares) agrees with the results presented here. However, the temperature for isotropic-nematic transition is slightly lower in the region of concentrations $0.0 < c \lesssim 0.5$, while for the rest of concentrations ($0.5 < c < 1.0$) this temperature is slightly higher. The boundary between the nematic phase and the coexistence region on the right-hand side appears to be slightly lower for the NcVT data, as compared to $N\Delta\mu VT$ data. In Section 6.5.3 we discuss further data from both ensembles and the reasons for deviations of the phase boundaries.

We now move to the last system considered in this chapter - the system with coupling constant $\varepsilon = 0.00$. The first observable for this system is the preferred average concentration of the mixture $\langle c(\Delta\mu) \rangle$ (Figure 6.30). Various curves here represent the system at different temperatures.

At high temperatures (Fig.6.30) there is a slight discontinuity in the gradient of the $\langle c(\Delta\mu) \rangle$ curve at $\Delta\mu_{coex}$. Overall, the behaviour of $\langle c(\Delta\mu) \rangle$ curves for the system does not differ from that of the previous system. For each temperature there is a unique value of $\Delta\mu_{coex}(T)$ and two preferred concentrations $c_1(T)$ and $c_2(T)$. As the temperature decreases, the distance between the two preferred concentrations Δc increases continuously as $T \rightarrow 0.0$. There is no temperature at which the $\langle c(\Delta\mu) \rangle$ curve exhibits a continuous or close to continuous behaviour.

The values of the preferred order parameters for a given $\Delta\mu$ for the system $\varepsilon = 0.00$ are very similar to those for the systems of $\varepsilon = 0.50$ shown in Figure 6.26. Throughout the investigated temperature range the order parameter changes its value from high non-zero to close-to-zero.

The phase diagram constructed from the data presented above is shown in Figure 6.31. The diagram comprises three areas, as in the previous three systems, however there is no horizontal line for this system, owing to the isotropy of B component. In the region of low concentration the isotropic phase remained approximately unchanged, as in the systems with $\varepsilon = 0.52$, $\varepsilon = 0.50$ and $\varepsilon = 0.45$. At concentrations between $c = 0.1$ and $c = 1.0$, the dependence of $T_{IN}(c_1, c_2)$ is approximately linear on its boundary with isotropic phase (c_1). For low concentrations ($c \lesssim 0.1$), the curve sharply decreases with a decrease of concentration and approaches zero at $c \rightarrow 0.0$.

Having moved from the isotropic phase system enters I+N coexistence region. For concentrations $0.0 < c \lesssim 0.84$ the system stays in the coexistence region as the temperature decreases further down to zero. For the range of concentrations $0.84 \lesssim c < 1.0$ the system enters a nematic phase and then re-enters I+N coexistence region as the temperature decreases.

The behaviour of the system with $\varepsilon = 0.00$ is similar to that of the three previous systems. There is a difference, however, in the size of the single coexistence region, which has increased.

The NcVT data for the coexistence boundaries (black squares) in general agrees with the results presented here. However, the temperature for isotropic-nematic transition is slightly lower in the region of concentrations $0.0 < c \lesssim 0.8$, while for the rest of concentrations ($0.8 < c < 1.0$) this temperature approximately coincides with the

boundary obtained from $N\Delta\mu VT$ within the error bars. The boundary between the nematic phase and the coexistence region on the right-hand side appears to be slightly lower for the $NcVT$ data, as compared to $N\Delta\mu VT$ data. In Section 6.5.3 we discuss further the data from both ensembles and the reasons for their slight inconsistencies.

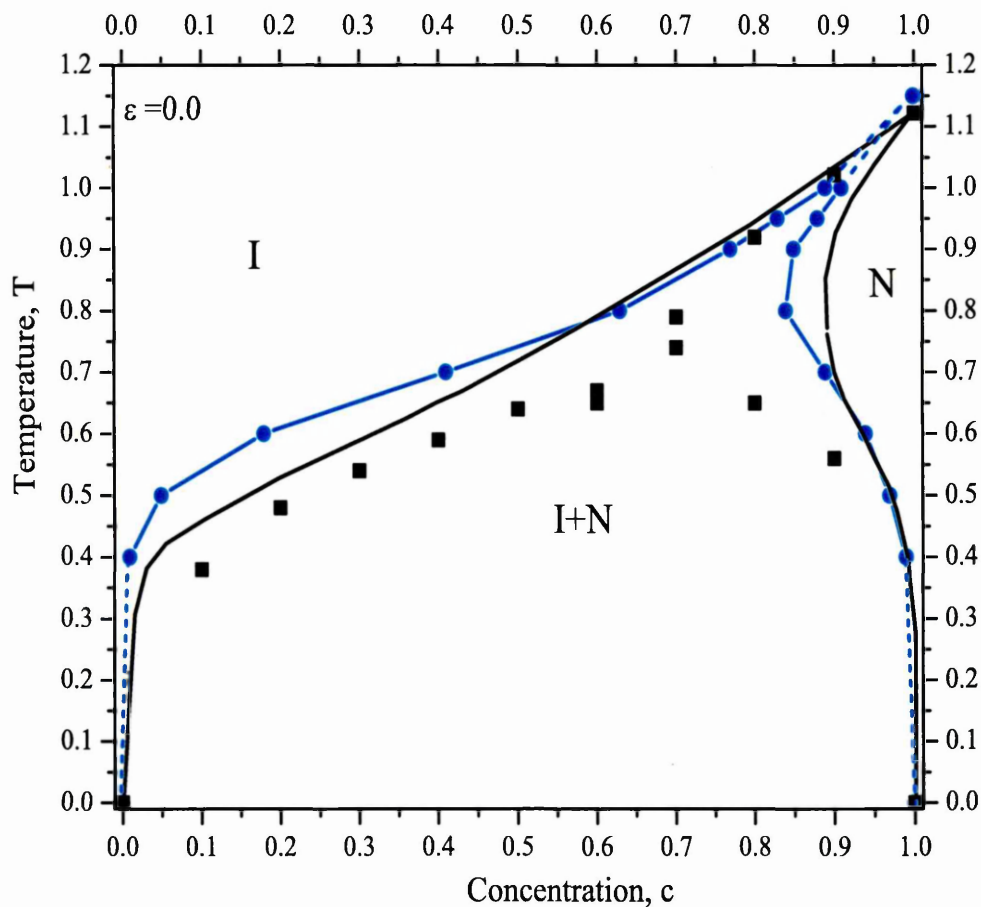


Figure 6.31: Phase diagram for the system with $\varepsilon=0.0$. Blue filled circles and blue lines represent the data points obtained from $N\Delta\mu VT$ Ensemble. Blue dotted lines represent approximation based on the data obtained from both ensembles. Black filled squares represent the data from $NcVT$ Ensemble. Black solid lines represent theoretical calculations of the phase boundaries for this system [177] (see also Figure 6.31).

6.5 Discussion Of $N\Delta\mu VT$ Results.

Now we come to the discussion of the results presented in this Chapter. First, we review some aspects of the phase diagram measurements about which there are accuracy problems. Then we discuss each of the phase region found, in Sections 6.5.1-6.5.3 before giving an analysis of the phase boundaries in Section 6.5.4.

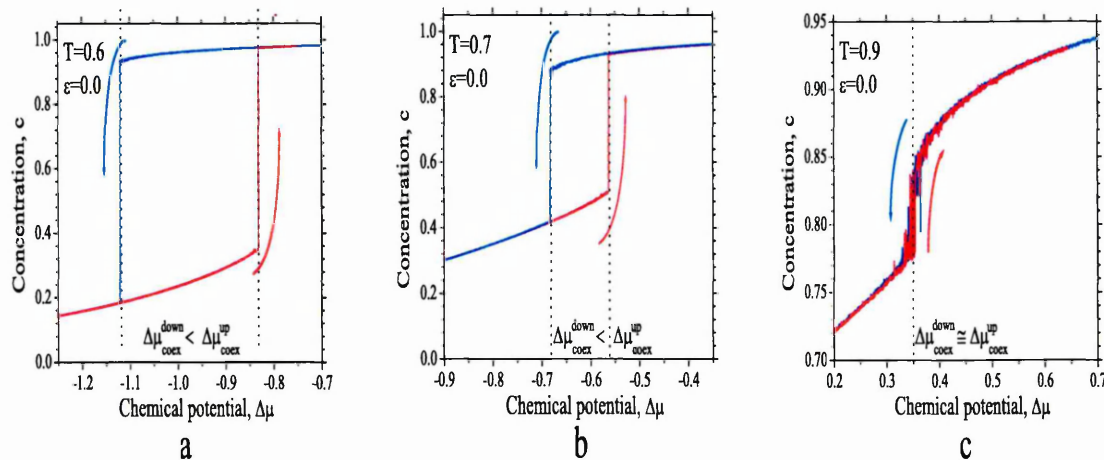


Figure 6.32: Hysteresis effect in the constant $N\Delta\mu VT$ ensemble. Blue lines represent simulations with decreasing $\Delta\mu$ values, red lines show the equivalent results obtained with increasing $\Delta\mu$ values.

At the beginning of Section 5.4 we pointed out that an appropriate determination of phase boundaries is dependent on an appropriate choice of observables. The thermodynamic potential of the $N\Delta\mu VT$ ensemble is the grand potential Ω , and therefore the most suitable observables in this case are the first derivatives of this potential. The observable most frequently used in the procedures described in this Chapter was $\langle c(\Delta\mu) \rangle = (d\Omega/d\Delta\mu)_{T=const}$, which exhibits a break or discontinuity at the first-order phase transition. Alternatively, one could measure $\langle c(T) \rangle = (d\Omega/dT)_{\Delta\mu=const}$, which in the case of the shallow slope of the coexistence region (i.e. the $T_{IN}(c_1, c_2)$ coexistence region for the system with $\varepsilon = 0.90$) gives a clearer picture in terms of coordinates for the discontinuities. Thus for the weak isotropic-nematic transition (e.g. case of the system with $\varepsilon \rightarrow 1$) the $\langle c(T) \rangle$ measurements were more appropriate, although, for the system size used, the accuracy of determination of c_1 and c_2 is somewhat limited in this region of ε . In this case, the $\langle P_2(\Delta\mu) \rangle_T$ measurements were

also found to be a useful alternative to the $\langle c(\Delta\mu) \rangle_T$ measurements in determining coexistence boundaries.

As the slope of the $T_{IN}(c_1, c_2)$ coexistence region becomes steeper the discontinuity in the $\langle c(\Delta\mu) \rangle$ curve becomes more pronounced, owing to the sharper form of the free energy function. However, the same effect increases another feature, which significantly affected the calculated phase diagram - the hysteresis, shown by the $\langle c(\Delta\mu) \rangle$ isotherms at the boundaries of the large I+N coexisting region. To quantify this effect, we show, in Figure 6.32, $\langle c(\Delta\mu) \rangle$ curves, which were measured in simulation sequences with, respectively, increasing and decreasing $\Delta\mu$ values. In Figure 6.32(a) we present such curves for the system with $\varepsilon = 0.00$ at temperature $T = 0.6$. As $\Delta\mu$ decreases (blue curve), the $\langle c(\Delta\mu) \rangle$ curve exhibits a sharp discontinuity at $\Delta\mu_{coex}^{down}$, yielding two concentration values c_1^{down} and c_2^{down} . When the simulation sequence is reversed, however, ($\Delta\mu$ increases, red curve) the $\langle c(\Delta\mu) \rangle$ curve exhibits its discontinuity at $\Delta\mu_{coex}^{up}$, with the two corresponding concentration values c_1^{up} and c_2^{up} . The concentration differences Δc_1 and Δc_2 , depend on $\Delta\mu_{coex}^{up} - \Delta\mu_{coex}^{down}$, which shrinks with increasing temperature, and on the steepnesses of the slopes on both sides of $\Delta\mu_{coex}$, which increase with temperature (Figures 6.32(a),(b),(c)). Although these two do not cancel each other out perfectly, they do lead to a relatively weak thermal dependence of $\Delta c_1(T)$ and $\Delta c_2(T)$. The hysteresis becomes negligible for $T \gtrsim 0.9$ (Figure 6.32(c)). In Figure 6.33 we present a phase diagram for the system with $\varepsilon = 0.00$, which is analogous to that presented earlier in Figure 6.31, this time showing the coexistence boundaries taking into account the hysteresis effect. From Figure 6.33 it is clear that the hysteresis is greatest at $T \approx 0.60$.

As was noted in Section 6.1, a more accurate estimate of c_1 and c_2 can be obtained by means of distribution histograms than is achievable by the other methods described; however, the former requires much more extensive calculations. It also ceases to be effective if Δc becomes too great. Even the faster approach of producing $\langle c(\Delta\mu) \rangle$ isotherms requires extensive scanning of the $\Delta\mu$ axis. This raised the dilemma of whether to decrease the $\delta\Delta\mu$ step between the $\Delta\mu$ points that make up the isotherm at the expense of decreasing the simulation run σ per point or increase σ while increasing $\delta\Delta\mu$. It would be more efficient to concentrate this effort immediately in the vicinity of the first-order phase transition, but this would require prior knowledge of the approximate location of $\Delta\mu_{coex}$ for a given T and ε . In Figure 6.34 we present plots of $\Delta\mu_{coex}$ against temperature for different values of ε . The form of $\Delta\mu_{coex}(T)$

can be seen to be approximately linear and independent of ε for all these systems. This information would, therefore, be used to estimate a relatively narrow $\Delta\mu$ range required for a given scan to include $\Delta\mu_{coex}$, since the information presented in Figure 6.34 could be used to predict the $\Delta\mu_{coex}$ value for a given system, based on only two $\Delta\mu$ points. Adjusting this approach enabled us to concentrate isotherm scans in relatively narrow a region about these predicted $\Delta\mu_{coex}$ values.

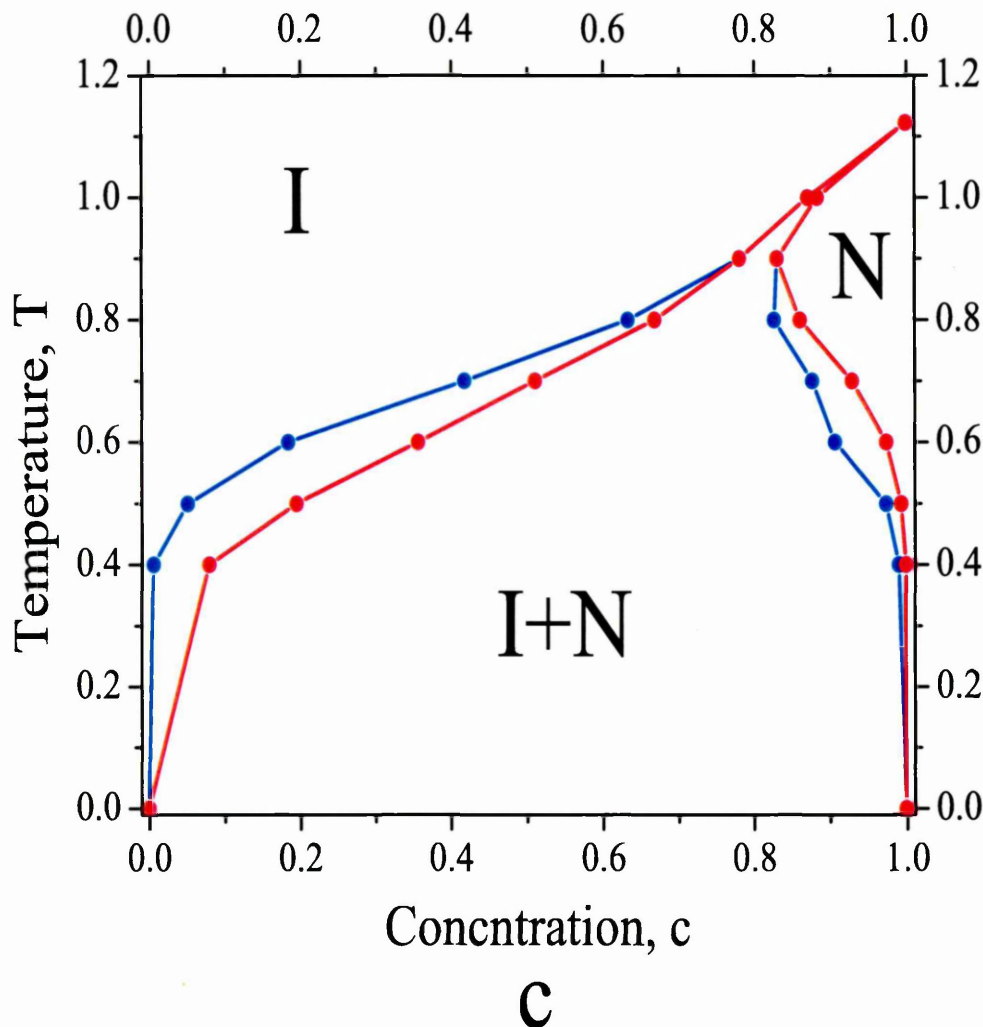


Figure 6.33: Phase diagram for $\varepsilon=0.00$. Red points represent the data calculated as $\Delta\mu$ increases, while blue points represent the data calculated as $\Delta\mu$ decreases. The difference between two data sets indicates the hysteresis experienced.

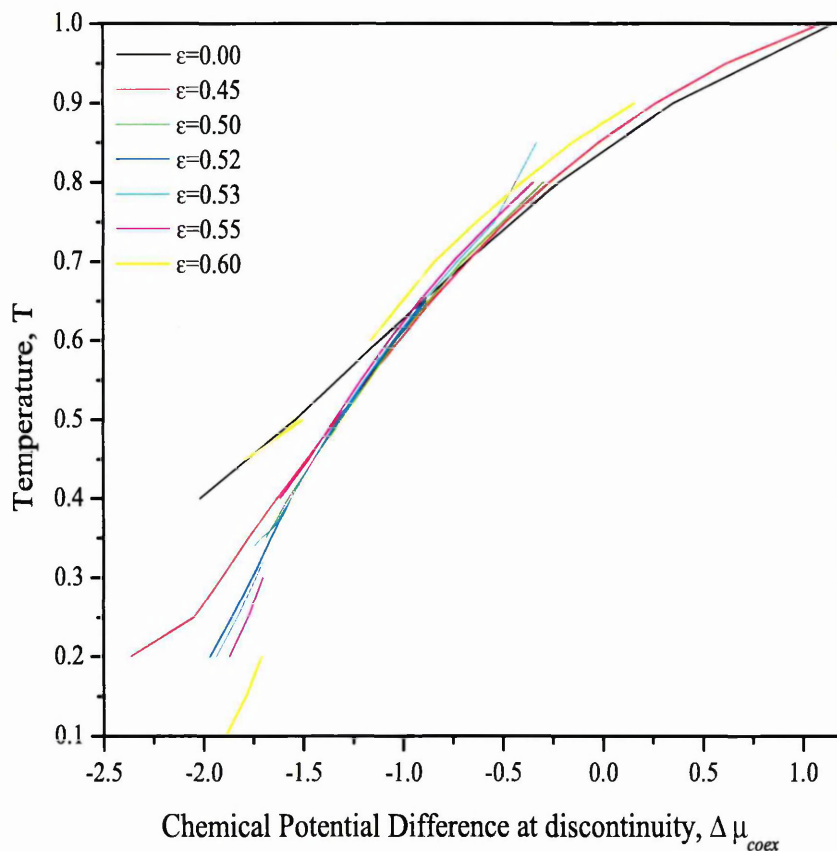


Figure 6.34: The ratio between $\Delta\mu_{coex}$ and T . Knowing this dependence, which is fairly linear for a large range of $\Delta\mu_{coex}$ and T , allowed the range of the scanned $\Delta\mu$ values (for which the transition occurs) to be significantly reduced. The discontinuities in some of the curves are due to two individual coexistence regions (I+N and N+N).

At the beginning of this Chapter we mentioned that concentration fluctuations, which are inversely proportional to the size of the system, allow the observation of two peaks on the concentration histogram (Figure 6.2). This same size effect minimizes the ‘kink’ in the Van der Waals equation of state. The smaller the effect in the the Van der Waals loop, the deeper into the metastable state the system is able to go. In the case of the system with $\varepsilon = 0.90$, this ‘kink’ is probably virtually flat, so that the system effectively moves continuously along the isotherm (Figures 6.5 and 6.6), while the order parameter changes relatively sharply, reflecting rapidly changing symmetry of the system (Figure 6.8). In other cases, where the value of Δc is large, the system experiences difficulty in moving from one preferred concentration

to another. A difficulty for phase diagram measurements is, therefore, present when these two phenomena are located close to each other on the isotherm path. For example, this results in insufficient resolution to indicate the small nematic phase in the bottom left corner of the phase diagram for $\varepsilon = 0.52$ (Figure 6.24 on page 184), since the $\langle c(\Delta\mu) \rangle$ isotherm does not always reveal two discontinuities.

Owing to these effects a difficulty also arises when calculating phase boundaries in the narrow range of temperatures (for values of ε close to 0.53), when, throughout the entire concentration region (from $c = 1.0$ to $c = 0.0$), the system remains in the nematic phase, while being close to two coexistence regions which are present at slightly higher and lower temperatures. In Chapter 5 we showed that as ε decreases this temperature region becomes narrower and vanishes at some ε_{coup} . In our $N\Delta\mu VT$ simulations the isotherms measured in this region changed continuously, but quite rapidly from very high to very low values of c and, thus, a criterion of a threshold steepness had to be devised in order to determine whether the discontinuity occurs for a given T . Attempts to validate this criterion by increasing the system size proved ambiguous.

Therefore, for systems with $\varepsilon = 0.55$, $\varepsilon = 0.53$ and $\varepsilon = 0.52$ we have used the order parameter data not only to determine the phases on both sides of the coexistence boundaries, but also to estimate the possible existence of such boundaries. Generally, at these temperatures, we assumed no discontinuity unless there was sufficient evidence to indicate otherwise. Consequently, a certain level of ambiguity remains, as to what is the lowest value of ε at which the phase diagram exhibits two distinct coexistence regions.

From the results presented in this Chapter, we see that the system exhibits six ‘transitions’ from one phase to another. Depending on its parameters (e.g. $c(\Delta\mu)$, T and ε), the system can undergo these transitions by four different routes. These routes are:

$$I \xrightarrow{\textcircled{1}} N \xrightarrow{\textcircled{3}} N + N$$

$$I \xrightarrow{\textcircled{2}} I + N \xrightarrow{\textcircled{4}} N + N$$

$$I \xrightarrow{\textcircled{2}} I + N \xrightarrow{\textcircled{5}} N \xrightarrow{\textcircled{3}} N + N$$

$$I \xrightarrow{\textcircled{2}} I + N \xrightarrow{\textcircled{5}} N \xrightarrow{\textcircled{6}} I + N \xrightarrow{\textcircled{4}} N + N$$

where the arrows represent decreasing temperature. As we have shown, all discontinuities of the $\langle c(\Delta\mu) \rangle$ isotherms are associated with concentrations which determine coexistence boundaries. Therefore, the entire phase behaviour can be described in terms of these four paths across the phase diagram. One of these boundaries (④) is not seen directly from the $N\Delta\mu VT$ results, but is assumed to be present, based on the $\langle P_2(\Delta\mu) \rangle$ data outside the coexistence region and on the NcVT results (transition at $T'_{tr}(c)$). The behaviour of the remaining five boundaries have been arranged in three groups and will be discussed in the following three sections. Section 6.5.1 will cover the $T_{IN}(c_1, c_2)$ coexistence region, which includes the first-order isotropic-nematic transition (steps ① and ⑤) and the isotropic-nematic transition, weakened by impurities (step ②). Section 6.5.2 will cover entry to the nematic-nematic demixing coexistence region (step ③). Section 6.5.3 will discuss particularities relating to the coupled single coexistence region, which occurs for $\varepsilon \lesssim \varepsilon_{couple}$; these include the phase re-entrance phenomenon (step ⑥) and the induced isotropic nematic transition (step ② revisited). This will be followed in Section 6.5.4 by an analysis of the phase diagram.

6.5.1 $T_{IN}(c_1, c_2)$ coexistence region

Let us begin with the system with $\varepsilon = 0.9$. The $\langle c(\Delta\mu) \rangle$ data does not reveal any distinct discontinuity in this curve (Figures 6.4-6.6), despite very thorough investigation of the region where the transition is expected (simulations within $T = 0.90-1.20$ with a step size of $\Delta T = 0.01$). However, the $\langle P_2(\Delta\mu) \rangle$ data reveal that the phase transition does in fact occur in this region (Figure 6.8). Further investigation of the region (using the $\Delta\mu = const$ method) supports the $\langle P_2(\Delta\mu) \rangle$ data as do the results obtained from the NcVT Ensemble (Chapter 5). For the reasons, given at the beginning of the discussion (Section 6.5), the $\langle c(\Delta\mu) \rangle_{T=const}$ curve exhibits effectively continuous behaviour with change in $\Delta\mu$. On the other hand, the $\langle P_2(\Delta\mu) \rangle$ and $\langle c(T) \rangle_{\Delta\mu=const}$ curves suggest a sharp transition. In the system with $\varepsilon = 0.9$, the slope of the $T_{IN}(c_1, c_2)$ coexistence region is very flat (Figure 5.9). Therefore, for isotherms in the range $0.9 \leq T \leq 1.15$, the concentration changes slowly as $\Delta\mu$ decreases, until it reaches c_2 , the coexistence boundary. The $\langle c(T) \rangle_{\Delta\mu=const}$ data suggest the presence of a coexistence region, which widens at $c \approx 0.5$. However, the transition is very unclear for concentrations close to $c = 0.0$ and 1.0 .

As ε decreases, the slope of the $T_{IN}(c_1, c_2)$ coexistence region becomes steeper. In Section 5.4.5 we considered the nature of $T_{IN}(c)$ and the dependence of its slope on c and ε ; we now propose to add to this discussion by commenting on the shape of the $T_{IN}(c_1, c_2)$ coexistence region. With the decrease of ε , the cigar shape of the $T_{IN}(c_1, c_2)$ region becomes more evident (the system with $\varepsilon = 0.6$, Figure 6.12). This type of behaviour has been discussed in theoretical works concerning mixtures [11,191] and reported in numerous experimental studies of LC [20,192–194], although the influencing factors in these two are different. Generally, all nematics in real life contain impurities. It is also known that impurities which differ in molecular structure depress the I-N transition temperature and, hence increase the slope of the $T_{IN}(c)$ curve. As mentioned earlier a binary mixture is a crude approximation to a system with impurities. The depression of the I-N transition temperature in such a system is connected with the width of the $T_{IN}(c_1, c_2)$ bi-phasic region and the entropy of the transition [191]:

$$T_{IN} - T_{IN}^{\varepsilon=1.0} = \frac{\Delta c}{\Delta S_{IN}} \quad (6.1)$$

where Δc is the width of the bi-phasic region and ΔS_{IN} is the transition entropy of the pure nematic ($\varepsilon = 1.0$) and there is a dimensional constant of value unity suppressed in the right hand side of 6.1 [191]. Therefore, impurities lead to a broadening of I-N coexistence and the appearance of a bi-phasic region [11,191]; they also minimize the entropy change, resulting in the transition becoming close to second-order.

With a further decrease in ε , the $T_{IN}(c_1, c_2)$ region becomes wider at $c \approx 0.5$ (for systems with $\varepsilon = 0.55$ and $\varepsilon = 0.53$, Figures 6.15, 6.19). The increase of this effect has arisen due to the increased difference in coupling between the two components. Lowering of ε can be related to quest nematogens that are less rod-like or less rigid in their molecular structure than their host, leading to a wider Δc gap and to a steeper slope of the $T_{IN}(c_1, c_2)$ region, as the system deviates from its pure composition ($c \rightarrow 0.5$ from either direction). However, this does not explain why Δc is much wider on the left-hand side of the diagram. In fact, the shape of the coexistence region is affected by several other factors, in addition to the presence of another nematogen with slightly different ε , which produces this cigar-shape effect. One of these factors was described by Mukherjee [195] and Luckhurst [177] in

their discussions of rod-sphere mixtures, which will be considered below. For the present, we note that as ε decreases, the system increasingly exhibits features of rod-sphere mixture systems in which the width of the bi-phasic coexistence region is proportional to the concentration of spheres in the system. Another factor is the entropy associated with the demixing of the system, the importance of which decreases with temperature. Since the coexistence region on the left-hand side of the diagram ($c \lesssim 0.5$) occurs at lower temperatures, than that on the right-hand side, the influence of this factor is lower for $c < 0.5$. The shape of the coexistence region is, therefore, a consequence of the first-order effect (present for all c) and the demixing effect (which enlarges the coexistence region at low temperatures). The radial distribution functions obtained at these state points using the NcVT Ensemble support this conclusion, since the short range function decreases more rapidly for $T < T_{IN}$. This demixing process is discussed further in the next Section.

6.5.2 Nematic-nematic coexistence region

The presence of the coexistence region which occurs due to the demixing of the two components is clearly seen in the data obtained from both ensembles, whereas the $T_{IN}(c_1, c_2)$ region is seen only in the data from the $N\Delta\mu VT$ Ensemble. The general aspects of the former coexistence, as set out in Section 5.4.2 for the NcVT Ensemble, also apply for the $N\Delta\mu VT$ Ensemble which we are currently discussing; thus here we will cover only aspects peculiar to the $N\Delta\mu VT$ data.

The data for the systems with $\varepsilon = 0.9$ and $\varepsilon = 0.6$, obtained using the $N\Delta\mu VT$ Ensemble, are found to be in good agreement with those obtained in the NcVT Ensemble (Figures 5.9, 5.15). Unlike the coexistence region induced by the first-order effects, the boundaries of the demixing region are clearly seen on the curves $\langle c(\Delta\mu) \rangle$ for all systems investigated (Figures 6.4, 6.10, 6.13, 6.16, 6.20, 6.25, 6.28, 6.30), the exception being in the region of temperatures close to T_c , where the discontinuity disappears for $T \geq T_c$. Note that here we consider only systems with $\varepsilon > \varepsilon_{couple}$. In fact the behaviour of the demixing region itself is similar to that of liquid-vapour coexistence, described elsewhere [127, 186]. Such a coexistence region can be approximated with the Guggenheim curve [196]. Although, this approximation does not take into account the anisotropic properties of the system, it still yields a good fit to the lattice model under investigation. For $\varepsilon > \varepsilon_{couple}$ the coexisting phases

are both nematic, thus the difference in anisotropy is relatively small and the shape of the curve is governed, predominantly, by the coupling constant difference, which can be interpreted as a miscibility coefficient.

6.5.3 Coupled single coexistence region

This section will discuss the systems with $\varepsilon \lesssim \varepsilon_{couple}$ and the particularities of the single coexistence region. According to the interpretation made of the results presented in this Chapter, the coupling of the two coexistence regions occurs in the region of $\varepsilon = 0.52\dots 0.53$. It should be noted that the data obtained from the system with $\varepsilon = 0.53$ suggest a possible coupling of these two regions; however, the $\langle c(\Delta\mu) \rangle$ curves in the region of ambiguity ($0.30 < T \lesssim 0.34$) calculated for the system with size 24^3 do not support the presence of a discontinuity with a large Δc in this region of temperatures, whereas for the system with $\varepsilon = 0.52$ the discontinuity is clearly present through the entire temperature region ($\langle c(\Delta\mu) \rangle$ data, Figure 6.20).

The first particularity associated with $\varepsilon < \varepsilon_{coup}$ systems is the presence of a B-rich nematic pocket in the area of low concentrations. The NcVT data clearly indicate the presence of such a phase for $c \lesssim 0.04$ (Section 5.1.3). The $\langle c(\Delta\mu) \rangle$ and $\langle P_2(\Delta\mu) \rangle$ data for the system with $\varepsilon = 0.52$ also suggest two coexistence regions at the same temperature (in the region around $T \approx 0.34$); there are clearly seen from the curves calculated with a small number of runs (Figure 6.22). Each transition has its own pair of concentrations, which define their coexistence boundaries. The concentration range separating the two regions is very small, however, so that in longer runs, the simulation appears to sample configurations with concentrations ranging across both coexistence regions. For certain values of $\Delta\mu$ and temperatures, four peaks on the concentration histogram, rather than two, are anticipated. However, since first three peaks (starting from the lower concentration) are close together, this may not be resolved using the original system size. On the other hand, with increased system size, the decreased width of the peaks may not allow for the sampling of all three at a single $\Delta\mu$.

The second particularity concerns the single coexistence region itself. The phase diagram for the system with $\varepsilon = 0.52$ (constructed using these results) has some

features not seen on any other diagram obtained by the two methods (Figure 6.24). The B-rich nematic phase in the area of low concentrations extends to temperatures higher than $T_{tr}^B \equiv T_{tr}^{\varepsilon=0.52}$, thus creating three coexistence regions. This is evident from the $\langle P_2(\Delta\mu) \rangle$ data for $\varepsilon = 0.52$ system. The first is the small isotropic-nematic coexistence region between the B-rich isotropic and B-rich nematic phases ($c \lesssim 0.15$); the second is the isotropic-nematic coexistence region, separating the B-rich isotropic and A-rich nematic phases (at higher temperatures than the first); and the third is the demixing region of coexistence of the two nematic phases, at lower temperatures. Therefore, at ε_{couple} , the two coexistence regions merge and initially create three coexistence regions. Correspondingly, the phase picture in the area of low concentrations becomes similar to that obtained by NcVT Ensemble, i.e. it contains of only two coexistence regions (Figure 5.27). Similar phase diagrams have been observed experimentally for a variety of binary systems including polymer chain LC mixtures (Chapter 2). In [20] experimental results suggested a small pocket of B-rich nematic phase in a case, similar to that seen in our system with $\varepsilon = 0.52$, where one of the mesogens was made sufficiently small (mesogen *E44*). For equivalent system with larger molecular mass (*E48*) the system's phase behaviour in [20] becomes similar to that of our systems with high ε (recall Figure 2.3 on page 18). Benmouda *et al*, using DSC and optical microscopy, observed similar phase behaviour for a PLC-LC mixture [104]. In [104], a pocket of B-rich nematic phase was also seen (Figure 2.4 on page 20). The Mean-Field Theory fit for this mixture [104] as well as FH-MS Theory calculated for the case described in [20] both support the presence of such B-rich nematic pocket.

As ε decreases, the coexistence region also extends to the high concentration side of the phase diagram, encroaching on the region of the A-rich nematic phase. The c_1 boundary remains in approximately the same position throughout a wide range of coupling constants ($0.00 \leq \varepsilon \lesssim 0.52$), while c_2 boundary moves to higher temperatures and concentrations. This is consistent with the results presented in Chapter 5, however the temperatures T_{tr} and T_d obtained from the NcVT results are generally lower than those indicated by the coexistence boundaries of the $N\Delta\mu VT$ data (Figures 6.29, 6.31). In Section 6.5.2 we underlined reasons, for these differences between the NcVT and $N\Delta\mu VT$ boundary prediction. In the parts of the coexistence envelope for which immiscibility effects are small, however ($T \gtrsim 0.7$), the agreement between these two ensembles is recoverable (Figures 6.29, 6.31).

We now come to the consideration of another particularity, phase re-entrance. As was shown in the last part of Section 5.4, phase re-entrance was predicted in [177] for the system with $\varepsilon = 0.0$ and explained using NcVT simulations on the $\varepsilon = 0.0$ version of the model used in Chapter 5. Recently, Bates showed the presence of this region by performing $N\Delta\mu VT$ simulation on this same system [179]. The coexistence boundaries identified in [179] and the present work are in good agreement, despite the relatively big difference in the system size (40^3 in [179]); the data presented here locate the coexistence boundaries at slightly lower temperatures than those in [179], but well within the stated error bars.

6.5.4 Alternative Interpretation. Generalizing.

So far, all of the coexistence regions have been interpreted in terms of the influence of entropy, interaction potential and internal energy, and some explanations have been offered as to the positions of the coexistence boundaries. Comparisons between the obtained results and theoretical and computer simulation works have been made, and parallels between the presented generic phase diagrams and existing experimental reports have been outlined.

In Chapters 5 and 6, the majority of the results have been presented and discussed by means of concentration-temperature phase diagrams. Understandably, this method was adopted as being accepted practice in the presentation of the phase behaviour of some systems, owing to the popularity of lyotropic and thermotropic LC. The use of coupling constant-temperature diagrams, on the other hand, is an unusual and relatively new approach, which often has a weaker relationship with reality. The only exception, perhaps would be novel LC devices with fixed composition, that change their anisotropic properties, for example by photo induction, which itself is a relatively unexplored and developing area. Nevertheless, we feel it informative to include such diagrams here (based on the $N\Delta\mu VT$ results), to enable comparison with analogous diagrams from the NcVT results, presented in Section 5.3.

The features of interest in these diagrams are the temperatures of discontinuity ($T_{tr}(c)$, $T_d(c)$ and $T'_{tr}(c)$ for NcVT) or, put another way, the boundary positions of the coexistence regions (determined by concentration and temperature for $N\Delta\mu VT$). In Figure 6.35 we present a schematic view of an $\varepsilon - T$ diagram, where it is recog-

nised that the locations of the phase boundaries (or functions in Figure 6.35) are determined by the chosen concentration. Before describing the curves or functions that fit the phase boundaries, we need to note the point $K(1.0, T_{IN}^A)$, where T_{IN}^A is the isotropic-nematic transition temperature of the single system of particles A (particles for which $\varepsilon = 1.0$). The first function to be presented, $f_1 = \varepsilon_{couple}$, is the

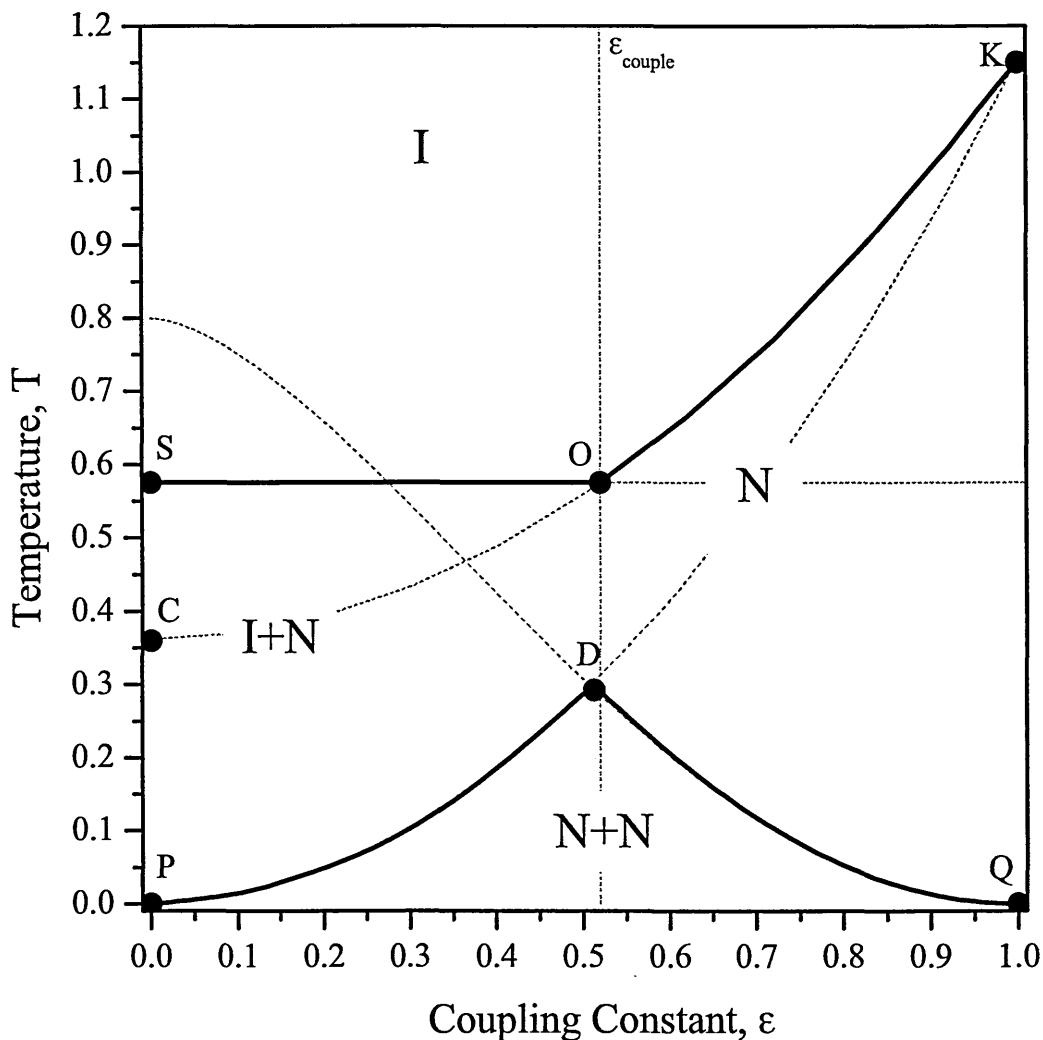


Figure 6.35: Generic form of T - ε phase diagram.

vertical line dividing the phase diagram into two areas - the area in which the two coexisting regions have coupled ($\varepsilon \lesssim \varepsilon_{couple}$) and the area in which they exist separately ($\varepsilon > \varepsilon_{couple}$). The second function is a parabola that includes the point $K(1.0, T_{IN}^A)$ and has its minimum at $P(0.0, 0.0)$ - $f_2(\varepsilon) = a\varepsilon^2$, where $a = T_{IN}^A$. This curve is the

isotropic-nematic transition line for the pure B-component system ($c = 0.0$) for any value of ε , and also effectively represents the isotropic-nematic transition of the B particles in the coexistence region (i.e. when A and B are well separated). Therefore, this function has a significance only in the range PD corresponding to the demixing region (function f_5 , discussed below). The third function is another parabola that includes the point $K(1.0, T_{IN}^A)$ and has its minimum at $C(0.0, c \cdot T_{IN}^A)$. The equation for this curve is $f_3(\varepsilon, c) = a\varepsilon^2 + b$, where $a = (T_{IN}^A - c \cdot T_{IN}^A)$ and $b = c \cdot T_{IN}^A$. This curve represents the boundary of the $T_{IN}(c_1, c_2)$ coexistence region with the isotropic phase (c_1) and assumes a linear dependence of the $T_{IN}(c)$ curve on concentration. This curve is a true representation of phase behaviour only in systems with $\varepsilon > \varepsilon_{couple}$ (OK -part), when the two coexistence regions are separated. In the case of the two being merged ($\varepsilon \lesssim \varepsilon_{couple}$), the boundary with the isotropic phase seems to remain unchanged as ε decreases (Section 5.3). This part of the boundary is, therefore, represented by the fourth function: $f_4(c) = (T_{IN}^A - c \cdot T_{IN}^A) \cdot \varepsilon_{coup}^2 + c \cdot T_{IN}^A$, which is simply a horizontal line that passes through point O , - the intersection of functions f_1 and f_3 . This line separates the isotropic phase from the rest of the diagram and effectively represents the boundary between the $T_{IN}(c_1, c_2)$ coexistence region and the isotropic phase (c_1) when $\varepsilon \lesssim \varepsilon_{coup}$. Functions f_4 and f_3 give the upper boundary of the $T_{IN}(c_1, c_2)$ coexistence region for low and high values of ε respectively (curve SOK). No analytical view of the other boundary (c_2) will be given, as the data that we required for this lie beyond the scope of this thesis (see Section 6.5.1). We have found that the form of the final boundary, $f_5(\varepsilon, c)$ can be fitted by the Guggenheim fit $G(c)$ for liquid-vapour coexistence [196] (see Section 6.5.2). Traditionally, the $G(c)$ curve is plotted in temperature-density coordinates (density is analogous to c in the model used here) with fixed ε . The critical curve [196] and the data obtained suggest that overall $f_5(\varepsilon, c)$ may be expected to decrease as $c \rightarrow 0.0$ or $c \rightarrow 1.0$, as for Guggenheim's curve. We were able to obtain data only in the region $\varepsilon > \varepsilon_{couple}$, to support the contention that $f_5(\varepsilon, c) \sim G(c) \cdot T_{IN}^A \cdot (\varepsilon - 1)^2$. In the region $\varepsilon \lesssim \varepsilon_{coup}$, the demixing boundary is distorted by the effect of the coupling of the coexistence regions, resulting in saturation of the value of the $f_5(\varepsilon, c)$ curve to some T_{sat} , as $\varepsilon \rightarrow 0.0$ for high concentrations (Figure 6.36). Therefore, the dependence of $f_5(\varepsilon \lesssim \varepsilon_{coup}, c)$ on ε in this region was simply fitted with a quadratic function which has a zero derivative at $(\varepsilon = 0.0, T_{sat})$ and connects to $f_5(\varepsilon > \varepsilon_{coup}, c)$ at ε_{coup} , the derivatives of the two curves being matched at ε_{coup} .

According to the NcVT results (Section 5.3), the functions f_1 - f_5 should describe the phase behaviour with reasonable accuracy for a wide range of concentrations ($0.1 < c < 0.9$). However, inconsistencies can be expected on the isotropic-nematic boundary (curve SOK), as $c \rightarrow 0.0$ in the region $\varepsilon \lesssim \varepsilon_{couple}$. Data from both ensembles suggest that the c_1 -boundary (SO) must gradually be transformed into CO as concentration decreases from $c \approx 0.1$ to $c = 0.0$ (for $c = 0.0$, $S = C$). On the other hand, f_5 must decrease significantly for $0.0 \leq c \lesssim 0.1$, so that the cross-point of f_5 and f_2 (point D) shifts along the PK curve as it approaches point P (for $c = 0.0$, $D = P$), being always below the c_1 -boundary (COK or SOK curves). Similar behaviour of f_5 is also anticipated for $c \rightarrow 1.0$ (for $c = 1.0$, $D = P$), although it should be borne mind that D will move along the PK curve less dramatically, owing to the asymmetric shape of the demixing curve (approximated here by $G(c)$). Depending on concentration, the boundary between the I+N and N regions will either follow or lie to the left of line OD and overall cannot be higher than SO or lower than f_5 . For concentrations $c \leq 0.5$ the (I+N)-(N) boundary lies close to the line connecting points O and D , even at very low concentrations ($c \lesssim 0.1$) when the extremely small B-rich nematic region extends between the (I+N) and (N+N) regions.

One feature of the real diagrams that was not included in this section is the width of the $T_{IN}(c_1, c_2)$ coexistence region, the upper boundary of which (c_1) is represented by the functions $f_4(c)$ and $f_3(\varepsilon, c)$ (curve SOK). We simply note that the other boundary (c_2) of the region cannot extend below the limit outlined by $f_2(\varepsilon)$ (curve PK), because temperatures below $f_2(\varepsilon)$ have nematic phases for both components of the mixture.

Let us now examine the calculated phase diagrams and compare them with the predictions discussed above (Figure 6.35). Following the pattern adopted in Section 5.3, we begin with the high concentrations. The diagram in Figure 5.43 in Section 5.3, for $c = 0.7$, suggests a stable nematic phase across the entire range of ε at $c > 0.7$. Let us, therefore, consider first the diagram for $c = 0.9$ (Figure 6.36). Here, the data points were obtained from the linear interpolation, based on the data obtained for c_1 and c_2 in Sections 6.2-6.4. The data from the NcVT (black-filled squares) and $N\Delta\mu VT$ (blue-filled circles) results for $c = 0.9$ in Figure 6.36 fit well with the functions f_1 - f_5 , described earlier. As expected, the nematic region in the centre of the diagram extends across the entire region of ε . The data for

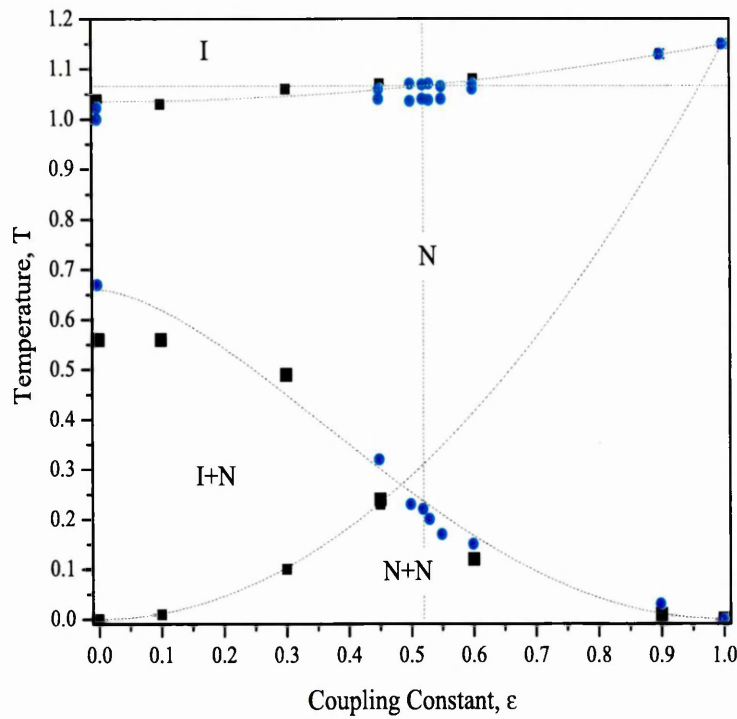


Figure 6.36: T - ϵ phase diagram for $c=0.90$. Dotted lines represent generic diagram, while filled blue circles and black squares respectively represent $N\Delta\mu VT$ and $NcVT$ data.

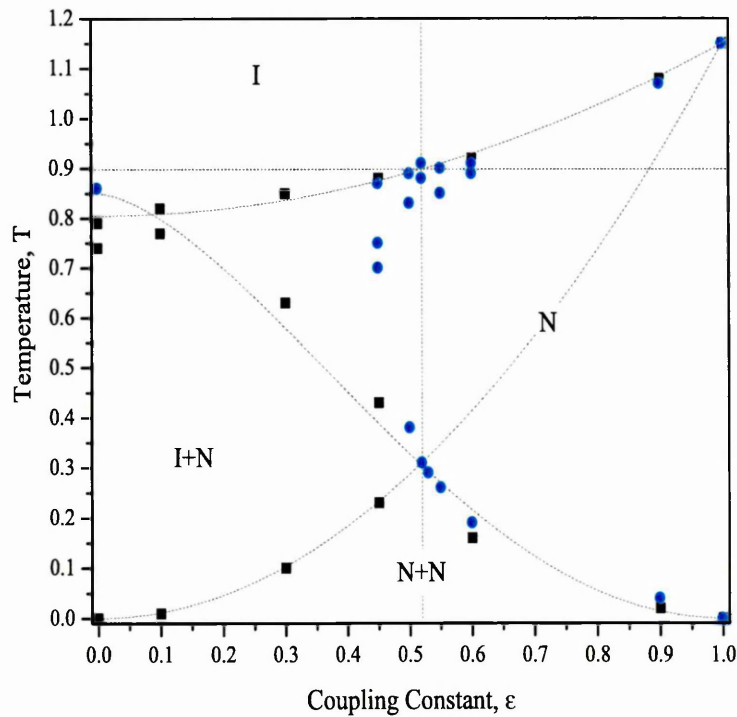


Figure 6.37: T - ϵ phase diagram for $c=0.70$. Dotted lines represent generic diagram, while filled blue circles and black squares respectively represent $N\Delta\mu VT$ and $NcVT$ data.

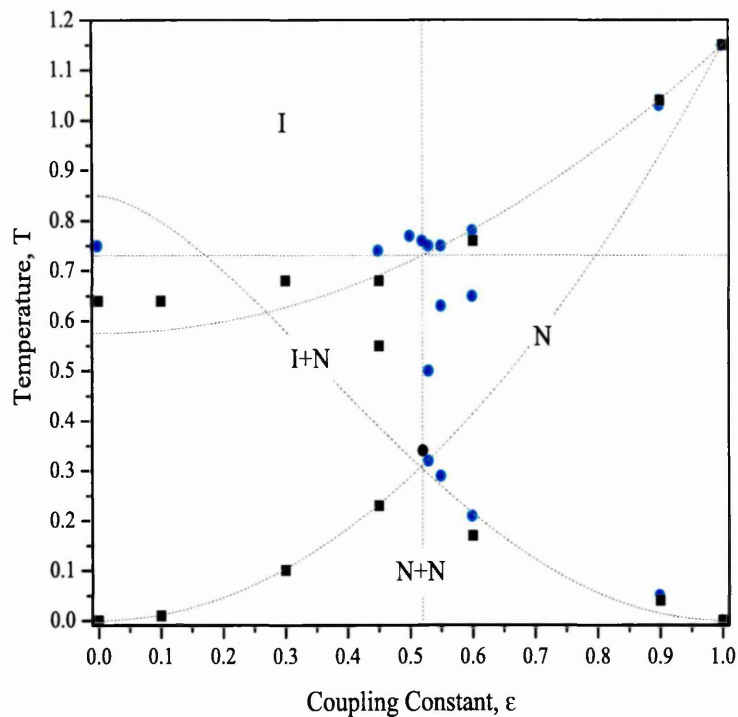


Figure 6.38: T - ε phase diagram for $c=0.50$. Dotted lines represent generic diagram, while filled blue circles and black squares respectively represent $N\Delta\mu VT$ and $NcVT$ data.

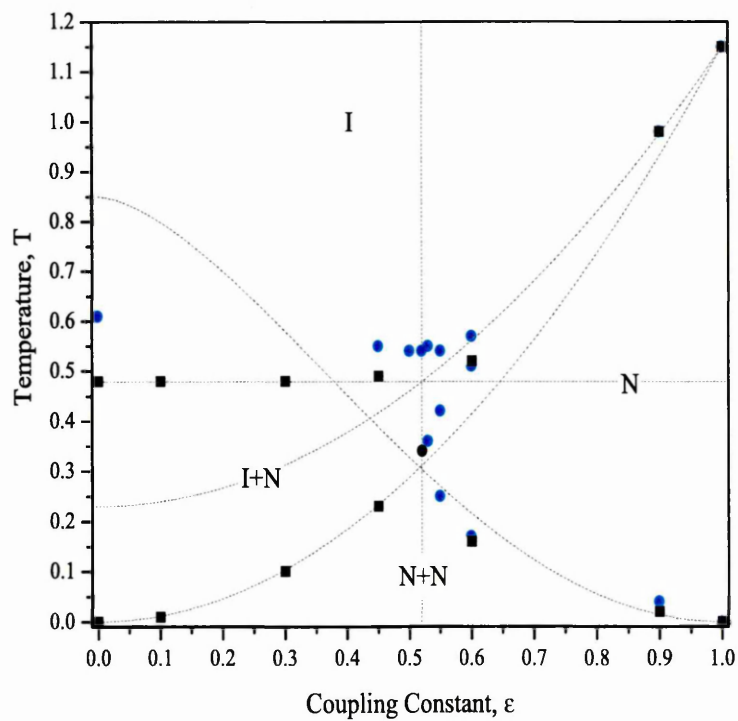


Figure 6.39: T - ε phase diagram for $c=0.20$. Dotted lines represent generic diagram, while filled blue circles and black squares respectively represent $N\Delta\mu VT$ and $NcVT$ data.

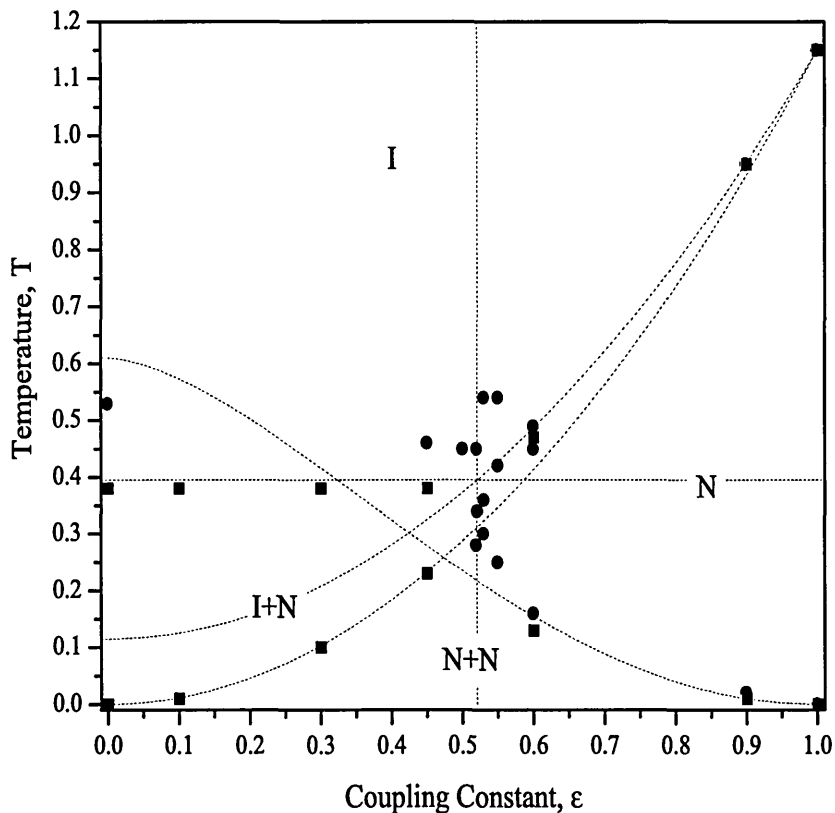


Figure 6.40: T - ϵ phase diagram for $c=0.10$. Dotted lines represent generic diagram, while filled blue circles and black squares respectively represent $N\Delta\mu VT$ and $NcVT$ data.

the demixing coexistence region follow $f_5(\epsilon, c)$ well. This region is divided in two, namely, the isotropic-nematic (above PD) and the nematic-nematic (below PD) coexistence regions. The PD curve is well reproduced by the $NcVT$ results, because at the I-N transition of the B particles, the system is well demixed, so the effect on the transition of the A particles at the interface is minimal.

As we move further down the concentration range ($c = 0.7$, Figure 6.37), several variations occur. The first is that the $T_{IN}(c_1, c_2)$ and demixing coexistence regions couple at $\epsilon < \epsilon_{coup}$, causing the disappearance of the c_2 boundary of the $T_{IN}(c_1, c_2)$ region and the boundary of the demixing region. Note, this doesn't occur for $c = 0.9$ (Figure 6.36) because these boundaries do not couple. This is because the phase diagram for $c = 0.9$ is located in the plain perpendicular to $c - T$ phase diagram for which the nematic region is always present over a certain temperature range. Thus, in spite of the coupling of the $T_{IN}(c_1, c_2)$ and demixing regions at lower c the nematic phase does not vanish at low ϵ for $c \gtrsim 0.9$. The $N\Delta\mu VT$ data show that for

$c = 0.7$ the nematic region, found at higher ε , terminates at $\varepsilon \approx 0.45$, whereas the NcVT data suggest that it extends as far as $\varepsilon \approx 0.10$. We believe the $N\Delta\mu VT$ data to be more accurate, since the observables used in the NcVT ensemble to identify these boundaries cannot be interpreted unambiguously for that range of c and ε .

The second major difference between the $c = 0.7$ and $c = 0.9$ diagram is that in the former point D (from Figure 6.35) moves closer to the vertical line ε_{coup} , as the entire boundary described by f_5 moves higher. The final variation is the lowering of the I-N curve (or c_1 boundary of the $T_{IN}(c_1, c_2)$ region). All data points agree well with the predicted lines in the region $\varepsilon \gtrsim \varepsilon_{couple}$ (curves DQ and OK), but in the low concentration part of the diagram the line SO does not appear to predict the c_1 boundary of the $T_{IN}(c_1, c_2)$ region. Indeed, the data from the NcVT ensemble closely follow curve CO , which suggests that the part of the boundary which is not merged with the demixing region (according to the NcVT data) is unaffected by this region and continues to decrease as ε^2 (CO curve) instead of remaining at fixed temperature

We move now to Figure 6.38, which gives the diagram for $c = 0.5$. The boundary of the demixing region couples with the $T_{IN}(c_1, c_2)$ region at higher ε at this concentration, than it did at the concentrations considered previously; the saturation of the growth of the demixing region by the $T_{IN}(c_1, c_2)$ region (or, equivalently, the resistance by the former to the change in slope of the latter) is greater at $c = 0.5$ than $c = 0.7$ and $c = 0.9$. Consequently, the data from the $N\Delta\mu VT$ results fit well with line SO . Although the points from the NcVT data continue to resemble a quadratic dependence their T values are shifted from CO to SO . At the lower concentrations ($c = 0.2$ and $c = 0.1$, Figures 6.39 and 6.40 respectively), the points from the NcVT data are well aligned to the line SO , whereas the data points obtained from the $N\Delta\mu VT$ results fall slightly higher. The possible reasons for the $N\Delta\mu VT$ results giving higher values for the isotropic-nematic transition temperature for the systems with $\varepsilon \lesssim \varepsilon_{couple}$, were discussed in Section 6.5.3. Here, we simply note that the remainder of the data corresponds well to the predicted curves. These include the (I+N)-(N+N) boundary (curve PD); the boundary between the demixed nematics of two types and the homogeneous nematic phase (curve QD); and the c_1 boundary separating the isotropic phase from the nematic phase (curve OK).

6.5.5 Conclusions Based on the NcVT, $N\Delta\mu VT$ Discussions

To conclude the discussions presented in Chapters 5 and 6 we summarise and repeat the main points mentioned in sections 5.4 and 6.5.

- In [197], authors used the Lebwohl-Lasher model for the binary mixtures of nematogens. They compared four different methods for particle exchange ((a) selecting a pair of unlike particles at random; (b) choosing a pair of nearest neighbours at random; (c) choosing a pair of nearest neighbours or next nearest neighbours at random; (d) selecting a pair of particles at random) and found them to give the same results. However, method (b) was found to be slow to converge. Methods (b-d) included also the possibility of exchanging like particles, which was avoided in our simulations. Thus, our approach is similar to (b), except the exchange of like particles, since only cases of unlike particles were considered. As the result of such an attempt to decrease the convergence time, probabilities of exchanging neighbouring unlike particles were $1/\eta_u$ instead of $1/6$ ($\eta_u = 0\dots 6$ is the number of unlike neighbours, page 43). Although, this does not satisfy the rule of microscopic reversibility in general, it speeds up the simulation and is unlikely to affect well mixed or well demixed areas or, in fact, the transition point between them and, therefore, would not affect a quantitative picture of the overall phase behaviour. This assumption is also supported by external results. The position of the phase boundaries were found to be in good agreement with results of Bates [179] for rod-sphere mixtures and theoretical predictions of Luckhurst *et al* [177]. However, such bias could make the interface between phases less distinct, which could explain a poor resolution of the boundaries at some concentrations (green points on phase diagrams).
- The phase behaviour of LC mixtures was studied using the Lebwohl-Lasher model in NcVT and $N\Delta\mu VT$ Ensembles for a comprehensive range of concentrations, temperatures and coupling constants. The simulation data were compared with existing experimental and simulation results and theoretical predictions.
- Novel approaches were suggested for the determination of the phase boundaries.

- The phase behaviour of the model was also considered in the alternative, temperature - coupling constant plane, and its generic form was determined.
- The NcVT and $N\Delta\mu VT$ results were found to be in good agreement when coexistence between two phases appeared only as a result of the first-order I-N transition.
- In the area where coexistence was also influenced by demixing, however, the NcVT results suggested a smaller coexistence region than that indicated by the more reliable $N\Delta\mu VT$ results.
- Hysteresis effects were clearly evident in the $N\Delta\mu VT$ simulations. While the NcVT data did not suffer such problems, the coexistence boundaries thus identified were subject to finite size error due to the large interfaces present in this ensemble.
- In both NcVT and $N\Delta\mu VT$ Ensembles the phase diagram revealed isotropic, nematic, and coexistence regions. However, only the results from the NcVT Ensemble showed the boundary between two different coexistence regions, while the phase reentrance of I+N phase coexistence predicted by G. Luckhurst [177] was clearly evident only in the $N\Delta\mu VT$ Ensemble.
- Asymmetry of the demixing region was solely due to the orientational anisotropy properties of the system investigated.
- Coupling of two I+N coexistence regions was determined to occur at $\varepsilon_{coup} \approx 0.52$.
- The size of the system as well as the introduction of another type of anisotropic particles was found to reduce the strength of the first-order isotropic-nematic phase transition.
- On the phase diagram, the slope of the I-N boundary was found to change with decrease of ε . However for $\varepsilon \lesssim \varepsilon_{coup}$ the slope remained approximately unchanged, owing to the effect of the demixing processes in the mixture.

Chapter 7

Results And Discussion. Ternary System. NcVT

In this chapter we present and discuss the results for the phase behaviour of the ternary system, based on the Lebwohl-Lasher lattice model. The results were obtained by performing Monte Carlo simulations in the Canonical Ensemble (NcVT). The model basis was described in Chapter 4. For most calculations we used a system of 16x16x16 particles, as for the previous two investigations. All results presented in this chapter were obtained in this way unless otherwise stated. The correlation length of run for this system is approximately the same as that of the binary system, around 5,000 run steps. Therefore, for such observables as the average energy function $\langle E(T) \rangle_{NcVT}$ and the average radial distribution function $\langle g^{AB}(r = 1, T) \rangle$, runs with 20,000 steps per point were performed, allowing an additional 5,000 steps for equilibration. For the calculation of the second-rank order parameter $\langle P_2(T) \rangle_{NcVT}$, we used from 50,000 to 200,000 steps per point. The temperature step for all $\langle E(T) \rangle_{NcVT}$ and $\langle g^{AB}(r = 1, T) \rangle$ data was $\Delta T = 0.005$. The temperature step used between calculations of $\langle P_2(T) \rangle_{NcVT}$ was $\Delta T = 0.02$.

The values chosen for the coupling constants for each of the three components of the mixture were $\varepsilon_A = 1.0$, $\varepsilon_B = 0.6$ and $\varepsilon_C = 0.2$. In what follows, the concentrations of these are denoted as c_A , c_B and c_C , although only two of them are independent. The entire phase behaviour will then be presented as a 3D phase diagram. In addition, for the sake of clarity, we will present some of the results as 2D phase diagrams that represent planar cuts through the 3D phase diagram.

In Section 7.1 we explain the geometry of these phase diagrams. Before any results are presented, in Section 7.2 some data from Chapter 5 will be mapped on the new 3D type of phase diagram. The presentation of data will then follow in Section 7.3. Owing to the large quantity of data collected we will present only selected results, presenting the data for concentrations which lie on distinct planes in the 3D phase diagram. These planes correspond to the bisectors of the equilateral triangle which forms base of the 3D phase diagram and are named after particle types A , B and C since they include the concentration points $c_A = 1.0$, $c_B = 1.0$ and $c_C = 1.0$ respectively (Sections 7.3.1-7.3.3). The presentation of results will be concluded with 3D phase diagrams in Section 7.4, where we will discuss the results presented in Sections 7.3.1-7.3.3.

Since all observables presented in this chapter were obtained at constant $NcVT$, the index ($NcVT$) is omitted in the notation. As in the binary system (Chapter 5), in the ternary system presented in this Chapter the more anisotropic particles are indexed as particles A , with coupling constant $\varepsilon_A = 1.0$, then the less anisotropic particles are indexed as particles B , with coupling constant $\varepsilon_B = 0.6$. In addition, a third type of particles is introduced and indexed as particles C . This type of particle is the least anisotropic of all three ($\varepsilon_C = 0.2$)

7.1 Geometry Of The Phase Diagram For The Ternary Mixture

In order to construct a concentration-temperature phase diagram for the binary system in Cartesian coordinates, two dimensions are sufficient (since the concentration can be defined by one parameter). However, for a ternary system, in which there are three components whose concentrations are not fixed, another dimension must be introduced. In the current model only two of the three concentrations are independent (Equation (7.1)).

$$c_A + c_B + c_C = 1.0 \quad (7.1)$$

This means that all possible concentrations are located on a single 2D surface. The closest structure for such a phase diagram is a 3D prism, a 2D concentration surface limited by an equilateral triangle plus another dimension for the temperature.

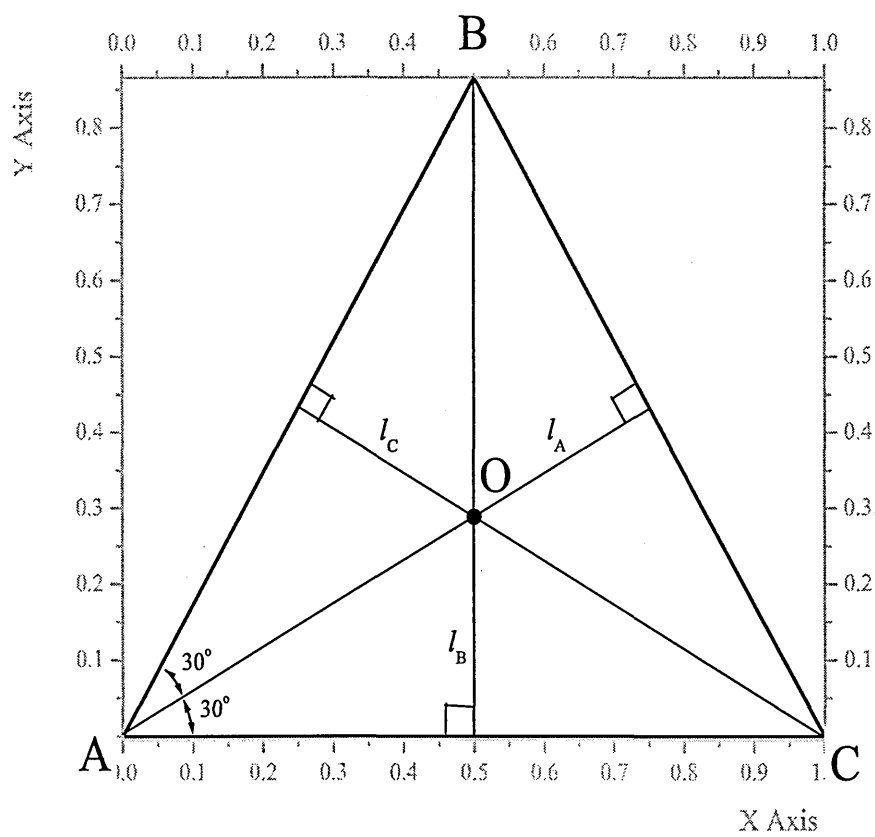


Figure 7.1: Geometry of the concentration surface for the ternary system

The coordinates, c_A , c_B and c_C do not, however, straightforwardly fill a Cartesian space (Figure 7.1). Suppose that the equilateral triangle ABC of the concentration surface is plotted on a Cartesian surface, so that $A = (0.0, 0.0)$, $B = (0.5, \frac{\sqrt{3}}{2})$ and $C = (1.0, 0.0)$. In this case, a point O on the concentration surface ABC represents a composition of the system with concentrations:

$$c_A = \frac{l_A}{l_A + l_B + l_C} \quad c_B = \frac{l_B}{l_A + l_B + l_C} \quad c_C = \frac{l_C}{l_A + l_B + l_C} \quad (7.2)$$

where l_A , l_B and l_C are the projections of O onto the sides BC , CA and AB respectively. A special case of the ternary system, which is equivalent to the general case of a binary system, occurs when the concentration of one of the three components is zero (i.e. $c_A = 0.0$ or $c_B = 0.0$ or $c_C = 0.0$).

In the next section, the data from three binary systems analogous to those presented in Chapter 5 will be used to construct phase diagrams on the faces of the 3D prism. these faces correspond to sides BC , CA and AB and represent phase diagrams for binary mixtures of particles B and C, particles C and A, and particles A and B respectively. To fit a 2D phase diagram of a binary mixture onto a face of 3D prism we used relations (7.3-7.5), where concentration values c of the binary systems were converted to x and y coordinates of the base ABC of the prism (Figure 7.1). Relation (7.3) converts the c -coordinate of the binary system of particles B and C, relation (7.4) converts the c -coordinate of the binary system of particles C and A and relation (7.5) converts the c -coordinate of the binary system of particles A and B; while T -coordinate remains unchanged.

$$x = (1 - c) \cos 60^\circ \quad y = (1 - c) \sin 60^\circ \quad \left(c_A = 0.0, \quad c = \frac{c_B}{c_B + c_C} \right) \quad (7.3)$$

$$x = c \quad y = 0.0 \quad \left(c_B = 0.0, \quad c = \frac{c_C}{c_A + c_C} \right) \quad (7.4)$$

$$x = 1 - \sin 30^\circ c \quad y = \cos 30^\circ c \quad \left(c_C = 0.0, \quad c = \frac{c_A}{c_A + c_B} \right) \quad (7.5)$$

To sample effectively the phase behaviour of the system inside the prism, one could randomly select points c_A , c_B and c_C retaining the constraint given in Equation (7.1). Alternatively, one could explore the concentration space by scanning across lines corresponding to one of the concentration values being held fixed. Then, all of the possible remaining concentration points $O_i(c)$ will depend only on one further variable, c , and will lie on a line which is parallel to the corresponding edge of the prism (BC for $c_A = \text{const}$, CA for $c_B = \text{const}$, AB for $c_C = \text{const}$). For example, if $c_B = \text{const}$, the Cartesian coordinates for any composition read as follows:

$$x = \frac{1}{2}c_B + c \quad y = \frac{\sqrt{3}}{2}c_B \quad c[0\dots 1] = \frac{c_A}{c_A + c_C} \quad (7.6)$$

where c is analogous to the concentration of the binary systems and represents the relative concentration of the remaining compounds, A and C. The majority of our calculations were performed using this method. This approach enabled us to cover comprehensively the entire concentration space (Figure 7.2), using twenty four $O_i(c_B, c)$ points with a relatively uniform distribution. We also conducted simulations at nineteen further points: one for the case $c_A = c_B = c_C = \frac{1}{3}$ and the rest for the three further planes (six points per plane). The three planes that we used for this were the three bisectors of the concentration triangle (Figure 7.1).

For such planes the values of all three concentrations are variable, while $O_i(c)$ still depends on only one parameter. The Cartesian coordinates for $O_i(x, y)$ are given in Equations 7.7-7.9:

$$x = \frac{1}{4} + \frac{c\sqrt{3}}{2} \cos 30^\circ \quad y = \frac{\sqrt{3}}{4} + \frac{c\sqrt{3}}{2} \sin 30^\circ \quad \left(c_B = c_C, \quad c[0\dots1] = \frac{c_A}{c_A + 2c_B} \right) \quad (7.7)$$

$$x = 0.5 \quad y = \frac{c\sqrt{3}}{2} \quad \left(c_A = c_C, \quad c[0\dots1] = \frac{c_B}{c_B + 2c_C} \right) \quad (7.8)$$

$$x = 1 - \frac{c\sqrt{3}}{2} \cos 30^\circ \quad y = 1 - \frac{c\sqrt{3}}{2} \sin 30^\circ \quad \left(c_A = c_B, \quad c[0\dots1] = \frac{c_C}{c_C + 2c_A} \right) \quad (7.9)$$

The results for the concentrations corresponding to points on these three planes, set out by the constraints Equations 7.7-7.9, are presented in Sections 7.3.1-7.3.3 respectively. These include the data for the points $c_A = c_B = c_C = \frac{1}{3}$.

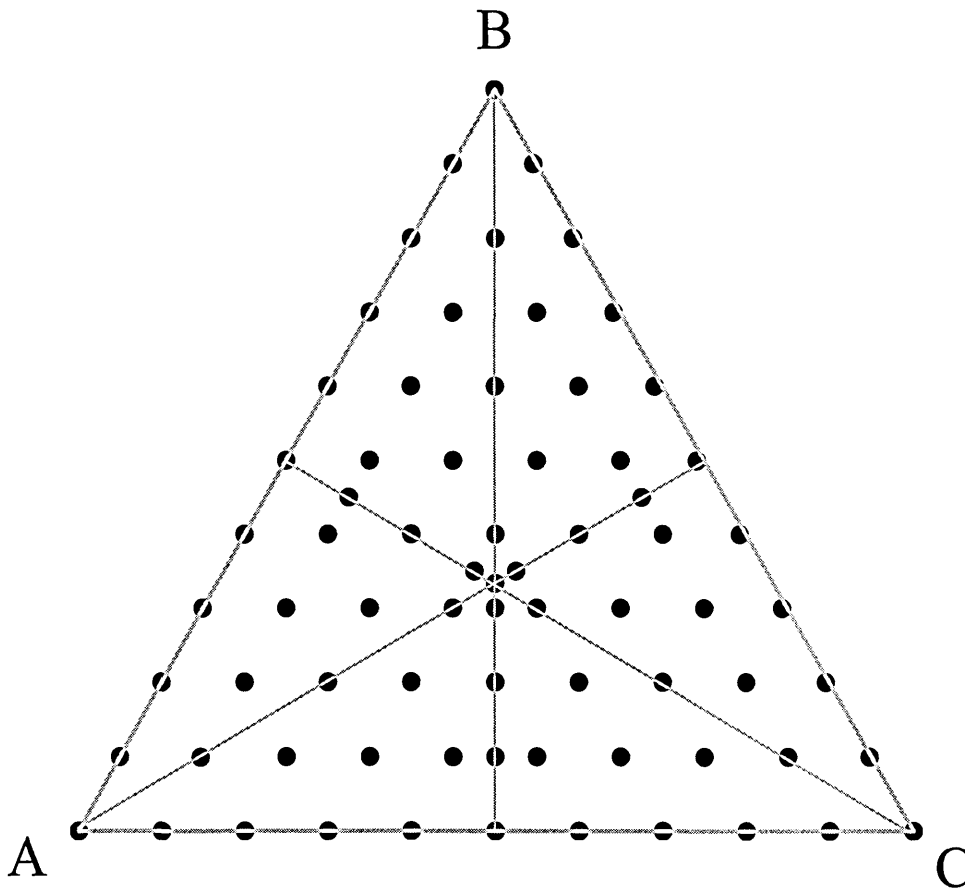


Figure 7.2: Concentration points investigated. 45 points

7.2 What We Know From Binary Systems

Earlier we described the geometry of the 3D phase prism for ternary system. Before we comment on the three binary systems that form the faces of the prism, let us first explain the notation to be used (Figure 7.3). For simplicity, these faces will be called face AB , face BC and face CA . These correspond to the components whose binary phase diagrams makes up each face. Similarly, the vertical edges of the prism, the temperature axes corresponding to the three pure components, will be called edge A , edge B and edge C respectively.

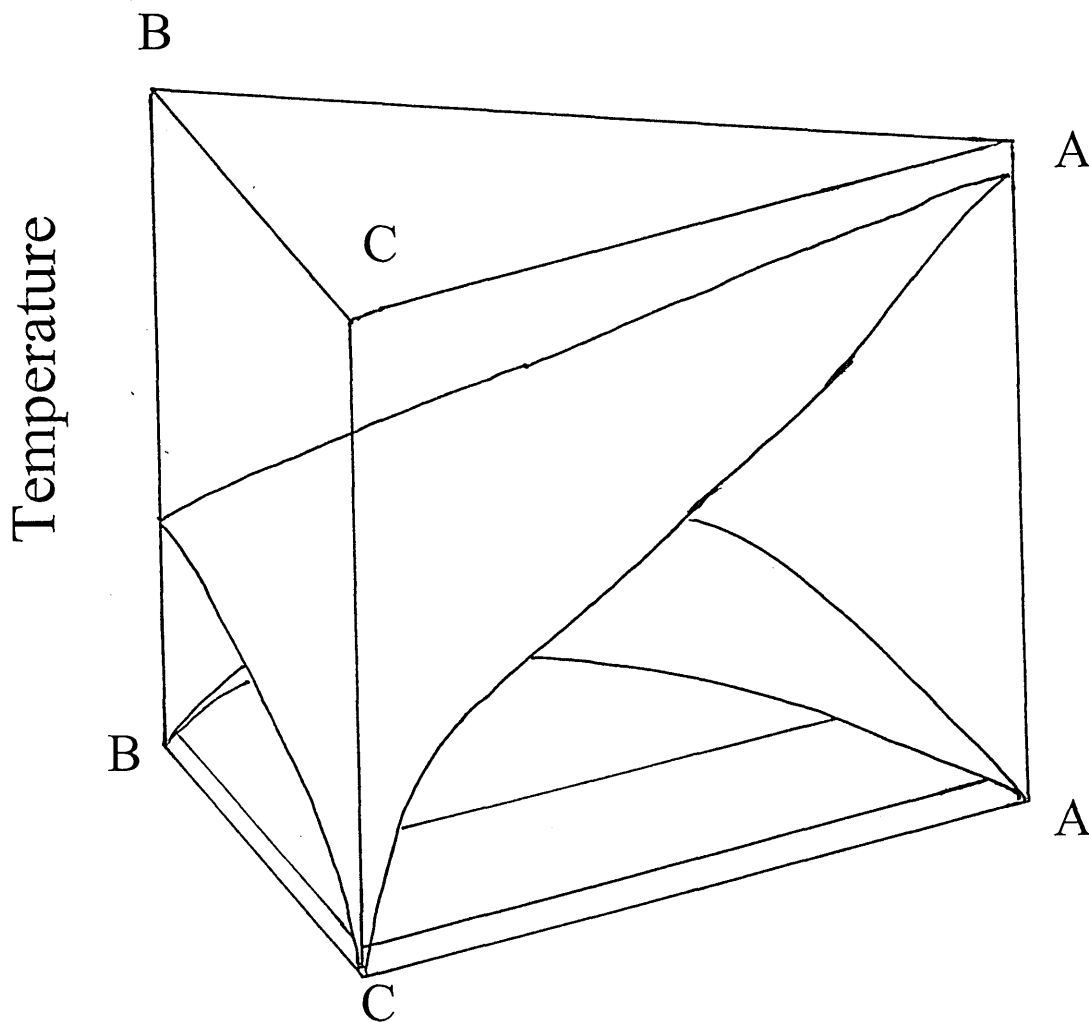


Figure 7.3: Representation of the data from Chapter 5 on faces of the 3D prism.

As was mentioned at the beginning of this Chapter, the system considered here comprises three components with coupling constants $\varepsilon_A = 1.0$, $\varepsilon_B = 0.6$ and $\varepsilon_C = 0.2$. Therefore, some data from Chapter 5 can be used to construct phase boundaries on the faces of the phase prism. The data for the binary system with $\varepsilon = 0.6$ (Figure 5.15, page 77) is rescaled to face AB using relation (7.5) and the system with $\varepsilon = 0.2$ (not presented before) is rescaled to face CA using relation (7.4). For face BC , using relation (7.3), the rescaled data of the binary system with $\varepsilon = 0.35$ (not presented before) was used (strictly, the binary system with $\varepsilon_B = 0.6$ and $\varepsilon_C = 0.2$ corresponds to a rescaling of a binary system with $\varepsilon \approx 0.33$). After transforming the concentration points using relations (7.3-7.5) the phase points were plotted onto the diagram, shown in Figure 7.3.

From this Figure one can intuitively envisage a smooth surface of isotropic-nematic transition which connects the I-N curves on faces AB , BC and CA , assuming that no anomalies occur once a third component is introduced. On each of the three vertical edges A , B and C of the prism, the I-N curves of the corresponding two faces meet at T_{IN}^A , T_{IN}^B and T_{IN}^C respectively. It is also likely that the nematic-nematic coexistence curves will encounter no anomalies on all three edges of the prism (A , B and C), as they meet at $T = 0.0$. At this stage it is difficult to predict any coexistence boundaries, especially below the demixing curve (the curve between any homogeneous phase and a coexistence region). Once one component of the mixture is segregated, the rest of the bulk can be treated as a binary mixture with the coupling constants of the corresponding components. However, it may be that this approximation will work only if the I-N transition temperatures of the pure components, which remain mixed in the bulk, lie below the demixing curve of the system. These, and other speculations will be revisited in Section 7.4, after all the results have been presented.

7.3 Results From Ternary Systems

We now come to consideration of the ternary system, that is, a system in which, unlike those in the previous section, all three concentrations are non-zero. First, in Sections 7.3.1-7.3.3 we consider the systems whose concentrations c_A , c_B and c_C vary in such a way that the composition of the system, defined by $O(c_A, c_A, c_B)$, falls on one of the bisectors of the concentration plane (base ABC of the phase

prism). This is achieved if the concentrations of two of the three components are equal ($c_A = c_B$, $c_A = c_C$ or $c_B = c_C$). For simplicity these bisector planes will be called plane C , plane B and plane A , respectively. In addition, we will refer to the composition of the system for planes A , B and C using the concentrations c_A , c_B and c_C respectively, meaning that the remaining two (equal) concentrations are derived from the relation appropriate to the corresponding plane (Equations (7.7-7.9)).

In Chapter 5 we introduced three temperatures of discontinuity, $T_{tr}(c)$, $T_d(c)$ and $T'_{tr}(c)$. These temperatures referred to different processes in the system. It was noted that, although $T_{tr}(c)$ was the discontinuity that always occurred at the highest temperature, the second highest discontinuity temperature was not always $T_d(c)$, but occasionally $T'_{tr}(c)$, owing to the coupling of the first two ($T_{tr}(c) = T_d(c)$, for selected c and ε). The ternary system will almost certainly exhibit more than three such discontinuity temperatures. Before performing thorough analysis, it is difficult to determine to which process each discontinuity temperature refers. Therefore, to avoid the confusion of re-labeling these discontinuity temperatures we index them appropriately as they appear when presenting the results, but defer explanation of these indices to Section 7.4 starting on page 254.

7.3.1 Phase Behaviour in the A-Plane.

The first plane considered is the bisector which starts from point A of the triangle base of the prism ($c_A + 2c = 1.0$, where $c = c_B = c_C$, Equation (7.7)).

The first observable that we present is the average internal energy of the system $\langle E \rangle$. Figure 7.4 shows the dependence of energy $\langle E(T) \rangle$ on temperature for various concentrations c_A . For all concentrations considered, the energy decreases with decreasing temperature. In addition, we observe a gradient discontinuity at temperatures $T_{tr}(c_A)$ on the $\langle E(T) \rangle$ curves for the entire concentration range. The numerical differential of $\langle E(T) \rangle$ (which is related to the heat capacity) reveals a peak at $T_{tr}(c_A)$, which we take to be a point of transition of the system. Let us consider the case $c_A = 0.8$. At first, the energy $\langle E \rangle$ has a negative value at high temperatures. This decreases slowly as the temperature falls until, at $T \approx T_{tr}(c = 0.8) = 0.94$, it starts to decrease more rapidly. The internal energy $\langle E(T) \rangle$ then decreases with a changed slope and shows some small deviations, until temperature is reduced to $T = 0$.

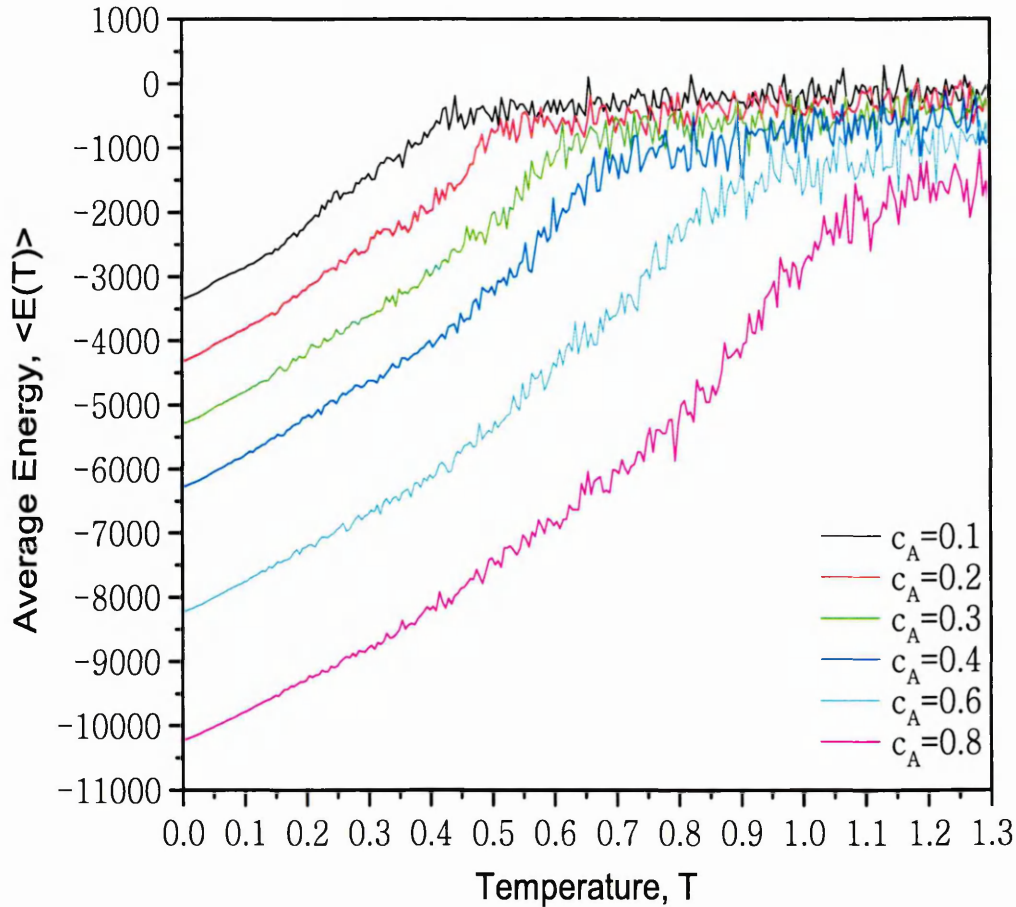


Figure 7.4: The thermal dependence of the energy for various c_A .

As c_A decreases, the entire $\langle E(T) \rangle$ curve moves to higher values but remains below zero, similar to the case of the binary system. However, the small deviations noted for $c_A = 0.8$, do not allow us to determine unambiguously any temperature of discontinuity except $T_{tr}(c_A)$ and $T'_{tr}(c_A)$. These temperatures will therefore be determined from collective analysis of other data, presented further in this section. In Table 7.1 we present the values of temperatures $T_{tr}(c_A)$ for the set of concentrations.

The dependence of the order parameter on temperature ($\langle P_2(T) \rangle$) for the given concentrations c_A is shown in Figure 7.5. The $\langle P_2(T) \rangle$ curves were obtained in an analogous fashion to that used for the binary system presented in Chapter 5 (Figure 5.2 on page 60). As is the case for the $\langle E(T) \rangle$ curves, for $c_A = 0.8$ the shape of the $\langle P_2(T) \rangle$ curve is very similar to that of the binary system with a high value

c_A	$T_{tr}(c_A)$	$T'_{tr}(c_A)$
0.1	0.42 ± 0.01	0.04 ± 0.01
0.2	0.47 ± 0.01	0.05 ± 0.01
0.3	0.56 ± 0.01	0.05 ± 0.01
0.4	0.61 ± 0.01	0.04 ± 0.01
0.6	0.77 ± 0.01	0.05 ± 0.01
0.8	0.94 ± 0.01	0.05 ± 0.01

Table 7.1: Table of temperatures obtained from $\langle E(T) \rangle$ data. These were derived from the points where the tangent of $\langle E(T) \rangle$ was at its steepest.

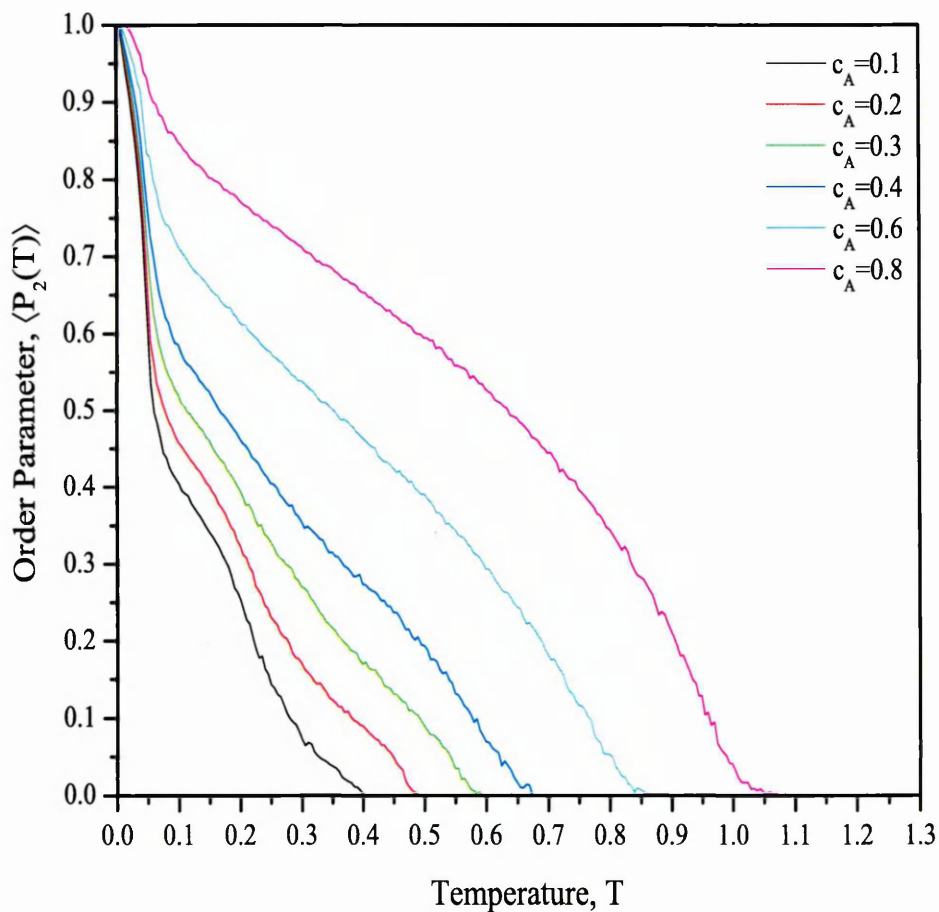


Figure 7.5: The second-rank orientational order parameter, $\langle P_2(T) \rangle$. Different curves represent different concentrations c_A .

of c (compare Figure 7.5 with Figures 5.19 on page 83, 5.29 on page 97 and 5.35 on page 106). From Figure 7.5 we see that the system undergoes the isotropic-nematic transition at temperature $T_{tr}(c_A = 0.8) \approx 1.02$. The value of $T_{tr}(c_A)$ decreases as c_A decreases (Fig.7.5). In addition, the gradient of the $\langle P_2(T) \rangle$ curve exhibits more changes as $c_A \rightarrow 0.0$. For example, at $c_A = 0.1$, as the temperature falls the curve undergoes an initial transition at $T_{tr}(c = 0.1) \approx 0.41$. Then, at $T_{dd}(c = 0.1) \approx 0.30$ the curve develops a steeper gradient, approaching a high value of the order parameter, before, at $T'_{tr}(c = 0.1) \approx 0.07$, the gradient increases still more as $\langle P_2(T) \rangle$ approaches its maximum value.

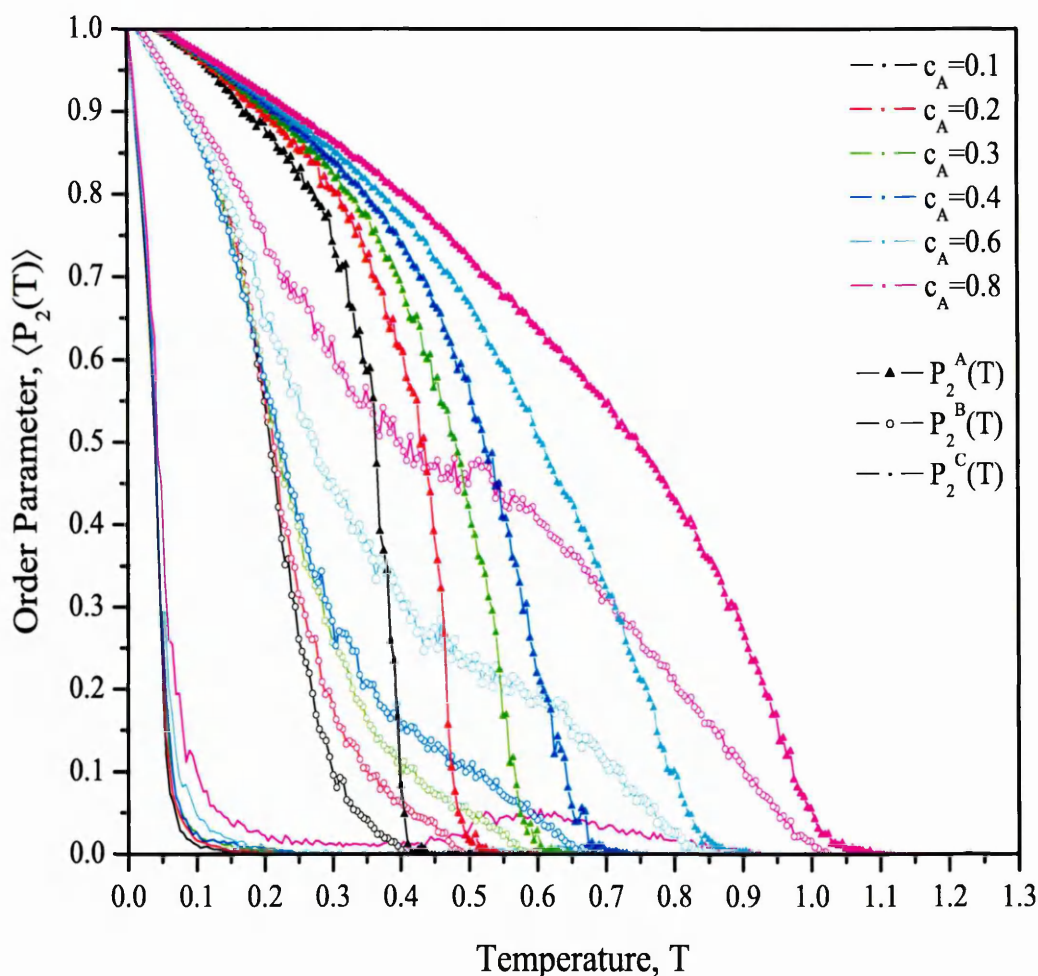


Figure 7.6: Temperature dependencies of the second-rank orientational order parameter shown individually for components A, B and C. Different colors of the curves represent different concentrations c_A . Filled triangles represent $\langle P_2(T)^A \rangle$ for particles A, empty circles - $\langle P_2(T)^B \rangle$ for particles B and dots - $\langle P_2(T)^C \rangle$ for particles C.

c_B	$T_{tr}(c_A)$	$T_d(c_A)$	$T_{dd}(c_A)$	$T'_{tr}(c_A)$
0.1	0.41 ± 0.05	0.41 ± 0.05	0.30 ± 0.05	0.07 ± 0.05
0.2	0.48 ± 0.05	0.48 ± 0.05	0.30 ± 0.05	0.07 ± 0.05
0.3	0.58 ± 0.05	0.58 ± 0.05	0.30 ± 0.05	0.07 ± 0.05
0.4	0.66 ± 0.05	0.66 ± 0.05	0.30 ± 0.05	0.07 ± 0.05
0.6	0.85 ± 0.05	0.62 ± 0.05	0.32 ± 0.05	0.08 ± 0.05
0.8	1.02 ± 0.05	0.58 ± 0.05	0.32 ± 0.05	0.09 ± 0.05

Table 7.2: Table of temperatures, obtained from $\langle P_2(T) \rangle$ data.

From the data presented in Chapter 5 we discovered that such deviations are caused by the mutual influence of the order parameters of each component. Let us, therefore, examine individually the order parameters of the components A ($\langle P_2 \rangle^A$), B ($\langle P_2 \rangle^B$) and C ($\langle P_2 \rangle^C$) (Figure 7.6). From this we see that, while the initial increase in orientational order occurs at the same temperature ($T_{tr}(c_A)$) for particles A and B at all c_A , the shapes of the $\langle P_2(T) \rangle$ curves for each type of particle differ significantly. In addition, a significant increase in $\langle P_2(T) \rangle$ for particles C does not occur except at very low temperatures (≈ 0.1), with a slight increase at $T \approx 0.6$ for high values of c_A . We comment first on the $\langle P_2(T) \rangle^A$ curves. For high values of c_A , the order parameter increases with a steady gradient, starting at $T_{tr}(c_A)$ and gradually approaching 1. As c_A decreases, the order parameter increases more steeply, starting at lower temperatures $T_{tr}(c_A)$. The $\langle P_2(T) \rangle^B$ curves are very distorted throughout the entire range of c_A . The order parameter for particles B increases approximately as a series of line segments. Similarly to the order parameter for particles A, $\langle P_2(T) \rangle^B$ curves start to increase at $T_{tr}(c_A)$, however the increase is less steep, as compared to that of particles A. As the temperature falls, the $\langle P_2(T) \rangle^B$ curves exhibit several changes in gradient, after which the order parameter increases sharply to 1.

For low values of c_A , the $\langle P_2(T) \rangle^C$ curves show a significant increase in the order parameter only at very low temperatures ($T \lesssim 0.1$). For high values of c_A , the order parameter of particles C increases with a shallow gradient after $T_{tr}(c_A)$ until, at $T_d(c_A)$ it falls back to a close-to-zero value. With a further decrease in temperature it increases sharply at $T \lesssim 0.1$. The latter increase of the order parameter occurs for all concentrations on plane A and does not seem to depend on concentration.

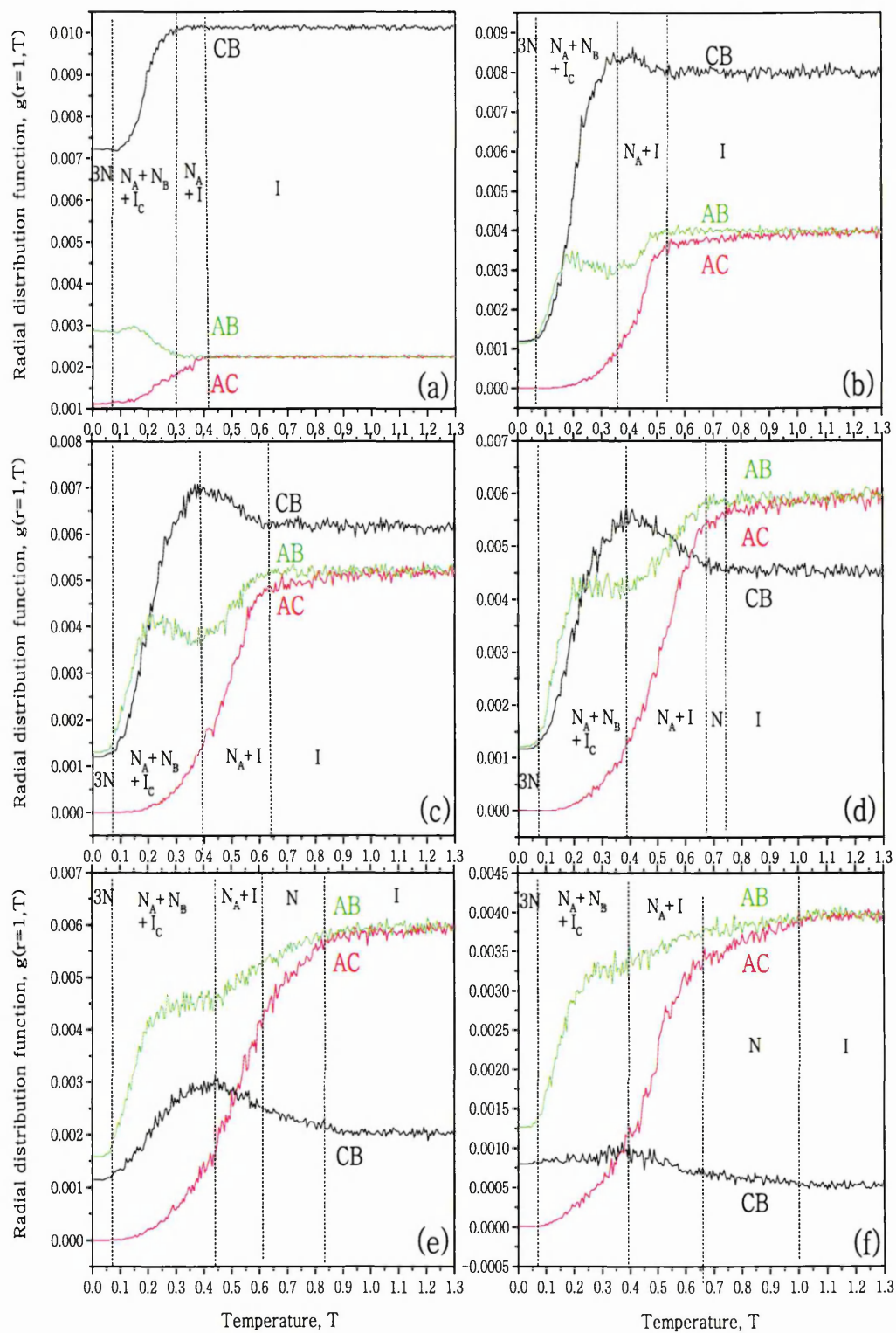


Figure 7.7: Dependencies of the three $g(r = 1)$ functions for the set of concentrations c_A . (a) $c_A = 0.1$, (b) $c_A = 0.2$, (c) $c_A = 0.3$, (d) $c_A = 0.4$, (e) $c_A = 0.6$, (f) $c_A = 0.8$.

The order parameter of all components reaches 1 as the temperature approaches zero. Figure 7.6 shows that the behaviour of the order parameter is more complex than that in single component or binary systems. We will discuss this further in Section 7.4. Table 7.2 shows the values of $T_{tr}(c_A)$ for the full set of concentrations. These values are in reasonable agreement with the values of $T_{tr}(c_A)$ obtained from the energy measurements.

The next observables we present are the radial distribution functions of the unlike particles. In Chapter 5 we discussed the nature of the radial distribution functions and the differences between the short and long range dependencies. We emphasise that here we present only the short range (i.e. $r = 1$) distribution functions and their dependence on temperature. In the binary systems, this dependence provided an adequate representation of the area of the interface between particles of different sorts. However, in the ternary system not one but three radial distribution functions of unlike particles are required to represent fully the structural changes in the system. In this case, therefore, they are not explicit representations of the area of the interface between particles, but rather an indicator of the average interrelationship between any two different types of particle at distance 1. The first function, $g^{AB}(r = 1, T)$, indicates the probability of particles A and B lying adjacent to each other; the second function, $g^{CA}(r = 1, T)$, indicates the probability of particles A and C being adjacent to each other; and the last function, $g^{CB}(r = 1, T)$, indicates the probability of particles C and B being adjacent to each other. This type of distribution function, rather than $g^{AA}(r = 1, T)$, $g^{BB}(r = 1, T)$ and $g^{CC}(r = 1, T)$, was chosen for our analysis of the structural changes because it is more sensitive to the relative repositioning of particles, whereas the other functions are better at indicating the level of segregation of any one type of particle from the rest of the system. Before moving on to the presentation of the data we stress that the values of the distribution functions are normalised according to the total number of particles in the system and not according to the number of particles of each individual type. They therefore also reflect the concentration of each particle type.

In Figures 7.7(a-e) we present these distribution functions for the set of concentrations c_A . The dashed lines represent phase boundaries, the positions of which are based on the $\langle P_2(T)^A \rangle$ and $\langle E(T)^A \rangle$ data, presented previously. At the beginning of this section we referred to this system (plane A) as being one of the closest to

a binary system in its behaviour. However, Figure 7.7 reveals structural behaviour not seen in any of the binary systems. Indeed, it is difficult even to examine any single distribution curve without referring to the other two in order to understand the structural changes in the system. Throughout the entire temperature range, the gradient of $g^{AB}(r = 1, T)$ changes its sign three times, while the gradient of $g^{CB}(r = 1, T)$ changes its sign only once and the sign in gradient of $g^{CA}(r = 1, T)$ remains unchanged. This happens for all concentrations, except $c_A = 0.1$ where these effects are diminished. Let us, therefore, examine all three curves simultaneously as the temperature decreases, starting from the lowest concentration (Figure 7.7(a)).

For the range of temperatures $T > T_{tr}(c_A = 0.1)$, the system is well mixed. The values of $g^{AB}(r = 1, T)$ and $g^{CA}(r = 1, T)$ are approximately equal, which indicates the equal proportions of components B and C in the system as well a uniform distribution of small amount of particles A in the bulk. When the temperature decreases below $T_{tr}(c_A = 0.1)$, the system moves from the isotropic phase and particles A begin to separate out. This can be seen from the decrease in $g^{CA}(r = 1, T)$. The other particles remain mixed, which is seen from unchanged values of $g^{CB}(r = 1, T)$ and $g^{AB}(r = 1, T)$ for temperatures just below $T_{tr}(c_A = 0.1)$. Indeed, snapshots of the system at $T_{dd}(c_A = 0.1) < T < T_{tr}(c_A = 0.1)$ show that particles A formed a drop, while the rest of the bulk (particles B and C) remained mixed. The order parameter data show that particles A developed a nematic order here, while particles C exhibited no orientational ordering and particles B had only a slightly increased order parameter. Overall, for temperatures $T < T_{dd}(c_A = 0.1)$ the functions $g^{CA}(r = 1, T)$ and $g^{CB}(r = 1, T)$ decrease, while $g^{AB}(r = 1, T)$ goes through a bulge as the temperature decreases. The decrease in $g^{CB}(r = 1, T)$ indicates the demixing of the remaining bulk; the corresponding decrease in $g^{AC}(r = 1, T)$ suggests that while separating out and forming a drop, particles A avoid contact with particles C. This can only result from the drop moving deeper inside a region occupied by compound B. The increase of $g^{AB}(r = 1, T)$ at $T_{dd}(c_A = 0.1)$ also supports this suggestion. The latter effect also coincides with the isotropic-nematic transition of particles B.

As the concentration of particles A increases (cases $c_A = 0.2 - c_A = 0.4$), the following changes in the three functions occur. The first concerns the isotropic phase, where the values of $g^{AB}(r = 1, T)$ and $g^{AC}(r = 1, T)$ increase with c_A and that of $g^{CB}(r = 1, T)$ decreases; this simply reflects the changing composition of

the system. The temperature at which all three functions first change ($T_{tr}(c_A)$) increases with increase in c_A . The second change concerns the appearance of a little maximum in $g^{CB}(r = 1, T)$, before the function decreases markedly and the appearance of a slight minimum in $g^{AB}(r = 1, T)$, before its bulge. These features occur just below $T_{tr}(c_A)$ and have their extrema at $T_{dd}(c_A)$. Moreover, they become more pronounced as c_A increases. The third change concerns the fact that for the temperatures $T < T_{tr}(c_A = 0.1)$ all three functions decrease, as the temperature decreases, with the exception of the two bulges on $g^{AB}(r = 1, T)$ and $g^{CB}(r = 1, T)$ mentioned previously.

When the temperature decreases below $T_{tr}(c_A)$, the system moves from the isotropic phase and particles A begin to separate out (decrease in $g^{AB}(r = 1, T)$ and $g^{CA}(r = 1, T)$). The number of interactions between particles of types B and C also increases (function $g^{CB}(r = 1, T)$). As in the case of low concentrations, snapshots of the system at $T_{dd}(c_A) < T < T_{tr}(c_A)$ show a droplet of particles A. Order parameter data indicate nematic order for particles A, and isotropic for particles C and B, although particles B exhibit a slight ordering in this range of temperatures. As temperature passes below $T_{dd}(c_A)$, $g^{AB}(r = 1, T)$ starts to increase, while all the other functions decrease. This coincides with the isotropic-nematic transition of particles B, according to Figure 7.6. In our examination of binary systems we discovered that when the system is in isotropic-nematic coexistence, with a low concentration of particles in the nematic phase (a small nematic drop in an isotropic bulk), the area of the interface increases slightly at the isotropic-nematic transition of the bulk (pages 88-93). In Section 7.4 we discuss where this is also the case for the ternary system.

However, some features remain unchanged with an increase in c_A . At high temperatures, the values of $g^{AB}(r = 1, T)$ and $g^{AC}(r = 1, T)$ are approximately equal, indicating the equal proportions of particles B and C. Similarly, at low temperatures the values of $g^{AB}(r = 1, T)$ and $g^{CB}(r = 1, T)$ are close, indicating that the interfaces between corresponding particle types have similar areas; meanwhile, the value of $g^{AC}(r = 1, T)$ remains consistently at zero, indicating that there is no contact between particles A and C.

As concentration c_A increases further ($c_A > 0.4$), the values of $g^{AB}(r = 1, T)$ and $g^{AC}(r = 1, T)$ continue to increase, while $g^{CB}(r = 1, T)$ decreases for ‘isotropic’

temperatures. However, at temperatures below $T_{tr}(c_A)$, these functions do not exhibit such sharp changes in their gradients as they do at lower values of c_A . As a result, the maximum in $g^{AB}(r = 1, T)$ and the minimum in $g^{CB}(r = 1, T)$ at $T_{dd}(c_A)$, become less pronounced as concentration increases. The $\langle P_2(T) \rangle$ data show nematic order for all particles in the range of temperatures $T_d(c_A) < T < T_{tr}(c_A)$, or more precisely, nematic order is clearly seen for particles A and B, while particles C exhibit some degree of nematic ordering, which is probably induced by the rest of the bulk. This points to the presence of a homogeneous nematic phase, which is particularly clearly present at $c_A = 0.8$. With further decrease in temperature the functions exhibit behaviour similar to that observed previously. However, owing to the changes in concentration, their values at high temperatures are changed (increased for $g^{AB}(r = 1, T)$, $g^{AC}(r = 1, T)$ and decreased for $g^{CB}(r = 1, T)$), while their values at $T \rightarrow 0.0$ remain virtually unchanged. As a result, the maximum in $g^{AB}(r = 1, T)$ and the minimum in $g^{CB}(r = 1, T)$ for $T < T_d(c_A)$ become less dramatic with increase in c_A .

Taking into account the ratio of the three components, the geometry of the system (PBC) and the data presented, the topology of the demixed system can be characterised as follows. For low concentrations ($c_A < 0.2$) the system sheds a nematic drop at first (A) before separating into two layers at lower temperatures (layers B and C), the drop remaining in layer B. As concentration increases ($0.2 \lesssim c_A \lesssim 0.3$), the system separates into a cylinder of A, wrapped in a cylinder of B, that are in the bulk C. As concentration increases further ($0.3 \lesssim c_A \lesssim 0.4$), the system separates into several layers, where layer B is always between A and C. With further decrease in concentration ($0.4 \lesssim c_A \lesssim 0.6$) the topology of the system is exactly reversed to that of $0.2 \lesssim c_A \lesssim 0.3$, with a cylinder of C in the middle. Finally, for large concentrations ($c_A \gtrsim 0.8$) the system separates into a C sphere, which is wrapped in B sphere, that are in the bulk A.

Using the same method as in Chapter 5 (pages 68, 92), we have constructed a 2D phase diagram for the ternary system considered from the energy, order parameter and distribution function data presented in this section. This phase diagram is a part of the complete 3D phase diagram, which will be presented in the next section and represents a ‘slice’ cut out by the plane A. The position of the plane A was described in the beginning of the present section and in Section 7.1. The 2D phase diagram is presented in Figure 7.8.

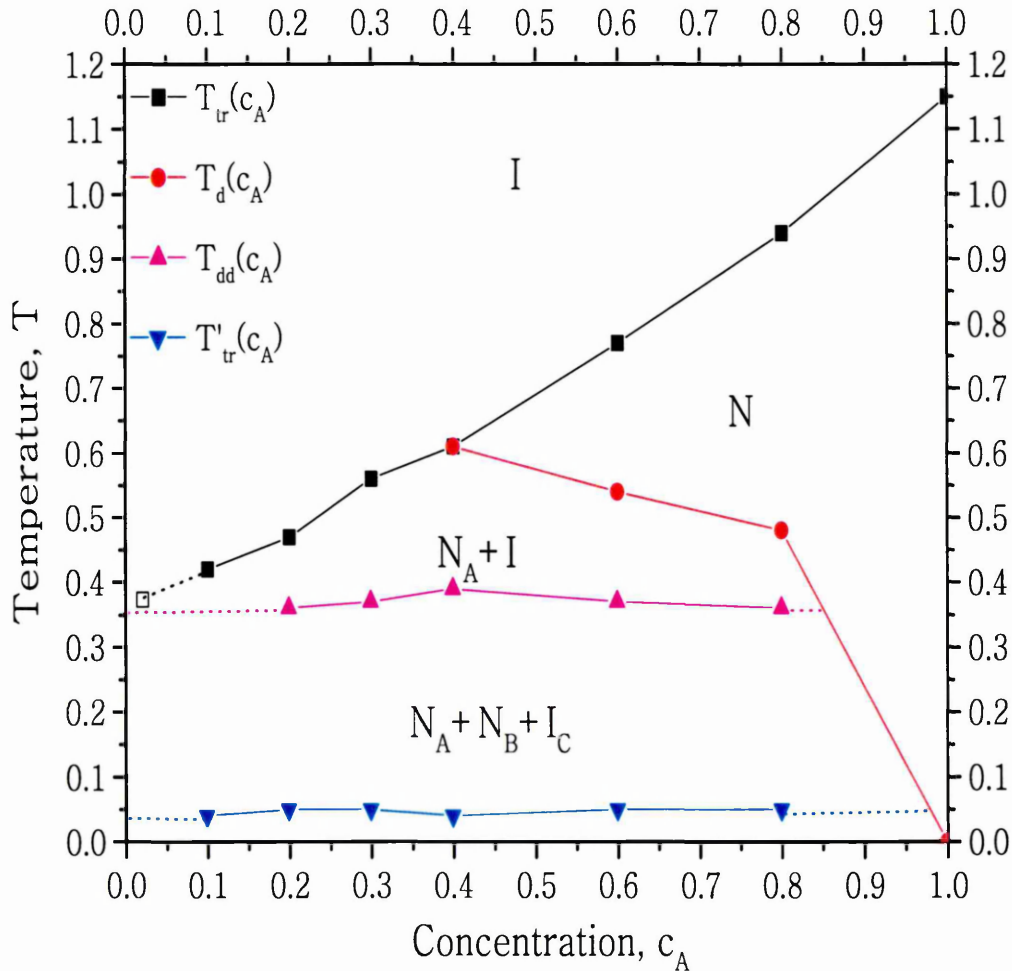


Figure 7.8: 2D phase diagram of the A-plane.

We describe all the regions on the phase diagram first and then comment on the boundaries between them. The diagram comprises five areas. The area on the top of the diagram, represents the isotropic phase. Below this region there are two regions, the coexistence of the isotropic phase and particle-A-rich nematic phase on the left hand side of the diagram, and the homogeneous nematic phase on the right hand side of the diagram. At lower temperatures is a region of of three phase coexistence. These phases are A-rich nematic, B rich nematic and C-rich isotropic. Finally, at the bottom of the diagram there is a region, where three nematic phases coexist.

The isotropic region extends to low temperatures for small values of c_A . The boundary between the isotropic phase and the rest of the phase diagram (henceforth $T_{tr}(c_A)$)

curve) is believed to be at $T = T_{tr}^{BC}(c = 0.5)$ (Figure 7.3) for $c_A = 0.0$ and at $T = T_{tr}(\varepsilon = 1.0) \approx 1.15$ (Table 5.1, page 59) for $c_A = 1.0$. Here, $T_{tr}^{BC}(c = 0.5)$ is the temperature of the isotropic nematic transition of the binary system of particles B and C with equal composition. For intermediate values of c_A , with c_A the $T_{tr}(c_A)$ curve varies approximately linearly.

The next curve is the boundary between $I + N_A$ coexistence region and the regions above it (henceforth $T_d(c_A)$ curve). This curve couples with the $T_{tr}(c_A)$ curve for $c_A \lesssim 0.4$.

Below this there is a boundary between the $I + N_A$ and $N_A + N_B + I_C$ coexistence regions (henceforth $T_{dd}(c_A)$ curve). The $T_{dd}(c_A)$ curve effectively represents the temperature of demixing of the remaining particles B and C. As it happens, the particles B also undergo their isotropic-nematic transition at this temperature. On the phase diagram in Figure 7.8 $c_B = c_C$ always, owing to the position of plane A on the 3D phase diagram (Section 7.1). Thus, the $T_{dd}(c_A)$ curve is a projection of the demixing curve of the binary mixture and, hence, the $T_{dd}(c_A)$ curve is effectively a horizontal line. Further discussion of this will follow in Section 7.4.

The last boundary on the phase diagram is the $T'_{tr}(c_A)$ curve, which indicates the isotropic-nematic transition of particles C - this too is a horizontal line. It is analogous to that seen in the binary system and its temperature is equal to that of $T'_{tr}(c)$ of the binary system of particles B and C.

All the phase regions found in Figure 7.8 are consistent with the phase diagrams defined with the appropriate binary systems. Further discussion of these results will follow in Section 7.4.

7.3.2 Phase Behaviour in B-bisector Plane.

The next plane considered has the bisector of plane AC as a base and goes to point B of the concentration triangle. The behaviour of this set of concentrations (which are constrained by $c_B + 2c_C = 1.0$, where $c = c_A = c_C$) exhibits some features not seen in the previous section. Plane B is one of most interesting considered in this thesis, primarily because the degree of anisotropy of particle B is intermediate between those of the other sites present. This means that as c_B decreases, the particles with

higher and lower values of coupling constant compete to have influence on particles B. This means that both enhancement and reduction of the ordering and structure of the system are achieved for some concentrations.

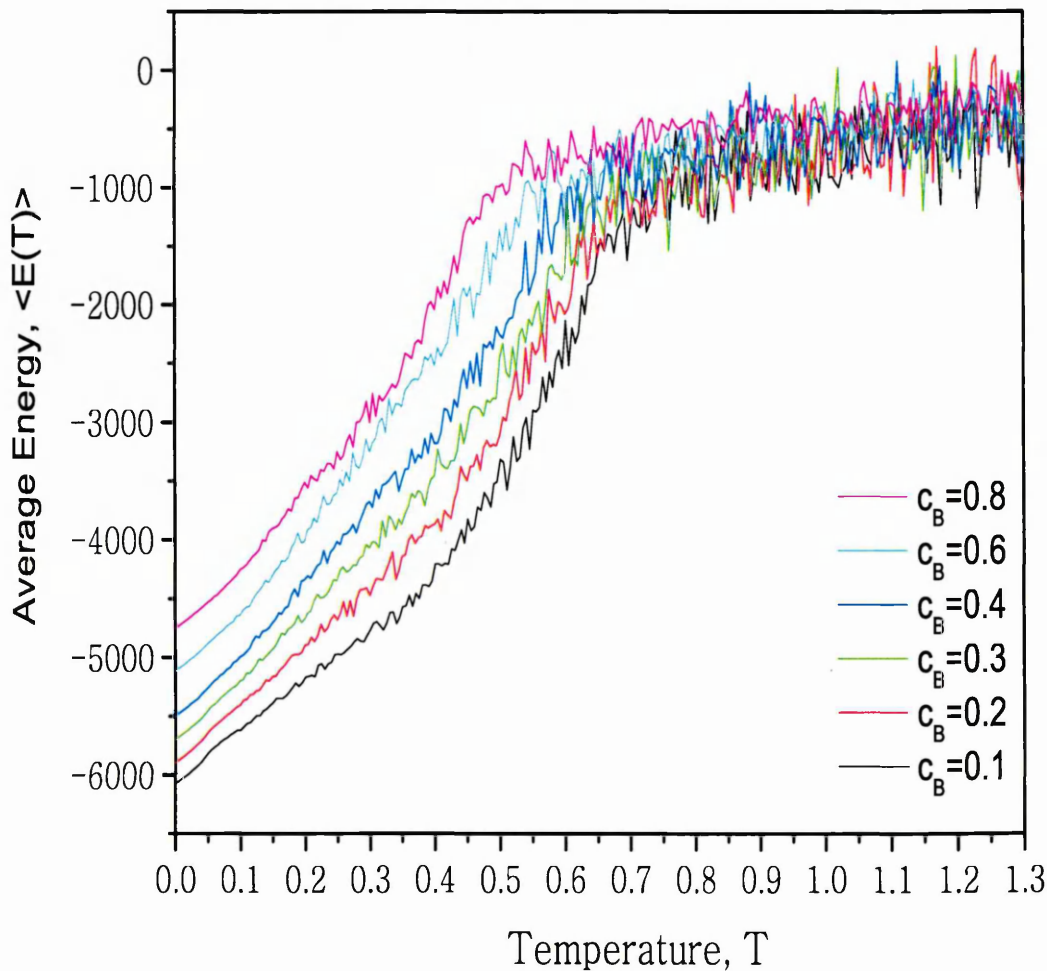


Figure 7.9: The thermal dependence of the energy for the set of concentrations c_B .

Let us consider first the average internal energy of the system $\langle E \rangle$. Figure 7.9 shows the dependencies of the energy $\langle E(T) \rangle$ on temperature for various concentrations c_B . For all concentrations, the energy decreases with a decrease in temperature. In addition, there is a gradient discontinuity at temperatures $T_{tr}(c_B)$ on the $\langle E(T) \rangle$ curves throughout the entire concentration range. The heat capacity data reveal a peak at $T_{tr}(c_B)$, which is accepted as a point of transition of the system.

c_A	$T_{tr}(c_B)$	$T'_{tr}(c_B)$
0.1	0.59 ± 0.01	0.04 ± 0.01
0.2	0.57 ± 0.01	0.05 ± 0.01
0.3	0.55 ± 0.01	0.05 ± 0.01
0.4	0.51 ± 0.01	0.04 ± 0.01
0.6	0.46 ± 0.01	0.05 ± 0.01
0.8	0.41 ± 0.01	0.05 ± 0.01

Table 7.3: Table of temperatures obtained from $\langle E(T) \rangle$ data. These were derived as a point where the tangent of $\langle E(T) \rangle$ is the steepest.

The behaviour of all $\langle E(T) \rangle$ curves for concentrations c_B is similar to that for concentrations c_A , presented earlier. Each curve experiences a number of discontinuities at two or more of the temperatures $T_{tr}(c_B)$, $T_d(c_B)$, $T_{dd}(c_B)$ and $T'_{tr}(c_B)$. As c_B decreases, the entire $\langle E(T) \rangle$ curve moves to lower values, unlike the behaviour observed in the case of plane A. In Table 7.3 we present the values of all temperatures, $T_{tr}(c_B)$ and $T'_{tr}(c_B)$ for the set of concentrations.

The dependence of the order parameter on temperature ($\langle P_2(T) \rangle$) for the same concentrations c_B is shown in Figure 7.10. The $\langle P_2(T) \rangle$ curves for different values of c_B retain their generic behaviour, that is the order parameter increases with a decrease in temperature, starting from $T_{tr}(c_B)$, and experiences a number of changes in gradient as it approaches its maximum value at $T \rightarrow 0.0$; however, with a change in concentration, its variations in value are not, as was the case with the $\langle P_2(T) \rangle$ curves shown in Figure 7.5, all in the same direction throughout the entire temperature range. Rather, as c_B decreases, the order parameter decreases at lower temperatures ($0.0 < T \lesssim 0.4$) but increases at higher temperatures ($0.4 \lesssim T \leq T_{tr}(c_B)$). For temperatures around 0.4 the value of the order parameter depends very little on concentration c_B . There are two significant changes in the gradient of the $\langle P_2(T) \rangle$ curves. The first occurs when the system undergoes the isotropic-nematic transition at temperature $T_{tr}(c_B)$; the second, at lower temperatures, occurs when other, as yet unknown processes drive the order parameter up. This happens at $T_{dd}(c_B) \approx 0.40$ and does not seem to depend significantly on concentration c_B (Table 7.4). Throughout the entire concentration range considered, $T_{tr}(c_B)$ decreases with increase in c_B , whereas the gradients of the order parameter curves become steeper. For all con-

centrations the order parameter approaches its maximum value when the gradient changes at $T_{dd}(c_B)$.

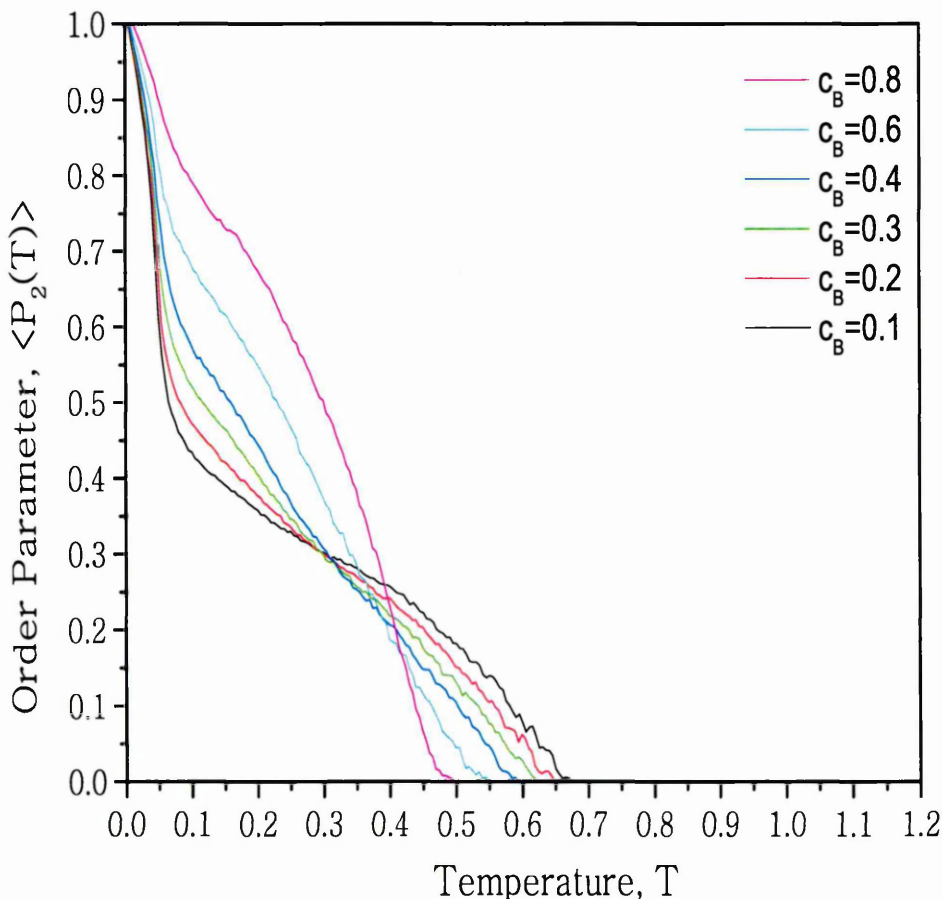


Figure 7.10: The second-rank orientational order parameter, $\langle P_2(T) \rangle$. Different curves represent different concentrations c_B .

Let us now examine individually the order parameters of components A ($\langle P_2 \rangle^A$), B ($\langle P_2 \rangle^B$) and C ($\langle P_2 \rangle^C$) (Figure 7.11). As was the case with variations in c_A (Figure 7.6), the initial increase in orientational order occurs at the same temperature ($T_{tr}(c_B)$) for particles A and B, but the shapes of the $\langle P_2(T) \rangle$ curves for each type of particle differ. In addition, as happened with variation in c_A , a significant increase in the value of $\langle P_2(T) \rangle$ for particles C occurs only at very low temperatures ($T_{dd}(c_B)$). However, the bulge of increased order parameter for high values of c_B ($c_B = 0.8$), which occurs at temperatures $T_d(c_B)$, is now more pronounced, as compared to the previous case ($c_A = 0.8$).

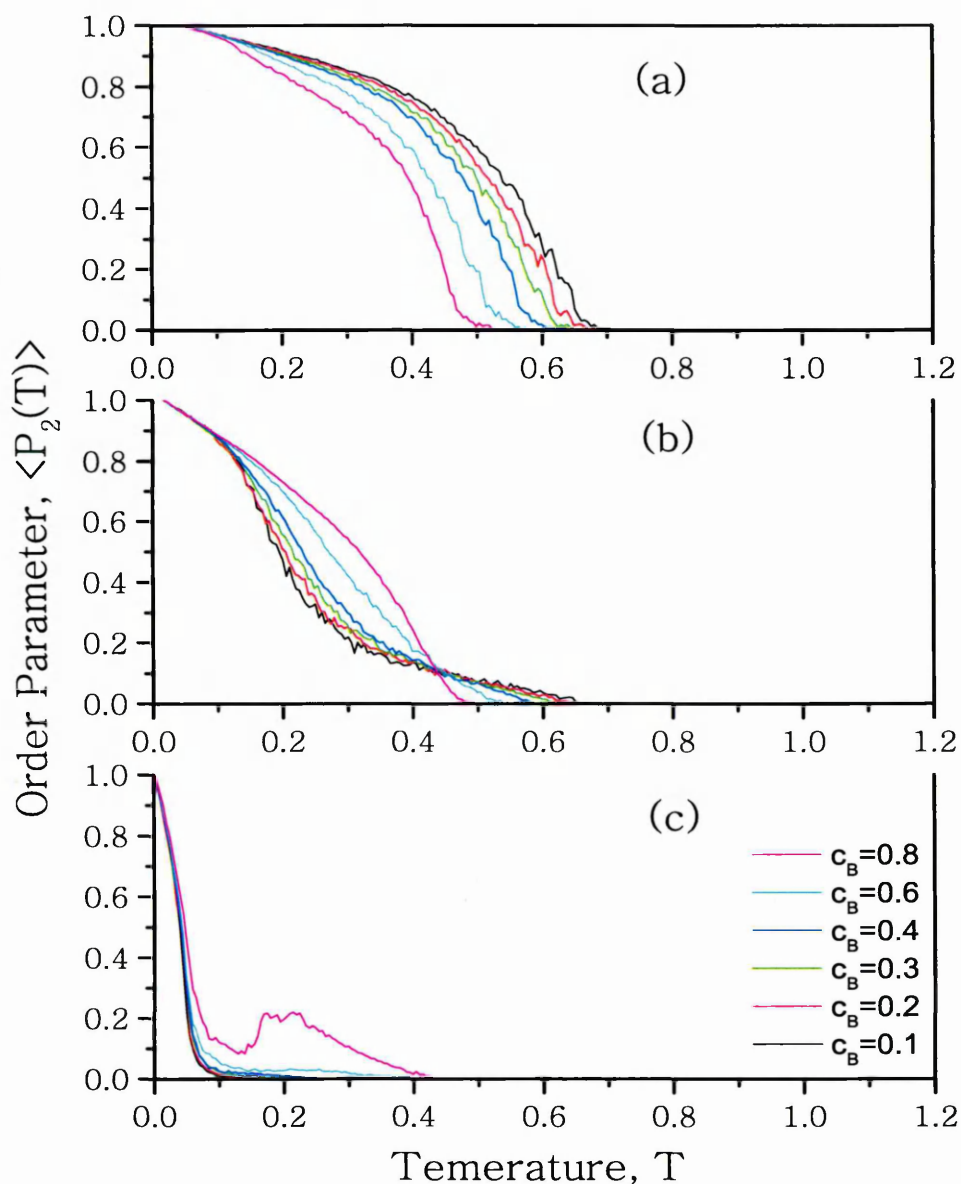


Figure 7.11: The thermal dependence of the second-rank orientational order parameter, shown individually for components A, B and C. Different curves represent different concentrations c_B . (a) $\langle P_2(T)^A \rangle$ for particles A. (b) $\langle P_2(T)^B \rangle$ for particles B. (c) $\langle P_2(T)^C \rangle$ for particles C.

Thus we comment first on individual order parameters for $c_B = 0.8$. The $\langle P_2(T)^A \rangle$ and $\langle P_2(T)^B \rangle$ curves for this concentration are relatively close to each other, increasing with similar gradients as the temperature falls, starting from $T_{tr}(c_B = 0.8)$. However, at $T_d(c_B = 0.8)$ there is a slight change in gradient on the $\langle P_2(T)^A \rangle$ curve, which correlates with the minimum in the order parameter of particles C, formed by the bulge.

c_B	$T_{tr}(c_B)$	$T_d(c_B)$	$T_{dd}(c_B)$	$T'_{tr}(c_B)$
0.1	0.66 ± 0.05	0.66 ± 0.05	0.39 ± 0.05	0.06 ± 0.05
0.2	0.64 ± 0.05	0.64 ± 0.05	0.40 ± 0.05	0.06 ± 0.05
0.3	0.61 ± 0.05	0.61 ± 0.05	0.42 ± 0.05	0.06 ± 0.05
0.4	0.58 ± 0.05	0.58 ± 0.05	0.45 ± 0.05	0.06 ± 0.05
0.6	0.53 ± 0.05	0.38 ± 0.05	N/A	0.07 ± 0.05
0.8	0.48 ± 0.05	0.17 ± 0.05	N/A	0.08 ± 0.05

Table 7.4: Table of temperatures $T_{tr}(c_B)$, $T_d(c_B)$, obtained from $\langle P_2(T) \rangle$ data. These were derived as a point where the tangent of $\langle E(T) \rangle$ is the steepest. Constraint B .

As c_B decreases, the $\langle P_2(T)^A \rangle$ and $\langle P_2(T)^B \rangle$ curves appear further apart, and the bulge of increased order parameter on the $\langle P_2(T)^C \rangle$ curve diminishes. We also note that the appearance of the $\langle P_2(T)^A \rangle$ and $\langle P_2(T)^C \rangle$ curves becomes similar to that observed in single component systems with coupling constants $\varepsilon = 1.0$ and $\varepsilon = 0.2$ respectively; while the gradient of the $\langle P_2(T)^B \rangle$ curve approaches that of the $\langle P_2(T)^A \rangle$ curve in the region of lower temperatures ($0.0 < T \lesssim 0.3$), and that of the $\langle P_2(T)^C \rangle$ curve in the region of higher temperatures ($0.3 \lesssim T \leq T_{tr}(c_B)$).

The value of the order parameter for all components reaches 1 as the temperature approaches zero. The ordering behaviour of the three components (Figure 7.11) suggests that the changing gradient of $\langle P_2(T) \rangle$ in Figure 7.10 reflects the behaviour of the order parameter for particles B. We will discuss this further in Section 7.4. Table 7.4 shows the values of $T_{tr}(c_B)$ for the full set of concentrations. These values are in good agreement with the values of $T_{tr}(c_B)$ obtained from the energy measurements.

The next observable we present is the radial distribution functions of the unlike particles $g^{AB}(r = 1, T)$, $g^{CA}(r = 1, T)$ and $g^{CB}(r = 1, T)$, the physical nature of which was dealt with briefly in the previous section. In Figures 7.12(a-e) we present the functions for the set of concentrations c_B . As in the previous case, the dashed lines represent boundaries between different phase regions.

Following the procedure adopted in the previous section, we examine all three curves simultaneously as the temperature decreases, except that this time we consider all concentrations at once. As with the distribution functions in the previous case, the

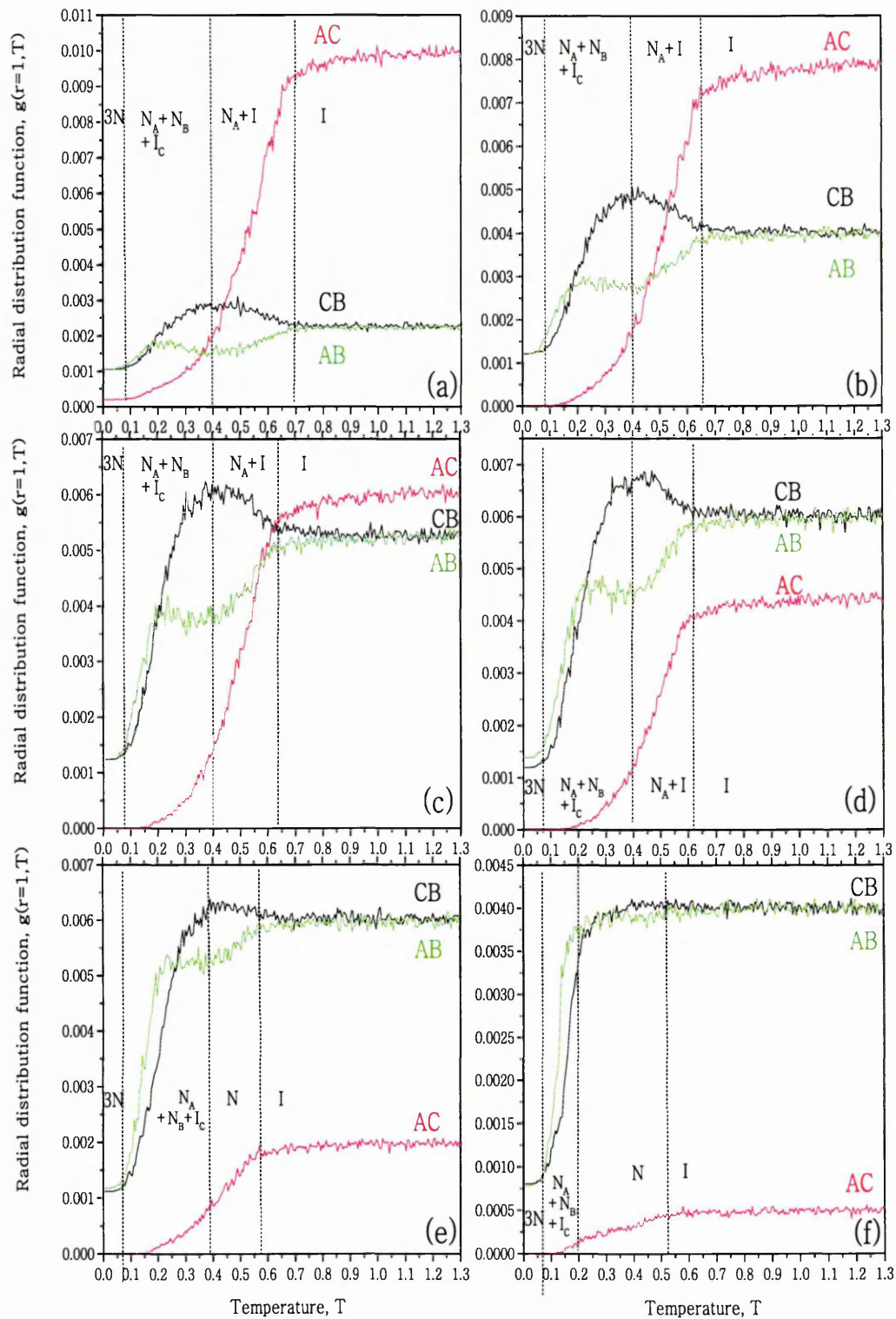


Figure 7.12: Dependencies of the three $g(r = 1)$ functions for the set of concentrations c_B . (a) $c_B = 0.1$, (b) $c_B = 0.2$, (c) $c_B = 0.3$, (d) $c_B = 0.4$, (e) $c_B = 0.6$, (f) $c_B = 0.8$.

gradient of $g^{AB}(r = 1, T)$ changes its sign three times, while that of $g^{CB}(r = 1, T)$ changes its sign once and the sign in the gradient of $g^{CA}(r = 1, T)$ remains unchanged, as temperature decreases. However, now this is true for all concentrations c_B . With an increase in concentration of particles B, the following changes in the three functions occur. The first relates to the isotropic phase, where the values of $g^{AB}(r = 1, T)$ and $g^{CB}(r = 1, T)$ increase and the value of $g^{AC}(r = 1, T)$ decreases, which reflects the proportion of the three components in the system. The temperature at which all three functions change ($T_{tr}(c_B)$) decreases with an increase in c_B . Throughout the whole concentration range considered, functions $g^{AB}(r = 1, T)$ and $g^{CB}(r = 1, T)$ have approximately equal values for both isotropic temperatures and as $T \rightarrow 0.0$. The equality of these two functions at high temperatures indicates the equal proportions of particles A and C in the system. At low temperatures their values are fairly close, indicating that the interface between particles A and B, and interface between particles C and B are of similar area size throughout the entire concentration range; this further suggests that the ways in which particles A and C demix from particles B are similar. A zero value of $g^{AC}(r = 1, T)$ at $T \rightarrow 0.0$ indicates no contact between particles A and C, as was found in the previous section. Depending on concentration, the topology of the demixed system changes from having two drops, one of particles A and the other of C, in a bulk of particles B (for high values of c_B), to having a bulk of particles A which is separated from a bulk of particles C by thin films of particles B. Snapshots for these concentrations at low temperature (not shown) support this characterisation.

However, between this topology and the homogeneous structure, there are a number of intermediate stages. For low values of c_B , the values of all functions exhibit gradient discontinuities at $T_{tr}(c_B)$. The $g^{AB}(r = 1, T)$ and $g^{AC}(r = 1, T)$ functions decrease (immediately below $T_{tr}(c_B)$), whereas the $g^{CB}(r = 1, T)$ function increases. The decrease in the first two indicates segregation of particles A, resulting in increased contact between particles C and B i.e. an increase of $g^{CB}(r = 1, T)$. Snapshots show that for $T < T_{tr}(c_B)$, particles A did indeed form a single domain while the $\langle P_2(T) \rangle$ data indicate nematic order for particles A. Meanwhile, the rest of the bulk (particles C and B) remained mixed and exhibited no (particles C) or little (particles B) ordering. This behaviour continues until $T_d(c_B)$, when the gradient of $g^{CB}(r = 1, T)$ changes its sign and the decrease in $g^{AB}(r = 1, T)$ is halted and even reversed to a small degree as the temperature continues to fall below $T_d(c_B)$.

At the same time, the $g^{AC}(r = 1, T)$ function continues to decrease. The $\langle P_2(T) \rangle$ data, along with snapshot views, indicate demixing of the remaining bulk (particles B and C) at this point, which is supported by the decrease in $g^{CB}(r = 1, T)$ and by the coincident isotropic-nematic transition of particles B. As they separate from particles B, particles C also push the former closer to particles A (as is reflected by the slight increase in $g^{AB}(r = 1, T)$), creating a film of particles B between the As and Cs. With further decrease of the temperature, the three phases continue to minimize their areas of interface as is clear from the decrease in all three distribution functions. While well demixed (at $T < T_d(c_B)$), the domain of particles C undergoes an isotropic-nematic transition at $T_{dd}(c_B)$ (which is evident from an increase in $\langle P_2^C(T) \rangle$ in Figure 7.11).

For high values of c_B , the values of all the functions remain unchanged as the temperature passes below $T_{tr}(c_B)$. The position of $T_{tr}(c_B)$ is clear, however, from the $\langle P_2(T) \rangle$ data (Figure 7.11). Although this shows a nematic order for all three types of particle, the distribution function exhibits no noticeable changes. This indicates a homogeneous nematic phase, resembles the behaviour of the distribution functions of unlike particles in binary mixtures with high values of c (Chapter 5). Subsequently, the $g^{AC}(r = 1, T)$ function decreases continuously, while $g^{AB}(r = 1, T)$ and $g^{CB}(r = 1, T)$ deviate slightly, down and up respectively, from the flat behaviour at around $T_d(c_B)$. Snapshots reveal that this relates to formation of small domains of particles A and C for temperatures slightly below $T_d(c_B)$ and the $\langle P_2(T) \rangle$ data indicate the nematic order of such domains. Then, as the temperature passes $T_{dd}(c_B)$, the domains grow quickly (within $\Delta T \approx 0.1$) and form two drops, one of particles A and one of particles C, which maintain their distance from each other. As these two domains grow, one (particles A) remains in the nematic phase but the other (particles C) returns to the isotropic phase until at $T'_{tr}(c_B)$ a sharp increase in $\langle P_2^C(T) \rangle$ points to the isotropic-nematic transition of particles C.

From the data presented in this section, we have constructed a 2D phase diagram for the ternary system 'sliced' by the plane B. The position of the plane B was described in the beginning of the present section and in Section 7.1. The 2D phase diagram is presented in Figure 7.13.

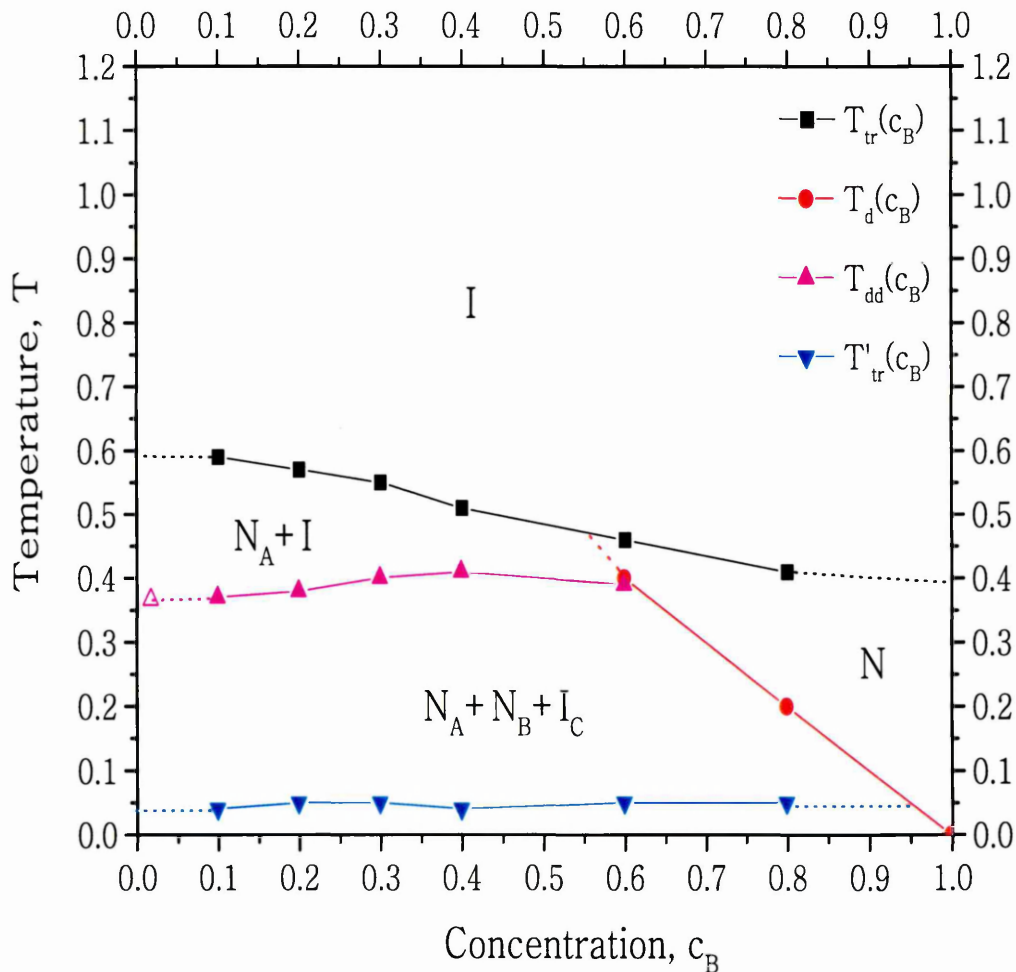


Figure 7.13: 2D phase diagram of the B-plane.

We use the order to describe the phase diagram adopted in the previous Section. The diagram comprises five regions. The area on the top of the diagram, represents the isotropic phase. Below this, there are two regions, the coexistence of the isotropic phase and particle-A-rich nematic phase on the left hand side of the diagram, and the homogeneous nematic phase on the right hand side of the diagram. Further below this is the first region of three phase coexistence. This comprises an A-rich nematic phase, a B rich nematic phase and a C-rich isotropic phase. Finally, at the bottom of the diagram there is a region, where the three nematic phases coexist. The difference between this phase diagram and that for plane A (Figure 7.8) lies in the values of the slopes. In Figure 7.13 the $T_{tr}(c_B)$ curve decreases with increase of c_B , unlike

the $T_{tr}(c_A)$ curve in Figure 7.8. The $T_d(c_A)$ curve that separates the homogeneous nematic from the coexistence region, is very steep, while $T_{dd}(c_B)$ and $T'_{tr}(c_B)$ remain unchanged. As the value of c_B increases $T_{tr}(c_B)$ curve changes continuously from $T_{tr}(c_B = 0.0) \approx 0.6$ to the value of the transition temperature for pure particles B ($T_{tr}(c_B = 1.0) \approx 0.41$).

The next curve is the boundary between $I + N_A$ coexistence region and the regions above it ($T_d(c_B)$ curve). This curve couples with the $T_{tr}(c_B)$ curve for $0.4 \lesssim c_B \lesssim 0.6$, which declines a little with increase of c_B . For the the concentrations $c_B > 0.6$ $T_d(c_B)$ declines quite steeply, approaching $T = 0.0$ as $c_B \rightarrow 1.0$.

Below this there is a boundary between the $I + N_A$ and $N_A + N_B + I_C$ coexistence regions ($T_{dd}(c_B)$ curve). As in the previous case (Figure 7.8), for temperatures $T < T_{dd}(c_B)$ the remaining particles B and C demix while the particles B also undergo the isotropic-nematic transition. On the phase diagram in Figure 7.13 $c_A = c_C$ always, owing to the position of plane B on the 3D phase diagram (Section 7.1). Thus, the difference between the $I + N_A$ and $N_A + N_B + I_C$ regions (and therefore the $T_{dd}(c_A)$ curve) becomes weaker as $c_B \rightarrow 0.0$.

The last boundary on the phase diagram is the $T'_{tr}(c_B)$ curve, which indicates the isotropic-nematic transition of particles C - again, this is a horizontal line. It is analogous to the horizontal line found in binary system and its temperature is equal to that of $T'_{tr}(c)$ of the binary systems with $\varepsilon = 0.2$. As in the previous case, $T'_{tr}(c_B) \approx T_{tr}(\varepsilon = 0.2)$, which is isotropic-nematic transition of single component system of particles C.

All of the values in Figure 7.13 are found to be in agreement with the data obtained from the earlier investigations of binary systems and the phase diagram in Figure 7.13 seems to concatenate well with that in Figure 7.8. Further discussion of these results will follow in Section 7.4.

7.3.3 Phase Behaviour in C-bisector Plane.

The next plane considered has the bisector of AB as a base, and starts from point C of the concentration triangle ($c_C + 2c = 1.0$, where $c = c_A = c_B$, Eq. 7.9). In this ternary system, the concentration of particles with the lowest anisotropy (particles

C) is subject to variation, while the concentrations of the other two components, both of which are more anisotropic, occupy equal portions of the rest of the volume available on the lattice. Owing to the concentration constraint imposed for plane C, this system might be expected to exhibit behaviour similar to that of binary systems with low values of ε .

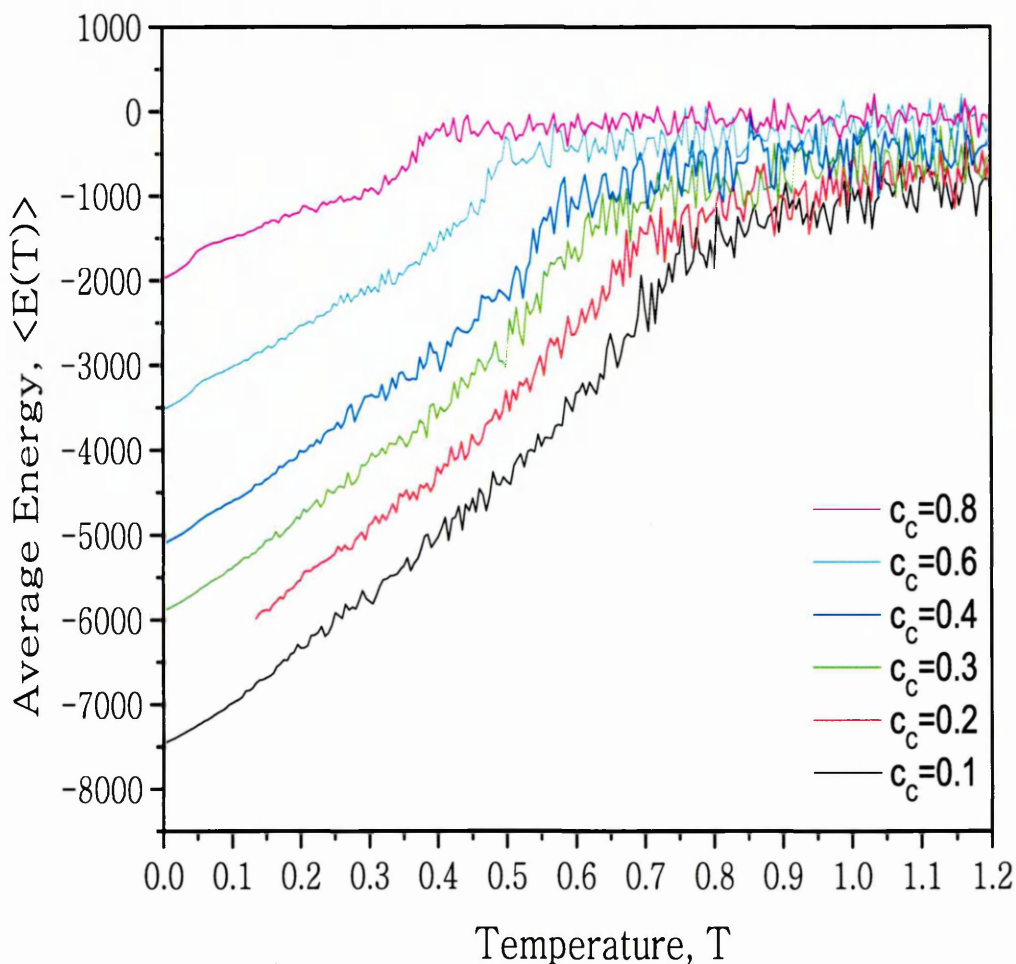


Figure 7.14: The energy dependence on temperature for the set of concentrations c_C .

Let us look at the average internal energy of the system $\langle E(T) \rangle$ (Figure 7.14). The Figure shows the dependencies of the energy $\langle E(T) \rangle$ on temperature for various concentrations c_C . The dependence of $\langle E(T) \rangle$ on temperature and concentration recalls the behaviour of the binary system with $\varepsilon = 0.10$ (for $c_C = (1 - c)$, where c is the

c_C	$T_{tr}(c_C)$	$T'_{tr}(c_C)$
0.1	0.66 ± 0.01	N/A
0.2	0.61 ± 0.01	N/A
0.3	0.55 ± 0.01	0.06 ± 0.01
0.4	0.50 ± 0.01	0.06 ± 0.01
0.6	0.43 ± 0.01	0.05 ± 0.01
0.8	0.35 ± 0.01	0.05 ± 0.01

Table 7.5: Table of temperatures, obtained from $\langle E(T) \rangle$ data. These were derived as a point where the tangent of $\langle E(T) \rangle$ is the steepest.

concentration of the binary system in Figure 5.33, page 104). For all concentrations considered, the energy decreases with decrease in temperature. As c_C decreases, the entire $\langle E(T) \rangle$ curve moves to lower values, behaviour similar to that of the binary system with $\varepsilon = 0.10$. The energy values of the system below the temperature of discontinuity $T_{tr}(c_C)$ change more rapidly with c_C than do those above, and the discontinuity becomes steeper as $c_C \rightarrow 1.0$. Again, this behaviour is similar to that of the binary system with $\varepsilon = 0.10$. The gradient discontinuities of $\langle E(T) \rangle$ in the region of temperatures $T < T_{tr}(c_C)$ indicate the occurrence of other processes below the isotropic-nematic transition temperature. In Table 7.1 we present the values of temperatures, $T_{tr}(c_C)$ and $T'_{tr}(c_C)$ for the set of concentrations.

The dependence of the order parameter on temperature ($\langle P_2(T) \rangle$) for the given concentrations c_C is shown in Figure 7.15. As is the case for the $\langle E(T) \rangle$ curves, the overall behaviour of the $\langle P_2(T) \rangle$ curve is similar to that of the binary system with $\varepsilon = 0.10$ (compare Figure 7.15 with Figure 5.35 on page 106). From Figure 7.15 we see that the system undergoes the isotropic-nematic transition at temperature $T_{tr}(c_C)$ for all concentration values. For $c_C = 0.6$, for example, the order parameter sharply increases at $T_{tr}(c_C = 0.6) \approx 0.48$, but approaches a low value (around 0.15) as the temperature falls. Then at $T_{dd}(c_C = 0.6) \approx 0.44$ the order parameter increases sharply, approaching its maximum value. On the other hand, for $c_C = 0.1$, the order parameter increases virtually linearly with decrease in temperature, starting from $T_{tr}(c_C = 0.1) \approx 0.76$. For all the intermediate concentration values, the behaviour of $\langle P_2(T) \rangle$ gradually changes from that which occurs for $c_C = 0.8$ to that which is seen for $c_C = 0.1$; there is, however, a weak discontinuity at $T_d(c_C)$.

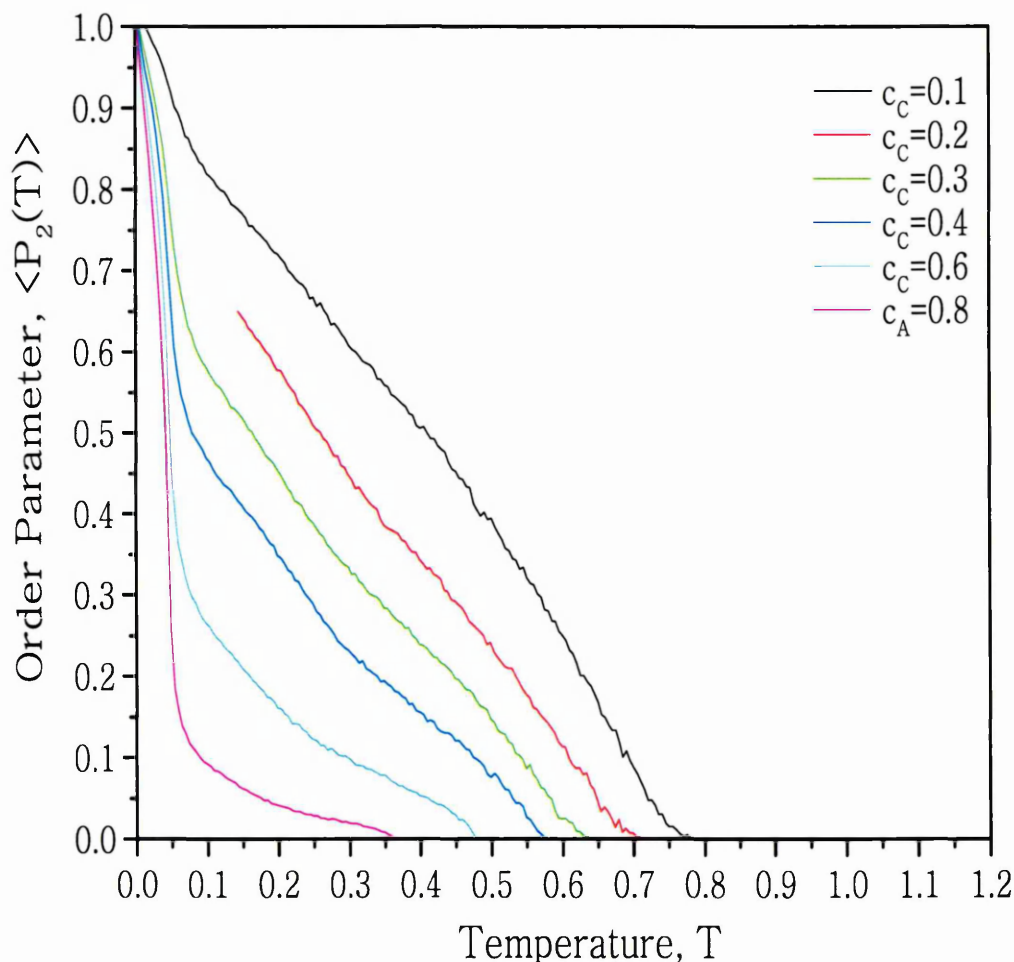


Figure 7.15: The second-rank orientational order parameter, $\langle P_2(T) \rangle$. Different curves represent different concentrations c_C .

Let us now examine individually the order parameters of components A ($\langle P_2 \rangle^A$), B ($\langle P_2 \rangle^B$) and C ($\langle P_2 \rangle^C$) (Figure 7.16). As with the previous two cases (Sections 7.3.1, 7.3.2), the increase in the orientational order occurs at the same temperature ($T_{tr}(c_C)$) for particles A and B. However, the shape of the $\langle P_2(T) \rangle$ curves for particles A resembles that of the characteristic curve, while the shape of the $\langle P_2(T) \rangle$ curves for particles B deviates from it. A significant increase in $\langle P_2(T) \rangle$ for particles C does not occur except at very low temperatures (≈ 0.1). There is also a shallow and virtually linear increase, which starts which $T_{tr}(c_C)$. For low values of c_C , however, this shallow linear increase develops into a small bulge (Figure 7.16); apart from this, the $\langle P_2(T) \rangle$ curves for particles C are similar in shape to those of the binary system (5.36, page 107). The gradient of the $\langle P_2(T) \rangle$ curves for particles B can

be divided in two sections. In the first, the low temperature section ($T \lesssim T_d(c_C)$), the gradient approaches that of component A. In the second, the high temperature section ($T_d(c_C) \lesssim T \lesssim T_{tr}(c_C)$), the gradient approaches that of component C.

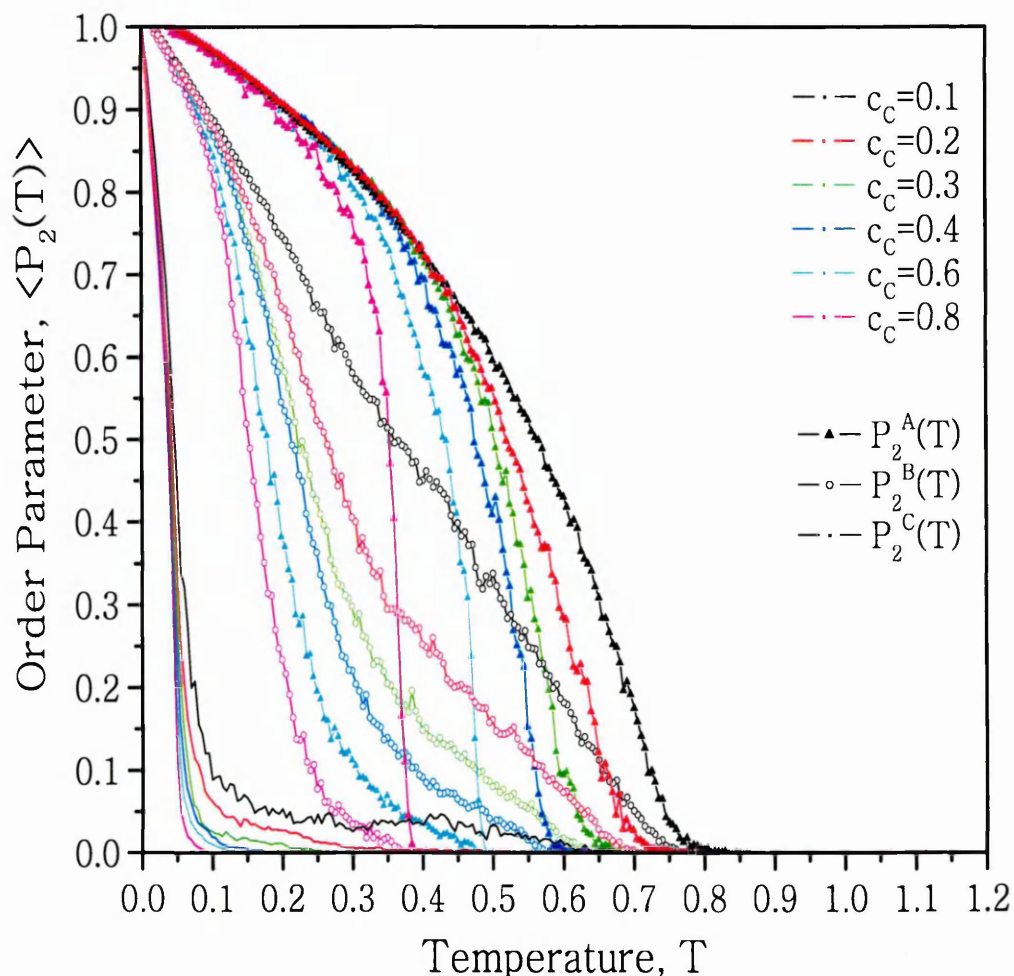


Figure 7.16: The second-rank orientational order parameter shown individually for components A and B. Dependence on the temperature. Different curves represent different concentrations c_C .

The order parameter of all components reaches 1 as the temperature approaches zero. We will discuss this further in Section 7.4. Table 7.6 shows the value of $T_{tr}(c_C)$ determined from the $\langle P_2(T) \rangle$ data for the full set of concentrations. These values are in reasonable agreement with the values of $T_{tr}(c_C)$ obtained from the energy measurements.

c_B	$T_{tr}(c_C)$	$T_d(c_C)$	$T_{dd}(c_C)$	$T'_{tr}(c_C)$
0.1	0.76 ± 0.05	0.30 ± 0.05	N/A	0.07 ± 0.05
0.2	0.70 ± 0.05	0.40 ± 0.05	0.40 ± 0.05	0.07 ± 0.05
0.3	0.64 ± 0.05	0.64 ± 0.05	0.41 ± 0.05	0.07 ± 0.05
0.4	0.57 ± 0.05	0.57 ± 0.05	0.42 ± 0.05	0.07 ± 0.05
0.6	0.48 ± 0.05	0.48 ± 0.05	0.44 ± 0.05	0.07 ± 0.05
0.8	0.37 ± 0.05	0.37 ± 0.05	N/A	0.07 ± 0.05

Table 7.6: Table of temperatures, obtained from $\langle P_2(T) \rangle$ data.

We move now to the next observable, the radial distribution functions of the unlike particles $g^{AB}(r = 1, T)$, $g^{CA}(r = 1, T)$ and $g^{CB}(r = 1, T)$ and their dependence on concentration c_C (Figures 7.17(a-e)).

As in the previous two cases, the dashed lines separate different phase regions determined from the $\langle P_2(T) \rangle$ and $\langle E(T) \rangle$ data. The behaviour of the distribution functions for concentrations c_C is in general similar to that seen in the previous two cases (Sections 7.3.1 and 7.3.2). The gradient of $g^{AB}(r = 1, T)$ changes its sign three times, while the gradient of $g^{CB}(r = 1, T)$ changes its sign only once and the sign in the gradient of $g^{CA}(r = 1, T)$ remains unchanged, as the temperature decreases. With an increase in concentration of particles C, the following changes in the three functions occur. The first relates to the isotropic phase ($T > T_{tr}(c_C)$), where the values of $g^{AC}(r = 1, T)$ and $g^{CB}(r = 1, T)$ increase and the value of $g^{AB}(r = 1, T)$ decreases, to reflect the proportions of three components in the system. For example, the equality of $g^{CB}(r = 1, T)$ and $g^{AB}(r = 1, T)$ throughout the entire range of c_C indicates the equal proportions of particles A and B in the system. While the gradient discontinuity in all three curves occurs at a single temperature $T_{tr}(c_C)$ for the end value of c_C , this temperature of discontinuity decreases with an increase in c_C .

Among the features that remain unchanged for all values of c_C considered are $g^{AC}(r = 1, T) \rightarrow 0.0$, for $T \rightarrow 0.0$; and $g^{AB}(r = 1, T) \approx g^{CB}(r = 1, T)$, for $T \rightarrow 0.0$ and $c_C \lesssim 0.4$. The close-to-zero value of $g^{AC}(r = 1, T)$ at low temperature indicates no contact between particles A and C. The similarity of $g^{AB}(r = 1, T)$ and $g^{CB}(r = 1, T)$ at low temperatures indicate that the areas of interface between the corresponding particles are similar. For example, the layer topology, where layers of particles A and C are separated by layers of particles B, would produce such values of $g^{AB}(r = 1, T)$, $g^{CB}(r = 1, T)$ and $g^{AC}(r = 1, T)$.

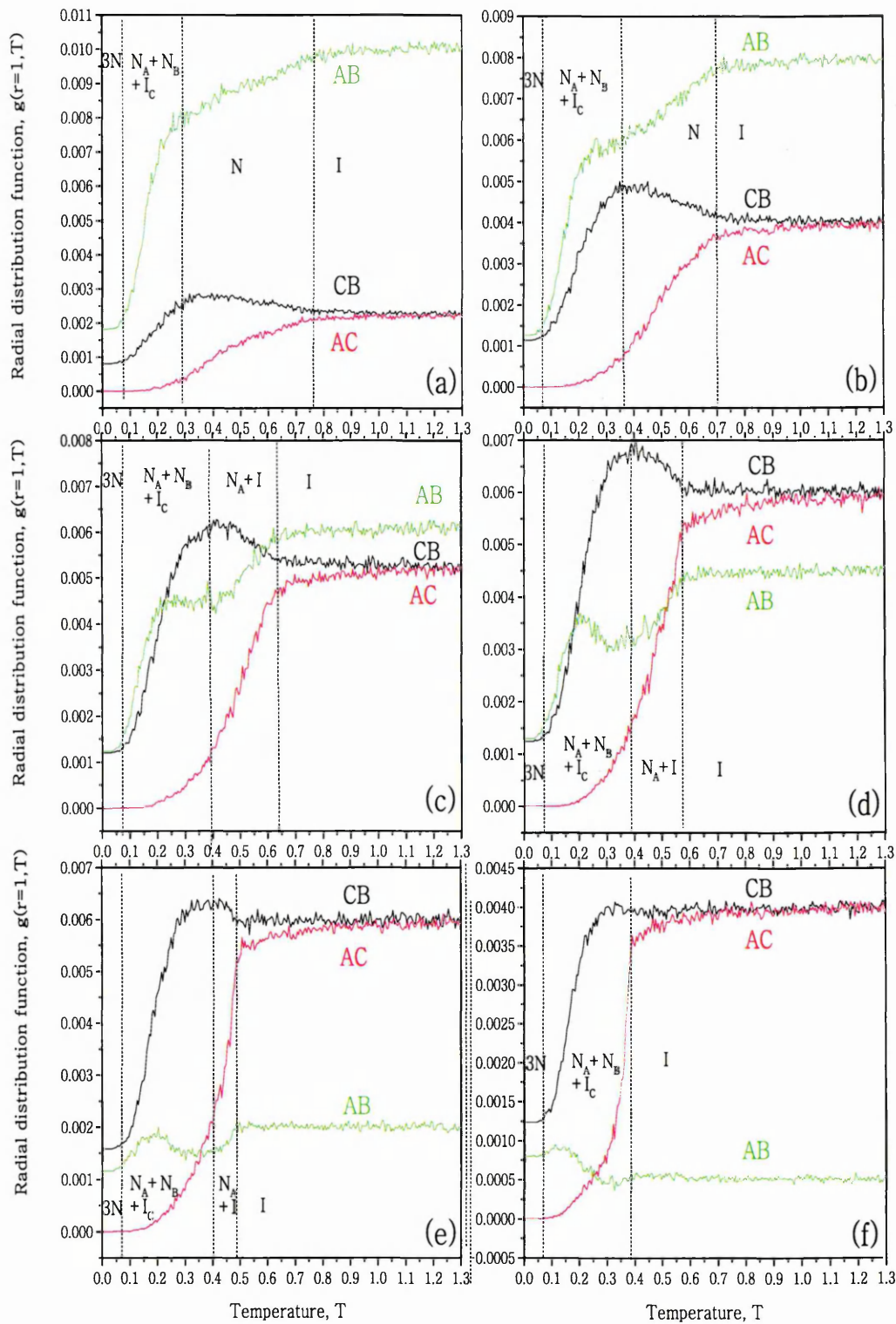


Figure 7.17: Dependencies of the three $g(r = 1)$ functions for the set of concentrations c_C . (a) $c_C = 0.1$, (b) $c_C = 0.2$, (c) $c_C = 0.3$, (d) $c_C = 0.4$, (e) $c_C = 0.6$, (f) $c_C = 0.8$.

Overall, according to snapshots of the system, the topology of the demixed system changes with c_C in exactly the same way as with c_A (see Section 7.3.1). This agrees with the results presented in Figure 7.17.

From the data presented in this section, we have constructed a 2D phase diagram for the ternary system ‘sliced’ in the plane C. The position of the plane C was described in the beginning of present section and in Section 7.1. The 2D phase diagram is presented in Figure 7.18.

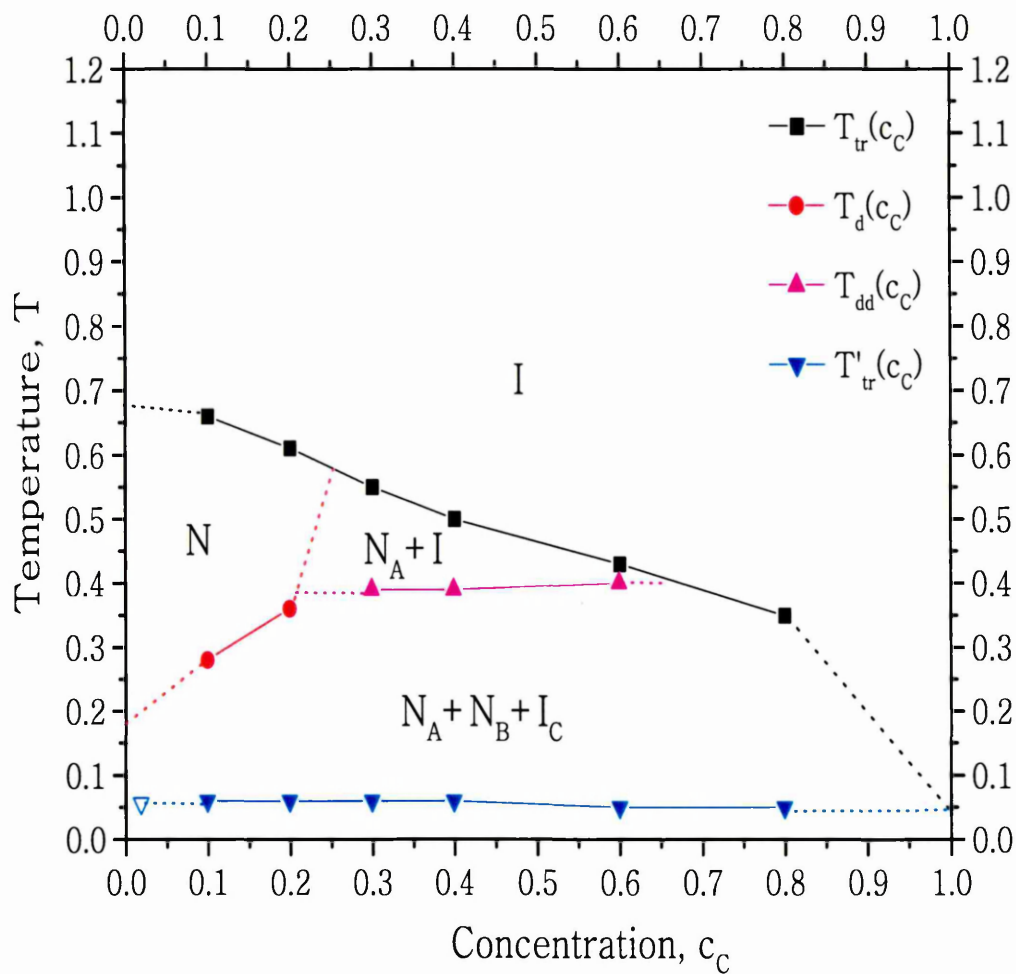


Figure 7.18: 2D phase diagram for C-plane.

The diagram comprises five regions, which are in the same order as those presented on previous phase diagrams. The area on the top of the diagram, represents the isotropic phase. Immediately below this there are three regions, the homogeneous

nematic phase on the left hand side of the diagram, the coexistence of the isotropic phase and particle-A-rich nematic phase in the middle of the diagram, and the coexistence of three phases ($N_A + N_B + I_C$) on the right hand side of the diagram. The latter also runs below the other two. Finally, at the bottom of the phase diagram there is a region, where three nematic phases coexist. The difference between three phase diagrams discussed, thus, lies in the slopes and locations of the phase boundaries and regions. Similar to the phase diagram presented in Figure 7.18, the $T_{tr}(c_B)$ curve decreases with increase of c_B , unlike the $T_{tr}(c_A)$ curve in Figure 7.8, where it increases with increase of c_A . The $T_{tr}(c_C)$ curve is believed to approach the transition temperature of the binary mixture $T = T_{tr}^{\varepsilon=0.6}(c = 0.5) \approx 0.76$ as $c_B \rightarrow 0.0$. On the other side of the diagram, at $c_C = 1.0$, the $T_{tr}(c_C)$ curve approaches $T = T_{tr}(\varepsilon = 0.2) \approx 0.05$. The nematic region on the phase diagram is located on the left hand side, unlike that in previous two diagrams. However, the boundaries $T_d(c_C)$ and $T'_{tr}(c_C)$ are consistent with those obtained for the other two diagrams.

All the values in Figure 7.18 are found to be in agreement with the data from investigation of binary systems and those discussed earlier in this Chapter. In the next section we discuss the results presented for the ternary mixture and will look at the phase behaviour as a whole, in form of 3D phase diagrams.

7.4 Discussion

In this Chapter only one ternary system was discussed, the coupling constants for each component being $\varepsilon_A = 1.0$, $\varepsilon_B = 0.6$ and $\varepsilon_C = 0.2$. The system's behaviour was considered in terms of changing two parameters, the temperature and the concentration ratio. Although the change in the temperature has direct implications to real systems, this is hardly the case for the concentration change, since applications of ternary mixtures with varied concentration ratio are rare. However, the changes along certain concentration planes, which can be represented by their respective 2D phase diagrams, relate to changes that are achievable in real systems. For example, planes A, B and C represent 50/50 binary mesogenic mixtures diluted by a mesogenic solvent. We intend to keep this section open and free from elaborate interpretation of the results. In the beginning of Section 7.3 we introduced discon-

tinuity temperatures. Now, after presenting phase diagrams we discuss the nature of these temperatures and the general phase behaviour of the system.

The first temperature, $T_{tr}(c)$ ($c = c(c_A, c_B, c_C)$), indicates the isotropic-nematic transition temperature of one or more components from the homogeneous isotropic phase. These temperatures form a $T_{tr}(c)$ curve on a 2D phase diagram (or the $T_{tr}(c)$ surface on the 3D phase diagram) which separates the homogeneous isotropic phase from the rest of the diagram. The value of $T_{tr}(c)$ increases as the ratio of more anisotropic particles increases (Figures 7.8 and 7.18). The slope of the $T_{tr}(c)$ curve on the phase diagram of B plane (Figure 7.13) is nearly horizontal and decreases as c_B increases. This is because, as c_B varies, pairs of particles B are interchanged with one more anisotropic and one less anisotropic particle, which keeps the overall value of $T_{tr}(c_B)$ only slightly dependent on c_B .

All the $T_{tr}(c)$ data are consistent with each other and with the results obtained for binary mixtures. The $T_{tr}(c)$ curves cross at $c_A = c_B = c_C = 0.33$ and correlate with their counterparts on the faces of the 3D prism.

The second temperature is $T_d(c)$. When this is seen, it separates a homogeneous nematic phase from the demixed regions below it; otherwise $T_d(c) = T_{tr}(c)$. For high and middle values of c_C the $T_d(c)$ curve indicates phase separation of the homogeneous phase into the isotropic-nematic coexistence region, where the segregated compound can be either in the isotropic phase (always particle C rich) or nematic phase (always particle A rich), depending on concentration. For low values of c_C , however the $T_d(c)$ curve is coupled with $T_{dd}(c)$ - the third discontinuity temperature, which signals a region on the phase diagram where all three compounds are well demixed into three domains, each rich in one of the types of particles. As was mentioned before, the $T_{dd}(c)$ data obtained for the A plane show that $T_{dd}(c)$ is virtually independent of c_A . This is explained by the fact that, throughout the entire concentration range, the ratio of particles B and C remains the same (50/50) while particles A are separated out both before and after the transition $T_{dd}(c)$. Thus, the phase separation process can be compared to that of the binary mixture of particles B and C. Indeed, the transition temperatures for this binary mixture correlate closely with those of the ternary mixture for concentrations c_A (Figure 7.8). As $c_A \rightarrow 0.0$ the $T_{tr}(c)$ curve of the ternary mixture vanishes, the difference between regions I and $N_A + I$ disappears and $T_{dd}(c)$ curve for ternary mixtures becomes equivalent

to $T_{tr}(c)$ for binary mixture BC. Uncertainty, however, arises regarding the $T_{dd}(c)$ surface for planes B and C. As the concentration ratio for these particles changes with change of c , the temperature at which particles B and C separate should vary. Nonetheless, the values for $T_{dd}(c)$ on these phase diagrams are approximately the same and correlate with $T_{dd}(c)$ data obtained for plane A. In addition, the value of $T_{dd}(c)$ coincides with the isotropic-nematic transition temperature of pure particles B. The last discontinuity temperature, $T'_{tr}(c)$, indicates the isotropic-nematic transition of particles C. Within error bars, this surface is a horizontal plane at the bottom of the diagram and is present for most concentrations within the demixing region. This surface is analogous to and includes the horizontal line $T'_{tr}(c)$ of the binary system with $\varepsilon = 0.2$. Its temperature is close to that of isotropic-nematic transition of particles C ($T_{tr}(\varepsilon = 0.2)$).

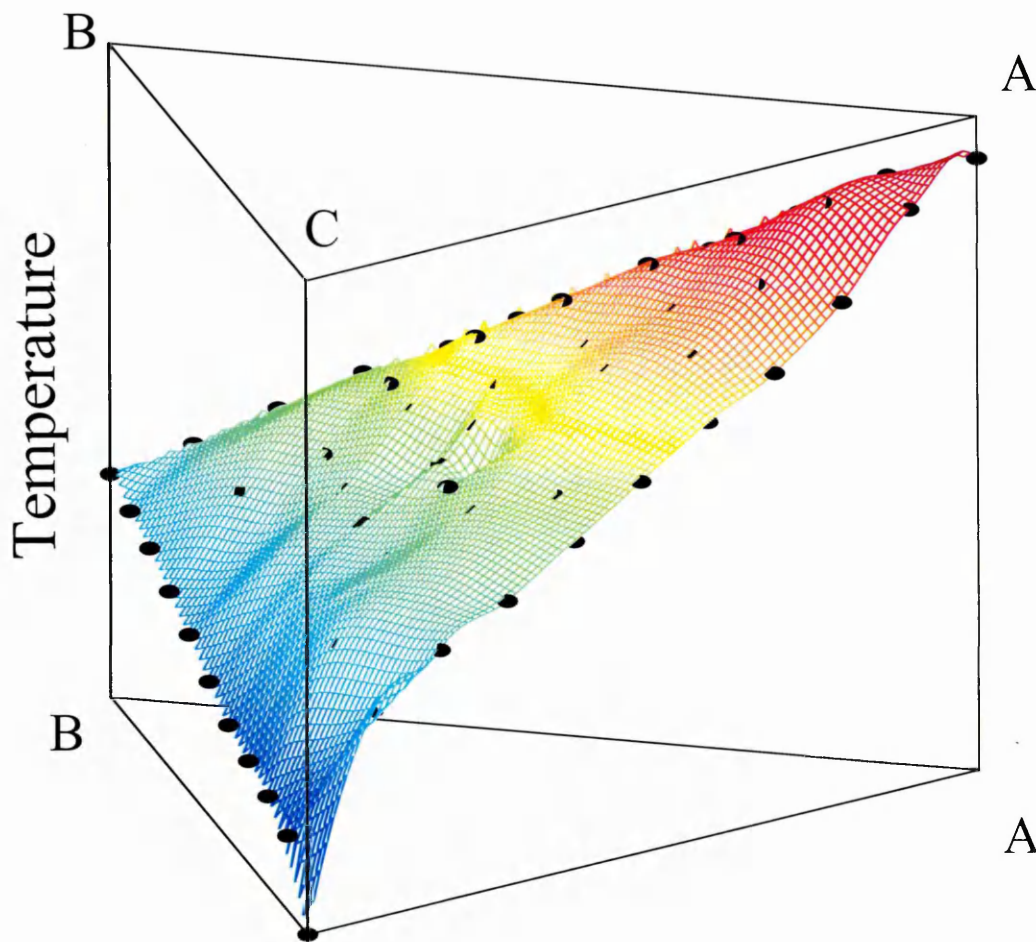


Figure 7.19: 3D phase diagram. The surface of isotropic nematic phase transition temperature $T_{tr}(c)$ for the ternary mixture. For convenience, the color gradient represents the temperature value for any given point on the surface.

Let us now discuss the rest of the data, presented on 3D phase diagrams (Figures 7.19-7.21). Owing to the amount of data produced, we concentrate only on the two surfaces that represent the $T_{tr}(c)$ and $T_d(c)$ discontinuity temperatures.

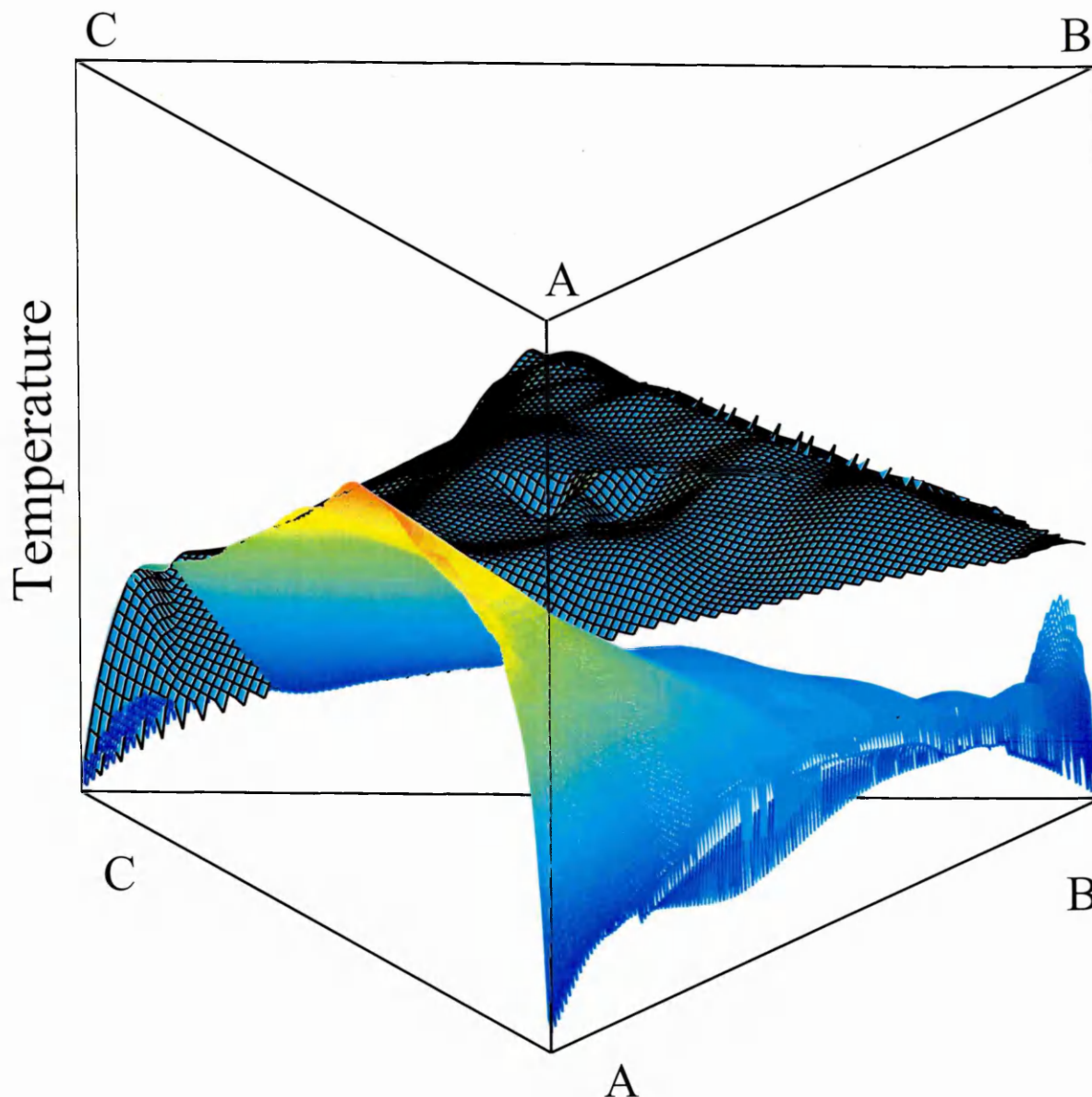


Figure 7.20: 3D phase diagram. $T_{tr}(c)$ and $T_d(c)$ surfaces for the ternary mixture. For convenience, the color gradient on $T_d(c)$ surface represents the temperature value for any given point.

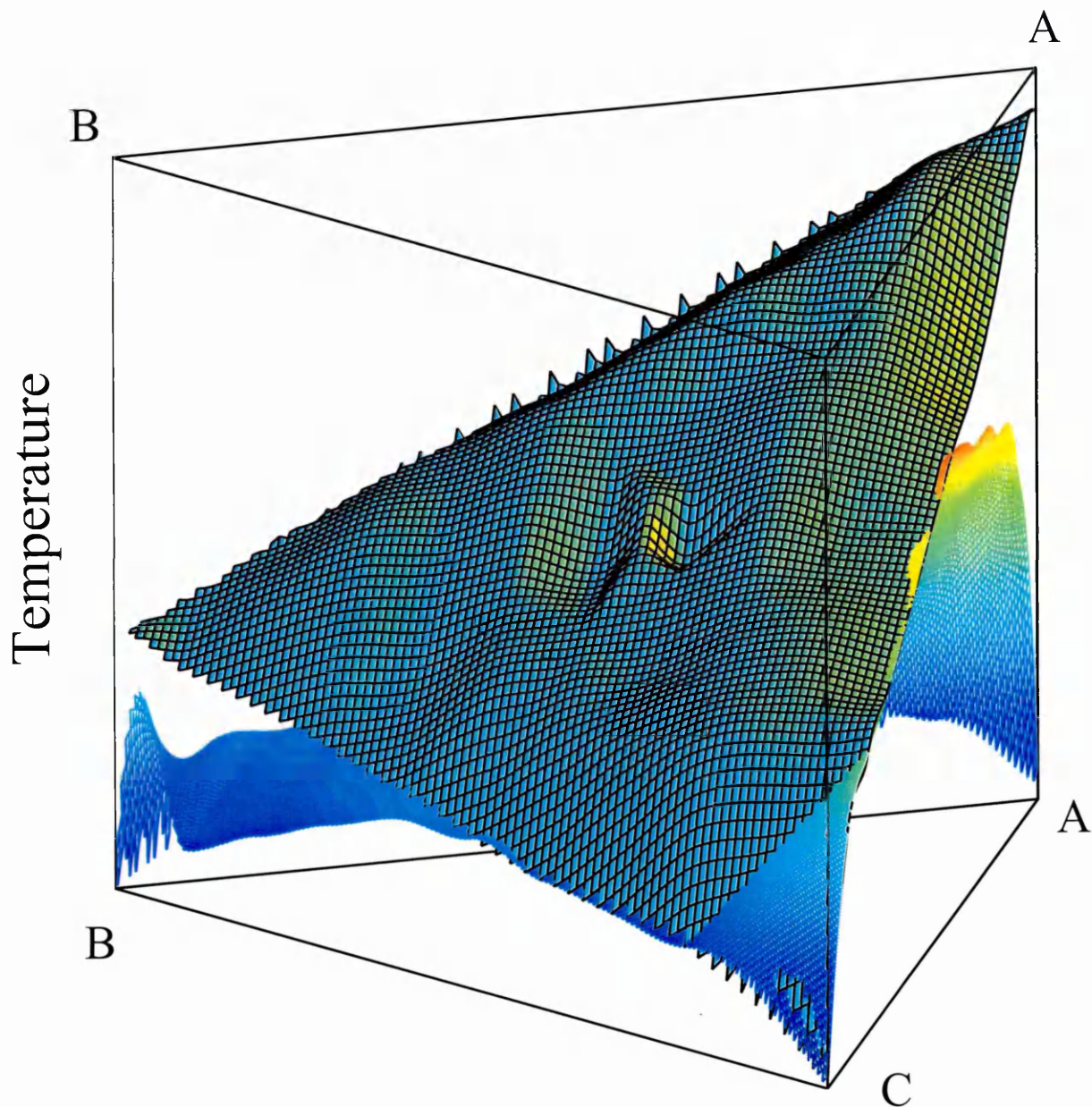


Figure 7.21: 3D phase diagram from an alternative viewing angle. $T_{tr}(c)$ and $T_d(c)$ surfaces for the ternary mixture. For convenience, the color gradient on $T_d(c)$ surface represents the temperature value for any given point.

Following the order adopted previously in this work we first discuss the isotropic-nematic surface $T_{tr}(c)$ ($c = (c_A, c_B, c_C)$) presented in Figure 7.19. The expected shape of the surface based on extrapolation of the behaviour of binary mixtures (Chapter 5 and Section 7.2) agrees, in general, with that presented in Figure 7.19. However, there are some important differences. The first is that the surface at a short distances from the faces of the 3D prism, extends to slightly higher temperatures than would be predicted. In other words, the surface constrained by the curves on

the three faces, does not have the minimum area, as expected, but rather forms bulges near the faces. The lowering of the surface on the faces and in the middle of the prism recalls the effect in binary system (Chapter 5). Phase diagrams for all systems with $\varepsilon \leq 0.45$ showed the isotropic-nematic curve to approach the ideal theoretical line most closely either in the region of equal concentration of the two components or in the region of the pure components ($c = 0.0$ and $c = 1.0$). In all other cases, the value of $T_{tr}(c)$ was found to be higher than the ideal behaviour line. This effect was discussed in Section 5.4 and was linked to the fact that the growing demixing envelope was distorting the $T_{tr}(c)$ curve. Thus we link the bulge and the minimum in the middle of the $T_{tr}(c)$ surface to the presence of the demixing region which distorts this surface. However, we are unable to draw any specific conclusions, because of the limited number of systems investigated.

The second surface to discuss is the surface $T_d(c)$. As mentioned above, for high concentrations of particles C this surface couples with $T_{tr}(c)$ surface distorting it slightly. We will concentrate on the part of the $T_d(c)$ surface that does not couple with $T_{tr}(c)$ surface. This is a region between face AB and the plane which roughly goes through the middle of faces CA and CB . The $T_d(c)$ surface along with the $T_{tr}(c)$ surface outline the boundaries for the homogeneous nematic phase. The nematic region extends to high temperatures in corner A of the prism, while $T_{tr}(c)$ surface constricts it in corner B. This behaviour is the same as that of the binary mixture with $\varepsilon = 0.60$ (AB mixture). As the concentration of particles C increases, surface $T_{tr}(c)$ moves to lower temperatures, while surface $T_d(c)$ extends to higher temperatures. Eventually, the two surfaces couple as the concentration of particles C reaches approximately 0.3. The coupling of the two surfaces does not seem to depend significantly on the relative concentration of the remaining two components (A and B). This agrees well with the previous results of binary systems. The values of the coupling constants for both A and B particles is higher than that for C particles. Thus, the relative concentration of particles A and B in ternary system is not expected to influence the position of the point at which coupling of the two surfaces occurs with respect to C plane. In other words, the point or rather line of coupling of the two surfaces should satisfy the relation (7.10), which in conjunction with relation (7.1) gives $c_C \approx 0.3$.

$$C_A + C_B \approx 1 - 0.3 \quad (7.10)$$

Phase diagrams for three planes (Figures 7.8, 7.13 and 7.18) do not show the nematic region on both sides of the concentration axis, unlike phase diagrams for binary mixtures (for example Figure 5.27 on page 93). In cases of planes A and B this is due to the fact that the limits $c_A \rightarrow 0.0$ and $c_B \rightarrow 0.0$ correspond to 50/50 binary mixtures of particles B and C, and A and C respectively, for which the nematic region is absent. In the case of plane C, however, the reason lies in the insufficient number of data points considered around $c_C \rightarrow 1.0$; otherwise we would certainly expect to see a small region of homogeneous nematic phase in the region of high c_C for the plane C.

We now briefly describe the remaining two surfaces, not present on the 3D phase diagrams shown. From the 2D phase diagrams discussed it is clear that the value of $T_{dd}(c)$ appears to be horizontal throughout the entire concentration range available for this surface (i.e. limited by surfaces $T_{tr}(c)$ and $T_d(c)$). We expected the $T_{dd}(c)$ surface to be tilted with higher temperature values closer to corner B and decreasing in the area closer to corner C. The reason for this was that the remaining isotropic phase and , hence, the $T_{dd}(c)$ temperature should be different for different values of c_B and c_C , given the data obtained from binary mixtures. Nonetheless, the $T_{dd}(c)$ surface proved virtually independent of concentration. This near-horizontal $T_{dd}(c)$ surface cannot be explained trivially and requires further investigation.

The $T'_{tr}(c)$ surface is also horizontal, similar to $T_{dd}(c)$ surface. This case is analogous to that of the binary system and, therefore, does not require any discussion additional to that which was given in Section 5.4. We may simply note that owing to the fact that all three components of the system are well demixed the behaviour of the system can be considered in terms of each individual component.

7.4.1 Interesting Observations

In Section 7.3.2 we presented results for a 50/50 binary mixture of mesogens A and C, diluted in the solution of particles B. For this particular concentration constrain, the $\langle P_2(T)^B \rangle$ curves all crossed at $T \approx 0.43$, $P_2(T) \approx 0.1$ (Figure 7.11(b)). For $c_B = 1.0$ the $\langle P_2(T)^B \rangle$ curve increases sharply at $T \approx 0.43$. As c_B decreases, the increase in $\langle P_2(T)^B \rangle$ occurs at progressively higher temperatures, owing to the increased ratio of particles A. These results raise the prospect that for any ternary mixture of

mesogens studied, it maybe possible to find a concentration ratio of particles A and C for which addition of a third component B will not affect the isotropic-nematic transition temperature throughout the entire concentration range c_B , but will affect the structure of the phase behaviour below $T_{tr}(c)$. Common sense suggests that the ratio of particles A and C has to be chosen such that $T_{tr}(c)$ for this binary mixture should coincide with $T_{tr}(c)$ of pure system of particles B.

In Figures 7.7, 7.12 and 7.17 we showed the radial distribution functions of unlike particles for planes A, B and C respectively. From these figures two main conclusions can be drawn about the three distribution functions, $g^{AB}(r = 1, T)$, $g^{CA}(r = 1, T)$ and $g^{CB}(r = 1, T)$. The first is that the general behaviour of each function does not depend on concentration. As temperature decreases, the gradient of $g^{AB}(r = 1, T)$ changes its sign three times, while that of $g^{CB}(r = 1, T)$ changes its sign once and the sign of the gradient of $g^{CA}(r = 1, T)$ remains unchanged for all concentrations, except very low concentrations. When the concentration of any of the components is less than 0.1, the minima or maxima of the relevant distribution function are diminished. Therefore, the behaviour of these three functions is dictated by the difference in the coupling constant of particles. The second conclusion is that the values of the three distribution functions at high ($T > T_{tr}(c)$) and low ($T \rightarrow 0.0$) temperatures can be explicitly determined from the concentration of the system. For high temperatures, all three components are well mixed and the probability to encounter particles of any two different types is directly dependent on the concentrations of these types only, irrespective of the difference in the coupling values. For low temperatures, however, the coupling constants are important in determining the $g(r = 1, T)$ values, although their influence is constant for all concentrations and knowledge of the exact values of coupling constants is not required. It is sufficient to know whether the value for one type is greater or smaller than the other. In the case of system investigated, it reads as:

$$\varepsilon_A > \varepsilon_B > \varepsilon_C \quad (7.11)$$

From these conclusions, the following general consequences can be derived. The distribution function of unlike particles for which the difference in the values of ε is the greatest (e.g. $g^{CA}(r = 1, T)$ in the system studied) will always approach zero value as $T \rightarrow 0.0$. The particles with highest level of anisotropy (A) always separate first segregating into the nematic phase, as temperature decreases. In

addition, the minimum in $g^{AB}(r = 1, T)$ (which will be discussed shortly) always coincides with a maximum in $g^{CB}(r = 1, T)$ and indicates the separation of the three components in a topology where particles B form a wall or shell, which separates particles A and C. For approximately equal proportions of the three components (e.g. $c_A \approx c_B \approx c_C \approx 0.33 \pm 0.1$) the values of the distribution functions $g^{AB}(r = 1, T)$ and $g^{CB}(r = 1, T)$ approach equal values for both $T \rightarrow 0.0$ and $T > T_{tr}(c)$, irrespective of relation (7.11). The equality of $g^{AB}(r = 1, T)$ and $g^{CB}(r = 1, T)$ at low temperatures means that the topology of the completely demixed system is either flat (layers, films), or cylindrical, where particles A and C form similar structures. For example, if $g^{CB}(r = 1, T \rightarrow 0.0)$ is slightly higher than $g^{AB}(r = 1, T \rightarrow 0.0)$ (Figures 7.7(a), 7.17(e,f)) then the topology of the system is a cylinder or sphere of particles A wrapped in a film of particles B, which floats in a bulk of particles C. If $g^{CB}(r = 1, T \rightarrow 0.0) < g^{AB}(r = 1, T \rightarrow 0.0)$, then the topology is similar but particles A and C swap. The suggestion made earlier about the kink in $g^{AB}(r = 1, T)$ for the binary system presented in Figure 5.25 (page 90) can also be used to explain the behaviour of the $g^{AB}(r = 1, T)$ curve in the ternary mixture. However, in the case of the binary system, the mixture was already separated and the only influence on the area of the interface or perturbation of the shape of the interface was due to the first order I-N transition of the less anisotropic particles. The kink in $g^{AB}(r = 1, T)$ in the ternary system is also associated with separation of particles B and C, as well as the I-N transition of particles B. While separating, particles C try to avoid contact with particles A, therefore increasing the contact area between particles A and B, hence the kink in $g^{AB}(r = 1, T)$ for temperatures below $T_{dd}(c)$.

Having presented this argument, the effect of the I-N transition in both cases should not be underestimated, as it might be a reason for the horizontal appearance of the $T_{dd}(c)$ surface, the value of which coincides with the position of the kink (the minimum of $g^{AB}(r = 1, T)$, to be precise). It is possible that particles B gradually develop ordered regions around the separated A-rich nematic drops or layers around temperatures of the I-N transition of the pure component B, which coincides with the temperature value of $T_{dd}(c)$ surface and the kink. In binary systems, the magnitude of the kink in $g^{AB}(r = 1, T)$, relative to the difference between maximum and minimum values of $g^{AB}(r = 1, T)$ on the entire temperature range, decreases with increase of nematic drop size. In the case of the ternary system it also decreases, suggesting similarities with the binary mixtures.

Chapter 8

Conclusions And Future Work

Here we summarise main points discussed in this Thesis and suggest possible further developments. We start with the binary systems and conclude with ternary mixtures.

The phase behaviour of binary mixtures was studied using the Lebwohl-Lasher model in $NcVT$ and $N\Delta\mu VT$ ensembles for a comprehensive range of concentrations, temperatures and coupling constants. The simulation data were compared with existing experimental and simulation results and theoretical predictions and were found to be in reasonable agreement. The Lebwohl-Lasher model is one of the simplest models, nonetheless it produced some interesting results and motivated some ideas, which helped in the understanding of the processes that influence the phase behaviour of the system. This phase behaviour was additionally considered in the alternative, temperature - coupling constant plane, and attempts were made to determine its generic form analytically (Section 6.5.4). Also it was shown that the asymmetry of the demixing region was solely due to the orientational anisotropy properties of the system investigated, and that the coupling of two I+N coexistence regions occurs at $\varepsilon_{coup} \approx 0.52$. Further work on these systems could, therefore, concentrate on formulation of more precise generic analytical descriptions of the phase behaviour in binary mixtures of mesogens. A significant additional step would then be to extend this approach to ternary mixtures.

During our studies of binary mixtures, novel approaches were suggested for the determination of the phase boundaries. In addition, evidence of the correlation between the change in the short range radial distribution and the isotropic-nematic transition was presented and discussed. This function has not been used previously to indicate

the isotropic-nematic transition. Also, this change in the structure on the short range might be the reason for the enhanced temperature of the transition. Thus, further studies of this effect are required, as it could yield a deeper understanding of the processes that determine the isotropic-nematic transition temperature in mixtures. Some features of the phase diagram (e.g. phase re-entrance predicted by G. Luckhurst [177]) were difficult to determine in the Canonical Ensemble, whereas other features (e.g. the boundary between the two phase coexistence regions I+N and N+N) were difficult to determine in the Semi Grand Canonical Ensemble. In both $NcVT$ and $N\Delta\mu VT$ ensembles, however, the phase diagrams revealed isotropic, nematic, and coexistence regions. The data from both ensembles were found to be in good agreement. The ternary mixture was studied in Canonical Ensemble only, whereas the advantage of using both ensembles was clearly shown in Chapters 5 and 6. Therefore, the future work could lie in improving the lattice model for ternary systems to work in the Semi Grand Canonical Ensemble as well.

On the phase diagrams for the binary mixtures, the slope of the I-N boundary was found to change with decrease of ε . However for $\varepsilon \lesssim \varepsilon_{coup}$ the slope remained approximately unchanged with ε , owing to the effect of the demixing processes in the mixture. This caused the isotropic-nematic transition temperature to be higher than expected. Also, the enhanced isotropic-nematic transition temperature in the remaining part of the $T_{tr}(c)$ curve created the ‘minimum’ in the middle. The 3D phase diagram for the ternary mixture also revealed a minimum on the $T_{tr}(c)$ surface in the region corresponding to equal concentrations of the three types of particle, as well as enhanced transition temperatures in other areas of the $T_{tr}(c)$ surface (as speculated in the beginning of Chapter 7). Suggested reasons for this are the influence of the demixing envelope in the area of high concentration of less anisotropic particles and changes in the short range structure of the mixture in the area of high concentration of more anisotropic particles. Future work, therefore, could concentrate on investigating the mechanisms that cause these enhanced transition temperatures and the ‘minimum’ in the middle of the $T_{tr}(c)$ surface.

The size of the system as well as the introduction of another type of anisotropic particles was found to reduce the strength of the first-order isotropic-nematic phase transition in binary mixtures. It is, therefore, expected that this effect will be even more marked in ternary mixtures. In addition, introduction of a third component into the model without changing system size would increase surface effects. Indeed,

the low temperature $g(r)$ results for the ternary mixture systems were subject to topological constraints imposed by the PBCs. When the size of the drop exceeded the limit imposed by the size of the simulation box, the domain turned into either a cylinder or a layer of separated components. Therefore, further investigations into the critical domain size could be undertaken, simulating much larger number of particles, so as to reduce this topological effect. Another extension of the work may lie in increasing the number of components in the system. Owing to the fact that, in reality, it is often difficult to achieve a 100% pure material, further simulation studies of poly-dispersions in mixtures could reveal the reasons for some inconsistencies between theory and the experiment, such as the strength of the isotropic-nematic transition. Our preliminary trial simulations with ten or more types of particle showed that the transition temperature and its strength depend strongly on the type of the distribution of particles with different coupling constants.

Owing to the specifics of the interaction potential used here, the phase diagrams do not show isotropic-isotropic coexistence. As mentioned earlier, this can be easily achieved by introduction of an extra term into the potential. While for binary mixtures this modification will add another phase region at the top of $T_{tr}(c)$ curve, the phase behaviour of ternary mixture for such model is difficult to imagine. Thus, further work may involve an investigation of poly-dispersed mixtures with one or more isotropic terms introduced to the interaction potential.

During the studies of ternary mixtures, many other uncertainties have arisen. Future work may, therefore, be dedicated to resolving these numerous uncertainties. Perhaps, the most interesting one is independence of the $T_{ad}(c)$ surface on concentration. Therefore, the detailed investigation of the processes behind the transition $T_{ad}(c)$ could be undertaken to obtain a better understanding of why this surface appears horizontal. One of the necessary conditions for this would be increase of the size of the system. Simulation studies of ternary systems and the systems with the higher number of components are relatively few. This is mainly due to the complexity of the problem. However, the model investigated in this thesis provides a cheap alternative to more complex models for such studies. Also, as the number of investigations in this area increases it would be useful to devise an appropriate visualisation approach to adequately represent the amount of information these systems produce. Perhaps, the solution lies in the employment of interactive visualisation applications, similar to that provided in Appendix A.

Appendix A

The Compact Disc.

Bibliography

- [1] P. A. Lebwohl and G. Lasher, *Phys. Rev. A* **6**, 426 (1972).
- [2] J. Billard, *Liquid Crystals of One- and Two- Dimensional Order* (Springer Series in Chemical Physics, 1980).
- [3] D. Vorländer, *Kristallinisch Flüssige Substanzen* (Enke, Stuttgart, 1908).
- [4] H. P. Hinov, *Mol. Cryst. Liquid Cryst. Letters* **136**, 221 (1986).
- [5] R. Webster, I. Withers, D. J. Cleaver, Personal Communication, Sheffield Hallam University (2001).
- [6] V. A. Levchenko, *J. Mol. Liq.* **85**, 197 (2000).
- [7] S. Chandrasekhar, *Liquid Crystals* (Cambridge University Press, Cambridge, 1992).
- [8] P. G. de Gennes, *The Physics Of Liquid Crystals* (Clarendon Press, Oxford, 1993).
- [9] S. Singh, *Phys. Rep.* **207**, 351 (1991).
- [10] S. Singh, *Phys. Rep.* **277**, 283 (1996).
- [11] C. Zannoni, in: G. R. Luckhurst, G. W. Gray (Eds.), *The Molecular Physics of Liquid Crystals* (Acad. Press, New York, 1979).
- [12] C. Hammond, *The Basics Of Crystallography And Diffraction* (Oxford University Press, Oxford, 1998).
- [13] S. Jen, N. A. Clarck, P. S. Pershan, E. B. Priestley, *Phys. Rev. Letters* **31**, 1552 (1973).

- [14] I. W. Hamley, S. Garnett, G. R. Luckhurst, S. J. Roskilly J. S. Pedersen, R. M. Richardson, J. M. Seddon, *J. Chem. Phys.* **104**, 10046 (1996).
- [15] V. N. Tsvetkov, *Acta Physicochim. (USSR)* **16**, 132 (1942).
- [16] R. Gupta, R. A. Vora, *Mol. Cryst. Liq. Cryst.* **106**, 147 (1984).
- [17] R. A. Vora, S. J. Rajput, *Mol. Cryst. Liq. Cryst.* **209**, 265 (1991).
- [18] R. Orwoll, R. Rhyne Jr., S. Christensen, S. Young, *J. Phys. Chem.* **81**, 181 (1977).
- [19] D. Chen, G. Luckhurst, *Trans. Faraday Soc.* **65**, 656 (1969).
- [20] M. C. Chang, H. W. Chiu, X. Y. Wang, T. Kyu, N. Leroux, S. Campbell, L. C. Chien, *Liq. Cryst.* **25**, 733 (1999).
- [21] T. Bouchaour, F. Benmouna, L. Leclercq, B. Ewen, X. Coqueret, M. Benmouna, U. Maschke, *Liq. Cryst.* **27**, 413 (2000).
- [22] P. J. Flory, *Principles of Polymer Chemistry* (Cornell University Press, Ithaca, 1965).
- [23] C. Khetrpal, N. Suryaprakash, S. Vivekanandan, *Chem. Phys. Lett.* **296**, 537 (1998).
- [24] J. Vaara, J. Lounila, J. Jokisaari, *Chem. Phys. Lett.* **296**, 541 (1998).
- [25] L. R. Humphries, P. G. James, G. R. Luckhurst, *Symp. Faraday Soc.* **5**, 107 (1971).
- [26] P. Palffy-Muhoray, D. A. Dunmur, W. H. Muller, D. A. Balzarini, *Liquid Cryst. and Ordered Fluids* **4**, 615 (1984).
- [27] C. Casagrande, M. Veyssie, H. Finkelmann, *J. de Physique Lettres* **43**, 671 (1982).
- [28] F. Benmouna, B. Peng, J. Ruhe, *Liquid Cryst.* **26**, 1655 (1999).
- [29] R. Pratibha, N. V. Mathusudana, *Mol. Cryst. Liquid Cryst. Letters* **1**, 111 (1985).
- [30] G. R. Luckhurst, *Mol. Cryst. Liquid Cryst.* **21**, 125 (1973).

- [31] F. Reinitzer, *Monatsh. Chem.* **9**, 421 (1888).
- [32] G. Friedel, *Ann. de Phys.* **18**, 273 (1922).
- [33] G. Pelzl, D. Demus, H. Sackmann, *Z. Phys. Chem.* **228**, 23 (1968).
- [34] G. Friedel, *Ann. de Phys.* **18**, 452 (1922).
- [35] O. Lehmann, *Z. Phys. Chem.* **4**, 462 (1889).
- [36] O. Lehmann, *Flüssige Kristalle* (Engelmann, Leipzig, 1904).
- [37] D. Vorländer, *Ber.* **39**, 803 (1906).
- [38] L. Gattermann, A. Ritschke, *Ber.* **23**, 1738 (1890).
- [39] F. Meyer, K. Dahlen, *Ann. Chem.* **326**, 331 (1903).
- [40] V. Fredericksz, V. Zolina, *Trans. Faraday Soc.* **29**, 919 (1933).
- [41] G. Foex, *Trans. Faraday Soc.* **29**, 958 (1933).
- [42] J. Zadoc-Kahn, *Ann. Physique (Series 2)* **6**, 455 (1936).
- [43] V. N. Tsvetkov, *Acta Physicochim. (USSR)* **19**, 86 (1944).
- [44] N. A. Tolstoi, L. N. Fedotov, *J. Exp. Theor. Phys. (USSR)* **17**, 564 (1947).
- [45] V. N. Tsvetkov, E. I. Ryumtsev, *Sov. Phys.-Crystallogr.* **13**, 225 (1968).
- [46] J. S. Dave, K. L. Vasanth, *Indian. J. Chem. Soc.* **7**, 498 (1969).
- [47] A. D. L. Chandani, T. Hagiwara, Y. Suzuki, Y. Ouchi, H. Takezoe, A. Fukuda, *Jap. J. Appl. Phys.* **27**, 729 (1988).
- [48] J. Lee, A. D. L. Chandani, K. Itoh, Y. Ouchi, H. Takezoe, A. Fukuda, *Jap. J. Appl. Phys.* **29**, 1122 (1990).
- [49] H. Orihara, T. Fujikawa, Y. Ishibashi, Y. Yamada, N. Yamamoto, K. Mori, I. Nakamura, Y. Suzuki, *Jap. J. Appl. Phys.* **29**, 333 (1990).
- [50] S. Merino, M. R. de la Fuente, Y. Gonzales, M. A. Perez Jubindo, B. Ros, J. A. Puèrtolas, *Phys. Rev. E* **54**, 5169 (1996).

- [51] Yu. P. Panarin, O. Kalinovskaya, J. K. Vij, J. W. Goodby, *Phys. Rev. E* **55**, 4345 (1997).
- [52] M. Buivydas, F. Gouda, S. T. Lagerwall, B. Stebler, *Liq. Cryst.* **23**, 77 (1997).
- [53] N. M. Shtykov, J. K. Vij, V. P. Panov, R. A. Lewis, M. Hird, J. W. Goodby, *J. Mater. Chem.* **9**, 1383 (1999).
- [54] Yu. P. Panarin, O. Kalinovskaya, J. K. Vij, *Appl. Phys. Letters* **72**, 1667 (1998).
- [55] K. Hiraoka, T. Tsumita, Y. Sugiyama, K. Monzen, Y. Uematsu, Y. Suzuki, *Jap. J. Appl. Phys.* **36**, 6847 (1997).
- [56] J. W. O'Sullivan, Yu. P. Panarin, J. K. Vij, A. J. Seed, M. Hird, J. W. Goodby, *Mol. Cryst. Liq. Cryst.* **4**, 997 (1997).
- [57] P. J. Collings, M. Hird, *Introduction To Liquid Crystals* (Taylor & Francis Ltd. London, 1997).
- [58] J. Watanabe, H. Komura, T. Niiori, *Liq. Cryst.* **13**, 455 (1993).
- [59] R. F. Bruinsma, C. R. Safina, *Phys. Rev. A* **43**, 5377 (1991).
- [60] E. A. L. Mol, G. C. L. Wong, J. M. Petit, F. Rieutord, W. H. de Jeu, *Physica B* **248**, 191 (1998).
- [61] Y. Takanishi, K. Hiraoka, V. K. Agrawal, H. Takezoe, A. Fukuda, M. Matsushita, *Jap. J. Appl. Phys.* **30**, 2023 (1991).
- [62] S. H. J. Idziak, C. R. Safinya, R. S. Hill, K. E. Kraiser, M. Ruths, H. E. Warriner, S. Steinberg, K. S. Liang, J. N. Israelachvili, *Science* **264**, 1915 (1994).
- [63] R. J. Plano, C. R. Safinya, E. B. Sirota, L. J. Wenzel, *Rev. Sci. Instruments* **64**, 1309 (1993).
- [64] R. G. Larson, *Rheol. Acta* **31**, 497 (1992).
- [65] J. W. Emsley, G. R. Luckhurst, C. P. Stockley, *Mol. Phys.* **44**, 565 (1981).
- [66] R.T. Syvitski, J.M. Polson, E.E. Burnell, *Int. J. Mod. Phys. C* **10**, 403 (1999).

- [67] T. Chandrakumar, E. E. Burnell, *Mol. Phys.* **90**, 303 (1997).
- [68] D. Sandstrom, A. V. Komolkin, A. Maliniak, *J. Chem. Phys.* **104**, 9620 (1996).
- [69] P. J. Barnes, A. G. Douglass, S. K. Heeks, G. R. Luckhurst, *Liq. Cryst.* **13**, 603 (1993).
- [70] J. B. S. Barnhoorn, C. A. Delange, E. E. Burnell, *Liq. Cryst.* **13**, 319 (1993).
- [71] J. W. Emsley, *Israel J. Chem.* **28**, 297 (1988).
- [72] G. R. Luckhurst, *J. Chem. Soc. Farad. Trans. II* **84**, 961 (1988).
- [73] D. Catalano, C. Forte, C. A. Veracini, J. W. Emsley, G. N. Shilstone, *Liq. Cryst.* **2**, 357 (1987).
- [74] B. Janik, E. T. Samulski, H. Toriumi, *J. Phys. Chem.* **91**, 1842 (1987).
- [75] D. Goldfarb, E. Lifshitz, H. Zimmermann, Z. Luzz, *J. Chem. Phys.* **82**, 5155 (1985).
- [76] , *Mol. Phys.* **90**, 303 (1997).
- [77] F. Roussel, J. P. Bayle, M. A. Khan, B. M. Fung, O. Yokokohji, T. Shimizu, H. Koh, S. Kumai, *Liq. Cryst.* **26**, 251 (1999).
- [78] G. R. Luckhurst and R. N. Yeates, *J. Chem. Soc. Faraday Trans.* **72**, 996 (1976).
- [79] D. Ionescu, G. R. Luckhurst, D. S. De Silva , *Liq. Cryst.* **23**, 833 (1997).
- [80] C. J. Dunn, P.J. Le Masurier, G. R. Luckhurst, *Phys. Chem. Chem. Phys.* **1**, 3757 (1999).
- [81] A. Arcioni, T. Tarroni, and C. Zannoni, *J. Chem. Soc. Faraday Trans.* **87**, 2457 (1991).
- [82] S. Jen, N. A. Clark, P. S. Pershan, E. B. Priestley, *J. Chem. Phys.* **66**, 4635 (1977).
- [83] L. G. P. Dalmolen, S. J. Picken, A. F. de Jong, W. H. de Jeu, *J. Phys. (Paris)* **46**, 1443 (1985).

- [84] G. N. Andreev, B. Jordanov, E. H. Korte, B. Schrade, *Appl. Spect.* **51**, 1753 (1997).
- [85] P. G. de Gennes, *C. R. Acad. Sci. B (Paris)* **274**, 142 (1972).
- [86] R. M. Richardson, J. M. Allman, G. J. McIntyre, *Liq. Cryst.* **7**, 701 (1990).
- [87] F. Jede, A. W. Stratmann, B. Schrader, *Mol. Cryst. Liquid Cryst.* **140**, 287 (1986).
- [88] A. J. Leadbetter, E. K. Norris, *Mol. Phys.* **38**, 669 (1979).
- [89] T. W. Stinson, J. D. Litster, *Phys. Rev. Letters* **25**, 503 (1970).
- [90] T. W. Stinson, J. D. Litster, *J. Appl. Phys.* **41**, 996 (1970).
- [91] T. W. Stinson, J. D. Litster, *Phys. Rev. Letters* **30**, 688 (1973).
- [92] E. I. Rjumtsev, M. A. Osipov, T. A. Rotinyan, N. P. Yevlampieva, *Liq. Cryst.* **18**, 87 (1995).
- [93] A. Adamczyk, *Mol. Cryst. Liq. Cryst.* **167**, 7 (1989).
- [94] C. Rosenblatt, A. C. Griffin, U. Hari, G. R. Luckhurst, *Liq. Cryst.* **9**, 831 (1991).
- [95] K. Fuhrmann, A. Martin, G. Maret, U. Tiesler, M. Ballauff, *J. Chem. Phys.* **98**, 4094 (1994).
- [96] N. Blachnik, H. Knepe, F. Schneider, *Liq. Cryst.* **27**, 1219 (2000).
- [97] S. J. Rzoska, J. Ziolo, *Liq. Cryst.* **17**, 629 (1994).
- [98] S. J. Rzoska, A. D. Rzoska, J. Ziolo, *Phys. Rev. E* **54**, 6452 (1996).
- [99] S. J. Rzoska, A. D. Rzoska, J. Ziolo, *Liq. Cryst.* **21**, 273 (1996).
- [100] S. J. Rzoska, A. D. Rzoska, J. Ziolo, *Phys. Rev. E* **55**, 2888 (1997).
- [101] A. D. Rzoska, *Liq. Cryst.* **24**, 835 (1998).
- [102] S. Koltzenburg, D. Wolff, J. Springer, O. Nuyken, *J. Polymer Sci. A* **36**, 2669 (1998).

- [103] F. Elias, S. M. Clarke, R. Peck, E. M. Terentjev, *Macromolecules* **33**, 2060 (2000).
- [104] F. Benmouda, B. Peng, J. R \ddot{u} he, D. Johannsmann, *Liq. Cryst.* **26**, 1655 (1999).
- [105] J. R. Dorfman, T. R. Kirkpatrick, J. V. Sengers, *Ann. Phys. Chem.* **45**, 213 (1994).
- [106] J. Mayer, T. Waluge, J. A. Janik, *Phys. Letters A* **41**, 102 (1972).
- [107] M. Sorai, T. Nakamura, S. Seki, *Bull. Chem. Soc. Japan* **47**, 2192 (1974).
- [108] M. A. Anisimov, V. M. Zaprudskii, V. M. Mamnitskii, E. L. Sorkin, *JETP Letters* **30**, 491 (1979).
- [109] M. A. Anisimov, S. R. Garber, V. S. Esipov, V. M. Mamnitskii, G. I. Ovodov, L. A. Smolenko, E. L. Sorkin, *Sov. Phys. JETP* **45**, 1042 (1977).
- [110] L. J. Yu, M. M. Labes, *Mol. Cryst. Liq. Cryst.* **54**, 1 (1979).
- [111] M. M. Naoum, G. R. Saad, R. I. Nessim, T. A. A. Aziz, *Liq. Cryst.* **25**, 165 (1998).
- [112] M. M. Naoum, A. A. Mansour, A. A. Bayoumy, *Liq. Cryst.* **27**, 243 (2000).
- [113] M. M. Naoum, A. A. Mansour, A. A. Bayoumy, *Liq. Cryst.* **27**, 177 (2000).
- [114] M. M. Naoum, R. I. Nessim, T. Y. Labeeb, *Liq. Cryst.* **27**, 889 (2000).
- [115] O. Kovalchuk, V. Reshetnyak, V. Yarmolenko, O. Yaroshchuk, *Mol. Cryst. Liq. Cryst.* **4**, 2487 (1998).
- [116] E. Wessels, US Patent Application **A1**, 20020077380 (2001).
- [117] A. Tomita, P. J. Jones, *SPIE Proceedings* **1665**, 274 (1992).
- [118] T. Bunning, John H. Dillon Medal Symposium **Session J2**, 001 (2002).
- [119] Y. H. Cho and B. K. Kim, *J. Polym. Sci., Phys.* **36**, 1393 (1998).
- [120] H. Finkelmann, H. J. Kock, G. Rehage, *Mol. Cryst. Liq. Cryst.* **89**, 23 (1982).
- [121] F. Benmouna, A. Daoudi, F. Roussel, L. Leclercq, J. M. Buisine, X. Coqueret, M. Benmouna, B. Ewen, U. Maschke, *Macromolecules* **33**, 960 (2000).

- [122] T. Kyu, H. W. Chiu, *Mol. Cryst. Liq. Cryst.* **287**, 27 (1996).
- [123] H. W. Chiu, T. Kyu, *J. Chem. Phys.* **103**, 7471 (1995).
- [124] Arnold-Sackman, *Z. Phys. Chem.* **213**, 145 (1960).
- [125] L. Onsager, *Ann. N. Y. Acad. Sci.* **51**, 627 (1949).
- [126] P. G. de Gennes, *Phys. Letters A* **30**, 454 (1969).
- [127] L. D. Landau, E. M. Lifshitz, *Statistical Physics, Vol. 1* (Pergamon, Oxford, 1980).
- [128] T. E. Faber, *Proc. Roy. Soc. London Ser. A* **375**, 579 (1982).
- [129] W. Maier, A. Saupe, *Z. Naturforsch. A* **13**, 564 (1958).
- [130] M. A. Cotter, *J. Chem. Phys.* **66**, 1098, 4710 (1977).
- [131] B. A. Baron, W. M. Gelbart, *J. Chem. Phys.* **67**, 5795 (1977).
- [132] P. Palfy-Muhoray, B. Bergesen, *Phys. Rev. A* **6**, 2704 (1987).
- [133] B. Cabane, W. G. Clark, *Phys. Rev. Letters* **25**, 91 (1970).
- [134] P. G. de Gennes, *Mol. Cryst. Liquid Cryst.* **12**, 193 (1971).
- [135] W. E. Morrell, J. H. Hildebrand, *J. Chem. Phys.* **4**, 224 (1936).
- [136] R. J. Field and M. Burger, *Oscillations and Traveling Waves in Chemical Systems* (John Wiley & Sons, Inc, 1985).
- [137] P. B. Belousov, A. M. Zhabotinskiy , *Local Journal*. Belousov was not able to get his discovery published until 1958. The first English translation of his original manuscript appeared in [136] (1951).
- [138] J. J. Tyson, *The Belousov-Zhabotinskii Reaction. Managing Ed. S. Levin. Lecture Notes in Biomathematics.* (Berlin: Springer-Verlag, 1976).
- [139] N. Metropolis, A. W. Rosenbluth, M. N. Rosenbluth, A. H. Teller, E. Teller, *J. Chem. Phys.* **21**, 1087 (1953).
- [140] M. P. Allen, D. J. Tildesley, *Computer Simulation of Liquids* (Clarendon Press, Oxford, 1987).

- [141] B. J. Alder and T. E. Wainwright, *J. Chem. Phys.* **27**, 1208 (1957).
- [142] B. J. Alder and T. E. Wainwright, *J. Chem. Phys.* **31**, 459 (1959).
- [143] A. Rahman, *Phys. Rev.* **136**, 405 (1964).
- [144] J. M. Hammersley, D. C. Handscomb, *Monte Carlo Methods* (Methuen, 1964).
- [145] N. Metropolis, S. Ulam, *J. Am. Stat. Ass.* **44**, 335 (1949).
- [146] W. Maier, A. Saupe, *Z. Naturforsch. A* **14a**, 882 (1959).
- [147] W. Maier, A. Saupe, *Z. Naturforsch. A* **15**, 287 (1960).
- [148] I. R. McDonald, *Mol. Phys.* **23**, 41 (1972).
- [149] R. Najafabadi, S. Yip, *Scripta Metall* **17**, 1199 (1983).
- [150] M. Mezei, *Mol. Phys.* **40**, 901 (1980).
- [151] M. Creutz, *Phys. Rev. Letters* **50**, 1411 (1983).
- [152] A. Z. Panagiotopoulos, *Mol. Phys.* **61**, 813 (1987).
- [153] A. Z. Panagiotopoulos, N. Quirke, M. Stapleton, D. J. Tildesley, *Mol. Phys.* **63**, 527 (1988).
- [154] J. E. Lennard-Jones, *Proc. Roy. Soc. London A* **106**, 463 (1924).
- [155] W. W. Wood and F. R. Parker, *J. Chem. Phys.* **27**, 720 (1957).
- [156] M. R. Wilson, M. P. Allen, *J. Comp. Mol. Design* **3**, 335 (1989).
- [157] J. G. Gay, B. J. Berne, *J. Chem. Phys.* **74**, 3316 (1981).
- [158] F. Leenhouts, W.H. de Jeu, A. J. Dekker, *J. de Physique* **40**, 989 (1979).
- [159] S. T. Wu, R. J. Cox, *J. Appl. Phys.* **64**, 821 (1988).
- [160] C. Chiccoli, P. Pasini, C. Zannoni, *Int. J. Mod. Phys. B* **11**, 1937 (1997).
- [161] G. Luckhurst, C. Zannoni, *Nature* **267**, 412 (1977).
- [162] E. Bergren, C. Chiccoli, P. Pasini, F. Semeria, C. Zannoni, *Phys. Rev. E* **50**, 2929 (1994).

- [163] U. Fabbri, C. Zannoni, *Molec. Phys.* **58**, 763 (1986).
- [164] C. Chiccoli, P. Pasini, C. Zannoni, *Liq. Cryst.* **2**, 39 (1987).
- [165] G.J. Fuller, G. R. Luckhurst, C. Zannoni, *Chem. Phys.* **92**, 105 (1985).
- [166] C. Chiccoli, P. Pasini, C. Zannoni, *Physica A* **148**, 298 (1988).
- [167] C. Chiccoli, P. Pasini, C. Zannoni, *Liq. Cryst.* **3**, 363 (1988).
- [168] F. Biscarini, C. Chiccoli, P. Pasini, C. Zannoni, *Mol. Phys.* **73**, 439 (1991).
- [169] G. R. Luckhurst, S. Romano, *Mol. Phys.* **40**, 129 (1980).
- [170] E. Bergren, C. Chiccoli, P. Pasini, F. Semeria, C. Zannoni, *Int. J. Mod. Phys. C* **4**, 1041 (1993).
- [171] E. Bergren, C. Chiccoli, P. Pasini, F. Semeria, C. Zannoni, *Phys. Lett. A* **176**, 428 (1993).
- [172] F. Biscarini, C. Chiccoli, P. Pasini, C. Zannoni, *Phys. Rev. Lett.* **75**, 1803 (1995).
- [173] Z. Zhang, O. G. Mouritsen, M. J. Zuckermann, *Phys. Rev. Letters* **69**, 2803 (1992).
- [174] D. Gonin and A. Windle, *Liq. Cryst* **23**, 489 (1997).
- [175] Z. Zhang, M. J. Zuckermann, O. G. Mouritsen, *Molec. Phys.* **80**, 1195 (1993).
- [176] R. Hashim, G. R. Luckhurst, S. Romano, *Liq. Cryst.* **1**, 133 (1986).
- [177] R. Hashim, G. R. Luckhurst, S. Romano, *Proc. R. Soc. Lond. A* **429**, 323 (1990).
- [178] J. M. Polson, E. E. Burnell, *Chem. Phys. Letters* **281**, 207 (1997).
- [179] M. A. Bates, *Phys. Rev. E* **64**, 051702 (2001).
- [180] D. Frenkel, B. Smit, *Understanding Molecular Simulation* (Academic Press, London, 1996).
- [181] M. Born, T. Von Karman, *Physic. Z.* **13**, 297 (1912).

- [182] W. H. Press, B. P. Flannery, S. A. Teukolsky, W. T. Vetterling, *Numerical Recipes in C* (Cambridge University Press, Cambridge, 1988).
- [183] A. M. Ferrenberg, R. H. Swendsen, *Phys. Rev. Lett.* **61**, 2635 (1988).
- [184] R. Friedberg, J. E. Cameron, *J. Chem. Phys.* **52**, 6049 (1970).
- [185] D. J. Cleaver, M. P. Allen, *Phys. Rev. A* **43**, 1918 (1991).
- [186] K. Huang, *Statistical Mechanics* (John Wiley & Sons, 1987).
- [187] J. Lee, J. M. Kosterlitz, *Phys. Rev. Letters* **65**, 137 (1990).
- [188] J. Lee, J. M. Kosterlitz, *Phys. Rev. B* **43**, 3265 (1991).
- [189] E. P. Sokolova, *Russ. J. Appl. Chem.* **67**, 798 (1994).
- [190] E. P. Sokolova, *J. Struc. Chem.* **34**, 747 (1993).
- [191] P. K. Mukherjee, *Mod. Phys. Letters B* **10**, 771 (1996).
- [192] L. V. Yelash, T. Kraska, *Phys. Chem. Chem. Phys.* **1**, 4315 (1999).
- [193] S. Delencos, A. Hadji Sahraoui, C. Kolinsky, J. M. Buisine, *Appl. Phys. A* **70**, 79 (2000).
- [194] F. M. van der Kooij, d. van der Beek, H. n. W. Lekkerkerker, *J. Phys. Chem. B* **105**, 1696 (2001).
- [195] P. K. Mukherjee, *J. Phys. C.M.* **10**, 9191 (1998).
- [196] E. A. Guggenheim, *J. Chem. Phys.* **13**, 253 (1945).
- [197] R. Hashim, G. R. Luckhurst, F. Prata, S. Romano, *Liq. Cryst.* **15**, 283 (1993).